Evaluation of Metal-Rich Primers for the Mitigation of Intergranular Stress Corrosion Cracking in Highly Sensitized Al-Mg Alloy AA5456-H116

A Dissertation

Presented to

the faculty of the School of Engineering and Applied Science

University of Virginia

---

in partial fulfillment
of the requirements for the degree

Doctor of Philosophy

by

Matthew E McMahon

May 2019

APPROVAL SHEET

This Dissertation
is submitted in partial fulfillment of the requirements
for the degree of
Doctor of Philosophy

Author Signature: Matt McMahon

This Dissertation has been read and approved by the examining committee:

Advisor: James Burns, John Scully

Committee Member: Dr. Robert Kelly

Committee Member: Dr. Sean Agnew

Committee Member: Dr. David Green

Committee Member: Dr. Fritz Friedersdorf

Committee Member: ________________________

Accepted for the School of Engineering and Applied Science:

Craig H. Benson, School of Engineering and Applied Science

May 2019

ABSTRACT

The efficacy of sacrificial anode-based cathodic protection for the mitigation of intergranular stress corrosion cracking (IG-SCC) is evaluated in highly sensitized Al-Mg alloy AA5456-H116 in a variety of conditions to inform the design of sacrificial coating systems for use in naval service. Specifically, the robust ability of applied cathodic polarization via potentiostat to successfully mitigate IG-SCC is demonstrated utilizing linear elastic fracture mechanics (LEFM) testing. The IG-SCC mitigation can be achieved despite increased Mg alloying and increased sensitization level in 0.6 M NaCl. These same evaluations in more aggressive NaCl and $MgCl_2$ environments demonstrate that (1) the efficacy of applied cathodic polarization trends with the breakdown potentials for the β and α-Al matrix, which change with environment, and (2) the efficacy of this mitigation method is reduced in increasingly aggressive salinity/pH conditions. Critically, these results confirm that a potential threshold at the β breakdown potential exists in the Al-Mg system, below which IG-SCC may be effectively suppressed. Increasingly negative applied potentials below this threshold are assessed to understand the effective window of applied cathodic potential on Al-Mg. The lower bound is demonstrated to be the applied potential threshold past which alkaline Al corrosion and hydrogen evolution aggressively occur. The IG-SCC phenomenon is demonstrated to occur below this threshold only when a sharp crack tip and elevated stress intensity are present, which is due to the low levels of localized charging that occur at the crack tip under severe cathodic polarization.

A variety of Zn-rich primers (ZRPs) were electrochemically evaluated through previously developed cycle testing as well as a newly developed galvanostatic pulse technique, which confirmed that these sacrificial anodic systems having finite current output and charge capacity are indeed able to maintain the necessary cathodic potentials to mitigate IG-SCC on AA5456-H116. However, these primers differ in their electrochemical polarizability, and their ability to maintain a protective coupled potential as the cathodic AA5456-H116 area increases (such as during crack growth), due to differences in Zn loading/resin choice. The least and most polarizable ZRPs were then evaluated in LEFM testing to evaluate their IG-SCC mitigation capabilities when galvanically coupled to or spray-deposited on highly sensitized AA5456-H116. These results demonstrate that IG-SCC mitigation occurs within a matter of seconds of the application of cathodic potential below the β breakdown threshold, regardless of the source of the potential, at a constant $K = 10$ MPa√m. Through spray-coating with the least polarizable ZRP, IG-SCC mitigation may be achieved over large coating defect widths such as 15 mm, as well as in conditions of varying crack geometry, in saturated NaCl. These findings are informed further through high level chemical stability modeling and experiment to assess secondary Zn^{2+} chemical protection effects.

The present results demonstrate a key list of metal-rich primer attributes necessary to achieve effective IG-SCC mitigation: (1) containing anodic pigments with corrosion potential below the IG-SCC threshold; (2) high pigment volume concentration and connectivity to achieve a consistently high magnitude of anodic charge output; (3) low electrochemical polarizability for robust galvanic coupling performance in dynamic galvanic coupling conditions (such as crack growth); and (4) low pore resistance/fast capacitive discharge response, to reduce delay in responding to an increase in exposed cathode area. These attributes may be optimized for IG-SCC mitigation purposes through specific combinations and selection of resin, pigment type, and loading density. The chemical stability/galvanostatic pulse techniques developed herein will enable more accurate prediction and mechanistic understanding of coating performance for further design optimization.

EXECUTIVE SUMMARY

Al-Mg alloys are currently employed in naval structures due to their combination of high strength-to-weight ratio, general corrosion resistance, and weldability. These alloys become susceptible to intergranular corrosion (IGC) and, with sufficient applied stress, intergranular stress corrosion cracking (IG-SCC) in aggressive marine conditions due to a coupled anodic dissolution – hydrogen embrittlement process involving the localized corrosion of the intergranular β phase (Al_3Mg_2). Cathodic polarization has been demonstrated to mitigate these degradation phenomena in 0.6 M NaCl on 4.5 wt.% Mg AA5083-H131 by maintaining passivity on both the Al surface and the β phase to stifle hydrogen production at the crack tip. However, the extension of this cathodic protection method has yet to be validated in more aggressive, service-relevant marine conditions, nor has this method been demonstrated effective in higher Mg content, more highly sensitized Al-Mg alloys that may also be utilized in naval service. Sacrificial anode-based cathodic protection systems also remain unevaluated for IG-SCC mitigation performance on Al-Mg. Therefore, the objectives of this dissertation are to evaluate the efficacy of cathodic polarization in IG-SCC mitigation on more highly sensitized, higher Mg content AA5456-H116 (relative to the AA5083 composition) over a range of aggressive full immersion saline conditions via potentiostatic control, and to determine if similarly effective mitigation may be achieved through use of anode systems with finite current output and charge capacity, such as Zn-rich primers (ZRP).

This dissertation is structured into four chapters that systematically build a framework to understand the robust nature of cathodic protection on AA5456-H116 under full immersion conditions through use of a potentiostat (infinite anode), pure Zn anodes, and ZRPs (finite anodes having fixed current output and charge capacity) in a variety of testing conditions for IGC/IG-SCC mitigation. The attributes required to suppress IG-SCC in this system are discussed. Following the

Introduction (Chapter 1), Chapter 2 evaluates the efficacy of cathodic protection via potentiostat over the polarization range of -1.7 volts versus Saturated Calomel Electrode (V_{SCE}) to -0.6 V_{SCE}, with emphasis on the 0.6 M NaCl environment. Chapter 3 evaluates four candidate Zn-rich primers through existing and newly developed electrochemical test methods to select optimal primer candidates and characteristics for highly effective IG-SCC mitigation performance. Chapter 4 combines the results of the previous two chapters to analyze ZRP performance in IG-SCC mitigation, which is assessed through galvanic coupling AA5456-H116 with both pure Zn anodes and ZRPs as well as spray-depositing ZRPs on AA5456-H116. Lastly, in Chapter 5, potential Zn^{2+} chemical protection effects are considered due to the use of Zn anodes, which is evaluated through experiment and theoretical modeling. The following is a more detailed description of each chapter.

Previous findings in the literature on AA5083-H131 (4.5 wt.% Mg) demonstrated successful IG-SCC mitigation in 0.6 M NaCl at intermediate to low alloy sensitization utilizing applied cathodic potentials as negative as -1.3 volts versus Saturated Calomel Electrode (V_{SCE}). These findings must be built upon to address more severe alloy composition (Mg), sensitization (NAMLT > 40 mg/cm^2), and environmental conditions potentially experienced in marine service to understand the efficacy of cathodic protection for IG-SCC mitigation. Therefore, Chapter 2 first evaluates the efficacy of applied cathodic polarization for IG-SCC mitigation on highly sensitized AA5456-H116 in four simulated marine environments: 0.60 M NaCl (pH 5.6), 5.45 M (saturated) NaCl (pH 6.2), 2.00 M $MgCl_2$ (pH 3.4), and 5.00 M (saturated) $MgCl_2$ (pH 2.4). These environments are considered a baseline to assess conditions that may be encountered in alternate immersion marine service, such as in deliquesced thin films at moderate to low humidity where salts accumulate. Therein, slow rising displacement tests are conducted in full immersion on fatigue pre-cracked single edge notch tensile (SENT) specimens polarized in the range of -0.8 V_{SCE}

to -1.1 V_{SCE}, which encompassed the bulk pitting potential of the α-Al matrix ($E_{pit\ (\alpha)}$) and/or the bulk pitting potential of the β phase ($E_{pit\ (\beta)}$). Thus, these evaluations consider polarization conditions under which the β and α phases are passive ($E_{applied} < E_{pit\ (\beta)}$), the β (and possibly α) is/are active ($E_{pit\ (\beta)} < E_{applied} < E_{pit\ (\alpha)}$), or, in the more aggressive saline environments, where both readily oxidize ($E_{applied} > E_{pit\ (\alpha)}$). These results demonstrate three main points: (1) cathodic polarization achieves the same magnitude of IG-SCC mitigation on highly sensitized AA5456-H116 as had been achieved on AA5083-H131 in 0.6 M NaCl, despite this alloy having 0.5 wt.% more Mg content and a higher NAMLT value; (2) the efficacy of applied polarization on IG-SCC trends with $E_{pit\ (\alpha)}$ and $E_{pit\ (\beta)}$, which change as a function of environment (thus achieved cathodic potentials which prove effective in one saline condition may not achieve the same mitigation in a more aggressive salinity); and (3) increasingly aggressive saline conditions reduce the potency of cathodic protection in IG-SCC mitigation. A threshold potential is demonstrated to exist in each of these environments below the β phase breakdown potential due to the same factors in operation to drive IG-SCC in each: (1) oxidation of the β/α phases to supply a significant cation content to the crack tip chemistry; (2) ingress of Cl^- for charge neutralization, driving Al oxide rupture; and (3) hydrolysis reactions at the crack tip driving hydrogen evolution and ingress in the fracture process zone.

The potential window in which IG-SCC suppression remains effective is unknown in Al-Mg alloys, which is pertinent information to further inform the design of sacrificial anode systems containing Mg (open circuit potential of -1.65 V_{SCE} in 0.6 M NaCl). There is concern that the use of excessive cathodic protection may cause hydrogen embrittlement in the substrate rather than suppress it, which has been demonstrated in similar alloys such as the AA7xxx-series. Therefore, the assessment of electrode potential-induced effects on IG-SCC susceptibility is then extended in

Chapter 2 to include potentials as negative as -1.7 V_{SCE} in 0.6 M NaCl. Electrochemical testing on highly sensitized AA5456-H116 at electrode potentials ≤ -1.1 V_{SCE} causes trenching on the bulk surface, which increases in severity with increasingly negative electrode potential as cathodic Al(Mn,Fe,Cr) particles drive localized alkalinization and Al dissolution. The trenching corrosion morphology is rounded, and hydrogen evolution occurs globally on the bulk alloy surface as well as within the trench in these cathodically polarized conditions, in contrast to the highly localized hydrogen evolution and sharp fissure-like corrosion inherent to IGC under anodic polarization. Two phenomena occur which separate the cathodically polarized crack tip conditions from the anodic: (1) hydrogen is evolved globally on the alloy surface at potentials ≤ -1.3 V_{SCE}, with low quantities of H absorption per unit area; (2) alkaline Al dissolution chemically blunts the crack tip with increasing time of exposure (reducing the effective stress concentration present at the crack tip). This coupled mechanism is proposed to suppress IG-SCC at applied potential ≤ -1.3 V_{SCE}, and is supported by interrupted LEFM testing at constant -0.8 V_{SCE}/-1.5 V_{SCE} which, after achieving IG-SCC while a sharp crack tip is present at K = 7.8 MPa√m, -1.5 V_{SCE}, the IG-SCC growth rate is demonstrated to decrease with increasing time of exposure and stress intensity.

Chapter 3 assesses the cathodic protection performance of four candidate ZRPs: 1 inorganic and 3 organic in resin type, all having different Zn loading percentages. These coatings are evaluated on highly sensitized AA5456-H116 in full 0.6 M NaCl immersion through use of the accelerated cycle test, which consists of a cyclic repetition of open circuit potential (OCP), electrochemical impedance spectroscopy (EIS), and potentiostatic hold steps. This test assesses sacrificial anode charge capacity and residual barrier effects on metal-rich primer galvanic protection. A worst-case galvanic couple with AA5456-H116 is simulated by polarizing the primers to the AA5456-H116 OCP, -0.85 V_{SCE}, for a total of 76 hours over the entirety of the cycle test. These results were then complemented by a newly developed galvanostatic pulse analysis, which together demonstrated primer polarizability, the efficiency of anodic charge output, as well as evidencing the underlying causes for these performance attributes such as pore resistance throughout cycle testing and the capacitive discharge delay time (or the rate of the primer's response to changing galvanic coupling conditions through increased anodic current output). These results demonstrate that the ZRPs with the highest anodic charge output, fast capacitive discharge time, and high Zn pigment loading are the least polarizable (most consistently maintain coupled potentials below $E_{pit\,(\beta)}$ during externally applied anodic current). Specifically, the inorganic ZRP (IOZRP) exhibits the highest anodic charge usage throughout the cycle test and achieves the fastest capacitive discharge time, enabling this primer to be the least polarizable and thus the top candidate to perform well in IG-SCC mitigation. High polarizability, in contrast, means that the sacrificial anode system achieves coupled potentials that increase quickly following the application of anodic current (which would occur during crack growth in Al-Mg), thus the magnitude of achieved IG-SCC mitigation decreases (or becomes negligible altogether). The epoxy polyamide-based ZRP is most polarizable of the candidates evaluated, achieving nearly 1/6 of the anodic charge usage as the and having the slowest capacitive discharge time despite similar Zn loading. Both of these coatings will be evaluated further in terms of IG-SCC mitigation performance utilizing LEFM test methods.

Chapter 4 considers the results of Chapters 2 and 3 to experimentally present a detailed evaluation of the performance of the IOZRP towards IG-SCC mitigation on highly sensitized AA546-H116. These analyses build a framework through which ZRP performance may be understood by evaluating the IG-SCC mitigation achieved in 0.60 M and 5.45 M NaCl by a pure Zn/AA5456-H116 galvanic couple, an AA5456-H116 galvanic couple with a ZRP plate, and lastly by spray-depositing the ZRP on the AA5456-H116. These evaluations seek to understand the ability of the Zn anodes to overcome three sources of Ohmic (IR) voltage drop on the path to polarizing the crack tip: the IR voltage drop in the anode, such as due to the resin in the ZRPs, the IR voltage drop in the scribe due to the resistance in the surface layer, and the IR voltage drop down the crack wake. To separate galvanic protection effects from possible secondary chemical protection effects that may be present when using Zn anodes, the galvanic coupling experiments house the Zn anodes in a microfilter to chemically isolate the Zn cations from the bulk saline environment. Galvanic coupling between pure Zn (surface area ratio as low as 1 Zn: 110 AA5456-H116) and AA5456-H116 is first demonstrated to achieve protective potentials of $\approx \leq -1.00$ V_{SCE}, which achieves similar IG-SCC mitigation as was observed under potentiostatic control. Similar results are achieved via galvanic coupling with ZRP panels having larger surface area (surface area ratio as low as 67 ZRP: 350 AA5456-H116). In 5.45 M NaCl, the ZRP-coated SENT specimens are thoroughly evaluated for IG-SCC mitigation performance in terms of the scribe width effects, or the size of the defect in the coating about the Mode I crack path, and the crack geometry effects. Utilizing the IOZRP, the scribe width is increased from 0.3 mm to 15.0 mm to evaluate the ability of the primer to continue to polarize the crack tip, and SENT specimens with double the crack wake thickness are employed with primer scribe width of up to 10 mm to understand the effect of crack geometry on primer performance. These results demonstrate that the IOZRP remains effective at polarizing the crack tip to potentials $\leq E_{pit\ (\beta)}$ with scribe width of 15 mm as well as with increased crack wake thickness, and the magnitude of protection depends on the coupled potential achieved. Unavoidably, as the area of exposed AA5456-H116 increases with increasing scribe width, the coupled potential increases by mixed potential theory to allow more crack growth to occur. Specifically, the increased influence of the IR voltage drop in the scribe and the increased

Al area are demonstrated to be critical factors, whereas the IR voltage drop in the crack wake remains relatively constant despite doubling the crack thickness. The more polarizable, worst performing epoxy polyamide-based Zn-rich primer performance was evaluated through spray-coating with 0.3 mm scribe width in 5.45 M NaCl, and due to this primer's polarizability a potential $> E_{pit\ (\beta)}$ was established which allowed rapid IG-SCC. These results support and validate the conclusions made in Chapter 3: metal-rich primer polarizability is a pivotal performance metric that dictates IG-SCC mitigation performance. Most importantly, these results demonstrate that the application of cathodic polarization achieves IG-SCC mitigation on highly sensitized AA5456-H116, regardless of the source of the polarization. What remains to be evaluated is the potential secondary chemical effects that may occur due to these primers' use, which may also serve to mitigate IG-SCC.

Chapter 5 is based on the chemical stability modeling method, which evaluates the chemical conditions for corrosion product formation as a function of pH and free ion content at fixed temperature. The models presented in the present work focus on the Zn system to quantify the effect of chloride content and Zn concentration on corrosion product formation. This modeling method is improved within this work to more accurately predict thermodynamic conditions for solid product stability, and these results correlate well with experimental findings concerning pure Zn as well as ZRP corrosion when tested in atmospheric conditions in the literature. Specifically, in dilute Cl^- environment Zn corrosion products form most readily between pH 4 and 14, with decreasing available Zn cation content required to form these products with increasing proximity to pH 9. With increasing $[Cl^-]$ the corrosion product stability decreases in the acidic region due to the increasing stability of Zn^{2+}, thus the Zn corrosion product formation region lies within pH 6-14, with the most favorable conditions occurring with proximity to pH 10. These models are complemented by experimental findings based on simulated Al-Mg alloy crack tip solution previously developed by Crane, Kelly, and Gangloff, where titration with $ZnCl_2$ solution provides insight into the effect of Zn content on the acidification at the crack tip.

The scientific contributions of this PhD research are as follows: the coupled anodic dissolution-hydrogen embrittlement mechanism which is hypothesized to drive IG-SCC is further supported and validated through cross-evaluation in a variety of aggressive saline environments. This correlation occurs because the same IG-SCC mechanics apply despite changing bulk pH/[Cl^-], thus the use of cathodic protection to mitigate IG-SCC is demonstrated to be effective in near worst case conditions: highly acidic, saturated saline environment on a high-Mg content, highly sensitized Al-Mg alloy. Through use of a potentiostat as well as galvanic coupling with pure Zn and ZRP, IG-SCC growth rate suppression of three orders of magnitude is demonstrated to occur at a constant stress intensity of 10 MPa√m in 0.6 M NaCl, which provides insight into the rate of acidified crack tip chemistry reversal during electrode potential control. The dissertation then addresses the attributes needed for IG-SCC suppression when utilizing sacrificial anodes. Critically, the ability of pure Zn and ZRP anodes to overcome the challenges imposed by various sources of IR voltage drop are assessed in full immersion conditions through correlation of electrochemistry and LEFM experimentation. An electrochemistry test method based on polarizability assessment is developed and proven effective through correlation with slow rising displacement testing to predict metal-rich primer performance in IG-SCC mitigation. Ultimately, an inorganic Zn-rich primer is experimentally proven to polarize the crack tip below $E_{pit\ (\beta)}$ in increasingly aggressive galvanic coupling conditions to significantly mitigate active crack growth as well as the onset of IG-SCC in highly sensitized Al-Mg SENT specimens. Overall, this work demonstrates that IG-SCC mitigation is achieved via applied cathodic potential in full immersion, chloride-containing environments, regardless of the source of the potential. These findings may inform future metal-rich primer development for IG-SCC mitigation in marine Al-Mg alloys components.

The following technological insights may be drawn from this PhD research. The window of applied potential in which IG-SCC mitigation may be consistently achieved in Al-Mg alloys is demonstrated to be -0.9 V_{SCE} to -1.2 V_{SCE} in 0.6 M NaCl, with significant corrosion and hydrogen evolution occurring outside of this voltage range. At applied potentials < -1.2 V_{SCE}, hydrogen evolution and absorption occur in a global manner about the alloy surface, and the occurrence of IG-SCC depends on the sharpness of the crack tip and the level of elevated stress concentration achieved. Furthermore, ZRPs are demonstrated to achieve potentials safely within this passive window. These primers may achieve low polarizability through maintenance of low pore resistance and a consistently high magnitude of anodic charge output, which may be improved by increasing the Zn loading and utilizing a porous and low resistivity resin. These desired primer attributes may be atypical of conventional formulations meant for long-term corrosion suppression. A test method is developed here to easily screen metal-rich primer candidates based on polarizability assessment. Low polarizability enables effective IG-SCC mitigation performance in a variety of aggressive surface area ratio, saline concentration, and crack geometry conditions. Increasing primer polarizability means that the system will achieve effective sacrificial anode-based cathodic protection only in select service conditions for IG-SCC mitigation. The long-term duration of effective protection achieved by Zn-rich primers (the service life) has not been assessed in this work. The addition of a topcoat, which may be utilized to improve primer service life as well as to reduce UV degradation, is demonstrated to be deleterious for IG-SCC mitigation, as this addition significantly increases the primer polarizability by masking the active Zn surface area.

ACKNOWLEDGEMENTS

Completing this research would not have been possible without the help of many selfless people, divine providence, and answered prayers. It takes a village, they say. I would like to express my sincerest gratitude to my co-advisors, James T. Burns and John R. Scully. I have been immeasurably fortunate to have such dedicated, passionate, and inspiring mentors, and am grateful for the unending support, oversight, and expert advice they have offered me over these past 3.5 years. Their lessons, insights, and patient guidance have enabled me to grow as a scientist, a researcher, and a person. Their competitive nature has sharpened my cornhole and ping pong skills also. I especially would like to thank them for guiding my development as a writer. Their consistent attention to clarity, precision, and linear logic have greatly assisted the completion of this dissertation in its final form.

I would also like to thank my dissertation committee for their valuable input on and consideration of this research. The collective knowledge and insight offered by Professors Robert Kelly, Sean Agnew, and David Green, as well as by Dr. Fritz Friedersdorf are all highly valued and appreciated.

Having a foot in two different research groups has given me a diversity of comradery and assistance both in and out of the lab. I have been blessed with wonderful friendship and support from all of the members of the Burns and Scully groups. You all have made this time in CESE truly memorable. I would especially like to thank R.J. Santucci, Jr. for his friendship and collaboration. I must also give special thanks to Patrick Steiner and Dr. Zachary Harris, who have been a wonderful source of friendship, support, and witty humor, not to mention an ever-resourceful team in load frame troubleshooting. Drs. Mary Lyn Lim and Noelle Co were pivotal

mentors who selflessly assisted my development from the very beginning of my graduate career, for which I am very grateful.

Reaching this point was possible only with the support of my family, friends, and loved ones. My family has endured the trials of doctoral research with me every step of the way, and has always been a source of love and encouragement. I cannot thank them enough for their support throughout my graduate career, and simply throughout life. From meeting her in my first month in Charlottesville, Jessica DeLalio has been by my side, helping in countless ways to lovingly help me see this research through to completion. The DeLalio family has been right there as well, and have truly been a second family to me. From the many first year study sessions all the way to now, Lavina Backman and Eric Hoglund have been strong and encouraging friends who have made the hard times enjoyable, and who continue to this day to teach me about these things called phonons.

This research was supported financially by the Office of Naval Research (Awards #N00014-15-1-2491 and #N00014-18-S-B001), with Dr. Airan Perez as the Scientific Officer. Charles Sprinkle and Adam Goff at LUNA Innovations Inc. were always willing to share insight on metal-rich primer selection and application, which was greatly appreciated.

TABLE OF CONTENTS

LIST OF FIGURES

CHAPTER 1

INTRODUCTION

1.1 NOMENCLATURE

AA5xxx-series = Aluminum Association 5000-series alloys (Al-Mg)
α – Al matrix = Al – 5 wt.% Mg solid solution
β = Al_3Mg_2
CPWC = critical pigment weight concentration
dcPD = direct current potential difference
DoS = degree of sensitization
DSC = differential scanning calorimetry
EBSD = electron backscatter diffraction
$E_{pit(\alpha)}$ = α – Al matrix pitting potential
$E_{pit(\beta)}$ = β phase pitting potential
FCC = face centered cubic
GPZ = Guinier Preston Zone
HCP = hexagonal close packed
IGC = intergranular corrosion
IG-SCC = intergranular stress corrosion cracking
IOZRP = inorganic zinc-rich primer
LEFM = linear elastic fracture mechanics
MRP = metal-rich primer
NAMLT = nitric acid mass loss test
OCP = open circuit potential
PVC = pigment volume concentration
PWC = pigment weight concentration
SCE = saturated calomel electrode
SDZ = solute depleted zone
SHTQ = solution heat treat and quench
SSSS = Mg supersaturated solid solution
TEM = transmission electron microscopy
UIT = ultrasonic impact treatment
ZRP = zinc-rich primer

1.2 PROBLEM STATEMENT

The Mg supersaturation that affords Al-Mg alloys a high general corrosion resistance, strength-to-weight ratio, and weldability for marine conditions also cripples these alloys over extended service. During the sensitization process, the Mg precipitates from solid solution to form the anodic intergranular β phase (Al_3Mg_2) in tropical ocean temperatures, rendering these alloys susceptible to both intergranular corrosion (IGC) and intergranular stress corrosion cracking (IG-SCC) under sufficient applied load. Together IGC and IG-SCC may reduce the expected service life of Al-Mg superstructural and/or hull components on U.S. naval vessels. Significant advances have been made towards understanding the sensitization, IGC, and IG-SCC mechanisms, and through this understanding the ability to mitigate the IGC/IG-SCC phenomena has been demonstrated through potentiostat-based cathodic protection. For increased service relevance, attention has now turned towards the optimized use of sacrificial anode-based cathodic protection to mitigate these modes of accelerated structural degradation.

The overall objective of this research is to understand the efficacy of applied cathodic protection via a range of sacrificial anode types towards IGC / IG-SCC mitigation in Al-Mg alloys in order to recommend optimal anode qualities necessary for effective use in service. No prior studies exist to evaluate the performance of service-relevant cathodic protection systems in IG-SCC mitigation for Al-Mg, which is an inherent deficiency in the current literature that disrupts the utilization of newfound mechanistic understanding to shape engineering solutions. Such a link between these fundamental findings and suitable applications is increasingly needed as Al-Mg naval structures grow increasingly susceptible in service.

This dissertation consists of an introduction followed by four main tasks that achieve the stated research objective. The relevant background on prior findings concerning Al-Mg alloy sensitization, the IGC / IG-SCC mechanisms, and cathodic protection is provided below, followed by review of the motivation and corresponding objective for each of the four tasks.

1.3 BACKGROUND

Solid solution strengthening through Mg addition and added cold work increase the strength of Al three-fold, resulting in the Aluminum Association 5000-series (AA5xxx-series). AA5xxx-series alloys are characterized by a high strength-to-weight ratio and general corrosion resistance, which have led to their increasing use in novel superstructure and/or hull designs for U.S. Naval vessels [1–3]. However, exposing AA5xxx-series to mildly elevated temperatures in service, such as the 40-50°C that is commonly experienced in near-equatorial marine environments, can lead to intergranular precipitation of the β phase (Al_3Mg_2) in a process called sensitization [4,5]. The β phase is highly anodic to the Al matrix, and in aggressive environments the dissolution of this phase can lead to severe intergranular corrosion (IGC), and intergranular stress corrosion cracking (IG-SCC) in the presence of an applied stress [6,7]. For this reason, understanding the physical characteristics and precipitation behavior of the β phase, as well as accurately quantifying the intergranular density of this phase, are necessary first steps to evaluate Al-Mg component integrity.

1.3.1 The Al_3Mg_2 (β Phase) Intermetallic: Characteristics and Precipitation

The precipitation of the β phase theoretically occurs in the following sequence in Al-Mg:

SSSS (α - Al matrix) → GPZ → β'' (Al_3Mg_2, LI_2) → β' (HCP) → β (Complex FCC)

where GPZ are Guinier Preston Zones and SSSS is the Mg supersaturated solid solution [8]. To form the SSSS in the Al-Mg system, the initially high Mg solubility of 14.9 wt.% is utilized at 450°C, though upon quenching to 23°C this solubility drops to 1.7 wt.%. The formation sequence of the β phase that is actually realized in marine service as well as the discrete versus continuous precipitation of this phase along grain boundaries has been debated in the literature.

Extensive TEM studies have been carried out on AA5083-H131 (4.5 wt.% Mg) at 100°C, with sensitization time ranging from 3 to 90 days, which found that no GPZ or intermediate phase formation occurs, but rather only equilibrium β phase formation during the 3 to 90 day period, and that discrete β precipitates transition to continuous ribbons following 15 to 30 days exposure (NAMLT value of 50 mg/cm^2) [9]. These findings were clarified through three-dimensional analysis using Ga embrittlement in AA5083-H131 to analyze β distribution on intergranular fracture surfaces following sensitization at 100°C for up to 30 days, which demonstrated only discrete precipitate formation [10]. These results were in agreement with work done by Lim et. al using phosphoric acid etching on AA5083-H131 sensitized at 100°C for up to 30 days, and at 80°C for up to 180 days (both achieving NAMLT $\approx$ 50 mg/cm^2), which demonstrated discrete intergranular β formation as well (Figure 1.1) [11,12]. Most importantly, Figure 1.1 illustrates the linear increase in intergranular β coverage with increasing NAMLT value, where high, discrete β-phase coverage grain boundaries are those covered by 70% or more in 2-dimensional linear distance and low β-phase coverage grain boundaries are those with less than 70% linear coverage. When covering a greater range of sensitization temperature, mass loss studies demonstrated that the sensitization performance peaks around 175°C, with the use of higher temperatures achieving lower β densities for equivalent exposure periods [13,14].

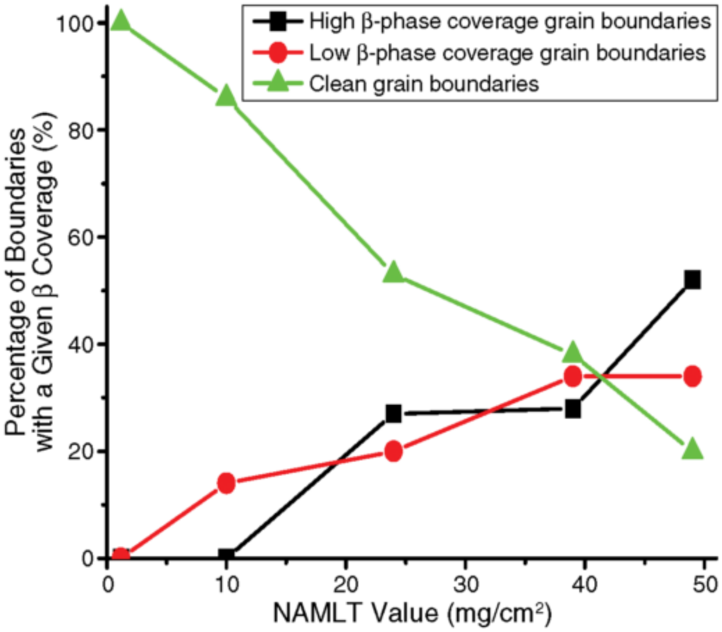

Figure 1.1: Percent intergranular β phase coverage achieved in AA5083-H131 through phosphoric acid etching following sensitization heat treatment at 100°C for up to 30 days [11].

Following these works, magnesium is known to diffuse through the α-Al matrix following extended exposure to temperatures as low as 40-50°C to heterogeneously precipitate as discrete β phase preferentially on grain boundaries [3]. Discrete β phase may range from 50 nm to 300 nm in length, depending on sensitization time and temperature [9,10,15]. The degree of sensitization (DoS) achieved in the Al-Mg alloys, or the density of β phase precipitates present on the grain boundaries, is commonly evaluated via the ASTM G67 Nitric Acid Mass Loss Test (NAMLT) [16]. This test, which measures mass loss due to grain fallout following 24-hour immersion in nitric acid, is the current standard for estimating Al-Mg alloy susceptibility to IGC and IG-SCC in service. Based on this test, Al-Mg alloy sensitization behavior has been thoroughly characterized at temperatures ranging from 50° to 220°C for AA5083-H131, as surveyed and compiled by Zhang et. al and shown in Figure 1.2 [17]. As shown in Figure 1.1.3, sensitization occurs more rapidly as

Mg content in Al-Mg alloys is increased [17]. Therefore, to avoid the wide range of conditions where sensitization may occur, stabilization heat treatments may be performed below the β solvus to promote intragranular β precipitation on Fe-based constituent particles, Mn dispersoids, or dislocation sites, though this procedure must be purposefully and carefully conducted so as not to worsen intergranular sensitization [3,18].

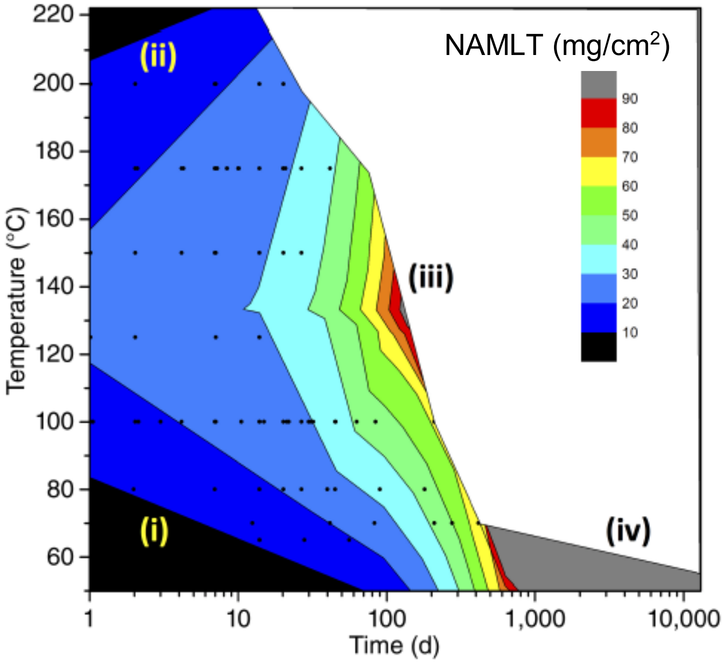

Figure 1.2: Compilation of literature data on the sensitization behavior of AA5083-H131, demonstrating the high degree of sensitization possible in these alloys [17].

The multitude of β precipitation studies have yielded considerable experimental datasets that have furthered mechanistic understanding. Based on their TEM findings from sensitization of AA5083-H131 at 100°C and 175°C, Goswami et. al concluded that intergranular β precipitation is driven through dislocation pipe diffusion of Mg through the Al matrix, due to the observation of faster β precipitation rates than could be explained through a diffusion-controlled collector plate mechanism [9,19]. Studies by D'Antuono et. al and Zhao et. al utilized various forms of TEM to

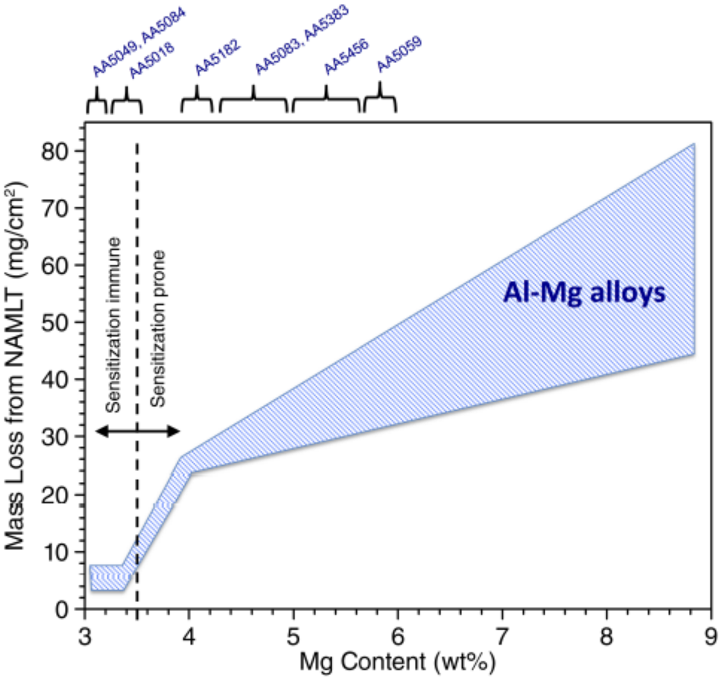

Figure 1.1.3: Sensitization behavior of Al-Mg alloys with increasing Mg content, shown here (blue region) for a constant sensitization of 7 days' duration at 150°C. As Mg content increases, sensitization occurs more rapidly in these alloys [17].

conclude that intergranular β precipitation behavior varies as a function of grain boundary misorientation [20] and plane [21], as well as dislocation density contained within the nearest grain [22]. In-situ heating of heavily cold-worked AA5456-H116 (~ 5.0 wt.% Mg) under TEM demonstrated more rapid and dense β precipitation with increasing dislocation density in nearest grains, in agreement with the dislocation pipe diffusion mechanism proposed by Goswami et. al [9,22]. At high energy grain boundary plane / misorientation combinations, β phase precipitation required longer exposure time than at lower energy boundaries, though the β precipitates grew to be larger in size [20,21]. The range of experimental sensitization datasets present in the literature have enabled the accurate modeling and prediction of intergranular β formation and overall degree of sensitization in Al-Mg alloys in both isothermal and cyclic thermal conditions (such as through daytime cycles) [23,24]. However, the direct relation of intergranular β density, quantified through means other than the rough NAMLT estimate, to overall alloy susceptibility to IG-SCC remains unfounded in the literature. These evaluations are necessary to further inform on the role of the β phase as well as the alloy mechanical properties in IG-SCC severity, as well as to critically assess the accuracy of the NAMLT procedure. To understand the influence of the β phase on the IGC/IG-SCC phenomena, the impact of the intergranular β phase on Al-Mg alloy mechanical properties must first be reviewed.

1.3.2 The Effect of Sensitization on Al-Mg Mechanical Properties

Numerous studies now exist in the literature that demonstrate increasing IG-SCC severity in Al-Mg alloys with increasing sensitization [4,25–29]. Mechanically, β phase formation and presence on a given grain boundary may introduce brittle phase constraint on the surrounding ductile Al-matrix, which has been calculated to decrease to zero strain after approximately eight β particle spacings (minimum of 450 nm) [7,30]. The three-dimensional Ga embrittlement method demonstrated in AA5083-H131 that prolonged sensitization at 100°C maintained discrete β phase, which increased in size and slightly decreased in spacing on the grain boundaries (average separation distance was 295 nm at NAMLT 49 mg/cm^2) [10]. Thus, in the highly sensitized condition constraint effects will be increased as β spacing decreases and as β size increases to increase the phase's yield strength [7]. The β phase yield strength may range from 1,400 MPa (β diameter = 90 nm, NAMLT 10 mg/cm^2 equivalent) to 1,800 MPa (β diameter = 150 nm, NAMLT 39-49 mg/cm^2 equivalent) [7]. Mg depletion on the grain boundary may also be a concern, as the formation of a solute depleted zone (SDZ) would locally reduce the alloy's yield strength.

However, studies have demonstrated that in 4.5 wt.% Mg-containing alloys the magnitude of solute depletion is 1.0 wt.% or less, and the amount of depletion that occurs decreases with increasing quantity of Mg alloying [9,31]. Al-Mg alloy yield strength is minimally affected by increased sensitization [28], though the fracture toughness has been demonstrated to increase from 36 MPa√m to 50 MPa√m following 200 hour sensitization heat treatment at 175°C [32]. Therefore, the effect of β spacing and constraint are considered the most pertinent effect of sensitization mechanically, both of which have implications in the susceptibility of the grain boundary to IG-SCC.

1.3.3 **Characterization of Sensitization Across Al-Mg Alloys and Tempers**

The NAMLT value [16] is the standard proxy for IGC / IG-SCC susceptibility, as these degradation phenomena increase in severity with increasing intergranular β density [32]. This value correlates well with alloy susceptibility to IGC / IG-SCC for a given composition and temper, as has been thoroughly validated for various Al-Mg alloys in 0.6 M NaCl conditions in the most susceptible S-L orientation, and to a lesser extent in the T-L [4,12,32,33]. However, cross-comparison of IG-SCC susceptibility in AA5xxx-series alloys of *varying* composition and/or temper has demonstrated that this test may mislead service life predictions [10,32–35]. Specifically, the IGC and fracture behavior of AA5083 (4.5 wt.% Mg content) varies considerably between constant NAMLT specimens having differing heat treatment and processing (i.e. H116, H131, and solution heat treat and quench (SHTQ) tempers) [32,33], as demonstrated in 0.6 M NaCl at -0.8 V_{SCE} (Figure 1.4). Such discrepancy in Al-Mg alloy susceptibility motivated extensive research into more selective and less destructive etchants to evaluate β density, which promoted phosphoric acid and ammonium persulfate etchants at specific pH values for the most effective evaluation [18,36,37]. Recent work by McMahon et al. [38] utilized a combination of ammonium persulfate etchant [36,37] and Electron Backscatter Diffraction (EBSD) mapping / overlay analysis on the same specimens tested in Figure 1.4 to explain this discrepancy in susceptibility. As shown in Figure 1.5, these evaluations demonstrated that the amount of intergranular β phase present in each of these alloys *at constant NAMLT 24 mg/cm*^{2} differs by up to 34.0% linear coverage, and the tempers having the highest intergranular β phase presence were those that were the most susceptible to IG-SCC at -0.8 V_{SCE} in 0.6 M NaCl [32,38]. The accurate quantification of linear β coverage is critical to predict IG-SCC severity in Al-Mg alloys due to the previously discussed importance of the β size, spacing, and overall intergranular β density on crack tip acidification, hydrogen diffusion, and hydrogen trapping to enable this environmental fracture mechanism. The achievement of the same NAMLT value in these AA5083-XXXX alloys despite such differences in β coverage suggest that nitric acid may preferentially attack the Al matrix in certain Al-Mg compositions/tempers, which negates the desired ability to cross-compare these Al-Mg variants. Similar differences in NAMLT results were demonstrated between AA5083-H116 and AA5456-H116. A more accurate linear intergranular β coverage metric was proposed through use of a complex ammonium persulfate etching/EBSD map overlay method, which may be relevant only to laboratory conditions [36,38].

There does not yet exist a more accurate, service-relevant chemical test method to evaluate β density, so the NAMLT procedure continues to be used, especially for single alloy comparison where the predictions from this test remain useful. These critical evaluations of the NAMLT procedure have demonstrated that there is need for a more accurate method to determine β density, but also that the DoS, when effectively quantified, does correlate well with Al-Mg alloy susceptibility. This correlation is due to the importance of the intergranular β density on IG-SCC susceptibility in Al-Mg, though slight differences in yield strength should also be considered due to constraint effects at the crack tip (which is a primary factor differentiating AA5083-H131, -H116, and -SHTQ) [39]. More thorough evaluation of the hypothesized mechanism of IG-SCC in Al-Mg will further inform the effect of the β phase dissolution and the occluded, aggressive crack tip chemistry formation on Al-Mg alloy performance in saline conditions.

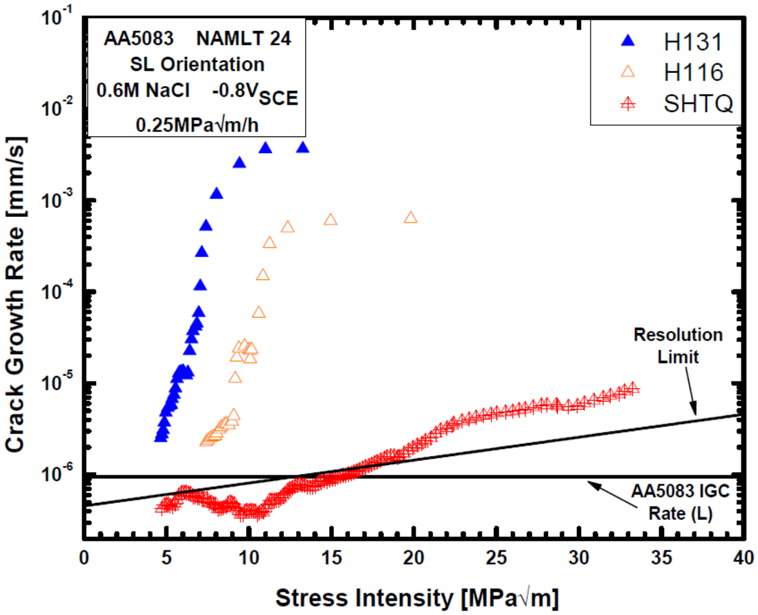

Figure 1.4: The variability of IG-SCC susceptibility between AA5083 alloys of differing temper despite constant NAMLT value of 22 mg/cm^2 [32].

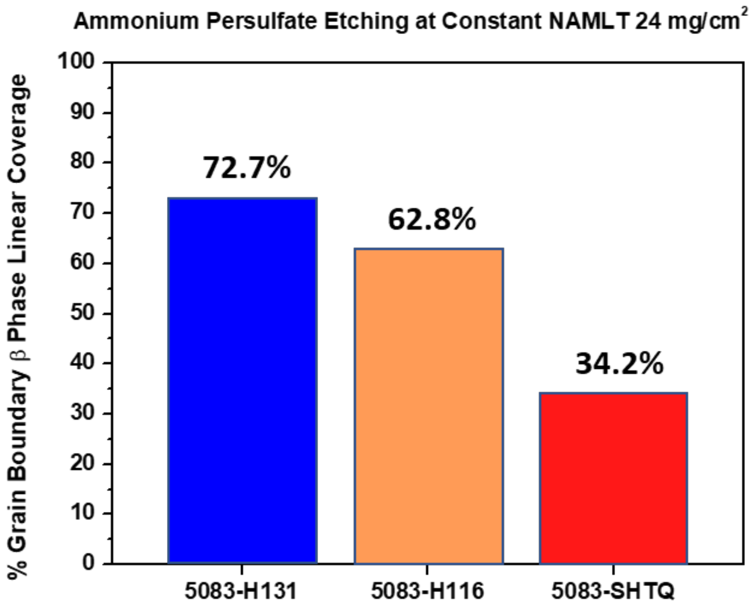

Figure 1.5: Ammonium persulfate etching and EBSD overlay results demonstrating the true β phase coverage for a constant NAMLT value across various Al-Mg alloys and tempers [38].

1.3.4 The IG-SCC Mechanism in Al-Mg

The close spacing that develops between β phase particles with increasing sensitization increases the ease of corrosion penetration along the grain boundaries in the form of deep fissures, thus the IGC phenomenon naturally forms sharp corrosion features that may act as effective stress concentrators under applied load. At the fissure/crack tip, the anodic dissolution of intergranular β phase causes the release of Al^{3+} and Mg^{2+}, which through hydrolysis leads to the formation of H^+ to acidify the occluded fissure / crack tip environment [6,7,26]

$$Al^{3+} + H_2O \xrightarrow{yields} H^+ + AlOH^{2+} \qquad \text{Equation 1.1}$$

$$Mg^{2+} + H_2O \xrightarrow{yields} H^+ + MgOH^+ \qquad \text{Equation 1.2}$$

Ingress of Cl^- is hypothesized to occur following β phase dissolution for charge neutralization, the presence of which is known to promote aluminum oxide rupture [40–42]. Specifically, the Al pitting potential decreases such that pitting occurs more readily as chloride concentration is increased [41,43,44] due to the affinity for Cl^- absorption into the electropositive oxide in acidic conditions [41,42,45]. These Cl^- enhanced oxide defects (either via destabilization or rupture) will promote anodic reactions on Al. The ingress of the Cl^- ions will also decrease the resistance of the crack tip oxide to mechanically induced ruptures caused by active crack tip strain rates [6,32,41,42,46]. In these conditions, bare Al will oxidize in the absence of the oxide to further enrich the cation content of the occluded chemistry [40,47,48]. β / α dissolution, acidification, and ohmic potential drop below the reversible H potential facilitates the enhanced generation of crack tip H and enables embrittlement by adsorbed hydrogen in the fracture process zone [6,7,25,33,39,46]. Specifically, it is hypothesized that adsorbed atomic H on the crack surface becomes absorbed such that it may diffuse to become trapped in the constrained plastic zone surrounding the nearest undissolved β phase particle 200-600 nm ahead of the crack [7,10]. While unconfirmed, crack propagation is speculated to occur through H crack nucleation and backward growth from the nearest undissolved β particle, to connect with the crack tip and allow acidified crack tip solution ingress for further cation/H evolution [7]. This general coupled anodic dissolution / hydrogen embrittlement mechanism causing IG-SCC in Al-Mg alloys has been recently supported through hydrogen enhanced decohesion modeling [6,7,26,32,33,49], though further evaluation is necessary to inform the specific H/β interactions and proposed H-crack nucleation around the proximal undissolved β particles.

The importance of the occluded crack tip chemistry formation to the occurrence of IG-SCC has been validated by Crane et. al, who showed that IG-SCC will still occur in an unsensitized AA5083-H131 specimen (minimal intergranular β presence) when tested in highly acidic, pH -0.4 simulated crack tip solution ($AlCl_3/MgCl_2$, 2.5 M Al^{3+}, 1.1 M Mg^{2+}, 7.7 M Cl^-) [6]. Thus, the formation of an acidified, occluded chemistry must be avoided to reduce IGC/IG-SCC susceptibility, and suppressing β phase corrosion in sensitized Al-Mg is a crucial means to achieve this goal. However, the majority of methods utilized to manage IGC/IG-SCC phenomena do not leverage this electrochemical relationship. Rather, the variety of methods currently utilized in marine service to reduce Al-Mg susceptibility to IGC/IG-SCC either preempt these phenomena through simply diagnosing sensitization followed by replacement, or through dealing with the aftermath (damage control) [1].

1.3.5 Service Practices for Al-Mg Alloy Maintenance in the Literature

Stress corrosion cracking has been problematic in Al-based Naval vessels for more than two decades, with increasing amounts of structural cracking arising especially in the AA5456-H116 superstructures of the CG-47 Class Cruisers as these components increasingly sensitize in service. To combat this issue, a range of techniques are now utilized on these vessels in the detection of sensitization, the mitigation of IG-SCC (after cracking has occurred to an observable extent), and in the replacement of corrupt Al-Mg material.

1.3.5.1 Detection of Sensitization in Marine Service

The NAMLT procedure remains the go-to method to predict DoS in Al-Mg alloys, however the destructive nature of this test is not always feasible for conduct on active vessel components. For this purpose, this test has been repurposed for repeatable application in service by means of the DoS Probe, which is essentially a portable potentiostat housed within a dilute 2% nitric acid solution that may be temporarily adhered to freshly cleaned and polished Al-Mg surfaces [1]. A schematic of this apparatus is shown in Figure 1.6. This device enables the measurement of sensitization within approximately 20 minutes following Al-Mg surface preparation, and accurately quantifies β density based on measurement of the corrosion current achieved over a fixed 0.5 in^2 area at 50°C, as increasing amounts of β coverage will lead to larger current output as more β dissolution occurs [1]. The complement to the DoS probe in service is phosphoric acid etching, which is done non-destructively on active AA5456-H116 components following surface polishing and requires only a portable light microscope to image the etched surface at 400-600x to qualitatively assess intergranular β presence [1,37].

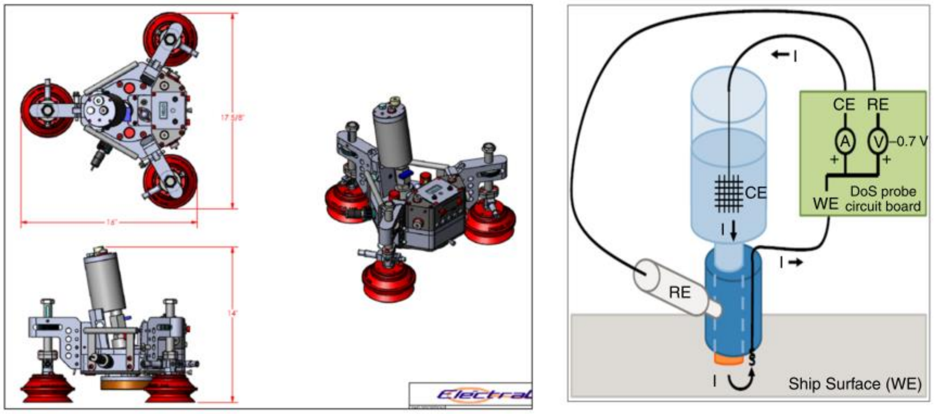

Figure 1.6: The Degree of Sensitization Probe currently used on the CG-47 Class Cruisers to detect alloy sensitization via a modified NAMLT procedure in service [1].

1.3.5.2 **Mitigation and Repair of Stress Corrosion Cracks Post-Hoc in Marine Service**

Maintenance on stress corrosion cracking phenomena in naval service is currently limited to mitigation following the observation of a significant crack formation, or to the re-unification of the cracked material / complete replacement of the material, depending on the severity of the damage. One method commonly used to 'heal' cracks on horizontal components such as the deck is Ultrasonic Impact Treatment (UIT), which through use of 3 mm diameter pins behaves similarly to an ultrasonic transducer to create continuous high intensity vibrations that causes severe plastic deformation. The resulting appearance of a cracked Al-Mg component following UIT is similar to a weld, though microcracks have been found due to the lack of alloy melting in this process [1].

In taking a different approach focused on introducing a physical barrier to block the corrosive environment and reduce stress intensity experienced by the actively cracking AA5456-H116 component, composite patch repair technologies are also being utilized to mitigate IG-SCC [1]. By 2016, composite patches were deployed on 11 naval vessels, with total surface area of 161.31 m^2, and had proven to effectively reduce IG-SCC and fatigue crack growth rates [1]. An example of a composite repair patch is illustrated in Figure 1.7. For faster crack coverage and weather-tightness with less required training for on-board personnel, a lower-strength bonded Al repair treatment is also being used [1]. The procedures following the aforementioned mitigation methods are shot peening and material replacement, which are time-consuming and costly processes that limit the readiness of these ships.

None of the currently deployed procedures for IGC/IG-SCC mitigation leverage the relationship between β/α dissolution and aggressive chemistry formation, and thus none of these methods truly aim to maintain Al-Mg component integrity and prolong service life. They all involve either deformation, masking, or replacement of the component, which reduces ship integrity/readiness and requires considerable maintenance and training. The use of electrochemically active systems to combat the initiation and growth of IGC/IG-SCC may be an economic alternative to extend AA5456-H116 component life. This dissertation seeks to address this deficiency and will do so through utilizing the influence of cathodic protection on IGC/IG-SCC.

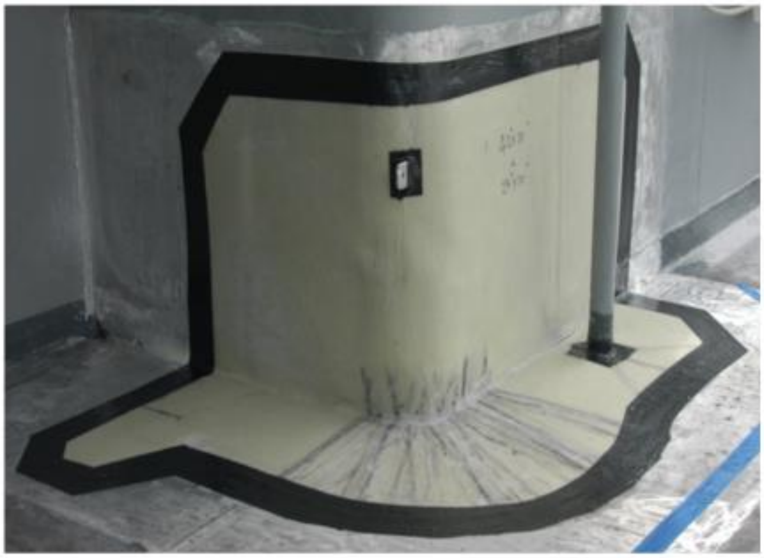

Figure 1.7: An example of a composite repair patch deployed on a CG-47 Class Cruiser to mask an active stress corrosion crack from the corrosive environment and reduce the stress intensity present to reduce further fatigue / IG-SCC growth [1].

1.3.6 **Potential Dependency of SCC in Al Precipitation Age-Hardened Alloys**

The mitigation of IG-SCC in Al-Mg alloys has been demonstrated in recent work using cathodic polarization [7,46]. As demonstrated previously in Equation 1.1 and Equation 1.2, the dissolution of the β phase and/or the α-Al matrix enable occluded acidification via hydrolysis reactions, thereby enabling the coupled anodic dissolution / hydrogen embrittlement mechanism that drives IG-SCC in the presence of sufficient stress. Previous work performed by Ai, Lim and Scully demonstrated that H diffusion is bulk diffusion controlled in AA5083-H131, with diffusivity ≈ 10^{-10} cm^2/s, meaning that whether the Al-Mg alloy is sensitized or not, formation of the necessary absorbed H content in these alloys with sufficient applied stress will promote IG-SCC, in agreement with the results of Crane et. al [6,50]. Cathodic polarization may lower the crack tip potential below $E_{pit(\beta)}$ and $E_{pit(\alpha)}$ to suppress the development of the aggressive crack tip chemistry, thus averting the hydrogen diffusion and embrittlement ahead of the crack. Similar environmental crack growth mitigation has been achieved in AA7xxx-series alloys [51–54] through use of electrode potential control to mitigate crack tip acidification caused by strain-induced Al oxidation. In the Al-Mg system, this environmental crack growth suppression was observed in fatigue pre-cracked, sensitized AA5083-H131 (4.5 wt.% Mg, NAMLT $\leq$ 40 mg/cm^2) tested in 0.6 M NaCl at cathodic potentials as negative as -1.3 V_{SCE} [6,7]. Modeling of the crack tip electrochemical conditions predicted that Ohmic voltage drop will cause the crack tip potential to trend towards -1.05 V_{SCE}, suggesting that in conditions where the β / α pitting potentials may be decreased to values more negative than this limit there will be less efficacy of cathodic protection for IG-SCC mitigation [6].

1.3.7 A Brief History of Cathodic Protection Afforded by Metal-Rich Primers

Metal-rich primers (MRPs) containing sacrificial anodic pigment may provide adequate cathodic protection on Al-Mg alloys if properly designed. A variety of MRPs have been formulated for Al alloy protection, such as Al- and Mg-based primers, hybrid alloy pigment systems (such as Al-Zn-In and Zn-Mg), and others [55–62]. However, no works currently exist in the literature to evaluate the IG-SCC mitigation performance of MRPs such as these on Al alloys. Environmental fracture mitigation is a more demanding scenario than typical corrosion mitigation, for which the majority of metal-rich primers are designed, due to the following requirements: (1) the increase in exposed Al area during crack growth increases the anodic current output demand on the sacrificial metal-rich primer system, which must meet this demand with a rapid response to passivate the freshly exposed Al as well as to halt further crack acidification and propagation; (2) the MRP must achieve sufficient throwing power, or the distribution of anodic current down the crack wake to polarize the crack tip; and (3) Ohmic voltage drop effects present in the MRP resin, the scribe (damaged region) in the MRP, and down the crack wake must also be overcome through output of a sufficient magnitude of anodic current such that the MRP is not decoupled from the crack tip. Specifically, thorough experimental evaluation is needed over a range of existent metal-rich primer systems having sacrificial anodic pigments such as Zn, Mg, and Al to elucidate the differences between these MRPs in terms of polarizability, or the ability to address newly exposed crack surface to halt further crack growth. On Al-Mg alloys, the successful MRP system would be able to consistently polarize the crack tip below $E_{pit\,(\beta)}$ to achieve the most effective level of sacrificial anode-based cathodic protection for IG-SCC mitigation.

Numerous Al-based primers are under development for long-term cathodic protection on Al substrates, though little published work exists concerning their performance in aggressive saline environments [55,60]. To date, Mg-rich primers have been the most thoroughly studied and have demonstrated considerable success in cathodically protecting Al alloys such as the AA2xxx-series against corrosion, with and without pretreatments or topcoats [57–59,63,64]. In terms of galvanic protection, however, pure Mg-rich primers often have short service life in aggressive full-immersion saline environments when mechanical abrasion is not present to expose new underlying Mg pigment [65]. Long-term protection is then primarily possible through the ability of Mg to protect through chemical inhibition and secondary barrier formation [56,57,66]. Pure Zn-based primer systems are typically not considered for Al protection due to the close proximity of their open circuit voltages (low ΔOCP) to those of numerous commercial Al alloys [56,60]. However, in comparison to Mg pigments, the more moderate Zn OCP (-1.09 V_{SCE} vs. -1.65 V_{SCE} in 0.6 M NaCl), lower self-corrosion rate, and higher allowable pigment loading may be well-suited to offer long-term cathodic protection to Al-Mg alloys (e.g. 5456-H116, OCP of -0.85 V_{SCE} in 0.6 M NaCl). The OCP of pure Zn lies within an electrode potential zone of low IGC/IG-SCC susceptibility for Al 5xxx-series alloys, making this high pigment loading beneficial and minimizing risk of cathodically-driven corrosion [6,46,67–70]. Furthermore, Zn-based coatings likely depend on galvanic coupling as well as secondary barrier formation to offer stable substrate protection [71,72]. Consideration of ZRPs to protect Al substrates is further bolstered by the long and successful history of ZRPs on steel [73]. All three of these MRP systems, as well as hybrid pigmented primer formulations, have yet to be investigated for environmental fracture mitigation on Al-Mg alloys, and the polarizability of these coatings is unknown. These primer attributes must be determined across the range of formulation types to address the potential use of MRPs for IG-SCC mitigation in service, as well as to inform future MRP design for this purpose on Al-Mg.

1.4 **MOTIVATION**

In service there exist alloys such as AA5456 that contain more Mg content than AA5083, with higher sensitization levels than NAMLT 40 mg/cm^2, which operate in atmospheric exposure conditions such as deliquesced thin films where the efficacy of infinite anode potentiostat-based cathodic protection remains unevaluated. These needs motivate further development on the efficacy of cathodic protection in more aggressive and realistic service conditions. The robustness of this mitigation strategy must be examined for more aggressive material compositions, loading environments, sensitization levels, and ranges of applied potential to more accurately encompass protected/unprotected service conditions. The sensitivity to excessively applied cathodic protection must also be assessed, the effect of which is unknown in terms of environmental fracture susceptibility in Al-Mg alloys. Furthermore, the use of potentiostat-based cathodic protection may not be possible about the entirety of a marine vessel. Therefore, finite sacrificial metal-rich primer systems must be assessed for their ability to achieve similar IG-SCC mitigation, and the required primer attributes must be determined to inform the choice of MRPs for service use as well as the design of future systems. The lack of such evaluation in previous work necessitates the design of new experimental evaluation methods to quantify MRP polarizability and performance mechanisms.

1.5 **OBJECTIVES**

The objective of this research is to further the understanding of sacrificial anode-based cathodic protection in IG-SCC mitigation on Al-Mg alloys, and through this understanding identify the critical metal-rich primer attributes necessary for optimized IG-SCC mitigation. These conclusions will be derived from experimental results concerning the IG-SCC severity in a range of aggressive saline / electrode potential conditions on highly sensitized (NAMLT 65 mg/cm^2) AA5456-H116, as well as through electrochemical studies on the polarizability and sacrificial anode-based cathodic protection afforded by pure Zn as well as a range of Zn-rich primer formulations. Baseline electrochemical / fracture experimentation and chemical stability modeling will together enable the interpretation of sacrificial anode-based cathodic protection performance results when selected sacrificial anode systems are utilized to mitigate IG-SCC on NAMLT 65 mg/cm^2 AA5456-H116 in full immersion conditions.

This dissertation assimilates the findings of four objectives, each of which is presented in a separate chapter. The background and justification for each chapter is summarized below. This work aims to subject potentiostat-based and finite anode-based cathodic protection systems to worst-case marine service scenarios in order to assess the limits of each IG-SCC mitigation method. Namely, AA5456-H116, which has a high Mg content of 5.0 wt.%, will be assessed in the nearly maximized sensitization condition of NAMLT 65 mg/cm^2, which constitutes 95% intergranular β coverage or more, and fatigue pre-cracked SENT specimens will be tested in the most susceptible S-L / S-T orientations. Testing environments will roughly simulate dilute / deliquesced thin film marine service conditions through use of dilute and saturated NaCl or $MgCl_2$ full immersion, which offers an experimental baseline to inform atmospheric type testing.

1.5.1 Chapter 2: The Efficacy of Potentiostat-Based Cathodic Polarization for IG-SCC Mitigation on AA5456-H116

Cathodic polarization in the range of -0.9 to -1.3 V_{SCE} has proven effective for the relatively low Mg content AA5083-H131 at NAMLT $\leq$ 40 mg/cm^2 in 0.6 M NaCl using potentiostat-based control (infinite anode) [6,7]. However, to transition towards engineering use, it is necessary to evaluate the robustness of this behavior over a wider range of conditions. Specifically, it is necessary to look at (1) more severe levels of alloy sensitization, (2) more aggressive bulk saline environments as a precursor to atmospheric environments, (3) different alloy compositions, and (4) different levels of cathodic polarization to determine if a specific window of applied potential exists for IG-SCC mitigation [70,74]. Therefore, the objectives of Chapter 2 are to experimentally quantify the potency of cathodic protection in aggressive saline / alloy sensitization conditions, as well as to determine the threshold past which applied cathodic polarization on AA5456-H116 may be deleterious rather than beneficial.

Chapter 2 answers the following questions:

- *Does potentiostat-based cathodic polarization remain effective for IG-SCC mitigation in the high Mg content AA5456-H116, and at maximized alloy sensitization (NAMLT 65 mg/cm^2)?*
- *How effective is potentiostat-based cathodic polarization for IG-SCC mitigation in more aggressive bulk salinities such as saturated NaCl or $MgCl_2$ in the applied potential range of -0.8 V_{SCE} to -1.1 V_{SCE}?*

- *Does a lower limit for effective cathodic polarization exist in the applied polarization range of -1.3 V_{SCE} to -1.7 V_{SCE}, and does IG-SCC occur following the onset of significant caustic corrosion in AA5456-H116?*

This chapter consists of two papers co-authored by J. R. Scully and J. T. Burns [46,75].

1.5.2 Chapter 3: Assessment of Zn-Rich Primers for the Galvanic Protection of Highly Sensitized AA5456-H116

Metal-rich primers have been utilized in a variety of engineering sectors for corrosion control [66,76,77], and may be promising for IG-SCC mitigation in Al-Mg alloys. However, these primers may achieve a wide range of sacrificial anode-based cathodic protection performance in service based on primer formulation and design, such as the choice of pigment type, pigment loading, and resin type/porosity. The allowable performance range in which MRPs may prove effective for IG-SCC mitigation on Al-Mg, if such a range even exists, is unknown. The mitigation of IG-SCC requires that these primers may overcome significant demands due to crack wake extension, rapid crack tip acidification, and Ohmic voltage drop in the resin, scribe, and crack wake. Further, metal-rich primers have seldom been considered for fracture mitigation, with the only such study in the literature being on high strength steels with Zn-rich primers [74]. Due to the more positive corrosion potential of these steels, the approximately -1.1 V_{SCE} established by these primers promoted hydrogen embrittlement. The Al-Mg system may be a better candidate for such protection due to the effective range of cathodic polarization extending to -1.3 V_{SCE} in 0.6 M NaCl [7]. Therefore, the objective of Chapter 3 is to assess the polarizability as well as the magnitude of sacrificial anode-based cathodic protection achieved by non-defected Zn-rich primers on highly sensitized AA5456-H116. New evaluation methods will be developed to screen these candidate systems for optimized performance, as well as to elucidate key coating qualities for in-service use. These studies will focus on four commercial primers containing Zn pigment embedded within either an inorganic or organic matrix.

Chapter 3 informs the following questions:

- *Can the selected MRP technologies apply and sustain the necessary coupled current densities and intermediate cathodic potentials on AA5456-H116 in full immersion conditions to establish cathodic polarization?*
- *As the ZRP is depleted of sacrificial Zn content, how is the achieved cathodic polarization affected?*
- *How may primer polarizability be effectively quantified, and why does this performance attribute vary significantly between ZRP systems?*

This chapter consists of a publication co-authored by J. T. Burns and J. R. Scully, with a conference proceeding considering the Mg/Al-Zn/Zn-containing primers provided in Appendix I [78,79].

1.5.3 Chapter 4: The Ability of Finite Anodes to Mitigate IG-SCC Under Simplified Galvanic Coupling Conditions

Large-scale engineering structures contain complex geometries and operate in harsh service conditions, and any coating system will inevitably experience defects (e.g. mechanical damage, environmental degradation, imperfect system installation, etc.). As such, there are three fundamental requirements for service-ready, finite sacrificial cathodic protection systems: (1) the ability to quickly suppress aggressive chemistries (to halt a growing crack); (2) long-term endurance in aggressive saline environments; and (3) applied potential must be sensed at the crack tip across different sacrificial anode spacings and for various crack geometries. Furthermore, these systems must overcome three main sources of Ohmic voltage drop acting to impede effective polarization of the crack tip, present in the high access impedance resin, the scribe, as well as down the crack wake/flank. The ability of select ZRP systems to achieve the list of required attributes will be experimentally assessed via LEFM test methods, utilizing select ZRP systems based on Chapter 3.

The objective of Chapter 4 is to assess the potential for rapid mitigation of active IG-SCC, as well as the mitigation of the onset of IG-SCC through various engineering-relevant methods. The ability to mitigate active IG-SCC via pure Zn anode- and Zn-rich coatings-based galvanic coupling will be evaluated via linear elastic fracture mechanics (LEFM) testing in 0.6 M NaCl at constant, post-IG-SCC threshold stress intensity of 10 MPa√m. Moving towards real service conditions, the final step in experimental complexity is to forgo the simplified galvanic coupling conditions and, instead, to apply the Zn-rich primer directly to the AA5456-H116 surface. These comparisons may begin to illustrate inefficiencies in the function of these coatings in IG-SCC mitigation due to effects of MRP activation time, effective potential distribution distance (throwing power), and pigment type, as well as demonstrating the influence of galvanic coupling on overall performance. The interpretation of these results will be informed by all of the previous chapters.

Chapter 4 will answer the following questions:

- *Once an aggressive chemistry has been formed to enable IG-SCC, can crack growth be mitigated, and if so, how quickly at constant stress intensity of 10 MPa√m?*
- *Do significant differences exist in the intermittent cathodic protection performance of a potentiostat, a pure Zn anode, or a Zn-rich primer?*
- *Is the magnitude of achieved IG-SCC mitigation dependent on bulk salinity, scribe width, and crack geometry?*

- *Does a polarizability threshold exist below which ZRP-based sacrificial anodic protection is ineffective for IG-SCC mitigation?*

This chapter consists of a publication co-authored by J. R. Scully and J. T. Burns [75].

1.5.4 Chapter 5: Potential Secondary Chemical Protection Effects of Bulk Chemistry Zn^{2+} Content on IG-SCC Severity in Al-Mg

The presence of Zn^{2+} ions have been demonstrated to affect anodic as well as cathodic kinetics in a variety of alloy systems [80–82]. The objective of Chapter 5 is to assess the potential effects of Zn cation content in the bulk environment on the severity of IG-SCC in AA5456-H116. Experimental work performed in Chapter 4 purposefully avoided potential secondary chemical protection effects by mitigating Zn cation dissolution into the bulk environment with a 3-5 μm pore diameter filter; the presence of these cations must to be quantified and understood in order to systematically assess primer performance in more realistic service conditions. Chemical stability modeling efforts will inform the equilibrium cation contents as well as the corrosion product present in Zn-based sacrificial anode systems under given conditions, which will then be tested experimentally to evidence any effects on IG-SCC severity in AA5456-H116 at fixed potential.

Chapter 5 will inform the following questions:

- *Does the presence of Zn^{2+} in the bulk environment have significant effect on the severity of IG-SCC in highly sensitized AA5456-H116, separate from cathodic polarization effects?*
- *What are the potential influences due to Zn-based corrosion product formation?*

This chapter contains one publication co-authored by R. J. Santucci and J. R. Scully [83], with baseline experimental evidence provided in Appendix II.

This dissertation will be concluded with a summary of overarching conclusions and a discussion on future work.

1.6 REFERENCES

[1] W.J. Golumbfskie, K.T. Tran, J.M. Noland, R. Park, D.J. Stiles, G. Grogan, C. Wong, Survey of detection, mitigation, and repair technologies to address problems caused by sensitization of Al-Mg alloys on navy ships, Corrosion. 72 (2016) 314–328. doi:10.5006/1916.

[2] R.B. Niederberger, J.L. Basil, G.T. Bedford, Corrosion and Stress Corrosion of 5000-Series Al Alloys in Marine Environments, Corrosion. 22 (1966) 68–73. doi:doi:10.5006/0010-9312-22.3.68.

[3] N.J.H. Holroyd, G.M. Scamans, Environmental Degradation of Marine Aluminum Alloys—Past, Present, and Future, Corrosion. 72 (2016). doi:10.5006/1927.

[4] F.S. Bovard, Sensitization and Environmental Cracking of 5XXX Aluminum Marine Sheet and Plate Alloys, in: D.A.Shifler (Ed.), Corros. Mar. Saltwater Environ. II Proc. Int. Symp., 2004: pp. 232–243.

[5] J.L. Searles, P.I. Gouma, R.G. Buchheit, Stress Corrosion Cracking of Sensitized AA5083 (Al-4.5Mg-1.0Mn), Mater. Sci. Forum. 396–402 (2002) 1437–1442. doi:10.4028/www.scientific.net/MSF.396-402.1437.

[6] C.B. Crane, R.. Kelly, R.P. Gangloff, Crack chemistry control of intergranular stress corrosion cracking in sensitized Al-Mg, Corrosion. 72 (2016) 242–263. doi:10.5006/1852.

[7] C.B. Crane, R.P. Gangloff, Stress corrosion cracking of Al-Mg alloy 5083 sensitized at low temperature, Corrosion. 72 (2016) 221–241. doi:10.5006/1766.

[8] M.J. Starink, A.-M. Zahra, β′ and β precipitation in an Al–Mg alloy studied by DSC and TEM, Acta Mater. 46 (1998) 3381–3397. doi:10.1016/S1359-6454(98)00053-6.

[9] R. Goswami, R.L. Holtz, Transmission Electron Microscopic Investigations of Grain Boundary Beta Phase Precipitation in Al 5083 Aged at 373 K (100 °C), Metall. Mater. Trans. A. 44 (2012) 1279–1289. doi:10.1007/s11661-012-1166-9.

[10] N. Birbilis, R. Zhang, M.L.C. Lim, R.K. Gupta, C.H.J. Davies, S.P. Lynch, R.G. Kelly, J.R. Scully, Quantification of Sensitization in AA5083-H131 via Imaging Ga-Embrittled Fracture Surfaces, Corrosion. 69 (2013) 396–402. doi:10.5006/0804.

[11] M.L.C. Lim, J.R. Scully, R.G. Kelly, Intergranular Corrosion Penetration in an Al-Mg Alloy as a Function of Electrochemical and Metallurgical Conditions, Corrosion. 69 (2013) 35–47. doi:10.5006/0722.

[12] M.L.C. Lim, R.G. Kelly, J.R. Scully, Overview of Intergranular Corrosion Mechanisms, Phenomenological Observations, and Modeling of AA5083, Corrosion. 72 (2016). doi:10.5006/1818.

[13] I.N.A. Oguocha, O.J. Adigun, S. Yannacopoulos, Effect of sensitization heat treatment on properties of Al–Mg alloy AA5083-H116, J. Mater. Sci. 43 (2008) 4208–4214. doi:10.1007/s10853-008-2606-1.

[14] D. Sampath, S. Moldenhauer, H.R. Schipper, K. Mechsner, A. Haszler, Decomposition of Solid Solution of the AA5083 Alloy upon Exposure to Elevated Temperatures, Mater. Sci.

Forum. 331–337 (2000) 1089–1094. doi:10.4028/www.scientific.net/MSF.331-337.1089.
[15] Y. Zhu, Characterization of beta phase growth and experimental validation of long term thermal exposure sensitization of AA5XXX alloys, University of Utah, 2013. http://adsabs.harvard.edu/abs/2013PhDT........12Z.
[16] ASTM, ASTM: G67-04 Standard Test Method for Determining the Susceptibility to Intergranular Corrosion of 5XXX Series Aluminum Alloys by Mass Loss After Exposure to Nitric Acid (NAMLT Test), ASTM International, West Conshocken, PA, 2004.
[17] R. Zhang, S.P. Knight, R.L. Holtz, R. Goswami, C.H.J. Davies, N. Birbilis, A survey of sensitization in 5xxx series aluminum alloys, Corrosion. 72 (2016) 144–159. doi:10.5006/1787.
[18] Y.-K. Yang, T.R. Allen, Determination of the β Solvus Temperature of the Aluminum Alloy 5083, Metall. Mater. Trans. A. 44 (2013) 5226–5233. doi:10.1007/s11661-013-1837-1.
[19] R. Goswami, G. Spanos, P.S. Pao, R.L. Holtz, Precipitation behavior of the ß phase in Al-5083, Mater. Sci. Eng. A. 527 (2010) 1089–1095. doi:10.1016/j.msea.2009.10.007.
[20] D. Scotto D’Antuono, J. Gaies, W. Golumbfskie, M.L. Taheri, Grain boundary misorientation dependence of β phase precipitation in an Al–Mg alloy, Scr. Mater. 76 (2014) 81–84. doi:10.1016/j.scriptamat.2014.01.003.
[21] Y. Zhao, M.N. Polyakov, M. Mecklenburg, M.E. Kassner, A.M. Hodge, The role of grain boundary plane orientation in the β phase precipitation of an Al–Mg alloy, Scr. Mater. 89 (2014) 49–52. doi:10.1016/j.scriptamat.2014.07.003.
[22] D. Scotto D’Antuono, J. Gaies, W. Golumbfskie, M.L. Taheri, Direct measurement of the effect of cold rolling on β phase precipitation kinetics in 5xxx series aluminum alloys, Acta Mater. 123 (2017) 264–271. doi:10.1016/j.actamat.2016.10.060.
[23] M.A. Steiner, S.R. Agnew, Modeling sensitization of Al–Mg alloys via β-phase precipitation kinetics, Scr. Mater. 102 (2015) 55–58. doi:10.1016/j.scriptamat.2015.02.012.
[24] M.A. Steiner, S.R. Agnew, Predictive sensitization modeling for AA5xxx aluminum alloys including non-isothermal cases, Corrosion. 72 (2016) 169–176. doi:10.5006/1675.
[25] R.H. Jones, D.R. Baer, M.J. Danielson, J.S. Vetrano, Role of Mg in the stress corrosion cracking of an Al-Mg alloy, Metall. Mater. Trans. A. 32 (2001) 1699–1711. doi:10.1007/s11661-001-0148-0.
[26] R.H. Jones, J.S. Vetrano, C.F. Windisch, Stress Corrosion Cracking of Al-Mg and Mg-Al Alloys, Corrosion. 60 (2004) 1144–1154. doi:10.5006/1.3299228.
[27] J.L. Searles, P.I. Gouma, R.G. Buchheit, Stress corrosion cracking of sensitized AA5083 (Al-4.5Mg-1.0Mn), Metall. Mater. Trans. A. 32 (2001) 2859–2867. doi:10.1007/s11661-001-1036-3.
[28] J. Gao, D.J. Quesnel, Enhancement of the Stress Corrosion Sensitivity of AA5083 by Heat Treatment, Metall. Mater. Trans. A. 42 (2010) 356–364. doi:10.1007/s11661-010-0375-3.
[29] E.C. Cormack, The Effect of Sensitization on the Stress Corrosion Cracking of Aluminum Alloy 5456, Naval Postgraduate School, 2012.
[30] S. Roitsch, M. Heggen, M. Lipinska-Chwalek, M. Feuerbacher, Single-crystal plasticity of the complex metallic alloy phase beta-Al-Mg, Intermetallics. 15 (2007) 833–837. doi:10.1016/j.intermet.2006.08.017.
[31] G. Yi, M.L. Free, Y. Zhu, A.T. Derrick, Capillarity Effect Controlled Precipitate Growth at the Grain Boundary of Long-Term Aging Al 5083 Alloy, Metall. Mater. Trans. A. 45

(2014) 4851–4862. doi:10.1007/s11661-014-2473-0.

[32] J. Gao, Experiments to explore the mechanisms of stress corrosion cracking, University of Rochester, 2011.

[33] M.E. McMahon, P.J. Steiner, A.B. Lass, J.T. Burns, The effect of temper and composition on the stress corrosion cracking of Al-Mg alloys, Corrosion. 73 (2017) 347–361.

[34] M.E. McMahon, P.J. Steiner, A.B. Lass, J.T. Burns, The effect of loading orientation on intergranular stress corrosion cracking in Al-Mg alloys, Corrosion. 73 (2017) 713–723.

[35] E. Bumiller, Intergranular corrosion in AA5XXX aluminum alloys with discontinuous precipitation at the grain boundaries, University of Virginia, 2011.

[36] S. Jain, Surface Spreading of Interganular Corrosion on Stainless Steels and Al-Mg (AA5XXX) Alloys, University of Virginia, 2011.

[37] Y.-K. Yang, T. Allen, Direct visualization of β phase causing intergranular forms of corrosion in Al–Mg alloys, Mater. Charact. 80 (2013) 76–85. doi:10.1016/j.matchar.2013.03.014.

[38] J. Buczynski, Electrochemical Analyses of Etchants Used to Detect Sensitization in Marine-Grade 5XXX Aluminum-Magnesium Alloys, University of Virginia, 2012.

[39] M.E. McMahon, R.L. Haines, J.M. Schulte, P.J. Steiner, J.T. Burns, Beta Phase Distribution in Al-Mg Alloys of Varying Composition and Temper, Corros. Draft. (n.d.).

[40] M.E. McMahon, P.J. Steiner, A.B. Lass, J.T. Burns, The effect of temper and composition on intergranular stress corrosion cracking in Al-Mg alloys, Corrosion. 73 (2017) 347–361. doi:10.5006/2317.

[41] P.M. Natishan, W.E.O. Grady, E. Mccafferty, D.E. Ramaker, Chloride Uptake by Oxide Covered Aluminum as Determined by X-Ray Photoelectron and X-Ray Absorption Spectroscopy, J. Electrochem. Soc. 146 (1999) 1737–1740. doi:10.1149/1.1391835.

[42] E. McCafferty, Sequence of steps in the pitting of aluminum by chloride ions, Corros. Sci. 45 (2003) 1421–1438. doi:10.1016/S0010-938X(02)00231-7.

[43] E. McCafferty, The electrode kinetics of pit initiation on aluminum, Corros. Sci. 37 (1995) 481–492. doi:10.1016/0010-938X(94)00150-5.

[44] H. Böhni, H.H. Uhlig, Environmental Factors Affecting the Critical Pitting Potential of Aluminum, J. Electrochem. Soc. 116 (1969) 906. doi:10.1149/1.2412167.

[45] E. McCafferty, Introduction to Corrosion Science, Springer, New York, NY, 2010.

[46] W.M. Carroll, C.B. Breslin, Stability of passive films formed on aluminium in aqueous halide solutions, Br. Corros. J. 26 (1991).

[47] M.E. McMahon, J.R. Scully, J.T. Burns, Mitigation of intergranular stress corrosion cracking in Al-Mg by electrochemical potential control, J. Miner. Met. Mater. 69 (2017) 1389–1397. doi:10.1007/s11837-017-2362-2.

[48] Z. Szklarska-Smialowska, Pitting corrosion of aluminum, Corros. Sci. 41 (1999) 1743–1767. doi:10.1016/S0010-938X(99)00012-8.

[49] G.S. Frankel, J.R. Scully, C. V Jahnes, Repassivation of Pits in Aluminum Thin Films, J. Electrochem. Soc. 143 (1996) 1834–1840. doi:10.1149/1.1836912.

[50] R.H. Jones, The Influence of Hydrogen on the Stress-Corrosion Cracking of Low-Strength Al-Mg Alloys, J. Miner. Met. Mater. 55 (2003) 42–46. doi:10.1007/s11837-003-0225-5.

[51] J.-H. Ai, M.L.C. Lim, J.R. Scully, Effective Hydrogen Diffusion in Aluminum Alloy 5083-H131 as a Function of Orientation and Degree of Sensitization, Corrosion. 69 (2013) 1225–1239. doi:10.5006/0987.

[52] X.Y. Zhang, R.G. Song, B. Sun, H. Lu, C. Wang, Effects of applied potential on the stress

corrosion cracking behavior of 7003 aluminum alloy in acid and alkaline chloride solutions, Int. J. Miner. Metall. Mater. 23 (2016) 819–826. doi:10.1007/s12613-016-1296-y.
[53] A. Zielinski, Hydrogen-enhanced stress corrosion cracking of aluminium alloys, Mater. Sci. 34 (1999) 20–26.
[54] D. Hardie, N.J.H. Holroyd, R.N. Parkins, Reduced ductility of high-strength aluminum alloy during or after exposure to water, Met. Sci. 13 (1979) 603–610.
[55] T.H. Nguyen, B.F. Brown, R.T. Foley, On the Nature of the Occluded Cell in the Stress Corrosion Cracking of AA 7075-T651—Effect of Potential, Composition, Morphology, Corrosion. 38 (1982) 319–326. doi:10.5006/1.3621692.
[56] C. Matzdorf, W. Nickerson, Active Aluminum Rich Coatings, 8,262,938 B2, 2012. doi:10.1074/JBC.274.42.30033.(51).
[57] P. Plagemann, J. Weise, A. Zockoll, Zinc-magnesium-pigment rich coatings for corrosion protection of aluminum alloys, Prog. Org. Coatings. 76 (2013) 616–625. doi:10.1016/j.porgcoat.2012.12.001.
[58] A.D. King, J.R. Scully, Sacrificial anode-based galvanic and barrier corrosion protection of 2024-T351 by a Mg-rich primer and development of test methods for remaining life assessment, Corrosion. 67 (2011) 1–22. doi:10.5006/1.3590330.
[59] M.E. Nanna, G.P. Bierwagen, Mg-rich coatings: A new paradigm for Cr-free corrosion protection of Al aerospace alloys, J. Coatings Technol. Res. 1 (2004) 69–80. doi:10.1007/s11998-004-0001-7.
[60] M.E. Nanna, G.P. Bierwagen, D. Battocchi, Magnesium Rich Coatings and Coating Systems, US 2007/0128351 A1, 2007. doi:10.1016/j.micromeso.2003.09.025.
[61] C. Matzdorf, W. Nickerson, Aluminum alloy coated pigments and corrosion-resistant coatings, 8,277,688, 2012. doi:10.1016/j.(73).
[62] F. Presuel-Moreno, M.A. Jakab, N. Tailleart, M. Goldman, J.R. Scully, Corrosion-resistant metallic coatings, Mater. Today. 11 (2008) 14–23. doi:10.1016/S1369-7021(08)70203-7.
[63] A.D. King, J.S. Lee, J.R. Scully, Finite Element Analysis of the Galvanic Couple Current and Potential Distribution between Mg and 2024-T351 in a Mg Rich Primer Configuration, J. Electrochem. Soc. 163 (2016) C342–C356. doi:10.1149/2.0171607jes.
[64] A.D. King, B. Kannan, J.R. Scully, Environmental degradation of a mg-rich primer in selected field and laboratory environments: Part 1-without a topcoat, Corrosion. 70 (2014) 512–535. doi:10.5006/0988.
[65] B. Kannan, A.D. King, J.R. Scully, Effect of pretreatments on Alloy 2024-T351 corrosion protection by magnesium-rich, nonchromium primer (MgRP): Laboratory characterization in full immersion, Corrosion. 71 (2015) 1093–1109. doi:10.5006/1700.
[66] A. Stander, NADC-MA-7063: Investigation of metallic pigments as corrosion preventatives in aircraft primers, 1970.
[67] R.J. Santucci Jr., B. Kannan, J.R. Scully, Electrochemical diagnostic cycle testing on magnesium and magnesium oxide-pigmented primers on 2024-T351, Corrosion. 74 (2017) 96–111. doi:10.5006/2547.
[68] M.S. Han, S. Ko, S.H. Kim, S.K. Jang, S.J. Kim, Optimization of corrosion protection potential for stress corrosion cracking and hydrogen embrittlement of 5083-H112 alloy in seawater, Met. Mater. Int. 14 (2008) 203–211. doi:10.3365/met.mat.2008.04.203.
[69] J.W. Watson, Y.Z. Shen, M. Meshii, Effect of cathodic charging on the mechanical

properties of aluminum, Metall. Mater. Trans. A. 19 (1988) 2299–2304. doi:10.1007/BF02645053.

[70] S.J. Kim, M.S. Han, S.K. Jang, Electrochemical characteristics of Al-Mg alloy in seawater for leisure ship: Stress corrosion cracking and hydrogen embrittlement, Korean J. Chem. Eng. 26 (2009) 250–257. doi:10.1007/s11814-009-0042-9.

[71] S.-J. Kim, Evaluating the electrochemical properties in the protection potential of material for use in Al vessels in seawater, Mater. Sci. Forum. 510–511 (2006) 158–161. doi:10.4028/www.scientific.net/MSF.510-511.158.

[72] X.G. Zhang, Corrosion and Electrochemistry of Zinc, 1st ed., Plenum Press, New York, 1996.

[73] F. Theiler, The rust preventing mechanism of zinc dust paints, Corros. Sci. 14 (1974). doi:10.1016/0010-938X(74)90001-8.

[74] R.A. Francis, Inorganic Zinc Silicate Coatings - The Early Days Part II: The Morgan Whyalla Pipeline, in: R.A. Francis (Ed.), Inorg. Zinc Coatings Hist. Chem. Prop. Appl. Altern., 2nd ed., The Australasian Corrosion Association Incorporated, Victoria, 2013: pp. 18–23.

[75] M.G. Koul, A. Sheetz, P. Ault, J. Repp, A. Whitfield, The Effect of Zn-Rich Coatings on the Corrosion and Cracking Resistance of High Strength Armor Steel, Corrosion. 70 (2014) 337–350. doi:10.5006/1027.

[76] M.E. McMahon, J.R. Scully, J.T. Burns, The effect of potential on stress corrosion cracking in a highly sensitized Al-Mg alloy, Mater. Sci. Eng. A, Draft. (2019).

[77] S.J. Feliu, R. Barajas, J.M. Bastidas, M. Morcillo, S. Feliu, Study of Protection Mechanisms of Zinc-Rich Paints by Electrochemical Impedance Spectroscopy, Electrochem. Impedance Anal. Ans Interpret. ASTM STP 1188. (1993) 438–449. doi:10.1520/STP18084S.

[78] J. Feliu S., M. Morcillo, S. Feliu, Deterioration of cathodic protection action of zinc-rich paint coatings in atmospheric exposure, Corrosion. 57 (2001) 591–597. doi:10.5006/1.3290386.

[79] M.E. McMahon, J.T. Burns, J.R. Scully, New Criteria for Substrate Protection Against Stress Corrosion Cracking in Al-Mg Alloys Based on Non-Polarizability of Zn-Rich Primers, Prog. Org. Coatings. (2019).

[80] M.E. McMahon, J.T. Burns, J.R. Scully, The effect of environment on metal-rich primer polarizability for the mitigation of stress corrosion cracking on highly sensitized Al-Mg, in: DoD Allied Nations 2019, n.d.

[81] S. Islam, Effects of Zn 2 + Concentration on the Corrosion of Mild Steel in NaCl Aqueous Solutions, J. Electrochem. Soc. 166 (2019) 83–90. doi:10.1149/2.1271902jes.

[82] D. Álvarez, A. Collazo, R. Figueroa, X.R. No, The Effect of Zn 2 + Ions on the Corrosion Behavior of Tinplate Immersed in Food-Simulating Solutions, Corrosion. 74 (2018) 7–8.

[83] D.M. Drazic, L.Z. Vorkapic, Inhibitory effects of manganeous, cadmium, and zinc ions on hydrogen evolution reaction and corrosion of iron in sulphuric acid solutions, Corros. Sci. 18 (1978) 907–910.

[84] M.E. McMahon, J.R. Scully, J.T. Burns, Erratum to: Mitigation of Intergranular Stress Corrosion Cracking in Al–Mg by Electrochemical Potential Control, J. Miner. Met. Mater. 69 (2017) 1724–1726. doi:10.1007/s11837-017-2432-5.

CHAPTER 2

The Efficacy of Potentiostat-Based Cathodic Polarization for IG-SCC Mitigation on AA5456-H116

2.1 Mitigation of Intergranular Stress Corrosion Cracking in Al-Mg by Electrochemical Potential Control

M. E. McMahon,[ǂ,*] J.R. Scully[*] and J. T. Burns[*]

Keywords: aluminum alloy, beta phase, cathodic protection, intergranular stress corrosion cracking, sensitization

[*] Center for Electrochemical Science and Engineering, Department of Materials Science and Engineering, University of Virginia, Charlottesville, VA 22904
[ǂ] Corresponding author. E-mail: mm5kn@virginia.edu

2.1.1 Abstract

Intergranular stress corrosion cracking in AA5456-H116 is suppressed via cathodic polarization in 0.6 M NaCl, saturated (5.45 M) NaCl, 2 M $MgCl_2$, and saturated (5 M) $MgCl_2$. Three zones of intergranular stress corrosion cracking (IG-SCC) susceptibility correlate with pitting potentials of unsensitized AA5456-H116 and pure β phase (Al_3Mg_2) in each aforementioned solution. These critical potentials reasonably describe the influence of α Al matrix and β phase dissolution rates on IG-SCC severity. Complete inhibition occurred at applied potentials of -1.0 and -1.1 V_{SCE} in 0.6 M NaCl. Whereas only partial mitigation of IG-SCC was achieved at -0.9 V_{SCE} in 0.6 M NaCl and at -0.9, -1.0, and -1.1 V_{SCE} in the more aggressive environments. Correlation of pitting potentials in bulk environments with IG-SCC behavior suggests an effect of bulk environment [Cl^-] and pH on the stabilized crack tip chemistry.

2.1.2 Introduction

AA5xxx-series alloys are increasingly used to replace heavier steel components in marine structures due to their high strength-to-weight ratio and general corrosion resistance [1]. The commercial AA5456 alloy is solid solution strengthened by a supersaturation of the Al-matrix with 5 wt. % Mg, as such mildly elevated temperatures can lead to precipitation of β phase (Al_3Mg_2)

on the grain boundaries after prolonged exposure to in-service temperatures [2]. This process is termed sensitization and is often quantified by the ASTM G-67 Nitric Acid Mass Loss test (NAMLT) [3]. The β phase is highly anodic to the matrix and in the presence of aggressive (e.g. aqueous chloride) environments can lead to severe intergranular stress corrosion cracking (IG-SCC) [4]. The NAMLT procedure is a rough proxy for IG-SCC susceptibility in Al-Mg alloys; specifically, Al-Mg alloys are considered resistant at NAMLT < 15 mg/cm^2, intermediate at 15 – 25 mg/cm^2, and susceptible at > 25 mg/cm^2 [3, 4]. The IG-SCC behavior is hypothesized to be governed by a coupled anodic dissolution process (of the β phase and possibly the Al matrix), which catalyzes the formation of an aggressive acidified local crack tip chemistry that facilitates the enhanced generation of crack tip H and enables embrittlement in the fracture process zone [5-7]. This mechanism has been validated by experiment as well as modeling under a recent extension of the hydrogen enhanced decohesion (HEDE) hypothesis to the Al-Mg system [5, 8].

Mitigation of IG-SCC has been demonstrated in recent work using cathodic polarization. Cathodic polarization can lower the crack tip potential below the critical pitting potentials which suppresses β and α breakdown, thus the development of the aggressive crack tip chemistry. This suppression was observed for sensitized AA5083-H131 (NAMLT ≤ 40 mg/cm^2) tested in 0.6 M NaCl [5, 6]. The efficacy of this mitigation strategy must be examined for more aggressive material compositions, loading environments, and sensitization levels. Marine service conditions entail alternating environmental conditions where deliquesced, thin film electrolytes with saturated salt concentrations can be present. While there are several unique aspects of the thin film environment, as a first step it is useful to quantify the IG-SCC behavior in the full immersion environments with similar high levels of salt concentration. Furthermore, service components can often experience severe NAMLT levels due to exposures to elevated operational temperatures over the extended component lifetimes (20-25 years). As such, the aim of the current study is to evaluate the efficacy of the polarization-based mitigation strategy in near-worst case saline and alloy sensitization scenarios; namely, more aggressive electrolyte chemistries, for AA5456-H116 (which has a higher bulk Mg content), and at a severe NAMLT level (65 mg/cm^2).

2.1.3 **Methods**

The specific material composition of the non-recrystallized, 5.7 cm thick AA5456-H116 plate utilized in this study and related mechanical properties are detailed elsewhere [8]. All AA5456-H116 alloy was heat treated at 100°C (373 K) for 14 days to reach the NAMLT value of 65 mg/cm^2 prior to fracture testing. Relative to typical sensitization levels of NAMLT 24 (3.5 days at 100°C) or 40 mg/cm^2 (6.75 days at 100°C), this sensitization is severe and constitutes 99% grain boundary coverage or more by the anodic β phase [5, 8].

Fracture mechanics testing was performed on single edge notch tensile (SENT) specimens of gauge width 17.33 mm and thickness of 6.62 mm, in the equally susceptible S-L and S-T orientations [9, 10] with an electrical discharge machined (EDM) notch of depth 1.45 mm placed at the plate half thickness (t/2). Open air fatigue precracking was done to 2.60 or 2.75 mm total depth, with the final stress intensity (K) being 2.5 or 3.5 MPa√m, respectively. Specimens were then tested under full immersion in a 200 mL acrylic cell, through which 2 L of aqueous 0.6 M NaCl (pH 5.6), saturated (5.45 M) NaCl (pH 6.2), 2 M $MgCl_2$ (pH 3.4), or saturated (5 M) $MgCl_2$ (pH 2.4) solution circulated at 20 mL/min at ambient temperature (sealed from surrounding environment, but not otherwise perturbed). The electrochemical environment of the SENT specimen (grounded through the grips) was held to a constant applied potential of -0.8, -0.9, -1.0, or -1.1 V_{SCE} *via* a floating ground potentiostat at ambient temperature. Slow rising displacement testing first consisted of a 5 or 10 hour hold under applied force of 1 or 2 kN (depending on the solution corrosiveness) and at the polarization of interest. Following this initial hold the specimen was loaded at an initial dK/dt of 0.25 MPa√m/h, achieved under grip displacement controlled rates of ≈0.0002 mm/min, until final fracture. Crack growth was monitored to 0.5 μm resolution with the direct current potential difference (dcPD) method, the details of which are described elsewhere [11]. Post test data analysis utilized Ramberg Osgood constants derived from compression testing stress-strain curves to carry out J-integral plastic corrections (K_J); the fundamentals and application of this approach are described elsewhere [12]. Two traditional fracture mechanics-based metrics of IG-SCC susceptibility will be reported: threshold stress intensity (K_{TH}) and Stage II crack growth rates (da/dt_{II}). In the current work two criteria are used to establish the K_{TH}: (1) the onset of Stage I crack growth which is typified by a significant increase in the slope of the da/dt vs. K_J relationship, and (2) exceeding the resolution limit. Stage I crack growth is terminated by a (nearly) K-independent plateau; this plateau value is traditionally deemed the Stage II crack growth (da/dt_{II}). Prior work established a function resolution limit (by testing in a dry nitrogen environment) largely associated with increases in crack tip plasticity that scales with K for the current slow rising displacement testing protocol [5]. This limit is indicated by the solid black line in the da/dt versus K_J plots to follow.

Electrochemical characterization of sensitization and potential thresholds for local corrosion of the alloy and β phase was performed to enhance the interpretation of fracture mechanics-based IG-SCC results. These analyses utilized a flat cell with platinum mesh as the counter electrode, a saturated calomel electrode fitted with a Luggin capillary as the reference electrode, and the as-received (NAMLT 4 mg/cm^2) AA5456-H116 alloy (S-T) or the pure β phase as the working electrode. The open circuit potential was stabilized in full immersion for 60 minute

(AA5456-H116) or 30 minute (pure β phase) durations prior to potentiodynamic analysis, which utilized a scan rate of 0.167 mV/sec. Specimens were polished to 1200 grit *via* silicon carbide paper in deionized water (AA5456-H116) or methanol (pure β phase) prior to electrochemical testing.

2.1.4 **Results**

2.1.4.1 ***Characterization of Sensitization***

Potentiodynamic analyses considered the unsensitized AA5456-H116 and β phase in full immersion. These results demonstrated the critical E_{pit} values governing the passivation or dissolution of the β and the α Al matrix, shown in Figure 2.1 in 0.6 M NaCl. The remaining environments yielded similar $E_{pit\,(\alpha)}$ and $E_{pit\,(\beta)}$ trends, the details of which are summarized in Table 2.I (EC section). These results framed three zones of electrochemical activity in each environment (illustrated in Figure 2.1). Zone 1 is the most aggressive region where applied potentials anodic to both $E_{pit\,(\alpha)}$ and $E_{pit\,(\beta)}$ cause both β and α matrix breakdown and local corrosion. Pitting would be expected at both grain boundaries and in the matrix. Zone 2 encompasses potentials cathodic to only $E_{pit\,(\alpha),}$ causing α dissolution to occur by passive dissolution while β remains highly active and corrodes by breakdown and local corrosion above $E_{pit\,(\beta)}$. Zone 3 exists at all potentials cathodic to both $E_{pit\,(\alpha)}$ and $E_{pit\,(\beta)}$, which is the passive zone for both phases. The pitting potentials in Table 2.I will be correlated with and used to interpret the observed IG-SCC trends. Open circuit potentials (OCPs) for AA5456-H116, NAMLT 4 mg/cm^2 are included to Table 2.I in each environment for reference based on the anodic potentiodynamic scans.

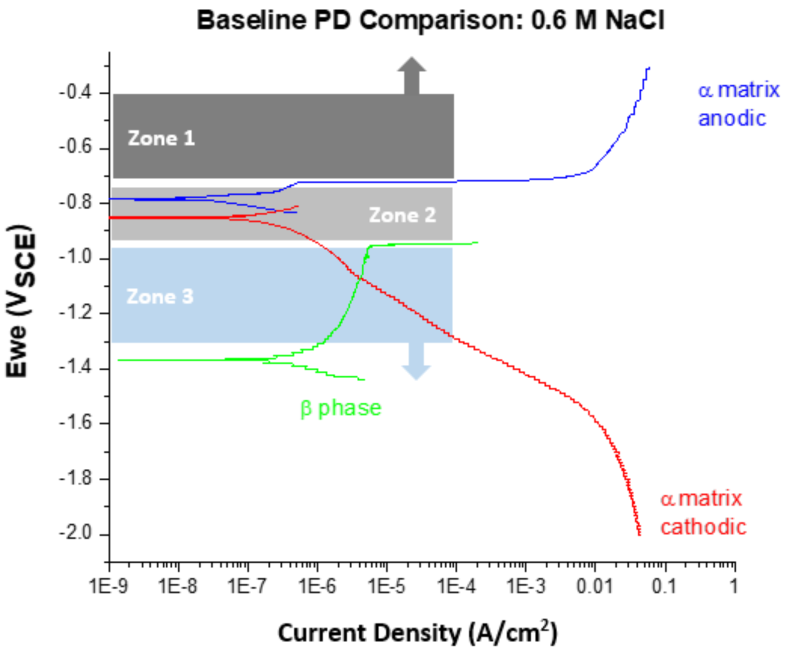

Figure 2.1: The effect of environment on E_{pit} *and* i_{pit} *of AA5456-H116, NAMLT 4* mg/cm^2 *(as-received), and pure β phase,* Al_3Mg_2*, showing the critical E window when IG-SCC will begin to shut down in 0.6 M NaCl. The trends in saturated NaCl, 2 M* $MgCl_2$*, and saturated* $MgCl_2$ *were similar and are represented numerically by pitting and open circuit potentials given in Table 2.I.*

Table 2.I: Critical Electrochemical and Fracture Mechanical Results

		0.6 M NaCl		**Saturated NaCl**		**2 M $MgCl_2$**		**Saturated $MgCl_2$**	
EC	**OCP (α) (V_{SCE})**	-0.78		-0.89		-0.95		-1.01	
	E_{pit} (α) (V_{SCE})	-0.70		-0.85		-0.82		-0.90	
	E_{pit} (β) (V_{SCE})	-0.95		-1.02		-1.00		-1.05	
LEFM		**K_{TH}**	**da/dt_{II}**	**K_{TH}**	**da/dt_{II}**	**K_{TH}**	**da/dt_{II}**	**K_{TH}**	**da/dt_{II}**
	-0.8 V_{SCE}	5.0	$1.0x10^{-3}$	3.0	$4.0x10^{-3}$	2.5	$5.0x10^{-3}$	2.0	$1.0x10^{-3}$
	-0.9 V_{SCE}	17.0	$1.0x10^{-4}$	4.0	$2.0x10^{-3}$	6.0	$2.0x10^{-3}$	4.0	$1.0x10^{-3}$
	-1.0 V_{SCE}	N/A	N/A	12.0	$3.5x10^{-4}$	9.0	$3.0x10^{-4}$	6.5	$9.0x10^{-4}$
	-1.1 V_{SCE}	N/A	N/A	13.0	$1.5x10^{-4}$	9.0	$2.0x10^{-4}$	9.0	$1.5x10^{-4}$

Table 2.I:Pitting potentials defining the zones of transitional passivity in the sensitized Al-Mg matrix, open circuit potentials, and specific K threshold and Stage 2 crack growth initiation points defining crack growth trends for each environment and applied potential. EC = electrochemical data, LEFM = linear elastic fracture mechanical data

2.1.4.2 *Characterization of IG-SCC Behavior*

Figure 2.2 illustrates the crack growth rates versus elastic-plastic stress intensity (da/dt versus K_J) for fracture mechanics testing at -0.8, -0.9, -1.0, and -1.1 V_{SCE} in all saline environments considered; also included is the previously established resolution limit [5]. These data show crack growth rates decrease in all environments with increasingly cathodic applied potentials. Some trends observed in Figure 2.2 do not demonstrate the traditional transition from Stage I to II, as such the da/dt_{II} values are functionally determined by the maximum crack growth rate achieved. The K_{TH} and da/dt_{II} are summarized for each applied potential and environment in Table 2.I. The results of the fracture mechanics testing and potentiodynamic scans are combined and shown graphically in Figure 2.3 for each environment and degree of polarization. It is critically important to recognize that (1) a distinct crack tip chemistry will develop, and (2) there will be ohmic (i.e. IR) drop from the SENT surface down the crack tip. Considering the former, since the E_{pit} values are dependent on the solution chemistry, it is necessary to evaluate the applicability of the bulk values to the crack tip processes that control the IG-SCC behavior. Considering the latter, due to IR drop the bulk applied potentials do not accurately describe the crack tip conditions which would be shifted to lower potentials (as indicated by the arrows on the plots). The magnitude of this shift is interdependent on the bulk/crack tip chemistry, bulk applied potential, and crack geometry. Prior research [6] suggested that over the range of polarizations and the loading geometries pertinent to the current study the IR drop would be < 100mV; pertinent expected deviations from this assumption will be noted when appropriate. The effect of both crack chemistry and IR drop on applicability of correlating the polarization data in Figure 2.1 with the IG-SCC data in Figure 2.2 will be explored further in the Discussion.

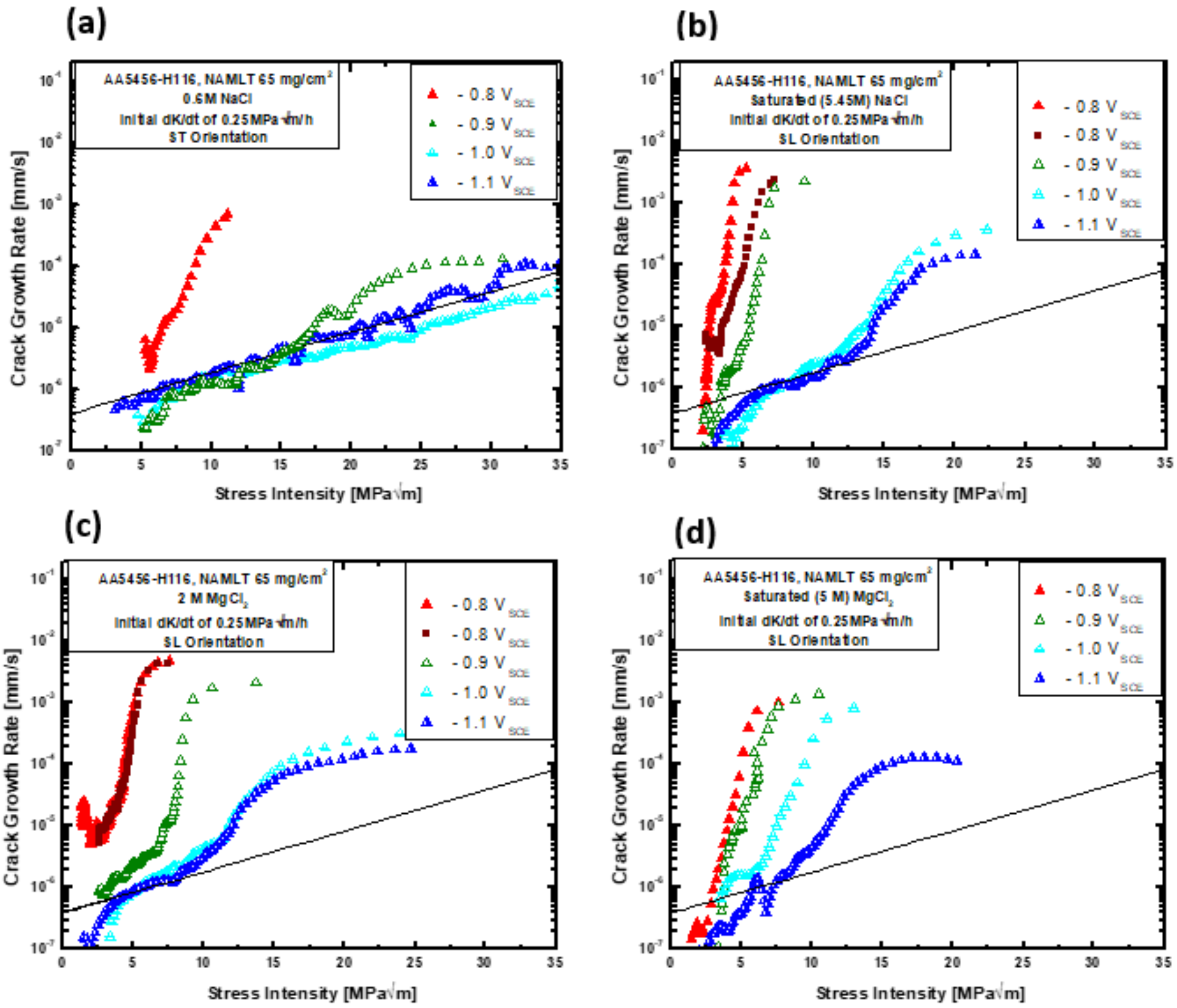

Figure 2.2: The effect of environment and electrochemical potential on the IG-SCC susceptibility of AA5456-H116, NAMLT 65 mg/cm2, showing mitigated IG-SCC rates at applied E increasingly near or more negative than $E_{pit\,(\alpha)}$ and $E_{pit\,(\beta)}$ in (a) 0.6 M NaCl, (b) saturated NaCl, (c) 2 M MgCl2, and (d) saturated MgCl2. Duplicate testing is demonstrated in (b) and (c) for the -0.8 V_{SCE} tests.

In 0.6 M NaCl (Figure 2.2 (A)), the most severe IG-SCC occurs in this environment at the bulk applied potential (E_{app}) of -0.8 V_{SCE} (K_{TH} = 10 MPa√m, $da/dt_{II} = 6\times10^{-4}$ mm/s), followed by the reduced severity at E_{app} of -0.9 V_{SCE} (K_{TH} = 17 MPa√m, $da/dt_{II} = 1\times10^{-4}$ mm/s). The applied potentials of -1.0 and -1.1 V_{SCE} follow the resolution limit, suggesting that no appreciable IG-SCC occurred. Therefore, Table 2.I shows only the K_{TH} and da/dt_{II} values, and Figure 2.3 shows minima K_{TH} and maxima da/dt_{II} points for the -0.8 and -0.9 V_{SCE} tests. The significant differences in dcPD indicated crack extension of 0.25 and 2.5 mm, which is illustrated by dashed red lines in Figure 2.4 for -0.8 and -1.1 V_{SCE}, respectively, tested in 0.6M NaCl. While crack wake dissolution associated with the aggressive crack chemistries compromise detailed analysis of the fracture morphology, the regions bounded by red dashed lines in Figure 2.4(A) are typical of previously observed IG-SCC morphologies and the da/dt values exceeded the resolution limit [5, 8]. Conversely, the dcPD reported crack advance for the -1.1 V_{SCE} (and -1.0 V_{SCE}) in 0.6 M NaCl are

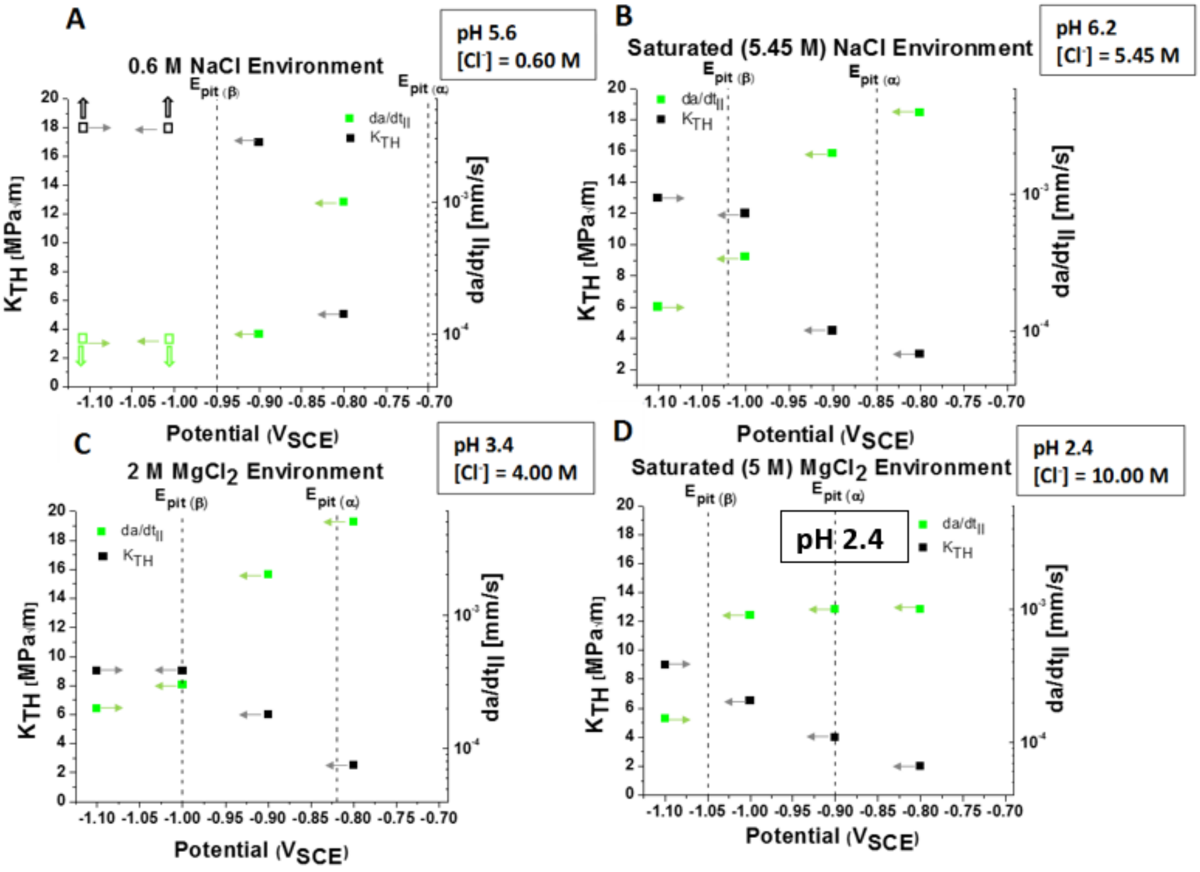

*Figure 2.3: Trends of K_{TH} increase and da/dt_{II} decrease with applied E_{SCE} becoming increasingly cathodic with respect to $E_{corr(\alpha)}$ and $E_{corr(\beta)}$ in **(a)** 0.6 M NaCl, **(b)** saturated NaCl, **(c)** 2 M $MgCl_2$, and **(d)** saturated $MgCl_2$. Lateral arrows indicate the effect of IR drop across the crack front, which affects the potential achieved at the crack tip by bulk environment polarization.*

likely due to plasticity influences (e.g. increased resistivity) on the dcPD signal, crack tip blunting, and/or ductile behavior rather than true IG-SCC (Figure 2.4(B)). This conclusion aligns with the similarity of these data to the resolution limit in Figure 2.2(A).

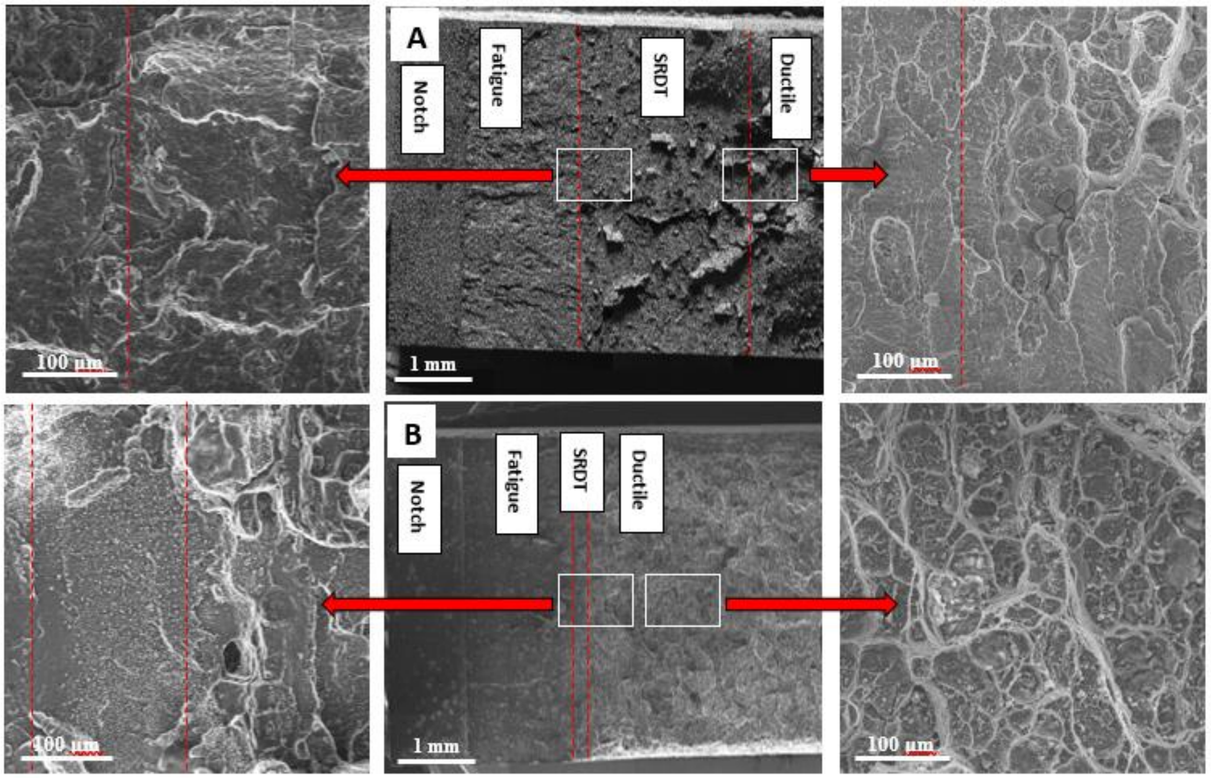

Figure 2.4: Fractography showing the mitigation of IG-SCC in AA5456-H116, NAMLT 65 mg/cm^2 in 0.6 M NaCl full immersion at potentiostatically held E of ***(a)*** *-0.8 V_{SCE} and* ***(b)*** *-1.1 V_{SCE}. Dashed red lines indicate the initiation (left) and completion (right) of slow rising displacement testing (SRDT) by dcPD results.*

In saturated NaCl (Figure 2.2(B)) at an E_{app} of -0.8 V_{SCE} the K_{TH} is 3-fold lower and the da/dt_{II} is 3-fold faster ($K_{TH} = 3$ MPa√m, $da/dt_{II} = 2.5 \times 10^{-3}$ mm/s) in comparison to 0.6 M NaCl at -0.8 V_{SCE}. The IG-SCC susceptibility in saturated NaCl is only slightly reduced going from -0.8 to -0.9 V_{SCE} ($K_{TH} = 4$ MPa√m, $da/dt_{II} = 2.0 \times 10^{-3}$ mm/s). However, decreasing from -0.9 V_{SCE} to -1.0 and -1.1 V_{SCE} results in an appreciable decrease in IG-SCC severity ($K_{TH} = 12$ MPa√m, $da/dt_{II} = 3.5 \times 10^{-4}$ mm/s, and $K_{TH} = 13$ MPa√m, $da/dt_{II} = 1.5 \times 10^{-4}$ mm/s, respectively). While a strong reduction in IG-SCC susceptibility (quantified via both K_{TH} and da/dt_{II}) is observed, the IG-SCC is not fully halted as was observed by polarizations to -1.0 and -1.1 V_{SCE} in 0.6 M NaCl.

The 2 M $MgCl_2$ environment (Figure 2.2(C)) shows severe IG-SCC at E_{app} of -0.8 V_{SCE} in terms of da/dt_{II} (K_{TH} = 2.5 MPa√m, da/dt_{II} = 5x10^{-3} mm/s). An intermediate severity level for this environment occurs at -0.9 V_{SCE} (K_{TH} = 6 MPa√m, da/dt_{II} = 2x10^{-3} mm/s). IG-SCC behavior is similar between the E_{app} values of -1.0 V_{SCE} (K_{TH} = 9 MPa√m, da/dt_{II} = 3x10^{-4} mm/s) and -1.1 V_{SCE} (K_{TH} = 9 MPa√m, da/dt_{II} = 2x10^{-4} mm/s). This grouping and the respective da/dt_{II} values are nearly coincident with the trends seen at -1.0 and -1.1 V_{SCE} in saturated NaCl (Figure 2.2(B) and Table 2.I (LEFM section)). These similar trends in IG-SCC behavior are evident when comparing Figure 2.3(B) and 2.3(C), with the major difference being the decreased IG-SCC susceptibility at -0.9 V_{SCE} in 2 M $MgCl_2$; this is consistent with the more negative values of $E_{pit\,(\alpha)}$ (and $E_{pit\,(\beta)}$) for saturated NaCl (Table 2.I).

Applied polarization has the least potent effect in full saturated $MgCl_2$ immersion (Figure 2.2(D)). At -0.8 V_{SCE}, IG-SCC initiation occurs at a very low threshold stress intensity (K_{TH} = 2 MPa√m), with increase in the initiation stress intensity at -0.9 V_{SCE} (K_{TH} = 4 MPa√m), -1.0 V_{SCE} (K_{TH} = 6.5 MPa√m), and -1.1 V_{SCE} (K_{TH} = 9 MPa√m). The da/dt_{II} plateaus at -0.8, -0.9, and -1.0 V_{SCE} (da/dt_{II} = 1x10^{-3} mm/s to 9x10^{-4} mm/s at -1.0 V_{SCE}), and then decreases at -1.1 V_{SCE} (da/dt_{II} = 1.5x10^{-4} mm/s). In comparison to the 2 M $MgCl_2$ (Figure 2.2(C)), the IG-SCC trends show most similarity for -0.9 V_{SCE} (da/dt_{II} = 2x10^{-3} versus 1x10^{-3} mm/s) and -1.1 V_{SCE} (da/dt_{II} = 2x10^{-4} versus 1.5x10^{-4} mm/s). The da/dt_{II} plateau between -0.8 V_{SCE} and -1.0 V_{SCE} is illustrated in Figure 2.3(D), with saturated $MgCl_2$ being the only environment in which this stagnation occurs.

2.1.5 **Discussion**

The IG-SCC results demonstrate two critical findings. First, that mitigation of the IG-SCC behavior is possible for high NAMLT levels (65 mg/cm^2) and aggressive environments pertinent to wet-dry cycles in simulated atmospheric conditions (represented by full immersion environments with chemistries that mimic seawater droplets). Second, quantitative metrics of IG-SCC susceptibility (K_{TH} and da/dt_{II}) demonstrate that the potency of the protection varies with bulk electrolyte composition. These findings can be analyzed in the context of the proposed coupled anodic dissolution and HEDE mechanism; specifically, evaluating how the $E_{pit\,(\alpha)}$ and $E_{pit\,(\beta)}$ values relate to the observed IG-SCC susceptibility. Potentiodynamic scans established three zones of electrochemical activity for each of the bulk environments examined: the highly active (both β and α matrix breakdown) (Zone 1), the transition towards passivity (only β dissolution) (Zone 2), followed by near complete passivity (no β or α breakdown) (Zone 3) (Figure 2.1, Table 2.I). The correlations presented in Figure 2.3 demonstrate that the dependence of K_{TH} and da/dt_{II} on the bulk loading environment correlate with the trends in $E_{pit\,(\alpha)}$ and $E_{pit\,(\beta)}$ as the environment is changed. In general, recall that this is based on the premise that a crack tip potential above $E_{pit\,(\beta)}$ will not only enable β phase dissolution but will critically enable crack tip acidification, hydrogen production and embrittlement. This dual dissolution/hydrogen embrittlement process is exacerbated when local α phase breakdown occurs as well to saturate the occluded crack tip chemistry and drop the crack tip pH even further. However, it is critical to recognize that the $E_{pit\,(\alpha)}$ and $E_{pit\,(\beta)}$ values are established via potentiodynamic scans of the bulk surface in the given environment, whereas the dissolution process pertinent to IG-SCC is at the crack tip where both the chemistry and the potential will be distinct from that in the bulk environments. The relative influence of the distinct crack tip chemistry and potential on observed K_{TH} and da/dt_{II} trends are discussed.

Considering the K_{TH} trends, it is necessary to revisit the testing protocol; specifically, after air pre-cracking the specimens were loaded into solution, polarized, and held at a low load for 5 or 10 hours. During this time, there is ingress of the bulk solution into the crack and a steady state chemistry develops (in many instances measurable IGC is observed). The chemistry developed during this hold time will be directly dependent on: (1) the bulk solution chemistry, (2) the crack tip potential (which is a function of the applied potential and the IR drop), (3) the ionic transport (Cl^- ingress and H^+ egress) between the bulk and the tip, (4) the volume fraction of the reactive β and surface to volume ratio of α/β to volume of electrolyte ratio in the crack tip, and (5) separation of anode and cathode. Since the chemistry that is initially developed within the crack will depend on the bulk solution, it is fully reasonable to expect this initial chemistry to be related to the bulk chemistry and the bulk $E_{pit\,(\alpha)}$ and $E_{pit\,(\beta)}$ values reported in Table 2.I. Evolution of the crack tip chemistry involves the dissolution of the β (and possibly the α) which creates elevated concentrations of Al^{3+} and Mg^{2+} in the occluded crack tip. Subsequent hydrolysis decreases the pH of the crack tip solution and Cl^- ingress from the bulk will occur to maintain charge neutrality. In the end, the overpotential for H production has been hypothesized to be a relevant proxy for the concentration of diffusible H available for embrittlement of the crack tip process zone. Critically, this parameter is the difference between the crack tip potential (which is the bulk applied potential minus the IR drop) and the reversible potential for the hydrogen evolution reaction which is a function of the pH (and to a lesser extent [Cl-]). Quantitative modeling of E_{tip} in bulk 0.6 M NaCl showed modest levels of IR drop at E_{app} of -0.730 V_{SCE} (E_{tip} = -0.817 V_{SCE}) to -1.020 V_{SCE} (E_{tip} = -1.050 V_{SCE}) in similar crack geometries and orientation considered here [6]. *In toto*, in the context of the aforementioned HEDE-based IG-SCC model, the changes in the bulk solution will have two primary influences. First, while complications associated with varying IR drop and subtleties of crack chemistry are recognized, it is reasonable to postulate that the changes in $E_{pit\,(\alpha)}$ and $E_{pit\,(\beta)}$ between different bulk environments will lead to different initial dissolution rates, that will then create the local chemistry, which will influence overpotential for H-production and thus should correlate with the observed changes in the K_{TH} behavior. Second, the steady state crack chemistry will be a balance between the generation of the occluded crack chemistry and the driving force for dilution of the chemistry due to the steep concentration gradient between the bulk and the tip. As the pH and [Cl-] of the bulk increases the concentration gradient between the bulk and tip is decreased, thus it is easier to maintain the occluded chemistry.

The correlation between bulk electrochemical behavior and K_{TH} trends is realized for potentials anodic to both $E_{pit\,(\alpha)}$ and $E_{pit\,(\beta)}$ (Zone 1), where complete dissolution of grain boundary β phase and fast α Al matrix dissolution elevate Al^{3+} and Mg^{2+} to set the initial crack chemistry at near the steady state aggressive pH (which was reported to be as low as 0.1 for AA5083 (NAMLT 22 mg/cm^2) cracking in the da/dt_{II} regime in 0.6 M NaCl solution polarized at -0.8 V_{SCE}) [6, 7]. For testing in Zone 1 at 2 M $MgCl_2$, saturated NaCl, and saturated $MgCl_2$, the K_{TH} values are very low (< 3 MPa√m) and near the resolution of the testing method (Figure 2.2). Duplicate tests in saturated NaCl (Figure 2.2(B)) and 2 M $MgCl_2$ at -0.8 V_{SCE} (Figure 2.2(C)) demonstrate the relative reproducibility of the K_{TH} and da/dt_{II} values shown in Table 2.I for this tensile testing method. Testing was not completed above $E_{pit\,(\alpha)}$ (-0.7 V_{SCE}) for the 0.6 M NaCl environment, however the higher observed thresholds at -0.8 V_{SCE} for this bulk environment are consistent with E_{app} being cathodic to $E_{pit\,(\alpha)}$, thus a less aggressive crack tip chemistry is able to form. There are four important findings for Zone 2 testing at applied potentials anodic to $E_{pit\,(\beta)}$ but cathodic to E_{pit}

$_{(\alpha)}$ (Of note, previous reports suggest that the α-breakdown potential in simulated crack tip solution (2.5 M Al^{3+}, 0.11 M Mg^{2+}, 7.7 M Cl^{-}) is roughly -0.9 V_{SCE}, and therefore the true $E_{pit\ (\alpha)}$ in the crack tip is likely bounded by -0.9 V_{SCE} and the values listed in Table 2.1 and Figure 2.3 [13]). First, for all bulk environments testing in Zone 2 results in less IG-SCC susceptibility than Zone 1, which is reasonable due to the reduced cation concentration available for hydrolysis when significant amounts of the α matrix are not dissolving. Second, within Zone 2 the K_{TH} values increase with increasingly cathodic polarization, consistent with the expected trends in β dissolution rates that are observed in Figure 2.1 for 0.6 M NaCl (and similar for other environments). Third, when comparing the K_{TH} values in Zone 2 the saturated $MgCl_2$ that exhibits the highest IG-SCC susceptibility has the lowest values of $E_{pit\ (\alpha)}$ and $E_{pit\ (\beta)}$, the 0.6 M NaCl is the most resistant and has the highest values of $E_{pit\ (\alpha)}$ and $E_{pit\ (\beta)}$, and the saturated NaCl and 2 M $MgCl_2$ show near identical susceptibility and have near identical values of $E_{pit\ (\alpha)}$ and $E_{pit\ (\beta)}$. Fourth, while the most severe $MgCl_2$ environment had the lowest pH and highest [Cl-] concentration in the bulk chemistry, the 2 M $MgCl_2$ (pH=3.4, [Cl-]=4 M) and saturated NaCl (pH=6.2, [Cl-]=5.45 M) environments showed similar IG-SCC behavior despite large changes in the bulk pH and [Cl-] values. This suggests that in Zone 2 the primary contribution of these parameters is indirect. While they set the $E_{pit\ (\alpha)}$ and $E_{pit\ (\beta)}$ values that control the development of the crack tip chemistry, these values work along with the applied potential and IR drop that in turn govern the overpotential for H production.

Cathodic polarization below both $E_{pit\ (\alpha)}$ and $E_{pit\ (\beta)}$ encompasses Zone 3 of IG-SCC susceptibility, and in all cases the susceptibility decreased as compared to Zones 1 and 2. This is most evident in 0.6 M NaCl, where IG-SCC trends follow the resolution limit at E_{app} of -1.0 and -1.1 V_{SCE} (Figure 2.2(A)), and no resolvable IG-SCC crack growth occurs (Figure 2.4(B), left).

While substantial retardation of the IG-SCC behavior was observed in Zone 3 for saturated NaCl, 2 M $MgCl_2$, and saturated $MgCl_2$ (Figure 2.2, Table 2.I) environments, complete inhibition of IG-SCC could not be achieved even at -1.0 V_{SCE} and/or -1.1 V_{SCE}. Several possible factors could be controlling this behavior. The most compelling argument stems from recent work that proposes that despite the applied level of polarization, the crack tip potential cannot be lower than the OCP of the α matrix in the crack tip solution [6, 14]. This work established on OCP value of -1.050 V_{SCE} for an aggressive saturated acidic crack tip solution. For the 0.6 M NaCl condition the $E_{pit\,(\beta)}$ is well above this level (-0.95 V_{SCE}) thus full inhibition is expected, however for the more aggressive solutions the $E_{pit\,(\beta)}$ values range from -1.00 to -1.05 V_{SCE} (Table 2.I). If only partial retardation of the β dissolution is achieved due to proximity to this threshold, then this would explain the incomplete inhibition of IG-SCC. Definitive conclusions based on this argument are precluded by uncertainties in the crack chemistry, thus the true crack tip OCP. Furthermore, the higher [Cl-] and lower pH values for the more aggressive solutions (as compared to the 0.6 M NaCl) may directly play a role. First, higher levels of [Cl-] (and to a lesser extent lower pH values) would reasonably lead to a higher propensity for localized metastable pitting events that occur in the passive regimes. Such localized events may sufficiently influence the crack chemistry to enable some level of IG-SCC, albeit at vastly reduced rates as compared to Zone 1 and 2. Second, even if the crack tip is polarized to below the $E_{pit\,(\alpha)}$ and $E_{pit\,(\beta)}$ such that there is no enhancement in the aggressiveness of the occluded crack tip chemistry, the low pH and high [Cl-] values from the bulk solution are likely sufficient to produce a crack tip H-overpotential that enables a threshold level of H-production for embrittlement. Such a hypothesis is consistent with prior research that showed that IG-SCC in unsensitized AA5083 could be promoted by testing in simulated occluded-crack solution [6].

While da/dt_{II} behavior essentially mirrors the trends observed between K_{TH} and the $E_{pit\,(\alpha)}$ and $E_{pit\,(\beta)}$, the correlation of bulk polarization behavior to Stage II crack growth behavior is complicated beyond that discussed for K_{TH}. Several factors for a growing crack will impact the critical crack tip chemistry and degree of IR drop that was assumed to result in a steady state chemistry prior to reaching K_{TH}. Specifically, crack progression will by definition create new (initially) unpassivated α surfaces and higher volume fractions of β to be released into the occluded volume, the crack geometry will scale with crack length and loading which will influence the pertinent ingress/egress behavior and IR drop, and complex gradients in solution chemistry can develop dependent on the rate of crack advance versus the pertinent reaction and diffusion rates. Despite the complications in observed behavior, Figure 2.3 suggests that the bulk $E_{pit\,(\alpha)}$ and $E_{pit\,(\beta)}$ and the arguments put forth above for the K_{TH} trends can be cautiously applied to describe the influence of bulk environment on the da/dt_{II} behavior. One outlying data trend is observed at -0.8 V_{SCE} in saturated $MgCl_2$; all other data suggest that this is the most aggressive solution. However, the da/dt_{II} value ($1x10^{-3}$ mm/s) is (1) the same as is observed at -0.9 V_{SCE} and (2) is well below that observed in saturated NaCl ($4x10^{-3}$ mm/s) and 2 M $MgCl_2$ ($5x10^{-3}$ mm/s). Both chemical and mechanics-based hypotheses could feasibly explain this observation. The aggressive environment could lead to chemical blunting of the crack tip, this would lower the crack tip stress field and potentially retard the crack growth [15]. This explanation is not fully satisfying considering that such behavior is not observed in other conditions where an equally aggressive crack tip solution would likely exist and that Stage II growth kinetics are not likely to be strongly dependent on the magnitude of K reduction expected. A chemical explanation is more satisfying, specifically there is likely a high level of resistivity of the crack tip solution due to high concentration of the bulk/crack tip environment, which limits concentration gradient driving force for egress. It is known that after a maxima the solution conductivity will begin to decrease as the chemistry approaches saturation [14, 16], therefore the IR drop will increase with increasing concentration. For saturated $MgCl_2$ solution an IR drop of up to ~100 mV_{SCE} would result in a crack tip potential in Zone 2 (intermediate susceptibility; below $E_{pit\ (\alpha)}$) rather than Zone 1 (highest susceptibility).

2.1.6 Conclusion

Mitigation of IG-SCC in AA5456-H116, NAMLT 65 mg/cm^2 with increasingly cathodic bulk solution applied potential is demonstrated in 0.6 M NaCl, saturated (5.45 M) NaCl, 2 M $MgCl_2$, and saturated (5 M) $MgCl_2$. Pitting potentials of the pure β phase and the α Al matrix (unsensitized AA5456-H116) in these bulk solution chemistries were shown to correlate with three zones of IG-SCC susceptibility. These three polarization ranges describe the rates of α Al matrix and β phase dissolution that set the crack tip chemistry that governs the coupled anodic dissolution-HEDE mechanism driving IG-SCC. In Zone 1 dissolution of both the α matrix and β causes rapid acidification and saturation of crack tip conditions that cause the most severe IG-SCC. Whereas IG-SCC inhibition is achieved by retarding the dissolution of either the α matrix (Zone 2) or both the α matrix and β (Zone 3). Correlation of the bulk polarization parameters ($E_{pit\ (\alpha)}$ and $E_{pit\ (\beta)}$) with the IG-SCC behavior demonstrates that the bulk environment can play an important influence of the development of the governing crack tip chemistry. These findings demonstrate the feasibility of the IG-SCC inhibition of a highly-sensitized alloy in concentrated electrolytes typical of atmospheric operating conditions. This work justifies further development of coating systems that aim to protect marine structures via cathodic protection systems using metal-based pigments that act as sacrificial anodes.

2.1.7 References

1. N.J.H. Holroyd and G.M. Scamans: *Corrosion,* 72, 136 (2015).
2. N.J.H. Holroyd and G.M. Scamans: *Scr. Metall. Mat.,* 19, 945 (1985).
3. ASTM: Standard Test Method for Determining the Susceptibility to Intergranular Corrosion of 5XXX Series Aluminum Alloys by Mass Loss After Exposure to Nitric Acid (NAMLT Test). In ASTM Standard G67. West Conshohocken, PA: ASTM International; 2004: 1.
4. M.L. Lim, R.G. Kelly, and J.R. Scully: *Corrosion,* 72, 198 (2016).
5. C.B. Crane and R.P. Gangloff: *Corrosion,* 72, 221 (2016).
6. C.B. Crane, R.G. Kelly, and R.P. Gangloff: *Corrosion,* 72, 242 (2016).
7. R.H. Jones, D.R. Baer, M.J. Danielson, and J.S. Vetrano: *Metall. Trans. A,* 32, 1699 (2001).
8. M.E. McMahon, P.J. Steiner, A.B. Lass, and J.T. Burns, *Corrosion* (2016) doi:http://dx.doi.org/10.5006/2317.
9. M. Seifi, Fatigue Crack Growth Properties of Al-Mg Alloys After Long-Time Low Temperature Exposures. *Ph.D. Dissertation.* Cleveland, OH: Case Western Reserve University; 2013.
10. L.P. Maduro, C.A.R.P. Baptista, M.A.S. Torres, and R.C. Souza: *Proc. Eng.,* 10, 1214 (2011).
11. R.P. Gangloff, D.C. Slavik, R.S. Piascik, and R.H. Van Stone, in: *Small-Crack Test Methods.* Vol.1, ed. J.M. Larsen and J.E. Allison, (Philadelphia, PA: ASTM, 1992) pp.116-168.
12. R.P. Gangloff, H.M. Ha, J.T. Burns, and J.R. Scully: *Metall. Trans. A,* 45, 3814 (2014).

13. M.L. Lim: Intergranular Corrosion Propagation in Sensitized Al-Mg Alloys. *Ph.D. Dissertation.* Charlottesville, VA: University of Virginia; 2016.

14. E. Bumiller: Intergranular Corrosion in AA5xxx Aluminum Alloys with Discontinuous Precipitation at the Grain Boundaries. *Master's Thesis.* Charlottesville, VA: University of Virginia; 2011.

15. M. Creager, P.C. Paris: *Int. J. Frac. Mech.,* 3, 247 (1967).

16. C.G. Zoski, *Handbook of Electrochemistry*, 1st ed. (New York, NY: Elsevier, 2007) pp. 58-60.

2.2 The Effect of Electrode Potential on Stress Corrosion Cracking in Highly Sensitized Al-Mg Alloys

M. E. McMahon [ǂ, *], J. R. Scully[*], and J. T. Burns[*]

[*] Center for Electrochemical Science and Engineering, Department of Materials Science and Engineering, University of Virginia, Charlottesville, VA 22904
[ǂ] Corresponding author. E-mail: mm5kn@virginia.edu

2.2.1 Abstract

The window of potential dependence wherein environmental cracking phenomena occur and are suppressed in highly sensitized AA5456-H116 is defined in Cl^- solution. Stress corrosion cracking (SCC) occurrence is compared with the propensity for attack, degradation, and gaseous H evolution/H absorption phenomena as a function of potential in the anodic and cathodic polarization regions. The SCC susceptibility is low in Al-Mg under cathodic polarization conditions and high in anodic polarization conditions. The lack of environmental cracking susceptibility at cathodic potentials directly scales with the per area levels of H generation that are expected to occur at the crack tip at each polarization level. Chemical blunting is then a secondary extrinsic strengthening mechanism at the crack tip to suppress cathodic crack growth from the standpoint of attenuation of the mechanical driving force. Chemical blunting is demonstrated to have no effect on the threshold stress intensity for SCC during anodic crack growth where the crack tip readily re-sharpens through the IGC/β phase dissolution process followed by H-induced crack advance.

2.2.2 Introduction

Aluminum Association 5xxx-series alloys are light-weight, moderate strength, and resistant to general corrosion making them well-suited for and increasingly used to replace steel components in marine superstructures [1,2]. The strength is achieved through supersaturation of the Al matrix with 5 wt.% Mg. However, at service temperatures of $\geq$ 313 K the Mg diffuses to grain boundaries to form intergranular β phase (Al_3Mg_2), which is anodic to the α-Al matrix [3–8]. In saline environments the preferential dissolution of the β phase leads to intergranular corrosion (IGC), and in the presence of an applied load, intergranular stress corrosion cracking (IG-SCC) [9–14]. The Nitric Acid Mass Loss Test (NAMLT) test codified in ASTM G67 [15] provides an estimate of grain boundary β phase density and thereby gauges susceptibility to IGC and IG-SCC. Specifically, it defines Al-Mg alloys as resistant at NAMLT < 15 mg/cm^2, intermediate at NAMLT 15 - 25 mg/cm^2, and susceptible at NAMLT > 25 mg/cm^2 [12,16]. These alloys may become sensitized as severely as NAMLT 65-70 mg/cm^2 [17].

Intergranular stress corrosion cracking is hypothesized to be driven by a coupling of the anodic β phase dissolution with hydrogen embrittlement effects leading to grain boundary decohesion [10,11,17–19]. Specifically, the aggressive environment developed from the local dissolution of β, and potentially α, enables high levels of H^+ generation and subsequent H production at the crack tip. The threshold for this hydrogen production in the anodic polarization region is thus the β breakdown potential ($E_{pit\ (\beta)}$, -0.92 V_{SCE} in 0.6 M NaCl [20]), and with increasingly positive applied potential the severity of the β/α dissolution increases to further promote H^+ generation [17]. The evolved hydrogen may adsorb at the crack tip, followed by absorption and diffusion ahead of the crack tip along grain boundaries. The hydrogen embrittlement at the grain boundaries is believed to assist the propagation of IG-SCC in the interβ and β/α ligaments by enabling grain boundary decohesion. This mechanism is supported by (1) observed environmentally-assisted crack growth rates that vastly exceed penetration rates of IGC [13,18,21] and (2) successful application of HEDE models to predict fracture behavior in the Al-Mg system [10,18,19].

Dissolution of the intergranular β phase is critical to the anodic IG-SCC mechanism in Al-Mg alloys [5,6,9,12,22–28]. This event provides three major inputs that enable the environmental fracture process. Specifically, intergranular β dissolution (1) drives acidification of the crack tip through hydrolysis reactions related to the combined release of Al^{3+} and Mg^{2+} [9,10]; (2) promotes Cl^- ingress for charge neutralization, which destabilizes the aluminum oxide layer in the immediate vicinity of the crack tip to enable α matrix oxidation, further driving crack tip acidification [29–31]; and (3) promotes a sharp crack tip due to the fissure-like intergranular corrosion and subsequent grain boundary decohesion. Previous work demonstrated that IG-SCC may be effectively mitigated in Al-Mg alloys by applying a mildly cathodic polarization via potentiostat-based control [10,17]. The degree of IG-SCC mitigation depends on the suppression of (1) pitting in the α matrix ($E_{pit\,(\alpha)}$) and (2) dissolution of the β phase ($E_{pit\,(\beta)}$), which in turn controls the extent of the crack tip acidification. Similar mitigation of anodic environmental cracking phenomena has been demonstrated in alloy systems susceptible to hydrogen environment-assisted cracking, such as steels [32–41], Ti alloys [42,43], Ni-base superalloys [44–46], and Al alloys [47] such as the AA7xxx-series [48–51]. Generally, for each of these systems the cathodic polarization precludes the development of an acidic crack tip environment, which suppresses the environmental cracking behavior.

However, in some systems there is a threshold level of cathodic polarization beyond which further polarization will induce aggressive H-induced cracking; specifically, this has been observed in Ni-, Fe-, and Al-based alloys [32,39,41,49,50,52]. This behavior is in large part due to the bulk cathodic generation of H and subsequent bulk uptake. Specifically, the hydrogen evolution reaction may evolve sufficient amounts of absorbed hydrogen upon net cathodic polarization of the entire alloy to enable H-induced cracking at potentials below this threshold [53,54]. Other effects may also be active, such as the formation of brittle hydrides with sufficient overpotential as well as corrosion effects, which may promote stress concentration and/or additional hydrogen evolution [40,55–57]. In these alloys, the oxide may readily support hydrogen evolution and charging when polarized below the reversible hydrogen potential (i.e. Ni- and Fe-based alloys), or the instability of the oxide in alkaline conditions enables dissolution, further hydrogen production, as well as potential charging (Al-based alloys). The amphoteric nature of Al and Al_2O_3 promotes the latter in the AA5xxx-series. Specifically, on AA5456-H116 the current density quickly begins to increase between -1.30 V_{SCE} and -1.35 V_{SCE} in 0.6 M NaCl, and alkaline corrosion may ensue as the hydroxyl concentration increases in the electrolyte to surpass the pH of 8.6 [58–61].

While IG-SCC was observed to be mitigated at -1.30 V_{SCE} on AA5083-H131, a systematic evaluation of the environmental cracking behavior of Al-Mg alloys at polarization levels below this level is lacking. Such a study is relevant to engineering application as there are ongoing efforts to use metal-rich primers (containing Zn, Mg, or Al) to inhibit IG-SCC of Al-Mg marine components via cathodic polarization [62–66]. Such primers can induce potentials as negative as -1.65 V_{SCE} (particularly where Mg is present [67–75]). As such, quantitative characterization of the environmental cracking behavior of Al-Mg alloys at high levels of cathodic polarization will fill a technical knowledge gap and inform the development of coatings-based mitigation strategies.

The overarching goal of the current effort is to understand the environmental cracking behavior of AA5456-H116 at various levels of cathodic polarization. Specifically, this work will address three major goals. First, to characterize the corrosion and environmental cracking behavior at various levels of cathodic polarization. Second, to quantitatively characterize the H-generation/uptake behavior as a function of polarization and develop an understanding of the mechanistic source of H in each case. Third, to interpret the bulk corrosion and H-generation data in the context of the crack tip conditions to inform the mechanism of environmental cracking for each polarization level. Finally, to use the understanding gained from the characterization and analysis above to ensure that testing methods for evaluating the environmental cracking behavior at cathodic polarization levels are rigorous. These goals will be achieved first through determination of the environmental fracture susceptibility under cathodic polarization in the range of -1.3 V_{SCE} to -1.7 V_{SCE}. This is followed by baseline evaluation of the corrosion damage and hydrogen evolution rate across the range of electrode potential possibly experienced on AA5456-H116 in service (-0.6 V_{SCE} to -1.7 V_{SCE}). The anodic and cathodic corrosion/fracture mechanisms will be further understood by evaluating pure β phase dissolution at all potentials. The combination of these results is utilized to begin to mechanistically understand why cathodic SCC may or may not occur under specific conditions and to inform specific testing considerations.

2.2.3 **Experimental Methods**

2.2.3.1 ***AA5456-H116 Material and Objectives for the Proceeding Sections***

The 5.7 cm thick AA5456-H116 plate utilized in this study was unrecrystallized, with composition and mechanical properties detailed in prior work [18]. Excised plates (S-T surface) and fracture specimens (S-L) were all heat treated at 100°C for 14 days to reach the NAMLT value of 65 mg/cm^2 prior to electrochemical and fracture testing [18]. As-received, excised AA5456-H116 plates (NAMLT 4 mg/cm^2) were utilized only in electrochemical potentiodynamic testing.

The procedures in the proceeding sections are related in the following ways. Fracture mechanics evaluations were first conducted from -1.3 V_{SCE} to -1.7 V_{SCE} and compared to the same at -0.8 V_{SCE} to -1.1 V_{SCE}, followed by modified replicate testing to elucidate the cathodic crack growth mechanism. These evaluations were complemented by electrochemical assessment of the corrosion in pure β phase and AA5456-H116 in the potential range of -1.7 V_{SCE} to -0.6 V_{SCE}, the corrosion type/morphology which occurs in the same potential range on AA5456-H116, and H uptake experiments. Critically, the electrochemical and H-metal interaction data aid in the interpretation of the LEFM data by demonstrating the affinity for hydrogen evolution/absorption in the anodic versus cathodic polarization regions, and by evidencing the resultant corrosion morphology that may affect the crack tip under acidic/alkaline conditions.

2.2.3.2 *IG-SCC Susceptibility as a Function of Potential in 0.6 M NaCl*

Fracture testing was performed on single edge notched tensile (SENT) specimens having gauge width of 17.25 mm, thickness of 6.62 mm, and electrical discharge machined notch of depth 4.85 mm placed at the plate mid-thickness (t/2) in the susceptible S-L orientation. Open air fatigue precracking was performed to 5.30 mm total crack depth, with the final stress intensity (K) being 3.5 MPa√m. Testing was conducted in full immersion in a 200 mL acrylic cell, where 2.0 L of non-deaerated 0.6 M NaCl solution was circulated at 20 mL/min at ambient temperature. The electrochemical conditions in these 0.6 M NaCl tests were controlled via a floating ground potentiostat at -1.3 V_{SCE}, -1.5 V_{SCE}, or -1.7 V_{SCE}. Select tests were also conducted in 0.6 M NaCl with NaOH added (pH 12.0) as well as in 0.5 wt.% ammonium thiocyanate (a hydrogen poison) +

0.6 M NaCl solution at -1.5 V_{SCE}. Prior to the onset of active loading a hold of 1.5 hours was conducted at a K of 2.0 MPa√m under protective potential of -1.1 V_{SCE}. Following this hold, the potential of interest was established and slow rising displacement was initiated at initial dK/dt of 0.25 MPa√m/hr corresponding to grip displacement rates of ≈ 0.00009 mm/min. This initial dK/dt rate was established over a 6-hour period (K increase from 2.0 to 3.5 MPa√m) during which the sample stabilized at the applied potential of interest. The stress corrosion cracking test then progressed from 3.5 MPa√m until final fracture or exceedance of the proportional limit of the material/SENT geometry. Lastly, a unique test setup was utilized in 0.6 M NaCl (natural pH of ≈ 5.75) which enabled fast crack growth at -0.8 V_{SCE} until K = 7.8 MPa√m, after which the applied potential was altered to -1.5 V_{SCE} for the remainder of the test. Select tests were conducted at constant K = 1 MPa√m and -1.5 V_{SCE} on fatigue pre-cracked SENT specimens for 1.5, 12.0, and 24.0 hours in 0.6 M NaCl, after which the specimens were stored in liquid nitrogen to halt corrosion effects. The mid-sections of these specimens were mounted in epoxy and polished through to the mid-thickness, with periodic imaging via optical microscopy (5,000x magnification) or SEM (20,000x magnification) to obtain average crack tip curvature values.

Crack growth was monitored via the direct current potential difference (dcPD) method with ≈ 0.5 μm resolution, the details of which are provided elsewhere [76]. Data analysis utilized Ramberg Osgood constants derived from compression stress-strain curves to develop J-integral plastic corrections (K_J), the process of which is described in detail elsewhere [18]. A resolution limit (governed by crack tip plasticity) for the dcPD method was previously determined through stress corrosion cracking testing on AA5083-H131 in dry nitrogen environment [10]. This limit is indicated as a solid black line in the da/dt versus K_J plots. Electron Backscatter Diffraction (EBSD) was utilized for grain mapping on fracture specimen cross sections at 20 kV, spot size 5 nm, 1 micrometer step size, and 400x magnification.

2.2.3.3 *Gaseous Hydrogen Collection as a Function of Potential in 0.6 M NaCl*

Electrochemistry was performed in controlled laboratory environment using 300 mL electrochemical flat cells, platinized mesh counter electrodes, and saturated calomel reference electrodes (SCE) to inform fracture testing procedures. For gaseous hydrogen collection testing, three different sample types were evaluated: NAMLT 65 mg/cm^2 and NAMLT 4 mg/cm^2 (unsensitized) AA5456-H116 plate of 5-7 mm thickness, as well as pure β phase. These were polished to 1200 grit finish in flowing water (5456) or in methanol (β phase) and an exposed area of 0.78 cm^2 (5456) or ≈ 0.05 cm^2 (β phase) served as the working electrode. Prior to this testing, previously developed hydrogen charging procedures were followed to charge the 0.6 M NaCl to hydrogen saturation (1.4 x10^{-5} (mole fraction) in water at 298 K [77]) using a platinum counter electrode and a platinum working electrode (smaller area for increased current density) at applied potential of -1.5 V_{SCE} for 1.5 hours [78]. For select tests and potentials, this charging method was also applied to 0.6 M NaCl with added NaOH (pH 12.0) and, at -1.5 V_{SCE} only, to 0.6 M NaCl with additions of 0.1 wt.% to 15.0 wt.% NH_4SCN.

All AA5456-H116 specimens were weighed prior to the initiation of corrosion testing, which took place in vertical flat cells with a 50 mL volumetric burette attachment to measure evolved gaseous hydrogen (H_2) content after being filled with the H-saturated 0.6 M NaCl solution. A 30-minute open circuit potential (OCP) step was utilized to stabilize the AA5456-H116 surface potential prior to testing. All hydrogen collection tests utilized potentiostatic control for 6 hours, however, at potentials near the AA5456-H116 OCP (-0.85 V_{SCE}), galvanostatic control was selectively utilized to validate the results obtained via potentiostatic control. Extended 48-hour hydrogen collection experiments were also conducted at potentials near the alloy OCP to alleviate concerns for the lack of potential corrosion initiation in these conditions over 6 hours, which showed no difference from the 6-hour exposure results. H_2 collection testing in 0.6 M NaCl was completed in triplicate, and averages were reported for each potential. Testing at potentials more positive than -0.79 V_{SCE} experienced accumulation of both corrosion product and H_2 in the vertical burette, thus the reported evolved H_2 volume averages were adjusted to account for the presence of the corrosion product volume.

2.2.3.4 ***Absorbed Hydrogen Evaluation as a Function of Potential in 0.6 M NaCl***

To quantify the differences in the amount of *absorbed* H between the anodic and cathodic polarization regions, the following experimental methods were utilized. Three fresh NAMLT 65 mg/cm^2 AA5456-H116 samples were procured per potential evaluated in the H_2 collection testing, as well as 3 baseline replicate samples (which remained uncorroded), all having dimensions 5.0 ± 1.0 mm x 5.0 ± 1.0 mm x 10.0 ± 0.5 mm. Prior to being corroded, each sample was engraved with a unique identifier and then sonicated in acetone, methanol, then deionized water (high purity, 18.2 mΩ resistivity) followed by compressed air drying. These samples were then polished under flowing water to 1200 grit via silicon carbide paper. In electrochemical flat cells, a 0.13 cm^2 area of each sample (minus the uncorroded replicates) was subjected to the same corrosion testing procedures as utilized in the H_2 collection testing: 30 minutes OCP followed by 6 hours under potentiostatic hold in 0.6 M NaCl (natural, non-H charged), where the AA5456-H116 served as the working electrode, platinum mesh as the counter electrode, and an SCE as reference. Each corroded sample was dried with compressed air and immediately stored in liquid nitrogen to inhibit hydrogen egress. These samples were then shipped on dry ice and evaluated via the inner gas fusion method per ASTM E1447-06 [79] by Luvak Laboratories, Inc. in Boylston, MA. Average absorbed H values, which are calculated from the three replicates produced, are reported at each potential, with the baseline absorbed H value (obtained through averaging the three non-corroded AA5456-H116 specimens) subtracted.

2.2.3.5 ***Characterization of Corrosion and Mass Loss as a Function of Potential in 0.6 M NaCl***

The specimens produced from the H_2 collection testing were cleaned of corrosion product in pure nitric acid for 5 minutes in accord with ASTM G-1 [80], followed by a deionized water wash, compressed air drying, and 12 hours of drying under vacuum prior to weighing for mass loss. Following this measurement, specimens were cross sectioned, mounted in epoxy, and polished to 1 micrometer in diamond suspension for corrosion type, depth, geometry, and penetration rate analyses. Non-mounted specimens were utilized for imaging purposes, such as to evaluate the composition and location of cathodic intermetallic particles relative to corrosion damage and to map the percent of the total surface area affected by corrosion.

White light interferometry (WLI) was utilized to determine the percent area of corroded Al surface with respect to the total at each potential considered in the range of -1.7 V_{SCE} to -0.6 V_{SCE} following the 6-hour H_2 collection tests. In order to gather an analytical baseline, uncorroded AA5456-H116 (polished to 1200 grit) was first evaluated to determine the polished surface roughness (maximum height deviation from the mean plane) of ±2 μm, as well as the data collection error of ±0.4% pixel coverage (equal to 0.00168 mm^2 of the total 0.42 mm^2 area analyzed in each scan). Damage depths greater than 2 μm were then identified as corrosion damage, and the WLI maps were binarized based on this criterion. Three 525 μm x 700 μm areas were mapped to establish the average corroding area (out of the total 0.78 cm^2 flat sample surface area) at each potential.

Intermetallic particle location and alkaline corrosion morphology analysis was conducted on the non-epoxy-mounted H_2 collection test specimens utilizing scanning electron microscopy (SEM) at accelerating voltage of 20 kV and spot size 5 nm at magnification of 400x, followed by the use of energy dispersive spectroscopy (EDS) to measure matrix/intermetallic compositions through mapping and/or line scans with the same settings but at magnification of 12,000x. All micrographs were obtained under high vacuum, 10^{-6} torr. Epoxy-mounted, corroded cross-section specimens were imaged using an inverted optical microscope at 20x magnification.

2.2.4 **Results**

2.2.4.1 ***IG-SCC Susceptibility under Anodic and Cathodic Polarization in 0.6 M NaCl***

Slow rising displacement LEFM testing was performed at the applied potentials of -1.3 V_{SCE}, -1.5 V_{SCE}, and -1.7 V_{SCE} in 0.6 M NaCl to evaluate the SCC susceptibility of AA5456-H116, NAMLT 65 mg/cm^2 under cathodic polarization. The results of these tests (Figure 2-5) demonstrate that no IG-SCC occurs in any of the three cathodic polarization conditions. Specifically, growth rates at these potentials remained relatively constant from K_J of 3.5 to 20.0 MPa√m, and lie below the crack tip plasticity-induced resolution limit for the majority of the LEFM test [10]. For comparison, tests conducted at -0.8 V_{SCE} and -1.1 V_{SCE} are included in Figure 2.5 [17]. These results demonstrate IG-SCC susceptibility at -0.8 V_{SCE} and immunity at -1.1 V_{SCE} (crack growth rate following the resolution limit, where no real IG-SCC occurred), consistent with prior findings [17,81]. Of note is that at -1.7 V_{SCE} the test could not be completed past K_J of 11.0 MPa√m at initial dK/dt of 0.25 MPa√m/hr due to the severity of the trenching which corroded away the dcPD wires used for crack growth measurement. These results will be complemented with additional, mechanism-specific LEFM tests to ascertain the specific influences driving this reduction in SCC susceptibility in 0.6 M NaCl.

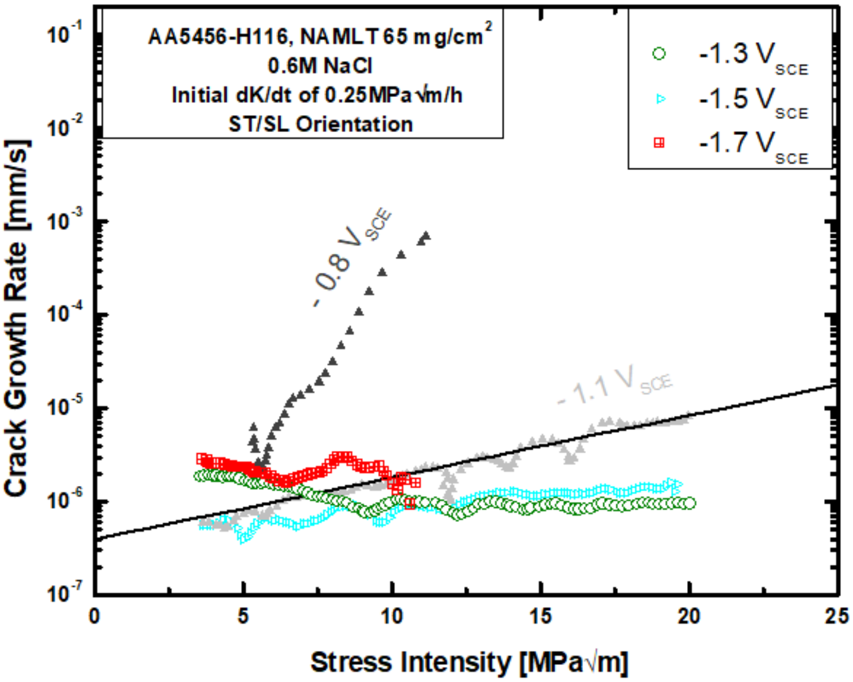

Figure 2.5: Stress intensity versus crack growth rate fracture trend detailing the effect of applied cathodic potential on SCC susceptibility in NAMLT 65 mg/cm² AA5456-H116 in 0.6 M NaCl.

2.2.4.2 *Modified LEFM Testing in Adjusted 0.6 M NaCl Environments to Inform the Lack of IG-SCC at Cathodic Potential*

The influence of preferential hydrogen recombination on cathodic crack growth was evaluated through LEFM testing in 0.6 M NaCl with added hydrogen poison, NH_4SCN. Literature efforts have demonstrated that H embrittlement is enhanced in the presence of hydrogen recombination poisons (such as cyanides, arsenic, antimony, selenium, phosphorous, and sulfur compounds), as these compounds promote hydrogen absorption instead of hydrogen recombination [60,82–87]. Various weight percent additions of NH_4SCN were evaluated for their ability to reduce the H_2 volume formed on AA5456-H116 at -1.5 V_{SCE} in 0.6 M NaCl (Figure 2.6) without drastically changing the overall chemistry/pH of the 0.6 M NaCl (which would affect the total volume of hydrogen formed) [82]. The results demonstrate that even 0.1 to 0.5 wt.% NH_4SCN causes a 2-fold reduction in observed H_2 gas to suggest that a higher level of atomic H has entered the material for a given hydrogen production rate. Higher concentrations of NH_4SCN, such as 5.0 or 15.0 wt.%, cause the bulk solution to become acidic and considerable solid product formation to occur with time at -1.5 V_{SCE}, which negates the assumption that similar hydrogen formation is achieved (or that the bulk chemistry is maintained) [82]. The addition of 0.5 wt.% NH_4SCN was chosen for use in fracture testing to attempt to maintain the solution chemistry, and a small volume of NaOH was added to achieve pH of 8.0 to avoid acidification of the bulk solution during LEFM

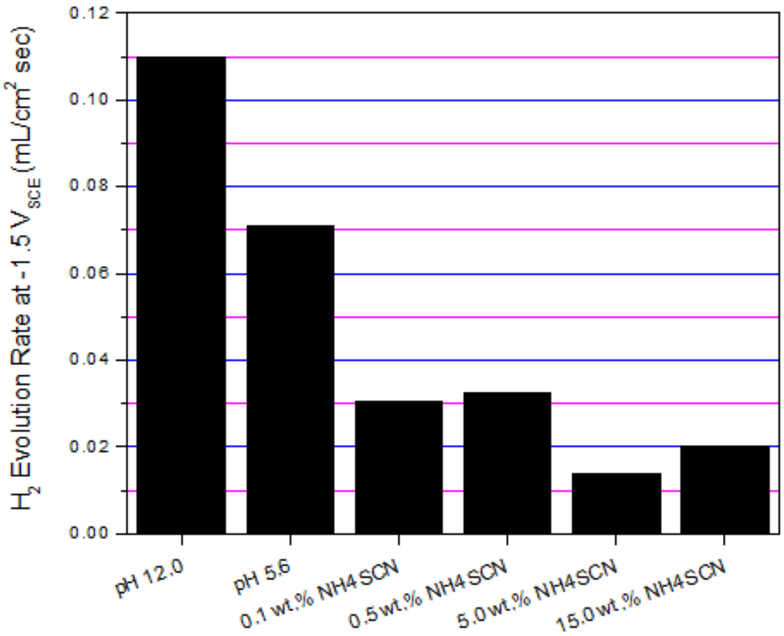

Figure 2.6: Gaseous hydrogen evolution results at -1.5 V_{SCE} on NAMLT 65 mg/cm^2 AA5456-H116 in 0.6 M NaCl immersion with alkaline (12.0) or natural (5.6) pH, or with various weight percent additions of NH_4SCN.

testing. Figure 2.7 shows LEFM testing results at -1.5 V_{SCE} utilizing this hydrogen absorption-promoting bulk solution (Figure 2.6), which demonstrate that no crack growth is achieved despite the use of the recombination poison.

The lack of hydrogen absorption due to the presence of an oxide permeation barrier was evaluated by testing in 0.6 M NaCl with NaOH added to achieve pH 12.0, where no stable oxide is present [61] and where hydrogen collection testing demonstrated that high volumes of hydrogen are produced (Figure 2.6). Figure 2.7 shows the LEFM results obtained from testing in this oxide-destabilizing environment. No SCC occurs, which confirms that a lack of H-uptake due the presence of an oxide at -1.5 V_{SCE} is not the cause for the lack of SCC susceptibility.

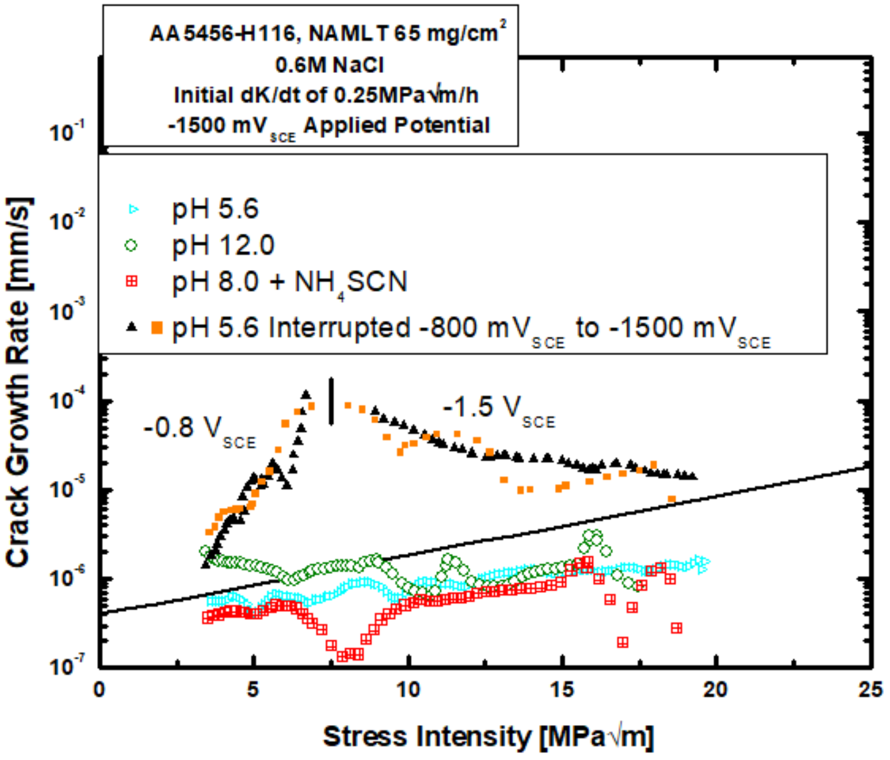

Figure 2.7: Stress intensity versus crack growth rate results on NAMLT 65 mg/cm^2 AA5456-H116 at constant applied potential of -1.5 V_{SCE} in 0.6 M NaCl, 0.6 M NaCl + NaOH (pH 12.0, where no stable oxide exists), and in 0.6 M NaCl containing 0.5 wt. % NH$_4$SCN (which promotes H absorption). Interrupted slow rising displacement tests were conducted at -0.8 V_{SCE} until K_J = 7.8 MPa√m followed by application of -1.5 V_{SCE} until K_J = 19.5 MPa√m, both with crack tip

chemistry dilution (solid black triangles) and without dilution (solid orange squares) to achieve cathodically-driven SCC.

It is also possible that the lack of SCC at cathodic potentials is due to chemically-induced blunting of the crack tip which removes the singularity and reduces the crack tip driving force for crack extension. This mechanism is well-documented in the literature [88,89], as is the effect of such blunting on the local crack tip stress field [90–94]. As detailed by Ford [88], in order to be a feasible extrinsic toughening mechanism, the alkaline Al corrosion process at the crack tip must be sufficiently fast to outpace the development of the mechanically induced (and H-embrittled) crack tip damage process zone. During the slow rising displacement testing reported in Figure 2.5, however, it is possible that such blunting occurs during the portion of the test where the K is below the threshold value for SCC (K_{ISCC}). The loss of the sharp crack tip at these sub-K_{ISCC} values would then compromise the rigor of the testing approach to accurately characterize the IG-SCC susceptibility at higher K. Specifically, the blunting at these low K values would be a testing protocol-induced artifact that would artificially toughen the material, and would manifest as an increase in K_{ISCC} (as observed in Figure 2.5). To experimentally determine the extent of crack tip blunting that occurs during cathodic polarization, LEFM specimens were fatigue precracked to establish a sharp crack front, followed by immersion in 0.6 M NaCl at -1.5 V_{SCE} for 1.5, 12.0, and 24.0 hours at K = 1 MPa√m. This protocol ensures that any blunting effects on the crack tip are due solely to corrosion. For comparison, the same testing procedure was utilized but at -0.8 V_{SCE} for 24.0 hours. Crack tip cross sectional images were taken at 3 locations along the crack front, and representative examples are shown in Figure 2.8. As these images illustrate, the crack tip at -0.8 V_{SCE} remains sharp, while the crack tip slowly broadens at -1.5 V_{SCE} in 0.6 M NaCl.

Specifically, the average of three crack tip curvature measurements taken through the half thickness of each specimen yielded values of 0.02 µm (-0.8 V_{SCE}, 24.0 hours), 0.09 µm (-1.5 V_{SCE}, 1.5 hours), 0.20 µm (-1.5 V_{SCE}, 12.0 hours), and 0.30 µm (-1.5 V_{SCE}, 24.0 hours). Thus, these results verify that chemical blunting is likely to occur during LEFM testing, warranting further evaluation.

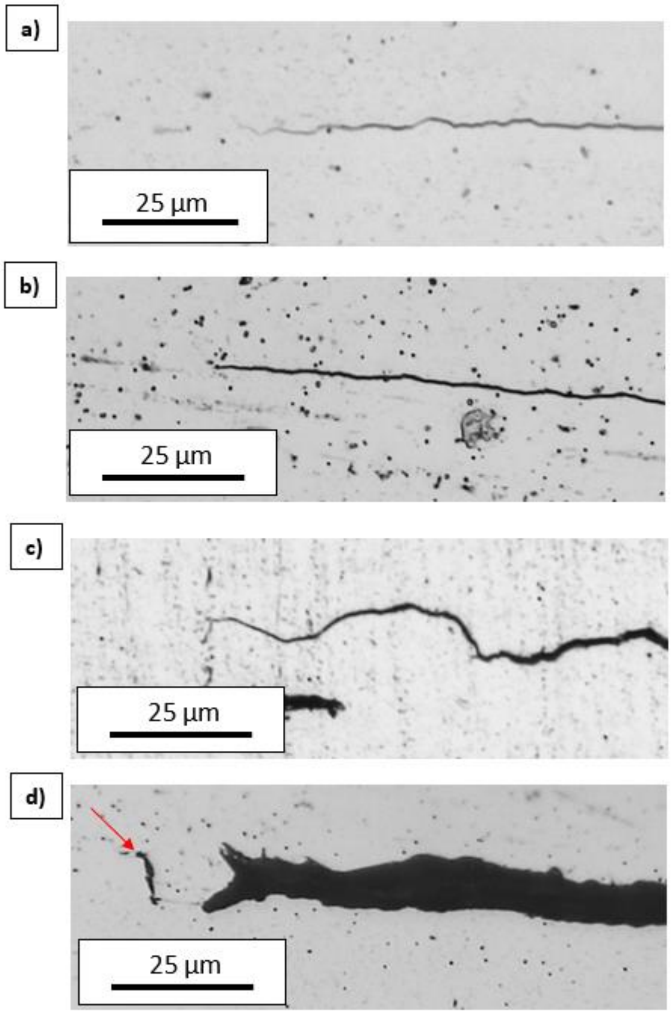

Figure 2.8: Optical images of the crack tip achieved during the constant K = 1 MPa√m potentiostatic hold testing at applied potential of ***(a)*** *-0.8 V_{SCE} for 24 hours, and -1.5 V_{SCE} for* ***(b)*** *1.5 hours,* ***(c)*** *12 hours and* ***(d)*** *24 hours in 0.6 M NaCl immersion.*

To deconvolute the possible impact of the low K blunting (which would be a testing artifact) from a true chemical inhibitive effect of cathodic polarization from a chemical standpoint, a modified LEFM testing procedure must be adopted wherein a sharp crack front is maintained at K values below K_{ISCC} prior to the application of severe cathodic polarization. Specifically, a rising stress intensity testing was initiated with applied potential of -0.8 V_{SCE} until K = 7.8 MPa√m such that fast crack growth occurred to maintain a sharp crack tip at increased stress intensity [17]. Two different testing conditions were performed following this portion of the LEFM testing. In the first testing procedure, once the K reached 7.8 MPa√m the polarization to -0.8 V_{SCE} was removed and the bulk 0.6 M NaCl environment was replaced with a continuous flow of deionized water in open circuit conditions and held at K = 1.0 MPa√m (below K_{ISCC}) for three days to dilute / remove the crack tip chemistry that had formed. At the end of the three days the sample was loaded back to K_J = 7.8 MPa√m in DI water (causing negligible crack length change or corrosion effects on the crack tip morphology), followed by the re-introduction of fresh 0.6 M NaCl bulk solution (pH 5.75). The sample was then simultaneously polarized to -1.5 V_{SCE} and subjected to a rising stress intensity rate of 0.25 MPa√m/hr. This protocol aims to establish and maintain a sharp IG-SCC crack at the high K of 7.8 MPa√m then expose it to the loading and cathodic polarization at once; the rinsing process aims to remove any complicating effects of the acidic crack tip conditions that would have been established during the testing at -0.8 V_{SCE}. In the second test, the polarization was simply switched from -0.8 V_{SCE} to -1.5 V_{SCE} at K = 7.8 MPa√m, without interruption to the flowing 0.6 M NaCl solution or to the slow rising stress intensity.

The results (Figure 2.7) for the solution replacement test (black solid triangles) and the test with no solution replacement (orange solid squares) conditions demonstrate that considerable crack growth is achievable at -1.5 V_{SCE}. This observation of cracking when the protocol is modified to ensure there is a sharp crack, suggests that the blunting (Figure 2.8) which occurs at low K values during the slow rising stress intensity tests may introduce a testing protocol-based artifact into the dataset in Figure 2.5. The intergranular nature of the cracking at cathodic potentials was confirmed via EBSD mapping of the crack tip on a cross-section (L-T surface) of a specimen tested at -0.8/-1.5 V_{SCE}, that was halted at -1.5 V_{SCE}, K = 13.0 MPa√m (Figure 2.9). However, while IG-SCC did occur after switching from -0.8 V_{SCE} to -1.5 V_{SCE}, the crack growth rate steadily declined (Figure 2.7). This slow decrease in crack growth rate is not consistent with the IG-SCC behavior observed under anodic polarization in Al-Mg alloys [10,17,18,81]. These findings warrant further evaluation to understand the mechanism of crack growth suppression at these cathodic potentials with increasing time of exposure.

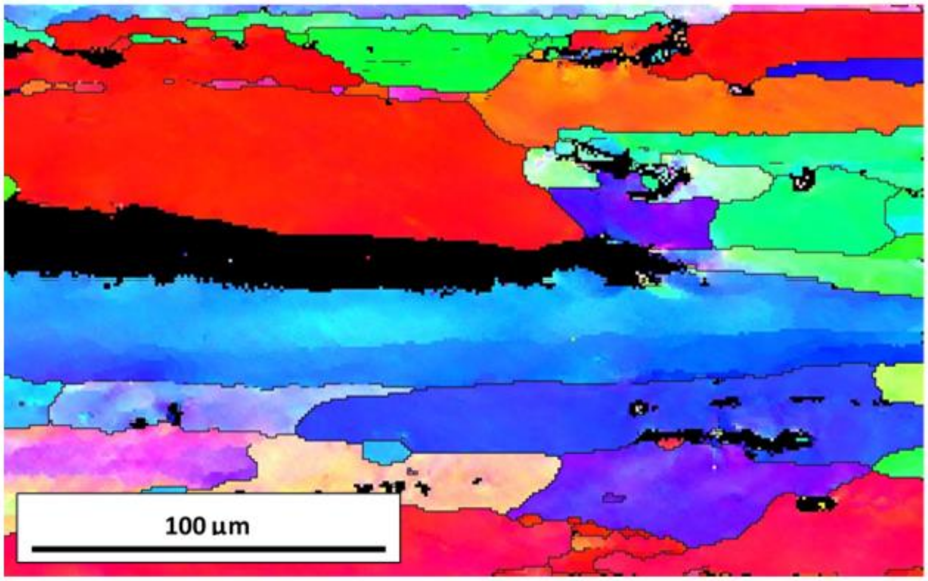

Figure 2.9: Electron backscatter diffraction grain map of the crack formed at K = 13.0 MPa√m, -1.5 V_{SCE} in 0.6 M NaCl in the interrupted -0.8/-1.5 V_{SCE} LEFM testing, demonstrating the intergranular nature of the cathodically-driven SCC in AA5456-H116.

2.2.4.3 ***Corrosion Morphology, Mass Loss Rate, and Corrosion Distribution from -1.7 V_{SCE} to -0.6 V_{SCE}***

To begin to inform the LEFM results, the corrosion morphologies, mass loss, and corrosion distribution achieved on NAMLT 65 mg/cm^2 AA5456-H116 were determined through 6-hour

Applied Potential (V_{SCE})	**Cross Section Analysis**
-0.60	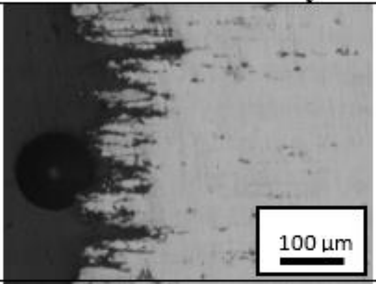
-0.70	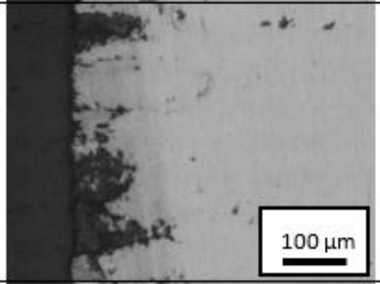
-0.73	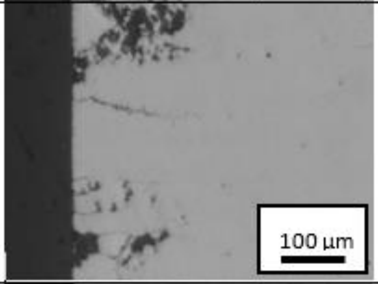
-0.75	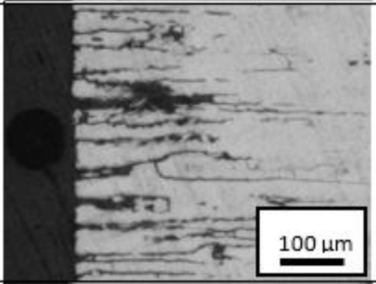
-0.77	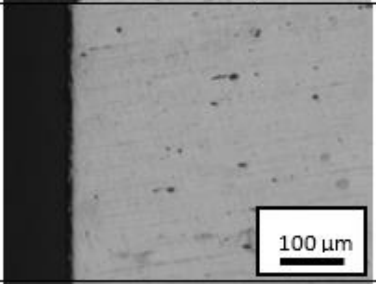
-0.79	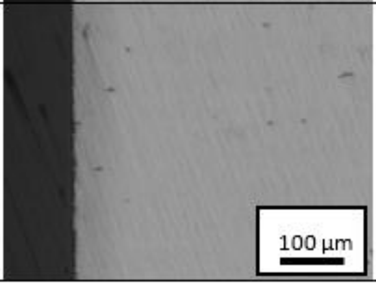

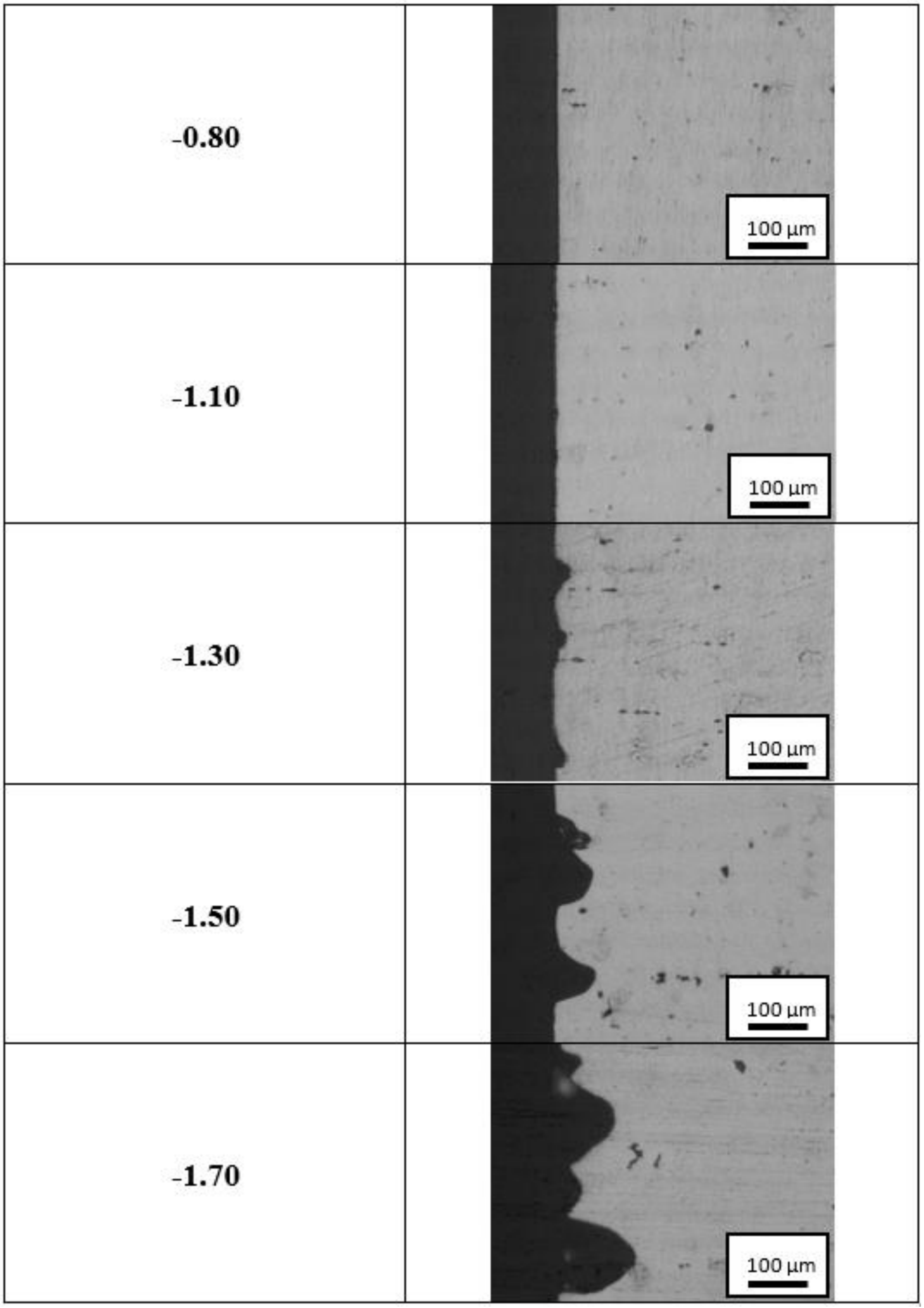

Figure 2.10: Cross sectional analyses on NAMLT 65 mg/cm^2 *AA5456-H116 demonstrating the transition in corrosion occurrence and morphology in the applied potential range of -0.60* V_{SCE} *to -1.70* V_{SCE} *after 6 hours of exposure in 0.6 M NaCl.*

potentiostatic hold tests in H-precharged 0.6 M NaCl at applied potentials of -1.7 V_{SCE} to -0.6 V_{SCE}. The corrosion morphology and severity results are shown in cross section in Figure 2.10. Previous work demonstrated that $E_{pit\ (\alpha)}$ is -0.73 V_{SCE}, and $E_{pit\ (\beta)}$ is -0.92 V_{SCE} for NAMLT 65 mg/cm^2 AA5456-H116 in 0.6 M NaCl [95]. The cross sections in Figure 2.10 agree with these results, specifically that Al pitting initiates at -0.73 V_{SCE}, and IGC is especially present at -0.75 V_{SCE}. No IGC is observed from -0.77 V_{SCE} to -0.90 V_{SCE}. Alkaline Al trenching begins at -1.10 V_{SCE} and increases in severity with increasing negative electrode potential (Figure 2.10). An SEM micrograph of the alkaline Al corrosion morphology obtained at -1.5 V_{SCE} is shown in Figure 2.11, where intermetallic particles are visible in the majority of the trenches. More detailed analysis of these intermetallic particles through EDS (Figure 2.12) concludes that the particles causing the formation of these trenches are generally Al(Mn,Fe,Cr), in agreement with prior findings on

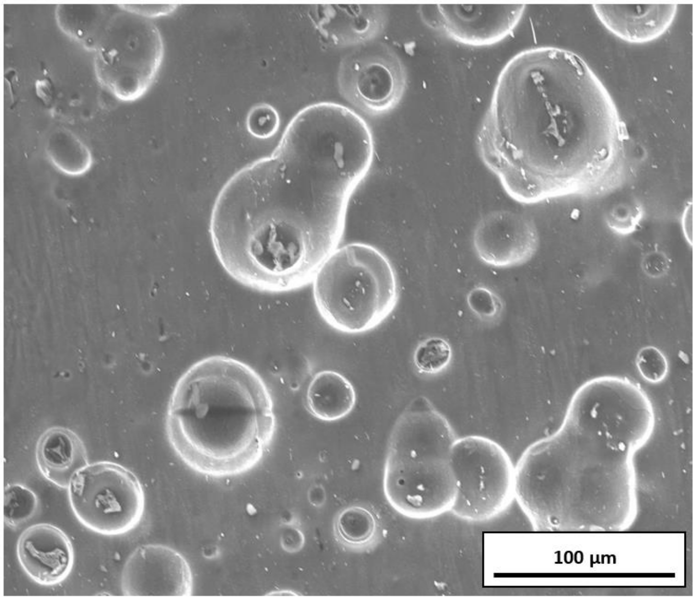

Figure 2.11: Scanning electron micrograph of the cathodic trenches present on the AA5456-H116 surface following 6 hours' potentiostatic hold at -1.5 V_{SCE} in 0.6 M NaCl, all of which are caused by intermetallic particles intersecting the alloy surface.

AA5083-H131 [96,97]. The alkaline corrosion severity on NAMLT 65 mg/cm^2 AA5456-H116 mirrored that of the unsensitized, NAMLT 4 mg/cm^2 AA5456-H116, though there was no occurrence of IGC in the unsensitized alloy due to the lack of β phase. This difference is especially apparent in the mass loss rate results shown in Figure 2.13, where negligible mass loss rate is achieved at -0.75 V_{SCE} in the unsensitized AA5456-H116 and the largest degree of mass loss rate occurs at that potential in the NAMLT 65 mg/cm^2 specimens. The mass loss rate is essentially the same between these sensitization levels where Al pitting occurs ($E_{applied} > E_{pit\ (\alpha)}$), while the sensitized AA5456-H116 achieves a slightly higher mass loss rate than in the unsensitized condition at $E_{applied} <$ -1.30 V_{SCE}. These results provide initial insight into the influence of the β phase in the anodic region (applied potential ($E_{applied} > E_{pit\ (\beta)}$ (-0.92 V_{SCE}))) versus the cathodic

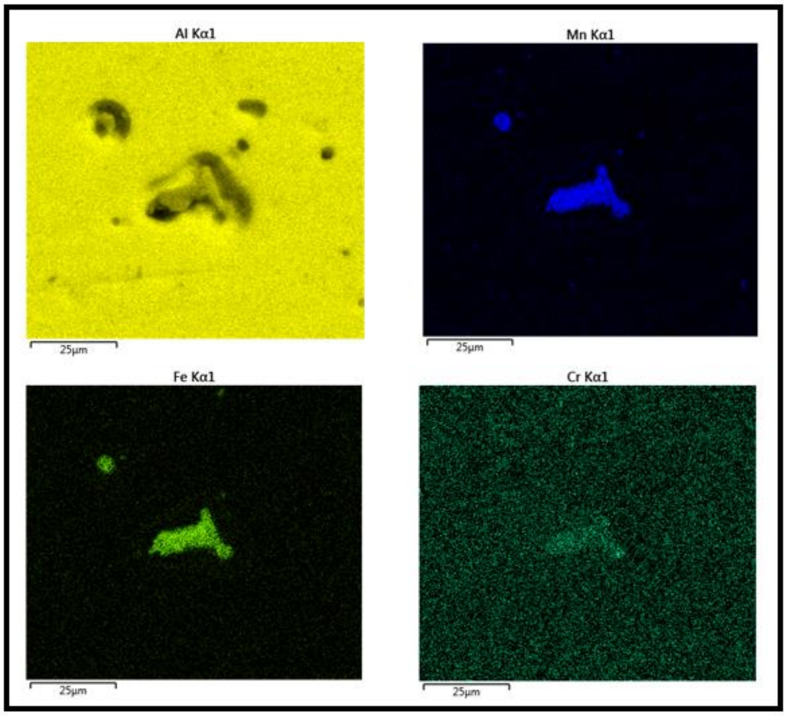

Figure 2.12: Energy dispersive spectroscopy results illustrating the Al, Mn, Fe, and Cr content of the intermetallic particles which cause the alkaline trenching phenomenon observed in AA5456-H116 in 0.6 M NaCl at applied potentials ≤ -1.1 V_{SCE}.

region ($E_{applied} < E_{pit\ (\beta)}$); the electrochemical activity of the β phase will be assessed more definitively later in the Results.

The distribution of the corrosion damage achieved during the 6-hour potentiostatic electrochemistry tests was analyzed via WLI, with results from this analysis shown in Figure 2.14 across the potential spectrum of -1.7 V_{SCE} to -0.6 V_{SCE}, as well as for the non-corroded AA5456-H116. The binarized corrosion maps, which consider any measured depth greater than 2 μm (based on the non-corroded result) to be corrosion damage, are also provided in Figure 2.14, which enabled the calculation of percent corroded surface area as a function of potential. These data will be considered further in relation to the experimentally measured hydrogen evolution rate.

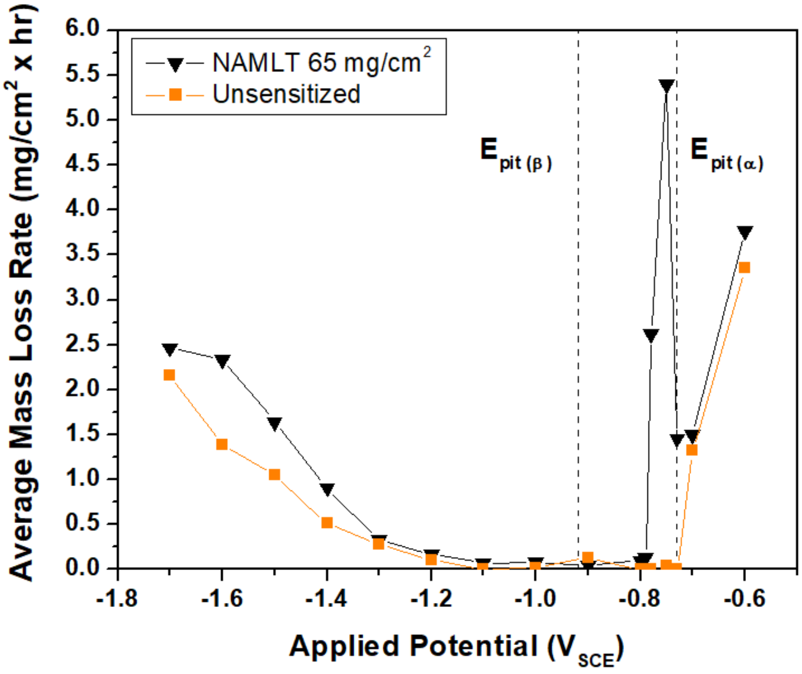

Figure 2.13: Average mass loss rate in NAMLT 65 mg/cm² and NAMLT 4 mg/cm² (unsensitized) AA5456-H116 following 6-hour potentiostatic hold in the range of -0.6 V_{SCE} to -1.7 V_{SCE} in 0.6 M NaCl.

<table>
<tr><th>Applied Potential (V_{SCE})</th><th>White Light Interferometry: Surface Analysis</th><th>Binarized Damage Area Analysis</th></tr>
<tr><td>Uncorroded AA5456</td><td>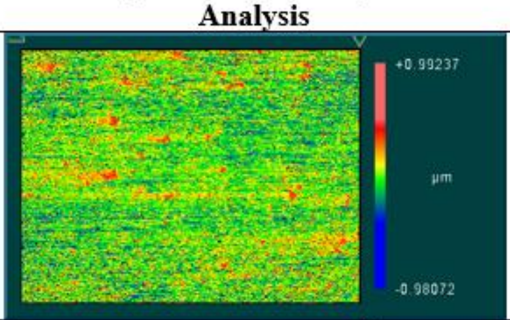
</td><td>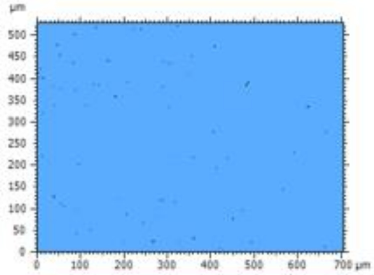
</td></tr>
<tr><td>-0.60</td><td>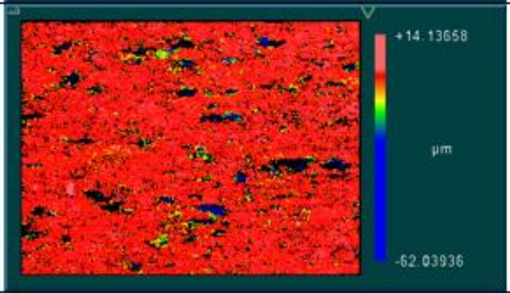
</td><td>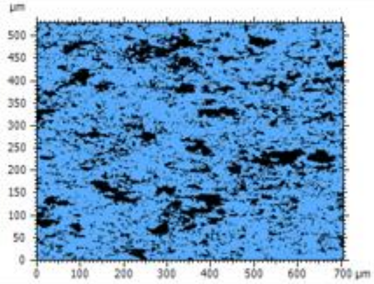
</td></tr>
<tr><td>-0.70</td><td>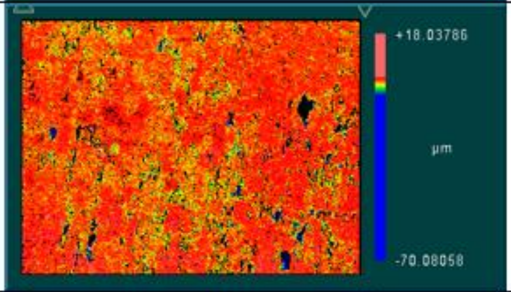
</td><td>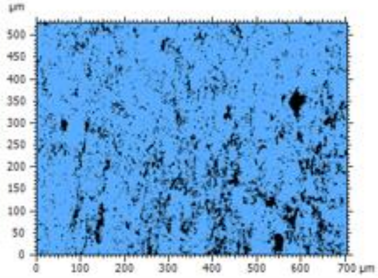
</td></tr>
<tr><td>-0.75</td><td>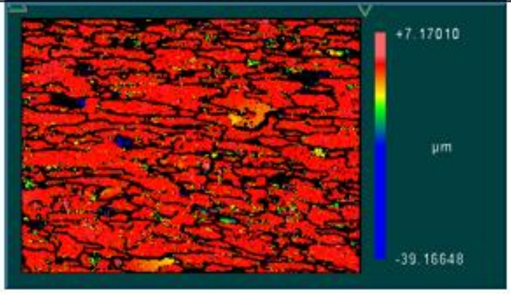
</td><td>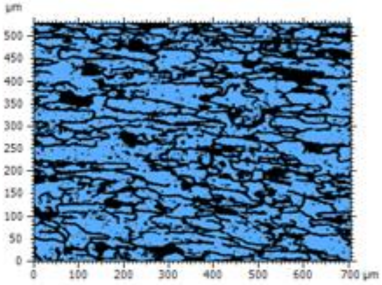
</td></tr>
<tr><td>-0.80</td><td>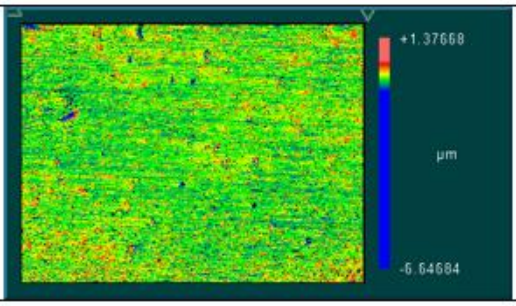
</td><td>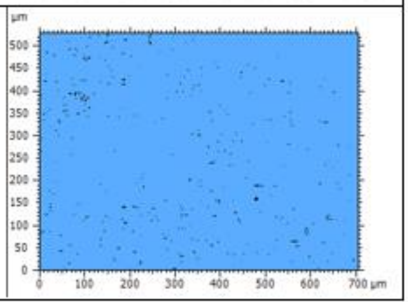
</td></tr>
</table>

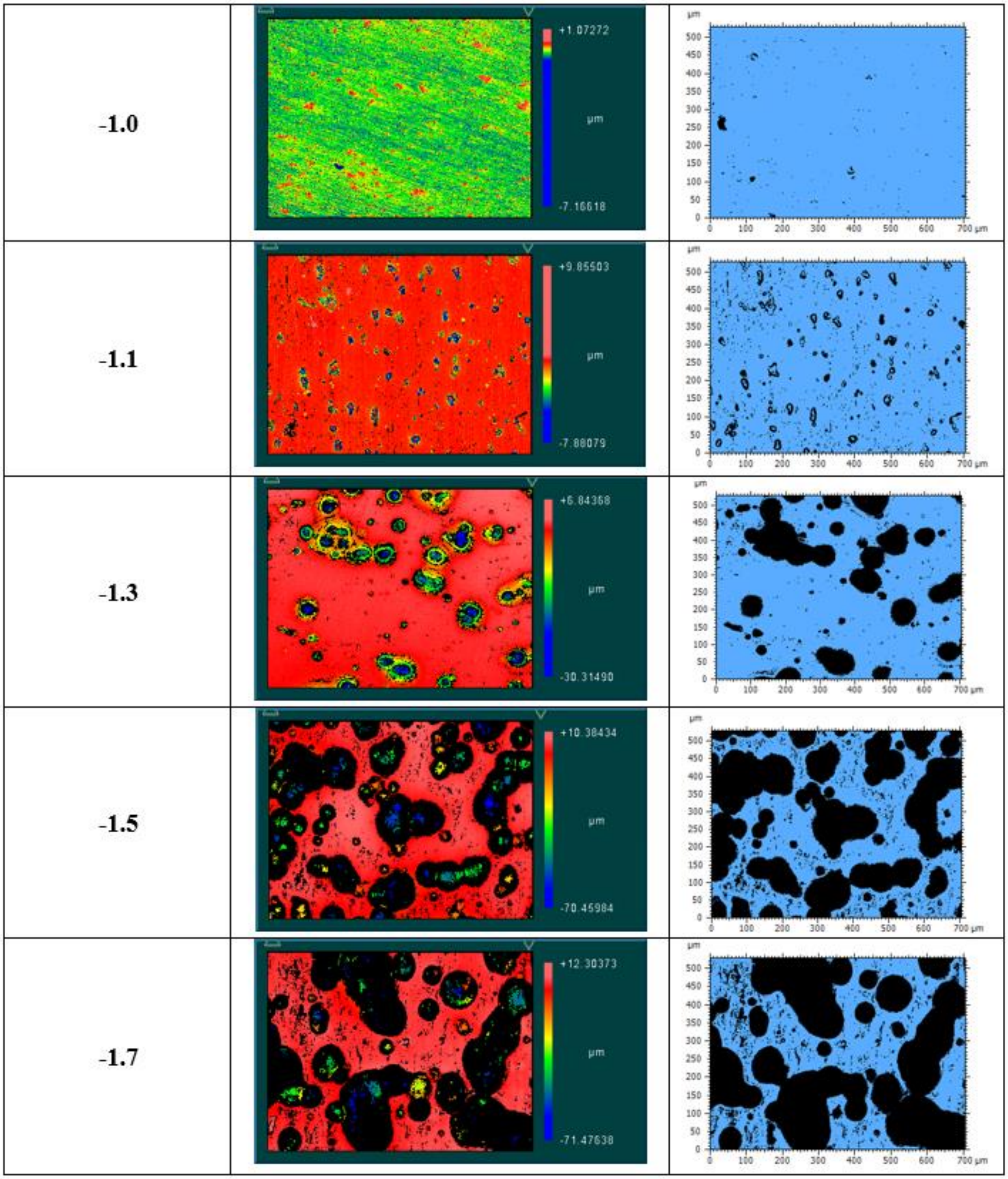

Figure 2.14: Total corroded surface area as a function of applied potential following the 6-hour potentiostatic hold experiments in H-precharged 0.6 M NaCl, determined via white light interferometry.

2.2.4.4 *H_2 Evolution Rate on AA5456-H116 and Pure β Phase in 0.6 M NaCl*

The gaseous hydrogen (H_2) evolution rate was obtained through volumetric collection and measurement during the 6-hour potentiostatic tests. Average (of three replicates) H_2 evolution rate and current density results on NAMLT 65 mg/cm^2 AA5456-H116 are illustrated from -1.7 V_{SCE} to -0.6 V_{SCE} for hydrogen pre-charged 0.6 M NaCl in Figure 2.15 (closed squares for H_2 evolution rate and open triangles for established anodic or cathodic current density). These results demonstrate that rapid H_2 evolution ensues at potentials more negative than -1.3 V_{SCE}, reaching rates as high as 7.8 mL/cm^2•sec at -1.7 V_{SCE}. In the cathodic polarization region, the increasing H_2 evolution rate parallels the increasing cathodic current density, which is similar to cathodic corrosion results obtained on 99.99% Al [75]. The potential region of -1.2 V_{SCE} to -0.8 V_{SCE}

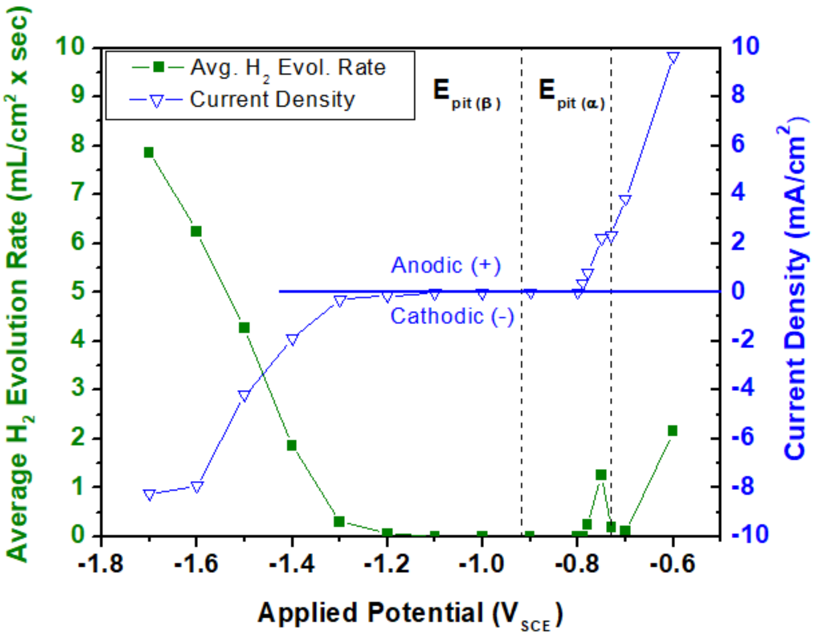

Figure 2.15: Average gaseous hydrogen evolution rate (solid squares) and current density (open triangles) on NAMLT 65 mg/cm^2 AA5456-H116 during 6-hour full immersion across the range of -0.6 V_{SCE} to -1.7 V_{SCE} in 0.6 M NaCl. These data consider the entire 0.78 cm^2 exposed area to contribute to hydrogen formation, resulting in the rate shown.

achieves limited H_2 evolution or corrosion. The current density begins to increase anodically at -0.79 V_{SCE}, and interestingly, H_2 evolution increases from this potential until -0.73 V_{SCE}, where a drop occurs before a subsequent increase as anodic Al matrix pitting initiates (Figure 2.15). These H_2 evolution results may be understood further through comparison with the corroding surface area results obtained via WLI, which is shown in Figure 2.16. As Figure 2.16 demonstrates, cathodic polarization at $E_{applied} \leq -1.40\ V_{SCE}$ causes the largest fraction of corroding surface area due to the alkaline trenching phenomenon, as well as the largest quantity of evolved H_2 across the potential range considered. The corrosion of the β phase at $E_{applied} \geq E_{pit\ (\beta)}$, which is critical to the IG-SCC mechanism, evolves less H_2 overall.

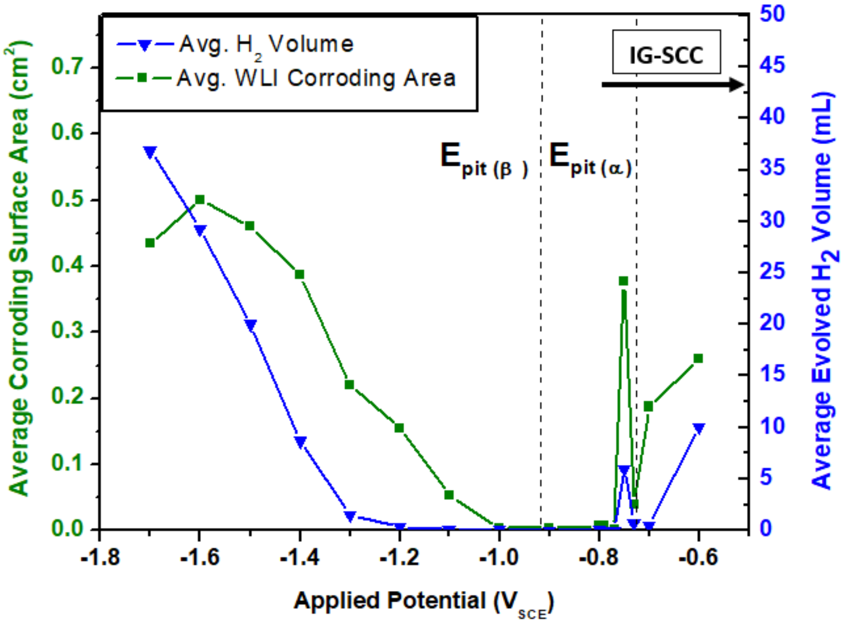

Figure 2.16: Average corroded AA5456-H116 surface area, as determined via WLI analysis, following 6-hour potentiostatic hold in H-charged 0.6 M NaCl full immersion. In comparison, the average total evolved H_2 volume is shown for each potential from the 6-hour potentiostatic hold. The known anodic potential region wherein IG-SCC is known to occur is indicated for reference.

Understanding the corrosivity of the β phase in the cathodic polarization region is crucial to understand the potential SCC mechanisms present in the anodic versus cathodic polarization regions, and thus to compare the subsequent SCC susceptibilities. Therefore, the potentiostatic hydrogen collection tests were repeated in hydrogen pre-charged 0.6 M NaCl on unsensitized (NAMLT 4 mg/cm^2) AA5456-H116 as well as pure β phase for comparison to the previous results obtained on NAMLT 65 mg/cm^2 AA5456-H116, as shown in Figure 2.17. These results demonstrate that the β phase substantially corrodes in the anodic polarization region ($E_{applied} > E_{pit (\beta)}$), as expected. The low plateau of H_2 evolution rate on the β phase at -1.3, -1.5, and -1.7 V_{SCE} demonstrates only slight β phase corrosion in the cathodic region that may be due to Al corrosion as well as the hydrogen evolution reaction. Low current densities are sustained on the pure β phase

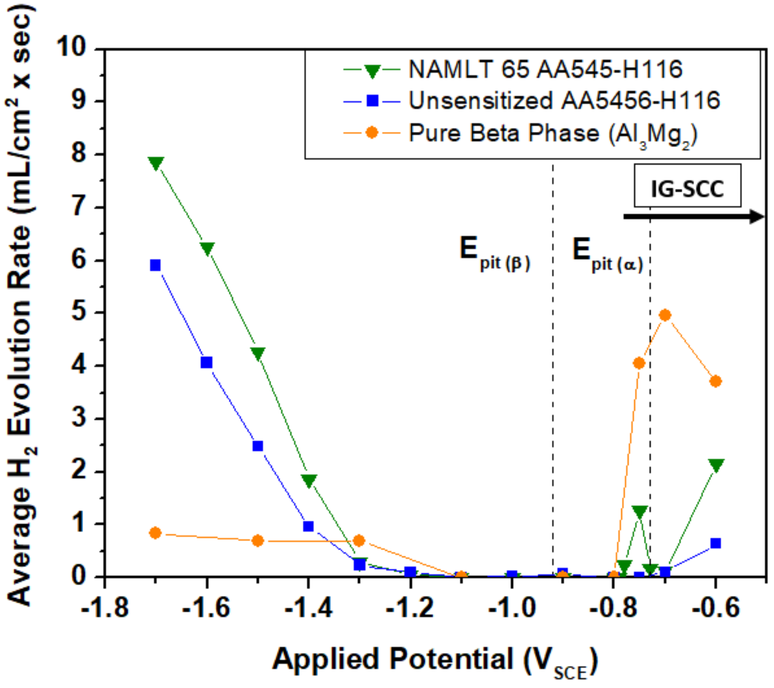

Figure 2.17: Average H_2 evolution rate analyses on NAMLT 65 mg/cm^2 and unsensitized (NAMLT 4 mg/cm^2) AA5456-H116 as well as pure β phase in 0.6 M NaCl throughout the applied potential range of -0.6 to -1.7 V_{SCE} (pure β evaluated over a reduced 1.5-hour period at -0.75 V_{SCE}, -0.70 V_{SCE}, and -0.60 V_{SCE} due to the corrosivity of these conditions and the β phase reactivity).

at these potentials, in support of this conclusion (not shown). The H_2 evolution rate findings are also in agreement with the mass loss rate data illustrated in Figure 2.13, where the anodic IGC corrosion mechanism is most effective at causing mass loss in NAMLT 65 mg/cm^2 AA5456-H116, followed by anodic Al pitting (preferential α oxidation with β oxidation), and lastly the cathodic Al trenching (where β does not contribute, and Al oxidation occurs mostly around Al(Mn,Fe,Cr) (Figure 2.12)). However, sole consideration of the H_2 volume produced from these corrosion reactions is not entirely representative of their impact on the AA5456-H116 IG-SCC susceptibility. Specifically, in order to impact the environmental cracking behavior, the H must be absorbed into the material at the crack tip (via either localized generation or diffusion from the bulk surface at the crack flanks). Directly relating the volume of H_2 evolved from a bulk surface to the absorbed H content at the crack tip is complicated by (1) potential differences in the degree of hydrogen recombination, (2) the location of the H generation (e.g. proximate to constituents versus at a crack tip), and (3) potential differences in the H uptake behavior possibly caused by potential dependent crack tip film stabilities. *In toto*, while these H_2 evolution rate data help guide the role of the various corrosion phenomena as cation/hydrogen sources in the potential range of -1.7 V_{SCE} to -0.6 V_{SCE}, the more important factor to consider for environmental cracking susceptibility is the rate of hydrogen absorption as a function of potential.

2.2.4.5 *Absorbed H Content as a Function of Potential in Sensitized AA5456-H116*

To fully consider the hydrogen contribution of the aforementioned corrosion phenomena towards the AA5456-H116 SCC susceptibility, the *absorbed* H content must be quantified. Hydrogen absorption testing was conducted using the same procedure as in the H_2 collection tests, except that the 0.6 M NaCl solution was not charged with hydrogen and the samples were immediately stored in liquid nitrogen after the 6-hour potentiostatic hold. The results from these evaluations are shown in Figure 2.18 with the background hydrogen content (13.3 ppm, determined via the 3 uncharged replicate specimens) subtracted. Figure 2.18 demonstrates that similar *total* amounts of atomic H are absorbed between the anodic and cathodic polarization regions. Specifically, hydrogen absorption occurred primarily from -1.30 V_{SCE} to -1.70 V_{SCE} in the cathodic polarization region, and in the anodic region the largest quantity of H absorption occurred in the IGC region.

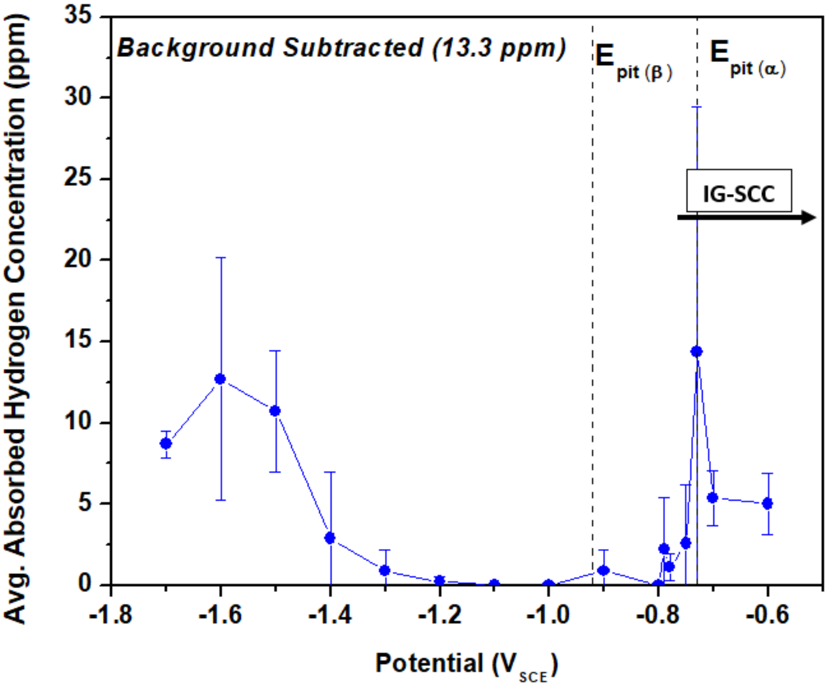

Figure 2.18: Mean absorbed H content and standard deviation obtained on AA5456-H116 at each applied potential in 0.6 M NaCl, evaluated via the inner gas fusion method. The background value of 13.3 ppm has been subtracted.

2.2.5 **Discussion**

In order for the hydrogen embrittlement phenomenon to occur during IG-SCC, hydrogen must: (1) evolve and adsorb on the Al surface, (2) diffuse to the crack tip process zone, and (3) interact with the microstructure to cause H embrittlement. As such, the proximity of the H absorption location to the crack tip process zone is critical to the potency of its effect on the environmental cracking behavior. The prior results demonstrated that severe cathodic polarization results in bulk absorbed H contents that are globally similar to those in anodic conditions (Figure 2.18). However, LEFM testing shows environmental cracking behavior that is retarded (completely for conventional slow rising displacement testing or partially when a sharp crack is maintained) as compared to anodic testing at -0.8 V_{SCE} (Figures 2.5 and 2.7). These findings warrant more detailed investigation as to the mechanism of crack growth suppression as well as the overall IG-SCC susceptibility of AA5456-H116 during cathodic polarization. Specifically, the following questions will be addressed:

1) What H generation phenomena occur throughout the polarization range considered?
2) Based on these phenomena, what can be inferred regarding the concentration of H generated at the crack tip?
3) How will the chemically-induced blunting phenomenon affect the mechanical conditions at the crack tip, and thus the environmental cracking susceptibility?
4) How does this understanding inform future testing protocols for LEFM-based characterization of SCC susceptibility?

2.2.5.1 *Mechanisms of H Generation During Polarization in Chloride Environment*

The corrosion evolution during anodic or cathodic polarization of Al-Mg varies due to differences in (1) the localized surface chemistry that is formed, and (2) the stability of the protective oxide that might function as a permeation barrier [75,98,99]. To further understand these differences during anodic and cathodic polarization, the Al-Mg solid solution may be related to pure Al based on similar electrochemical properties [7]. The corrosion and H-evolution behavior of pure Al (as a proxy for AA5456-H116) under both anodic and cathodic polarization conditions will be discussed.

2.2.5.1.1 Hydrogen Evolution during Anodic Polarization of Sensitized Al-Mg

The stability of Al_2O_3 is critical under anodic polarization conditions because this oxide layer will dictate the rate of anodic/cathodic reactions present on the Al surface [100,101]. As demonstrated in Figure 2.19, the oxide layer is destabilized with increasingly anodic polarization in Cl^- solution, and this destabilization is especially present as pitting occurs and the pH is acidified [30,31,102–104]. At an actively strained, sensitized Al-Mg crack tip two phenomena may occur

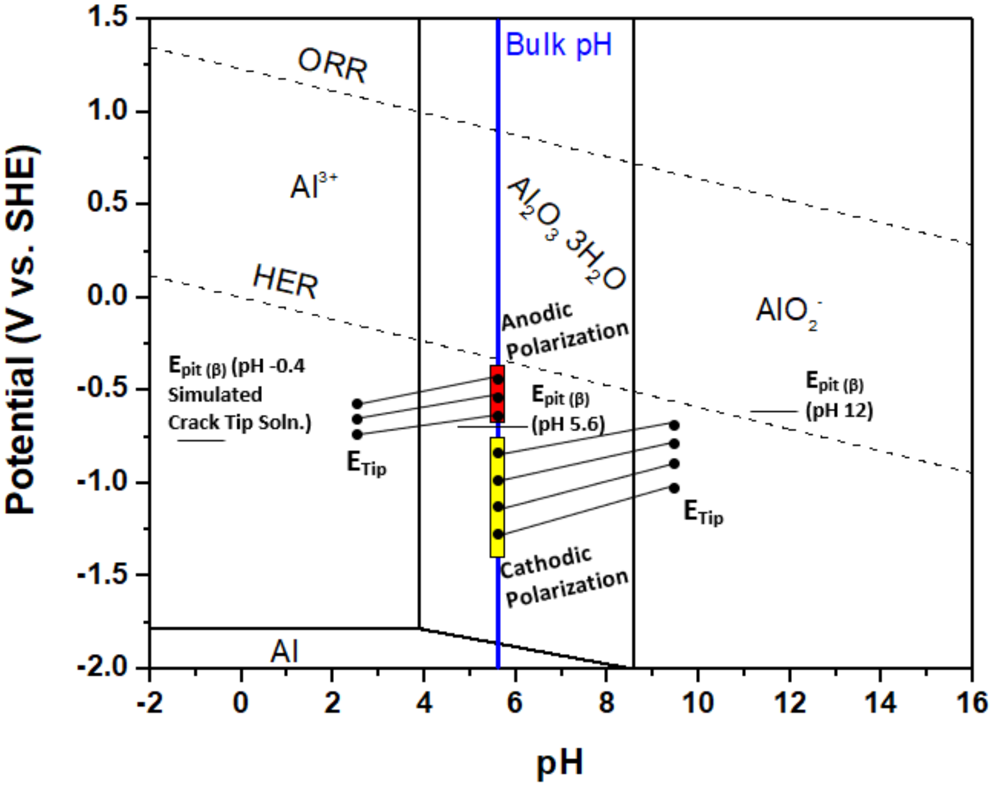

Figure 2.19: Aluminum E (volts versus Standard Hydrogen Electrode (SHE))-pH diagram demonstrating the polarization range where anodic (red region) and cathodic reactions (yellow region) are driven in the present work, and the consequent effects on the potential/pH of the electrochemical system (demonstrated schematically, specific crack tip potential/pH values are not experimentally verified). This analysis demonstrates that the hydrogen evolution reaction

will be the dominant cathodic reaction on AA5456-H116 in 0.6 M NaCl (bulk pH 5.6). The ohmic voltage drop effect as well as the effect of anodic/cathodic polarization on the crack pH are illustrated, resulting in the shifted crack tip potential (E_{tip}). $E_{pit\,(\beta)}$ is shown for relative comparison in simulated crack tip solution (pH -0.4) [1], natural 0.6 M NaCl (pH 5.6), and 0.6 M NaCl + NaOH (pH 12.0).

under anodic polarization: (1) strain-induced dislocation motion will rupture the oxide to expose bare Al surface area, and (2) the dissolution of the Al_3Mg_2 releases Al^{3+} and Mg^{2+}, which causes ingress of Cl^- ions for charge neutrality [9,105]. Cl^- interaction with the oxide will decrease the resistance of the crack tip oxide to mechanically induced ruptures caused by active crack tip strain rates [9,17,18,30,31,102–104,106]. As oxide rupture increasingly occurs to expose fresh Al surface at the crack tip, HER will occur at higher rates on the bare Al surface:

$$2H^+ + 2e^- \rightarrow H_2 \qquad \text{Equation 2.1}$$

Furthermore, an intermediate step in the HER process may cause atomic H formation [40,82,107,108]. The release of Al^{3+} and Mg^{2+} during β phase dissolution thermodynamically enables proton formation through both Al- and Mg-cation hydrolysis:

$$Al^{3+} + H_2O \rightarrow AlOH^{2+} + H^+ \quad \text{and} \quad Mg^{2+} + H_2O \rightarrow MgOH^+ + H^+ \qquad \text{Equation 2.2}$$

The acidified chemistry created by these hydrolysis reactions (Figure 2.19) will be localized to the crack tip, and has been demonstrated to achieve negative pH values and high [Cl^-] through titration of $MgCl_2$ into the $AlCl_3$-containing solution [9,109,110]. Based on the Nernst Equation, ohmic voltage drop, and the ability of Cl^- to increase the activity of H [111], these crack tip conditions will locally increase the overpotential for H production, thus enhancing the H available for adsorption and subsequent diffusion into the crack tip damage process zone to enhance IG-SCC via the H-embrittlement mechanism [17,18,23]. Through this process anodic polarization creates a localized, acidified crack tip chemistry to drive aggressive IG-SCC [9,17].

2.2.5.1.2 Hydrogen Evolution and Alkaline Corrosion during Cathodic Polarization of Sensitized Al-Mg

As demonstrated in Figure 2.19, cathodic polarization may destabilize the oxide through alkalinization. Cathodic polarization initially drives the reduction of water on Al_2O_3,

$$H_2O + e^- \rightarrow \tfrac{1}{2} H_2 + OH^- \qquad \text{Equation 2.3}$$

which promotes alkalinization of the bulk Al surface and/or the crack wake environment [112,113]. The hydroxyl ions adsorb onto Al_2O_3 and cause oxide thinning by chemical dissolution,

$$Al_2O_3 + 2OH^- \rightarrow 2AlO_2^- + H_2O \qquad \text{Equation 2.4}$$

which promotes a more negative bulk Al surface potential and increases the overpotential for HER (Equation 2.1) [57,113]. Above the pH of ~ 8.6, Al_2O_3 chemical dissolution occurs more rapidly than formation [61]. Exposure of the bulk Al surface through dissolution of the oxide enables HER to progress at an increasing rate with increase in the hydrogen overpotential (increasingly negative applied potential) [106,112,114,115]. The loss of the oxide layer will cause the aluminum corrosion to be limited only by the rate of the electrochemical reaction [57,75]:

$$OH^- + Al + H_2O \rightarrow AlO_2^- + 3/2\, H_2 \qquad \text{Equation 2.5}$$

Under these alkaline conditions (Figure 2.19) the formation of H_2 due to Equation 2.5 and atomic H/H_2 due to HER will occur across the global alloy surface, and will be less favored at the crack tip due to Ohmic voltage drop effects down the crack wake (driving the surface potential anodically (lower hydrogen overpotential)) [9]. However, the trenching phenomenon, otherwise known as cathodically-induced corrosion, may disrupt the reactions occurring across the global Al surface as penetrating intermetallic particles are fast cathodic reaction sites [97,116–118]. In contrast to the anodic polarization conditions, the H formation under cathodic polarization (due to HER and/or alkaline trenching) will occur in a well-distributed manner across the bulk Al surface rather than preferentially in the localized crack tip environment. Hence, under cathodic polarization ohmic voltage drop effects will decrease the hydrogen overpotential. The corrosion mechanisms will inform the estimation of effective H generation at the crack tip in both anodic and cathodic polarization conditions.

2.2.5.2 *Effective H Generation at the Crack Tip as a Function of Potential*

It is necessary to distill the bulk H-absorption data reported in Figure 2.18 to per area contribution, and by doing so it is possible to isolate and provide an estimate of the H generation at the crack tip, thus de-emphasizing the less potent contributions of H generation on the crack flanks. A first step in this process is using the WLI analysis (Figure 2.14) to quantify the portion of the flat sample surface area where corrosion is observed. However, the three-dimensionality of the various corrosion morphologies must also be considered since H generation will be occurring on the evolving corroded surfaces as well; this requires more detailed consideration of surface area created at depth into the specimen surface. The conditions created in both cathodic and anodic polarization regions have been systematically evaluated in the prior sections to construct the contributing surface area approximation procedure, which is detailed in the Appendix (2.2.9). These corrosion conditions and the resulting surface morphology are detailed in Figure 2.20 for the cathodic trenching and IGC polarization regions, demonstrating the method of exposed surface area approximation as well as the regions of the surface considered to be significantly H-forming. As shown in Figure 2.20, the cathodic corrosion morphology was approximated as halved ellipsoids, and the IGC/Al pitting phenomena were approximated as cones. The entirety of the exposed area is considered significantly H-forming in the cathodic polarization region where alkalinization and trenching occurs. In contrast, the exposed area during anodic Al pitting is limited due to the local oxide destabilization and rupture at isolated sites (Figure 2.19). Hence, in the IGC region, only the fissure/crack tip is considered to be significantly H-forming due to the more stable condition of the global oxide (Figure 2.20).

2.2.5.3 *Approximation of the Corroding Surface under Anodic and Cathodic Conditions*

The effective corroding, H-forming area results following the 3-D surface area approximation (Figure 2.20) are shown in Figure 2.21 along with the area calculated from a binary analysis of the WLI images in Figure 2.14. These data demonstrate greater than an order of

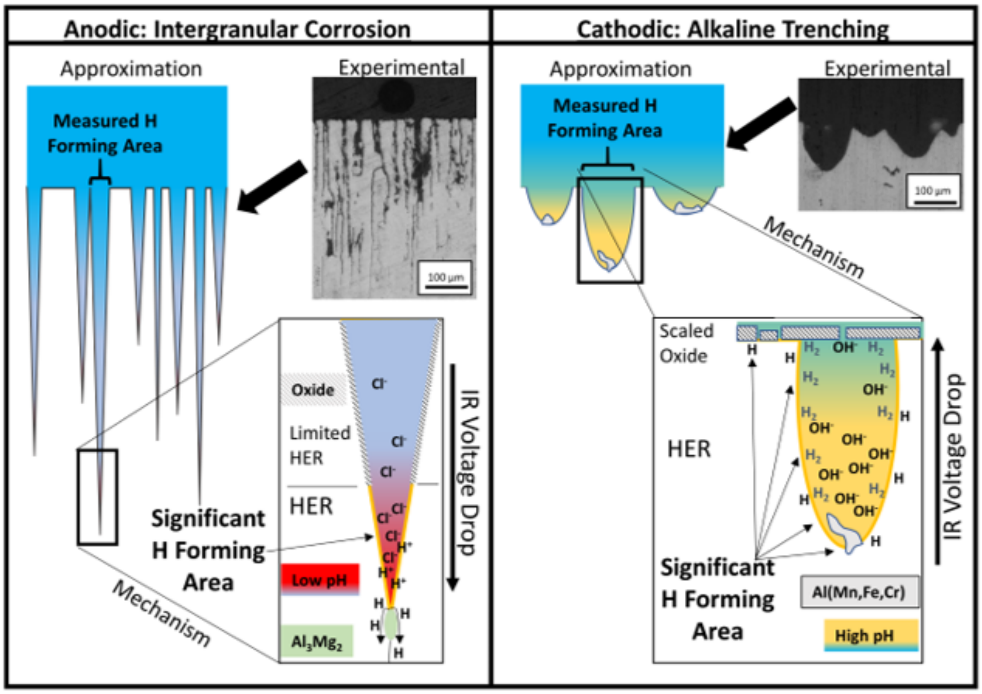

Figure 2.20: Schematic illustrating the geometric approximation scheme in two dimensions as well as the corrosion mechanisms that informed these procedures in the anodic (IGC) and cathodic (trenching) potential regions. These H-forming surface area calculations considered the three-dimensional corroding space (cones for IGC morphology, ellipsoids for the trenching morphology) to more accurately normalize the H evolution results on AA5456-H116.

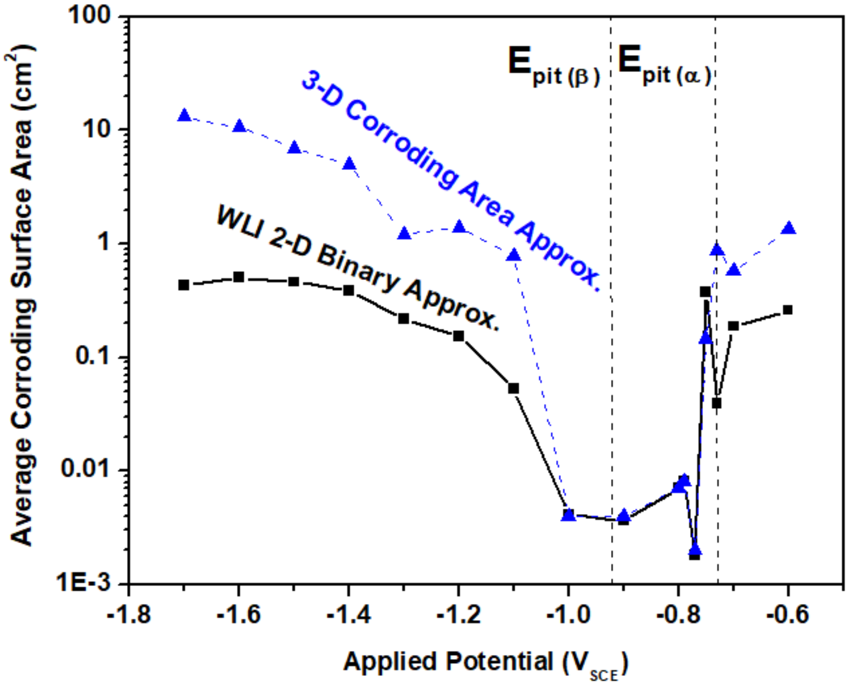

Figure 2.21: Results of the corroding surface area (H-forming) evaluation which considered the three-dimensional morphology approximations illustrated in Figure 2.20, demonstrating the difference with the binary analyses obtained via white light interferometry (WLI, Figure 2.14).

magnitude increase in the estimated H-forming surface area in the cathodic region due to consideration of the trench geometry. A minor reduction in the H-forming surface area is observable in the IGC region due to only the fissue/crack tip being considered significantly H-forming, and a similar increase as in the cathodic region occurs in the anodic pitting region as the knife-like geometry is considered. These results will be utilized to understand the hydrogen evolution per contributing unit of corroding area at each potential to elucidate the potential effect of hydrogen evolution location/transport on IG-SCC susceptibility.

2.2.5.4 *Normalized Hydrogen Charging as a Function of Applied Potential*

By normalizing the absorbed H data (Figure 2.18) by the calculated H-forming surface areas (Figure 2.21) it is possible to estimate the amount of absorbed H per unit area; such data are shown in Figure 2.22. These normalized results demonstrate a marked difference in the ability of anodic versus cathodic polarization to charge Al-Mg with H at the crack tip. Specifically, the broad nature of the hydrogen evolution in the cathodic polarization region leads to a low quantity of absorbed H per unit of contributing area, whereas the highly localized nature of the corrosion in the anodic polarization (IGC) region (which absorbs similar total amounts of hydrogen as the cathodic region (Figure 2.18)) leads to a large quantity of H absorption per unit of contributing area. Moreover, at the crack growth rates achieved at -1.5 V_{SCE} (Figure 2.7), the absorbed H cannot diffuse at high enough rates to dilute the concentration at the crack tip, having a bulk diffusivity ≈ $1x10^{-10}$ cm^2/s [21] (ie. in 10 seconds, the crack may propagate 1.0 µm while the absorbed H at the

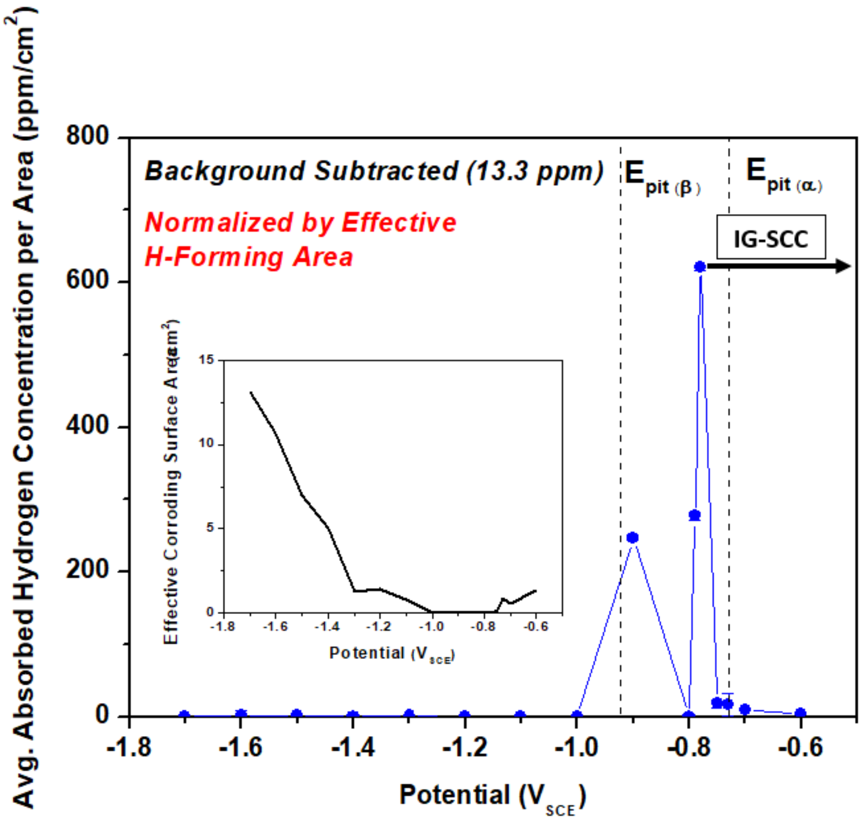

Figure 2.22: Average H absorption per unit of contributing area of AA5456-H116 as a function of applied potential in 0.6 M NaCl, demonstrating a high affinity for H absorption in the IGC region.

crack tip could only have diffused 0.3 μm). In order to use the data in Figure 2.22 to interpret the environmental cracking trends, it is necessary to argue that the per area H absorption data are applicable to the H generation taking place at the crack tip. For anodic conditions this is reasonable as the β/α dissolution and local chemistry that forms within an IGC fissure is expected to be largely similar to crack tip conditions (Figures 2.17 and 2.20). For cathodic conditions, the matrix dissolution observed at the crack tip (Figure 2.8) suggests that a similar oxidation process occurs at the crack tip as that observed on the bulk material (Figure 2.10). It is reasonable to conclude that the low values of absorbed H per area in the cathodic region (Figure 2.22) correlate with the lack of environmental cracking susceptibility observed in Figure 2.5. However, two important additional considerations must still be addressed: (1) while the levels of H absorbed per area are low, they are still finite thus may contribute to the environmental cracking behavior, and (2) the results in Figure 2.7 demonstrate that if a sharp crack is maintained, then cracking is observed at cathodic potentials (-1.5 V_{SCE}.)

2.2.5.5 ***Additional Influences Affecting SCC Susceptibility at Cathodic Potentials***

Figures 2.7 and 2.8 demonstrate that there can be significant chemical blunting of the crack tip during cathodic polarization. Such blunting will remove the stress singularity and reduce the local crack tip stresses. The extent of this reduction can be estimated using an approach by Creager and Paris concerning the effective stress along the Mode I plane when a given crack tip curvature exists [94]:

$$\sigma_x = \frac{K_I}{\sqrt{2\pi r}} cos\frac{\theta}{2}\left[1 - sin\frac{\theta}{2} sin\frac{3}{2}\theta\right] - \frac{K_I}{\sqrt{2\pi r}}\frac{\rho}{2r} cos\frac{3}{2}\theta \qquad \text{Equation 2.6}$$

where σ_x = the stress present in the Mode I fracture plane, K_I is the stress intensity under Mode I loading, r is the vector length defining the angle of interest (θ) from the Mode I plane, and ρ is the radius of curvature. The Mode I stress was calculated using average crack tip curvature values (e.g. Figure 2.8) of 0.02 µm (-0.8 V_{SCE}, 24.0 hours), 0.09 µm (-1.5 V_{SCE}, 1.5 hours), 0.20 µm (-1.5 V_{SCE}, 12.0 hours), and 0.30 µm (-1.5 V_{SCE}, 24.0 hours). The results are shown in Figure 2.23 for the stress intensities of 5.0, 10.0, 15.0, and 20.0 MPa√m, utilizing $r = 2 \times 10^{-7}$ m (the smallest distance from the crack tip which may be considered at these K/ρ values utilizing the present equation), and θ = 0° (the pure Mode I plane). These results demonstrate the decrease in σ_x with increasing crack tip curvature, specifically reducing σ_x by 75.4% after 24 hours at -1.5 V_{SCE}. These findings suggest that the chemically induced blunting during the increasing K portion of the test that is below K_{ISCC} could affect SCC susceptibility. For example, if the intrinsic K_{ISCC} was 7.8 MPa√m for cathodically-driven cracking, 24 hours of immersion in 0.6 M NaCl at -1.5 V_{SCE} would be

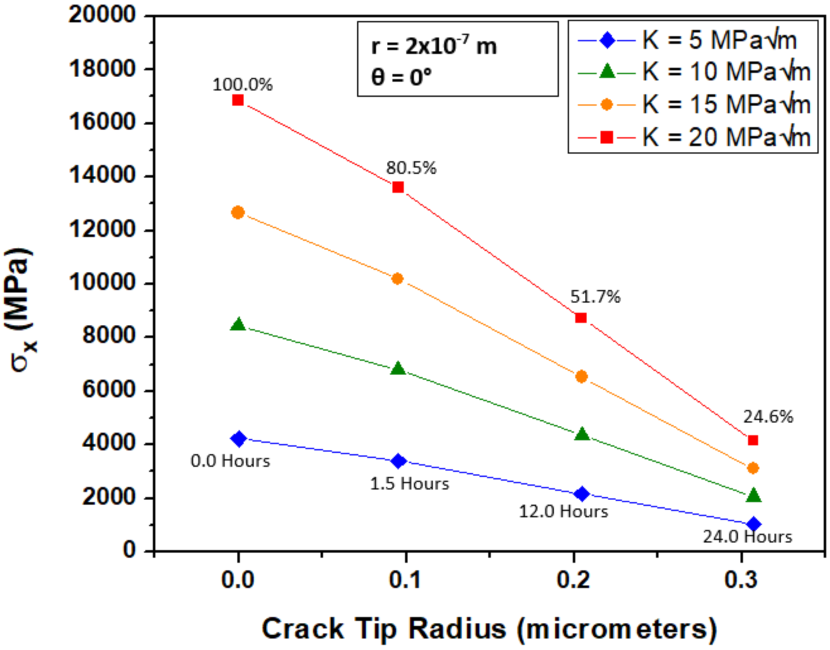

Figure 2.23: Stress component present at the crack tip for a range of stress intensities, demonstrating the reduction in effective stress as crack tip curvature increases. The angle from the Mode I plane was taken to be 0° (purely in the Mode I plane), and the vector radius was 2×10^{-7} m in this calculation. The initially sharp crack tip curvature is represented by the point at 0.0 hours and 100% σ_x, and the subsequent points are marked based on the time of immersion in 0.6 M NaCl at -1.5 V_{SCE}, K = 1 MPa√m, with the percent stress that would be experienced in the Mode I plane relative to the sharp crack tip indicated above the K = 20 MPa√m points.

necessary for the K to rise from 2.0 to 7.8 MPa√m (with a dK/dt of 0.25 MPa√m/hr), and during this time the crack would blunt and the σ_x (on the Mode I plane) would be reduced by 75.4%.

While the details of the failure criteria that lead to cracking is controversial [119], in a decohesion paradigm the crack advance will occur when a local tensile stress exceeds some breaking stress representative of the material resistance [120], and this threshold will decrease with increasing local H concentration. As such, for cathodic polarizations, it is reasonable that the combination of lower levels of H concentration (Figure 2.22) and blunting-induced reduction in the local tensile stresses (Figure 2.23) will result in a reduction in the susceptibility to environmental cracking.

2.2.5.6 ***Validation of the Proposed Cathodic IG-SCC Suppression Mechanism***

The proposed mechanism driving the IG-SCC suppression consists of a combination of low levels of H-charging (due to the lack of β dissolution and reduced H overpotential at the cathodic crack tip), and chemical blunting to reduce the effective stress concentration. This hypothesis can be evaluated via additional LEFM testing to address two questions. First, will IG-SCC occur if faster strain rates are imposed that would eliminate the time needed for the blunting of the crack during (1) the sub-K_{ISCC} regime, and (2) the crack growth process. Second, is it possible to re-sharpen the crack tip and to reinitiate IG-SCC after blunting has occurred?

To evaluate the former, two LEFM experiments were conducted at a strain rate of 4.0 MPa√m/hr; this rate is eight-fold faster than those previously run. To confirm that this loading rate does not diminish the environmental effect by outpacing the H diffusion ahead of the crack tip, initial experiments were performed at -0.8 V_{SCE} in 0.6 M NaCl. Similar behavior for loading rates of 0.25 and 4.00 MPa√m/hr in Figure 2.24 demonstrates that the IG-SCC susceptibility at -0.8 mV$_{SCE}$ is not dependent on loading given the expectation of a small H-charged fracture zone via a moving line source analysis (≈ 0.1 μm) [21,47,95] and a small critical H-diffusion distance [9,10]. Simply stated, the faster loading rates do not diminish effects of H-embrittlement. The same LEFM test was then conducted but with applied potential of -1.5 V$_{SCE}$ in 0.6 M NaCl to determine if a rapid rise in K to exceed the K$_{ISCC}$ will result in cracking susceptibility by outpacing the effects of the chemical blunting. At the strain rate of 4.0 MPa√m/hr, approximately 1.5 hours would be necessary to reach a K of 7.8 MPa√m, which at -1.5 V$_{SCE}$ would result in a crack tip similar to that shown in Figure 2.8(b). The results of this test, shown in Figure 2.24, demonstrate that the increased strain rate was unsuccessful at driving IG-SCC, and the crack growth rate quickly decreased following the initiation of testing at K = 3.5 MPa√m. Non-uniform crack growth of approximately 1 mm was observed during slow rising displacement during this as well as a replicate test.

It is also of interest to understand the effect of the blunting at cathodic potentials on mitigating subsequent cracking at more susceptible anodic potentials; specifically, to determine if a blunted crack tip will impact the onset of anodic crack growth (e.g. increase the K$_{ISCC}$). This is technologically relevant to loss in galvanic protection by a metal-rich primer and restoration of more positive coupled potentials. The chemical blunting phenomenon is investigated through performing a 24-hour potentiostatic hold at -1.5 V$_{SCE}$, K = 1 MPa√m on a fatigue precracked

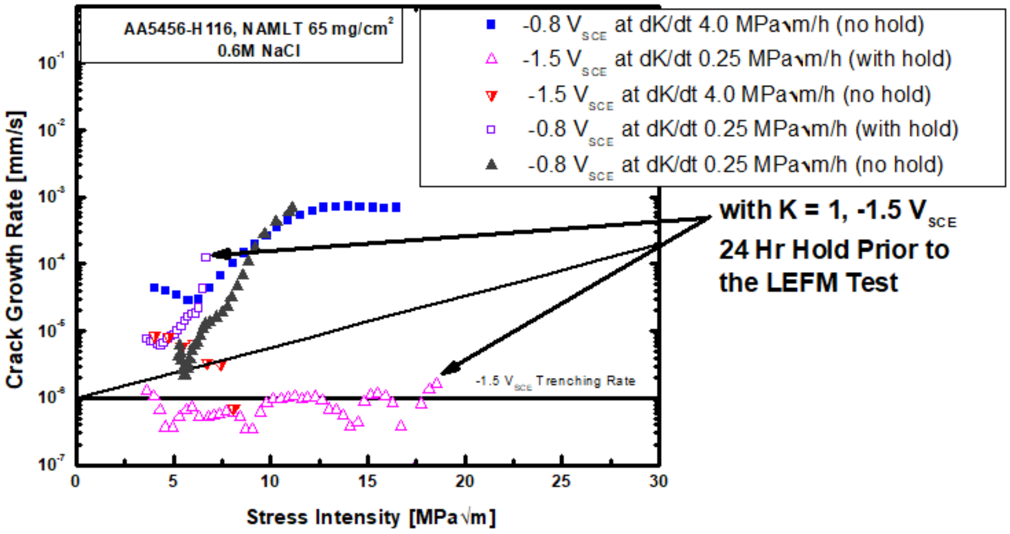

Figure 2.24: Fracture testing data demonstrating the effect of strain rate and corrosion mechanism on IG-SCC susceptibility in AA5456-H116 in 0.6 M NaCl. The resolution limit for the strain rate of 4.0 MPa√m/hr is shown for comparison with the LEFM testing conducted with the same.

specimen, which would produce a blunted crack tip akin to Figure 2.8(d). Following this 24-hour hold an increasing K test is performed (at 0.25 MPa√m/hr) at either -1.5 V_{SCE} or -0.8 V_{SCE} in 0.6 M NaCl. These results are shown in Figure 2.24. First, the results confirm that no cracking occurs at -1.5 V_{SCE} with the intentionally blunted crack. However, even with a pre-blunted crack, subsequent increasing K testing at -0.8 V_{SCE} shows that the K_{ISCC} is not increased and the growth rate behavior aligns with tests performed without the pre-blunted crack tip.

The results in Figure 2.7, where cracking at the cathodic potential of -1.5 V_{SCE} is achieved if the sample is tested at -0.8 V_{SCE} to a K value above an assumed K_{ISCC}, suggested that there was a potentially important role of chemical blunting in understanding the lack of environmental cracking behavior observed in Figure 2.5 at cathodic potentials. This view is consistent with the blunted morphologies observed in Figures 2.8 and 2.9 and the calculated reductions on crack tip stress level reported in Figure 2.23. Furthermore, the decreasing growth rates observed in Figure

2.7 after transitioning from -0.8 V_{SCE} to -1.5 V_{SCE}, suggests a possible role of real-time blunting of the active tip. However, the fact that no cracking is observed during the K increasing testing at -1.5 V_{SCE} at 4.0 MPa√m/hr (where there would be insufficient time to blunt the crack) suggest that chemical blunting may not be the sole governing factor. Additionally, testing of the purposefully pre-blunted notch at -0.8 V_{SCE} clearly showed significant cracking susceptibility, with the K_{ISCC} being unaffected by the blunted tip. These results strongly suggest that the level of H-generation (controlled by the relevant crack tip electrochemical processes and chemistries) is the dominant feature controlling the observed susceptibility levels in Figure 2.5. Specifically, the H absorption per area trends reported in Figure 2.22 correlate with the observed susceptibility and are likely controlling; with the effects of chemical blunting playing an important (Figure 2.7) but secondary (Figure 2.24) role.

2.2.6 Conclusion

The present work set out to evaluate the window of potential dependency of IG-SCC in highly sensitized AA5456-H116. This dependence was first informed through evaluation of the Al-Mg environmental fracture susceptibility in the anodic and cathodic polarization regions. Assessment of the corrosion and hydrogen evolution achieved on AA5456-H116 and on pure β phase throughout the potential range of -0.6 V_{SCE} to -1.7 V_{SCE} informed the LEFM testing results. The following conclusions were reached concerning the alloy susceptibility and underlying environmental fracture mechanism in these cathodic conditions:

- The Al-Mg environmental fracture susceptibility is low under cathodic polarization conditions ($E_{applied} \leq -1.0$ V_{SCE}) compared to the high susceptibility achieved in anodic conditions (i.e. -0.8 V_{SCE})

- The lack of environmental cracking susceptibility at cathodic potentials directly scales with the per area levels of H generation that are expected to occur at the crack tip at each polarization level.
- Chemical blunting serves as a secondary effect in the amphoteric Al-Mg crack tip to suppress cathodic crack growth. This extrinsic strengthening mechanism reduces stress concentration and increases the K_{ISCC} through increasing crack tip curvature
- Chemical blunting has no effect on K_{ISCC} during anodic crack growth where the crack tip readily re-sharpens through the β/α phase dissolution and H-crack propagation process

Data Availability Statement

All data presented in the present work will be provided upon reasonable request.

2.2.7 **Appendix**

2.2.7.1 ***Approximation of the Corroding Surface under Cathodic Conditions***

As informed by the corrosion mechanism discussion above, the approximated surface geometries for the cathodic polarization region are outlined in Figure 2.20, which illustrates the surface areas contributing to H-formation both on the bulk Al surface and within the trenches. The clean, rounded nature of the cathodic trenching warrants approximation of these features as halved ellipsoids to compute the new surface area, wherein the short transverse dimensions are assumed to be the same (“a” = “b”):

$$\frac{1}{2}\ Ellipsoid\ Surface\ Area = 2\pi\left(\frac{(a\cdot b)^{1.6}\cdot(a\cdot c)^{1.6}\cdot(b\cdot c)^{1.6}}{3}\right)^{1/1.6} \qquad \text{Equation 2.7}$$

Measurement of the average short (a,b) and long transverse (c) dimensions for the trenches formed at each potential utilized the cross section analyses following the 6-hour potentiostatic hold tests in 0.6 M NaCl, such as those provided in Figure 2.10. The error associated with non-uniform cross sectioning of the trench features through the midsection was offset through analysis of as many as 30 trenches per potential to obtain average dimensions. An average number of trenches was quantified per unit area via the WLI mapping results (Figure 2.14). Both the average bulk surface (e.g. surface where no trenches are observed) and the trench surface area were considered to contribute to H-formation under cathodic polarization (Figure 2.20).

2.2.7.2 ***Approximation of the Corroding Surface under Anodic Conditions***

Figure 2.19 demonstrates that HER will be promoted as the cathodic reaction during the anodic polarization of AA5456-H116 due to the inherently negative corrosion potential of this alloy (-0.85 V_{SCE}, or -0.61 V_{SHE}). Anodic polarization will promote acidic conditions, which will subsequently promote more negative potentials (oxide rupture in Cl conditions + Ohmic voltage drop effects, increasing the H overpotential and the affinity for HER to occur) [9]. Over the global alloy surface, the rate of HER will be considerably lower than in the IGC fissure tips since the oxide layer will remain thermodynamically stable, which will limit HER as it will serve as a permeation barrier. Thus, below $E_{pit(\alpha)}$, corrosion damage will be localized to the grain boundaries where the deleterious β phase creates a susceptible corrosion path, and so only a small fraction of the total fissure area (the immediate vicinity of the fissure/crack tip) will be considered to contribute significantly to the H-evolution process. This anodic mechanism and the subsequent H-forming area approximation are illustrated in Figure 2.20. Above $E_{pit(\alpha)}$, Al pitting occurs within the IGC fissures, creating a knife-like morphology (Figure 2.10). The oxide rupture known to occur above $E_{pit\ (\alpha)}$ due to Cl^- will promote HER on the bulk surface, so the entire surface area will be considered significantly H-forming in the case of Al pitting.

As informed by the analysis above, calculation of the IGC surface area morphology contribution will be approximated as a cone (without the base), and only 10% of the total surface area will be considered to contribute significantly to H-formation due to the localized, acidified chemistry and corrosion reactions present at the fissure/crack tip. The knife-like Al pitting observed to occur in AA5456-H116 roughly creates a similar geometry, though the entire evolved surface as well as the original bulk sample surface are considered significantly H-forming. These evolved, corroding surface areas will be approximated as conical geometries with only lateral surfaces:

$$Lateral\ Conical\ Surface\ Area = \pi \cdot r \cdot l \qquad \text{Equation 2.8}$$

where the average radius (*r*) was measured at the IGC/pit intersection with the bulk Al surface and the average length (*l*) consisted of the vertical depth measurements obtained on cross sections similar to those shown in Figure 2.10. The cross-section error was offset through similar methods as utilized in the cathodic polarization region.

2.2.8 **References Cited**

[1] N.J.H. Holroyd, G.M. Scamans, Environmental Degradation of Marine Aluminum Alloys—Past, Present, and Future, Corrosion. 72 (2016). doi:10.5006/1927.

[2] W.J. Golumbfskie, K.T. Tran, J.M. Noland, R. Park, D.J. Stiles, G. Grogan, C. Wong, Survey of detection, mitigation, and repair technologies to address problems caused by sensitization of Al-Mg alloys on navy ships, Corrosion. 72 (2016) 314–328. doi:10.5006/1916.

[3] R.K. Gupta, R. Zhang, C.H.J. Davies, N. Birbilis, Influence of Mg Content on the Sensitization and Corrosion of Al-xMg(-Mn) Alloys, Corrosion. 69 (2013) 1081–1087. doi:10.5006/0948.

[4] M.A. Steiner, S.R. Agnew, Predictive sensitization modeling for AA5xxx aluminum alloys including non-isothermal cases, Corrosion. 72 (2016) 169–176. doi:10.5006/1675.

[5] N. Birbilis, R. Zhang, M.L.C. Lim, R.K. Gupta, C.H.J. Davies, S.P. Lynch, R.G. Kelly, J.R. Scully, Quantification of Sensitization in AA5083-H131 via Imaging Ga-Embrittled Fracture Surfaces, Corrosion. 69 (2013) 396–402. doi:10.5006/0804.

[6] M.L.C. Lim, J.R. Scully, R.G. Kelly, Intergranular Corrosion Penetration in an Al-Mg Alloy as a Function of Electrochemical and Metallurgical Conditions, Corrosion. 69

(2013) 35–47. doi:10.5006/0722.

[7] D.R. Baer, C.F.W. Jr, M.H. Engelhard, M.J. Danielson, R.H. Jones, J.S. Vetrano, Influence of Mg on the corrosion of Al, J. Vac. Sci. Technol. A. 18 (2000) 131–136. doi:10.1116/1.582129.

[8] R.H. Jones, D.R. Baer, M.J. Danielson, J.S. Vetrano, Role of Mg in the stress corrosion cracking of an Al-Mg alloy, Metall. Mater. Trans. A. 32 (2001) 1699–1711. doi:10.1007/s11661-001-0148-0.

[9] C.B. Crane, R.. Kelly, R.P. Gangloff, Crack chemistry control of intergranular stress corrosion cracking in sensitized Al-Mg, Corrosion. 72 (2016) 242–263. doi:10.5006/1852.

[10] C.B. Crane, R.P. Gangloff, Stress corrosion cracking of Al-Mg alloy 5083 sensitized at low temperature, Corrosion. 72 (2016) 221–241. doi:10.5006/1766.

[11] R.H. Jones, The Influence of Hydrogen on the Stress-Corrosion Cracking of Low-Strength Al-Mg Alloys, J. Miner. Met. Mater. 55 (2003) 42–46. doi:10.1007/s11837-003-0225-5.

[12] M.L.C. Lim, R.G. Kelly, J.R. Scully, Overview of Intergranular Corrosion Mechanisms, Phenomenological Observations, and Modeling of AA5083, Corrosion. 72 (2016). doi:10.5006/1818.

[13] M.L.C. Lim, R. Matthews, M. Oja, R. Tryon, R.G. Kelly, J.R. Scully, Model to predict intergranular corrosion propagation in three dimensions in AA5083-H131, Mater. Des. 96 (2016) 131–142.

[14] D. Mizuno, R.G. Kelly, Galvanically Induced Intergranular Corrosion of AA5083-H131 Under Atmospheric Exposure Conditions: Part 1—Experimental Characterization, Corrosion. 69 (2013) 580–592. doi:10.5006/0812.

[15] ASTM, ASTM: G67-04 Standard Test Method for Determining the Susceptibility to Intergranular Corrosion of 5XXX Series Aluminum Alloys by Mass Loss After Exposure to Nitric Acid (NAMLT Test), ASTM International, West Conshocken, PA, 2004.

[16] Standard Test Method for Determining the Susceptibility to Intergranular Corrosion of 5XXX Series Aluminum Alloys by Mass Loss After Exposure to Nitric Acid (NAMLT Test) 1, Annu. B. ASTM Stand. i (2004) 5–7. doi:10.1520/G0067-04.2.

[17] M.E. McMahon, J.R. Scully, J.T. Burns, Mitigation of intergranular stress corrosion cracking in Al-Mg by electrochemical potential control, J. Miner. Met. Mater. 69 (2017) 1389–1397. doi:10.1007/s11837-017-2362-2.

[18] M.E. McMahon, P.J. Steiner, A.B. Lass, J.T. Burns, The effect of temper and composition on the stress corrosion cracking of Al-Mg alloys, Corrosion. 73 (2017) 347–361.

[19] M.E. McMahon, P.J. Steiner, A.B. Lass, J.T. Burns, The effect of loading orientation on intergranular stress corrosion cracking in Al-Mg alloys, Corrosion. 73 (2017) 713–723.

[20] M.E. McMahon, J.T. Burns, J.R. Scully, New Criteria for Substrate Protection Against Stress Corrosion Cracking in Al-Mg Alloys Based on Non-Polarizability of Zn-Rich Primers, Prog. Org. Coatings. (2019). In Review.

[21] J.-H. Ai, M.L.C. Lim, J.R. Scully, Effective Hydrogen Diffusion in Aluminum Alloy 5083-H131 as a Function of Orientation and Degree of Sensitization, Corrosion. 69 (2013) 1225–1239. doi:10.5006/0987.

[22] D. Tanguy, B. Bayle, R. Dif, T. Magnin, Hydrogen effects during IGSCC of pure Al–5Mg alloy in NaCl media, Corros. Sci. 44 (2002) 1163–1175. doi:10.1016/S0010-938X(01)00140-8.

[23] M. Seifi, N.J.H. Holroyd, J.J. Lewandowski, Deformation rate and sensitization effects on environmentally assisted cracking of Al-Mg naval alloys, Corrosion. 72 (2016) 264–283.

doi:10.5006/1949.

[24] J.L. Searles, P.I. Gouma, R.G. Buchheit, Stress Corrosion Cracking of Sensitized AA5083 (Al-4.5Mg-1.0Mn), Mater. Sci. Forum. 396–402 (2002) 1437–1442. doi:10.4028/www.scientific.net/MSF.396-402.1437.

[25] D.R. Baer, C.F. Windisch, M.H. Engelhard, M.J. Danielson, R.H. Jones, J.S. Vetrano, Influence of Mg on the corrosion of Al, J. Vac. Sci. Technol. a-Vacuum Surfaces Film. 18 (2000) 131–136. doi:10.1116/1.582129.

[26] Y. Zhu, Characterization of beta phase growth and experimental validation of long term thermal exposure sensitization of AA5XXX alloys, University of Utah, 2013. http://adsabs.harvard.edu/abs/2013PhDT........12Z.

[27] R. Goswami, R.L. Holtz, Transmission Electron Microscopic Investigations of Grain Boundary Beta Phase Precipitation in Al 5083 Aged at 373 K (100 °C), Metall. Mater. Trans. A. 44 (2012) 1279–1289. doi:10.1007/s11661-012-1166-9.

[28] R. Zhang, S.P. Knight, R.L. Holtz, R. Goswami, C.H.J. Davies, N. Birbilis, A survey of sensitization in 5xxx series aluminum alloys, Corrosion. 72 (2016) 144–159. doi:10.5006/1787.

[29] P.M. Natishan, W.E.O. Grady, E. Mccafferty, D.E. Ramaker, Chloride Uptake by Oxide Covered Aluminum as Determined by X-Ray Photoelectron and X-Ray Absorption Spectroscopy, J. Electrochem. Soc. 146 (1999) 1737–1740. doi:10.1149/1.1391835.

[30] E. McCafferty, Sequence of steps in the pitting of aluminum by chloride ions, Corros. Sci. 45 (2003) 1421–1438. doi:10.1016/S0010-938X(02)00231-7.

[31] E. McCafferty, The electrode kinetics of pit initiation on aluminum, Corros. Sci. 37 (1995) 481–492. doi:10.1016/0010-938X(94)00150-5.

[32] Y. Lee, R.P. Gangloff, Measurement and modeling of hydrogen environment-assisted cracking of ultra-high-strength steel, Metall. Mater. Trans. A Phys. Metall. Mater. Sci. 38 A (2007) 2174–2190. doi:10.1007/s11661-006-9051-z.

[33] B.F. Brown, Stress Corrosion Cracking in High Strength Alloys, in: J.C. Scully (Ed.), Theory SCC Alloy., NATO Scientific Affairs Division, Brussels, Belgium, 1971: p. 186.

[34] P. Buckley, B. Placzankis, J. Beatty, R. Brown, Characterization of the Hydrogen Embrittlement Behavior of High-Strength Steels for Army Applications, in: Corros. 94, NACE International, Houston, TX, 1994: p. Paper No. 57.

[35] G. Burnell, D. Hardie, R.N. Parkins, Stress corrosion and hydrogen embrittlement of two precipitation hardening stainless steels, Br. Corros. J. 22 (1987) 229–237.

[36] K.B. Das, W.G. Smith, R.W. Finger, J.N. Masters, Hydrogen embrittlement of cathodically protected 15-5 PH stainless steel, in: Proc. 2nd Int. Congr. Hydrog. Met., Pergamon, Oxford, UK, 1977.

[37] P.S. Tyler, M. Levy, L. Raymond, Investigation of the conditions for crack propagation and arrest under cathodic polarization by rising step load bend testing, Corrosion. 47 (1991) 82–87. doi:10.5006/1.3585857.

[38] D.P. Dautovich, S. Floreen, The stress corrosion and hydrogen embrittlement behavior of maraging steels, in: NACE-5 Stress Corros. Crack. Hydrog. Embrittlement Iron Base Alloy., NACE International, Houston, TX, 1977: p. 82.

[39] B.A. Kehler, J.R. Scully, Predicting the effect of applied potential on crack tip hydrogen concentration in low-alloy martensitic steels, Corrosion. 64 (2008) 465–477. doi:10.5006/1.3278484.

[40] W.H. Hartt, C.C. Kumria, R.J. Kessler, Influence of potential, chlorides, pH, and

precharging time on embrittlement of cathodically polarized prestressing steel, Corrosion. 49 (1993) 377–385. doi:10.5006/1.3316064.

[41] R. Nishimura, The effect of potential on stress corrosion cracking of type 316 and type 310 austenitic stainless steels, Corros. Sci. 34 (1993) 1463–1473. doi:10.1016/0010-938X(93)90241-8.

[42] L.M. Young, G.A. Young, J.R. Scully, R.P. Gangloff, Aqueous environmental crack propagation in high-strength beta titanium alloys, Metall. Mater. Trans. A. 26 (1995) 1257–1271. doi:10.1007/BF02670620.

[43] D.G. Kolman, J.R. Scully, Understanding the potential and pH dependency of high-strength β-titanium alloy environmental crack initiation, Metall. Mater. Trans. A Phys. Metall. Mater. Sci. 28 (1997) 2645–2656. doi:10.1007/s11661-997-0021-x.

[44] Z.D. Harris, J.D. Dolph, G.L. Pioszak, B.C. Rincon Troconis, J.R. Scully, J.T. Burns, The Effect of Microstructural Variation on the Hydrogen Environment-Assisted Cracking of Monel K-500, Metall. Mater. Trans. A Phys. Metall. Mater. Sci. (2016) 1–23. doi:10.1007/s11661-016-3486-7.

[45] R. Gangloff, H. Ha, J. Burns, J. Scully, Measurement and Modeling of Hydrogen Environment-Assisted Cracking in Monel K-500, Metall. Mater. Trans. A. 45 (2014) 3814–3834.

[46] N. Totsuka, Z. Szklarska-Smialowska, Effect of Electrode Potential on the Hydrogen-Induced Igscc of Alloy 600 in an Aqueous Solution At 350 C., Corrosion. 43 (1987) 734–738. doi:10.5006/1.3583860.

[47] J.R. Scully, G.A. Young, S. Smith, Hydrogen Embrittlement of Aluminum and Aluminum-Based Alloys, in: R.P. Gangloff, B.P. Somerday (Eds.), Gaseous Hydrog. Embrittlement Met. Energy Technol., 1st ed., Woodhead Publishing Limited, Cambridge, UK, 2012: pp. 707–768.

[48] X. yan Zhang, R. guo Song, B. Sun, H. Lu, C. Wang, Effects of applied potential on the stress corrosion cracking behavior of 7003 aluminum alloy in acid and alkaline chloride solutions, Int. J. Miner. Metall. Mater. 23 (2016) 819–826. doi:10.1007/s12613-016-1296-y.

[49] A. Zielinski, Hydrogen-enhanced stress corrosion cracking of aluminium alloys, Mater. Sci. 34 (1999) 20–26.

[50] D. Hardie, N.J.H. Holroyd, R.N. Parkins, Reduced ductility of high-strength aluminum alloy during or after exposure to water, Met. Sci. 13 (1979) 603–610.

[51] T.H. Nguyen, B.F. Brown, R.T. Foley, On the Nature of the Occluded Cell in the Stress Corrosion Cracking of AA 7075-T651—Effect of Potential, Composition, Morphology, Corrosion. 38 (1982) 319–326. doi:10.5006/1.3621692.

[52] J.A. Lillard, R.G. Kelly, R.P. Gangloff, Effect Of Electrode Potential On Stress Corrosion Cracking And Crack Chemistry Of A Nickel-Base Superalloy, in: Corros. 97, NACE International, Houston, TX, 1997.

[53] D.G. Enos, A.J. Williams, G.G. Clemeña, J.R. Scully, Impressed-Current Cathodic Protection of Steel-Reinforced Concrete Pilings: Protection Criteria and the Threshold for Hydrogen Embrittlement, Corrosion. 54 (1998) 389–402. doi:10.5006/1.3284867.

[54] X. Li, J. Zhang, Y. Wang, B. Li, P. Zhang, X. Song, Effect of cathodic hydrogen-charging current density on mechanical properties of prestrained high strength steels, Mater. Sci. Eng. A. 641 (2015) 45–53. doi:10.1016/j.msea.2015.06.003.

[55] S. Hinotani, Y. Ohmori, F. Terasaki, Effect of Nickel on Hydride Formation and

Hydrogen Embrittlement in Ni - Cr - Fe Alloys, Mater. Sci. Eng. 74 (1985) 119–131.
[56] O. Barrera, D. Bombac, Y. Chen, T.D. Daff, P. Gong, D. Haley, Understanding and mitigating hydrogen embrittlement of steels : a review of experimental , modelling and design progress from atomistic to continuum, J. Mater. Sci. 53 (2018) 6251–6290. doi:10.1007/s10853-017-1978-5.
[57] E. van de Ven, H. Koelmans, The Cathodic Corrosion of Aluminum, J. Electrochem. Soc. (1976) 143–144.
[58] S.J. Kim, M.S. Han, S.K. Jang, Electrochemical characteristics of Al-Mg alloy in seawater for leisure ship: Stress corrosion cracking and hydrogen embrittlement, Korean J. Chem. Eng. 26 (2009) 250–257. doi:10.1007/s11814-009-0042-9.
[59] S.-J. Kim, Evaluating the electrochemical properties in the protection potential of material for use in Al vessels in seawater, Mater. Sci. Forum. 510–511 (2006) 158–161. doi:10.4028/www.scientific.net/MSF.510-511.158.
[60] J.W. Watson, Y.Z. Shen, M. Meshii, Effect of cathodic charging on the mechanical properties of aluminum, Metall. Mater. Trans. A. 19 (1988) 2299–2304. doi:10.1007/BF02645053.
[61] M. Pourbaix, Atlas of Electrochemical Equilibria in Aqueous Solutions, National Association of Corrosion Engineers, 1974.
[62] P. Plagemann, J. Weise, A. Zockoll, Zinc-magnesium-pigment rich coatings for corrosion protection of aluminum alloys, Prog. Org. Coatings. 76 (2013) 616–625. doi:10.1016/j.porgcoat.2012.12.001.
[63] A.M. Simões, D. Battocchi, D.E. Tallman, G.P. Bierwagen, SVET and SECM imaging of cathodic protection of aluminium by a Mg-rich coating, Corros. Sci. 49 (2007) 3838–3849. doi:10.1016/j.corsci.2007.03.045.
[64] X. Wang, G.S. Frankel, Protection Mechanism of Al-Rich Epoxy Primer on Aluminum Alloy 2024-T3, Corrosion. 73 (2017) 1192–1195.
[65] J. Wang, Y. Zuo, Y. Tang, The study on Mg-Al rich epoxy primer for protection of aluminum alloy, Int. J. Electrochem. Sci. 8 (2013) 10190–10203.
[66] A. Stander, NADC-MA-7063: Investigation of metallic pigments as corrosion preventatives in aircraft primers, 1970.
[67] A.D. King, B. Kannan, J.R. Scully, Environmental degradation of a mg-rich primer in selected field and laboratory environments: Part 1-without a topcoat, Corrosion. 70 (2014) 512–535. doi:10.5006/0988.
[68] R.J. Santucci Jr., B. Kannan, J.R. Scully, Electrochemical diagnostic cycle testing on magnesium and magnesium oxide-pigmented primers on 2024-T351, Corrosion. 74 (2017) 96–111. doi:10.5006/2547.
[69] M.E. Nanna, G.P. Bierwagen, Mg-rich coatings: A new paradigm for Cr-free corrosion protection of Al aerospace alloys, J. Coatings Technol. Res. 1 (2004) 69–80. doi:10.1007/s11998-004-0001-7.
[70] M.E. Nanna, G.P. Bierwagen, D. Battocchi, Magnesium Rich Coatings and Coating Systems, US 2007/0128351 A1, 2007. doi:10.1016/j.micromeso.2003.09.025.
[71] D. Battocchi, A.M. Simões, D.E. Tallman, G.P. Bierwagen, Electrochemical behaviour of a Mg-rich primer in the protection of Al alloys, Corros. Sci. 48 (2006) 1292–1306. doi:10.1016/j.corsci.2005.04.008.
[72] R.J. Santucci, M.E. McMahon, J.R. Scully, Utilization of chemical stability diagrams for improved understanding of electrochemical systems: evolution of solution chemistry

towards equilibrium, Npj Mater. Degrad. 2 (2018) 1. doi:10.1038/s41529-017-0021-2.

[73] H. Takahashi, K. Fujiwara, M. Seo, The cathodic polarization of aluminum covered with anodic oxide films in a neutral borate solution-II. Film breakdown and pit formation, Corros. Sci. 36 (1994) 689–699. doi:10.1016/0010-938X(94)90074-4.

[74] R. Gundersen, K. Nisancioglu, Cathodic protection of aluminum in seawater, Corrosion. 46 (1990) 279–285. doi:10.5006/1.3585103.

[75] M. Mokaddem, P. Volovitch, F. Rechou, R. Oltra, K. Ogle, The anodic and cathodic dissolution of Al and Al-Cu-Mg alloy, Electrochim. Acta. 55 (2010) 3779–3786. doi:10.1016/j.electacta.2010.01.079.

[76] R.P. Gangloff, D.C. Slavik, S. Piascik, R.H. Van Stone, Direct current electrical potential measurement of the growth of small cracks, in: J.M. Larsen, J.E. Allison (Eds.), Small-Crack Test Methods, American Society for Testing and Materials, Philadelphia, PA, 1992: pp. 116–168.

[77] L.H. Gevantman, Solubility of Selected Gases in Water, in: W.M. Haynes (Ed.), CRC Handb. Chem. Physics, 91st ed., Taylor and Francis, Boca Raton, FL, 2010: pp. 80–83.

[78] A.D. King, N. Birbilis, J.R. Scully, Accurate electrochemical measurement of magnesium corrosion rates; A combined impedance, mass-loss and hydrogen collection study, Electrochim. Acta. 121 (2014) 394–406. doi:10.1016/j.electacta.2013.12.124.

[79] ASTM E1447-16: Standard Test Method for Determination of Hydrogen in Titanium and Titanium Alloys by the Inert Gas Fusion Thermal Conductivity Method 1, ASTM Int. (2016). doi:10.1520/E1447-09R16.2.

[80] ASTM International, Standard Practice for Preparing , Cleaning , and Evaluating Corrosion Test, Significance. 90 (1999) 1–9. doi:10.1520/G0001-03R11.2.

[81] M.E. McMahon, J.R. Scully, J.T. Burns, Erratum to: Mitigation of Intergranular Stress Corrosion Cracking in Al–Mg by Electrochemical Potential Control, J. Miner. Met. Mater. 69 (2017) 1724–1726. doi:10.1007/s11837-017-2432-5.

[82] M. Ichiba, K. Takai, J. Sakai, Effects of Test Conditions on Corrosion Reactions and Hydrogen Absorption in Hydrogen Embrittlement Tests Using an Ammonium Thiocyanate Solution, ISIJ Int. 56 (2016) 397–404. doi:10.2355/isijinternational.ISIJINT-2015-288.

[83] A. Yonezu, R. Kusano, X. Chen, On the mechanism of intergranular stress corrosion cracking of sensitized stainless steel in tetrathionate solution, J. Mater. Sci. 48 (2013) 2447–2453.

[84] S. Tagaki, T. Yuki, Application of NH4SCN Aqueous Solution to Hydrogen Embrittlement Resistance Evaluation of Ultra-high Strength Steels, ISIJ Int. 52 (2010) 329–331.

[85] P. Novak, R. Yuan, B.P. Somerday, P. Sofronis, R.O. Ritchie, A statistical, physical-based, micro-mechanical model of hydrogen-induced intergranular fracture in steel, J. Mech. Phys. Solids. 58 (2010) 206–226. doi:10.1016/j.jmps.2009.10.005.

[86] E. Akiyama, S. Li, Electrochemical hydrogen permeation tests under galvanostatic hydrogen charging conditions conventionally used for hydrogen embrittlement study, Corros. Rev. 34 (2016) 103–112. doi:10.1515/corrrev-2015-0049.

[87] R.D. Kane, M.S. Cayard, ROLES OF H2S IN THE BEHAVIOR OF ENGINEERING ALLOYS: A REVIEW OF LITERATURE AND EXPERIENCE, in: Corros. 98, 1998: pp. 1–28.

[88] F.P. Ford, Status of Research on Environmentally Assisted Cracking in LWR Pressure

Vessel Steels, J. Press. Vessel Technol. 110 (1988) 115–128.

[89] F.P. Ford, M.J. Povich, The Effect of Oxygen Temperature Combinations on the Stress Corrosion Susceptibility of Sensitized Type 304 Stainless Steel in High Purity Water, Corrosion. 35 (1979) 569–574.

[90] Z. Kuang, The Stress Field Near the Crack Tip and the Fracture Criterion, Eng. Fract. Mech. 16 (1982) 19–33.

[91] M. Zappalorto, P.A. Carraro, Stress distributions for blunt cracks and radiused slits in anisotropic plates under in-plane loadings, Int. J. Solids Struct. 56 (2015) 136–141. doi:10.1016/j.ijsolstr.2014.11.024.

[92] G.E. Beltz, D.M. Lipkin, L.L. Fischer, Role of crack blunting in ductile versus brittle response of crystalline materials, Phys. Rev. Lett. 82 (1999) 4468–4471. doi:10.1103/PhysRevLett.82.4468.

[93] L. L. Fischer, G. E. Beltz, The effect of crack blunting on the competition between dislocation nucleation and cleavage, J. Mech. Phys. Solids. 49 (2001) 635–654. http://www.sciencedirect.com/science/article/B6TXB-42G0KKY-8/2/c02583bdbcdcbdc4187fe711c1c727d0.

[94] M. Creager, P.C. Paris, Elastic Field Equations for Blunted Cracks in Reference to Stress Corrosion Cracking, Int. J. Fract. Mech. 3 (1967) 247–252.

[95] M.E. McMahon, J.R. Scully, J.T. Burns, Mitigation of Intergranular Cracking in Al-Mg Alloys via Zn-Based Electrode Potential Control in Sodium Chloride Solution, Corrosion. (2019). In Review.

[96] A. Aballe, M. Bethencourt, F.J. Botana, M.J. Cano, M. Marcos, Localized alkaline corrosion of alloy AA5083 in neutral 3.5% NaCl solution, Corros. Sci. 43 (2001) 1657–1674. doi:10.1016/S0010-938X(00)00166-9.

[97] A. Aballe, M. Bethencourt, F.J. Botana, M.J. Cano, M. Marcos, Influence of the cathodic intermetallics distribution on the reproducibility of the electrochemical measurements on AA5083 alloy in NaCl solutions, Corros. Sci. 45 (2003) 161–180. doi:10.1016/S0010-938X(02)00067-7.

[98] G.A. DiBari, H.J. Read, Electrochemical behavior of high purity aluminum in chloride containing solutions, Corrosion. 27 (1971) 483–493.

[99] T.T.M. Tran, B. Tribollet, E.M.M. Sutter, New insights into the cathodic dissolution of aluminium using electrochemical methods, Electrochim. Acta. 216 (2016) 58–67. doi:10.1016/j.electacta.2016.09.011.

[100] C.B. Bargeron, R.C. Benson, Analysis of the gases evolved during the pitting corrosion of aluminum in various electrolytes, J. Electrochem. Soc. 127 (1980) 2528–2530.

[101] J.P. Popic, D.M. Draz, Corrosion rates and negative difference effects for Al and some Al alloys, J. Appl. Electrochem. 29 (1999) 43–50. https://link.springer.com/content/pdf/10.1023/A:1003447018115.pdf.

[102] W.M. Carroll, C.B. Breslin, Stability of passive films formed on aluminium in aqueous halide solutions, Br. Corros. J. 26 (1991).

[103] H. Böhni, H.H. Uhlig, Environmental Factors Affecting the Critical Pitting Potential of Aluminum, J. Electrochem. Soc. 116 (1969) 906. doi:10.1149/1.2412167.

[104] E. McCafferty, Introduction to Corrosion Science, Springer, New York, NY, 2010.

[105] C. Mi, N. Lakhera, D.A. Kouris, D.A. Buttry, Repassivation behaviour of stressed aluminium electrodes in aqueous chloride solutions, Corros. Sci. 54 (2012) 10–16. doi:10.1016/j.corsci.2011.08.053.

[106] V.A. Marichev, An ambiguity of the cathodic polarization effect on crack growth during stress corrosion cracking of aluminum alloys, Werkstoffe Und Korrosion. 34 (1983) 62–67.

[107] H. Suzuki, D. Kobayashi, N. Hanada, K. Takai, Y. Hagihara, Existing State of Hydrogen in Electrochemically Charged Commercial-Purity Aluminum and Its Effects on Tensile Properties, Mater. Trans. 52 (2011) 1741–1747. doi:10.2320/matertrans.M2011035.

[108] E. Akiyama, S. Li, Electrochemical hydrogen permeation tests under galvanostatic hydrogen charging conditions conventionally used for hydrogen embrittlement study, Corros. Rev. 34 (2015).

[109] M.L.C. Lim, Intergranular Corrosion Propagation in Sensitized Al-Mg Alloys, The University of Virginia, 2016.

[110] E. Rodil, J.H. Vera, Individual activity coefficients of chloride ions in aqueous solutions of MgCl2, CaCl2 and BaCl2 at 298.2 K, Fluid Phase Equilib. 188 (2001) 15–27.

[111] F.E. Critchfield, J.B. Johnson, Effect of Neutral Salts on the pH of Acid Solutions, Anal. Chem. 31 (1959) 570–572. https://pubs.acs.org/sharingguidelines (accessed January 18, 2019).

[112] S.M. Moon, S.I. Pyun, The corrosion of pure aluminium during cathodic polarization in aqueous solutions, Corros. Sci. 39 (1997) 399–408. doi:10.1016/S0010-938X(97)83354-9.

[113] R.D. Armstrong, V.J. Braham, The mechanism of aluminium corrosion in alkaline solutions, Corros. Sci. 38 (1996) 1463–1471. doi:10.1016/0010-938X(96)00037-6.

[114] R.L. Liu, S. Thomas, J.R. Scully, G. Williams, N. Birbilis, An experimental survey of the cathodic activation of metals including Mg, Sc, Gd, La, Al, Sn, Pb, and Ge in dilute chloride solutions of varying pH, Corrosion. 73 (2017) 494–505. doi:10.5006/2282.

[115] C. Laurent, F. Scenini, T. Monetta, F. Bellucci, M. Curioni, The contribution of hydrogen evolution processes during corrosion of aluminium and aluminium alloys investigated by potentiodynamic polarisation coupled with real-time hydrogen measurement, Npj Mater. Degrad. 1 (2017) 1–7. doi:10.1038/s41529-017-0011-4.

[116] W.K. Johnson, Recent developments in the pitting corrosion of aluminum, Br. Corros. J. 6 (1971) 200–204.

[117] H. Ding, L.H. Hihara, Galvanic corrosion and localized degradation of aluminum-matrix composites reinforced with boron carbide particulates, ECS Trans. 16 (2009) 39–53.

[118] Y. Zhu, K. Sun, G.S. Frankel, Intermetallic Phases in Aluminum Alloys and Their Roles in Localized Corrosion, J. Electrochem. Soc. 165 (2018) C807–C820. doi:10.1149/2.0931811jes.

[119] S.P. Lynch, No Title, in: R.P. Gangloff, B.P. Somerday (Eds.), Gaseous Hydrog. Embrittlement Mater. Energy Technol. Vol 1., Woodhead Publishing Limited, Cambridge, UK, 2012: pp. 274–346.

[120] R.P. Gangloff, Hydrogen asisted cracking of high strength alloys, in: J. Petit, P. Scott (Eds.), Compr. Struct. Integr. Environ. Assist. Fract., Elsevier, New York, NY, 2003: pp. 31–101.

CHAPTER 3

Assessment of Zn-Rich Primers for the Galvanic Protection of Highly Sensitized AA5456-H116

3.1 New Criteria for Substrate Protection Against Stress Corrosion Cracking in Al-Mg Alloys Based on Non-Polarizability of Zn-Rich Primers

M. E. McMahon [ǂ, *], J. T. Burns[*], and J. R. Scully[*]

[*] Center for Electrochemical Science and Engineering, Department of Materials Science and Engineering, University of Virginia, 395 McCormick Rd., Charlottesville, VA 22904
[ǂ] Corresponding author. E-mail: mm5kn@virginia.edu

Keywords: aluminum, sacrificial protection, zinc primer, polarizability, stress corrosion cracking, electrochemical impedance spectroscopy

3.1.1 Abstract

One inorganic and three organic Zn-rich primers (ZRPs) without a pretreatment or a topcoat were evaluated on highly sensitized aluminum alloy 5456-H116 in 0.6 M NaCl for their ability to suppress intergranular corrosion (IGC) and intergranular stress corrosion cracking (IG-SCC) based on the achievement and maintenance of protective potentials in simulated galvanic coupling conditions. These evaluations utilized a combination of existing criteria (e.g. the need to establish an intermediate cathodic potential) and additional new criteria based on fast anodic response and low polarizability. Ethyl silicate, epoxy, epoxy polyamide, and polyurethane resins were considered. Accelerated electrochemical cycle testing in full 0.6 M NaCl immersion demonstrated that anodic charge usage in the candidate ZRPs was dependent on the pore resistance rather than on theoretical anodic charge capacity. Electrochemical impedance spectroscopy modeling of cycle testing data demonstrated that the ZRPs with low pore resistance also had the fastest anodic discharge time. Galvanostatic pulse testing demonstrated that the ZRPs with the highest anodic charge usage and low pore resistance were also the least polarizable. These analyses propose relevant metrics to evaluate the effectiveness of Zn-rich primers in suppressing IGC/IG-SCC on highly sensitized 5456-H116 in aggressive alternate immersion environment.

3.1.2 **Introduction**

Modern AA5xxx-series alloys are increasingly used to replace heavier steel components in marine structures due to their high strength-to-weight ratio and general corrosion resistance [1,2]. However, these components have experienced significant in-service intergranular corrosion (IGC) and stress corrosion cracking (IG-SCC) degradation after only 1-2 years in service [3,4]. AA5xxx-series alloys are solid solution strengthened by a supersaturation of the Al- (α) matrix with 4-5 wt. % Mg. This Mg addition can lead to facile precipitation of the β phase (Al_3Mg_2) on the grain boundaries after prolonged exposure to in-service temperatures as low as 40°C; this process is termed sensitization [5]. The β phase is highly anodic to the matrix thus in aggressive (e.g. aqueous chloride) environments, rapid dissolution can occur to cause IGC [3] and/or IG-SCC in the presence of a stress [6,7]. The extent of sensitization is typically quantified by the ASTM G-67 Nitric Acid Mass Loss Test (NAMLT) [8], making this metric a rough proxy for IGC / IG-SCC susceptibility. Materials are rated as resistant at NAMLT < 15 mg/cm^2, intermediate at 15 – 25 mg/cm^2, and susceptible at > 25 mg/cm^2 [3,8–11], with long-term sensitization at low temperature often achieving NAMLT values as high as 65-70 mg/cm^2 [12,13].

Sensitized Al-Mg alloys are highly susceptible to IGC and IG-SCC at potentials between the β phase pitting potential ($E_{pit\,(\beta)}$, -0.92 V_{SCE} in 0.6 M NaCl) and the α matrix pitting potential ($E_{pit\,(\alpha)}$, -0.72 V_{SCE} in 0.6 M NaCl), and susceptibility worsens at potentials more positive than $E_{pit\,(\alpha)}$ [3,14]. The extent of IGC produced in Al-Mg alloy 5456-H116 (NAMLT 65 mg/cm^2) during 100 hours of galvanostatic hold is illustrated in Figure 3.1. The IG-SCC behavior is hypothesized to be governed by a coupled anodic dissolution process (of the β phase and the α matrix), which also

Applied Current Density (A/cm^2)	Potential Achieved in the Last 50 Hours	Intergranular Corrosion Damage
3 x 10^{-3}	**-0.76 V$_{SCE}$**	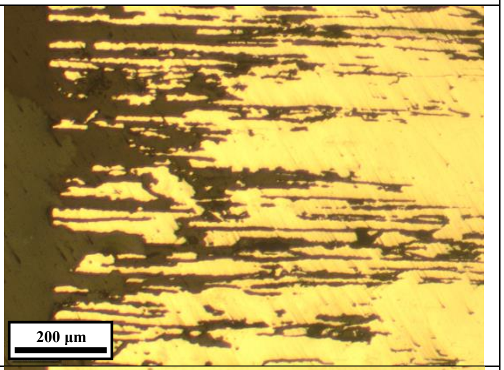
8 x 10^{-4}	**-0.79 V$_{SCE}$**	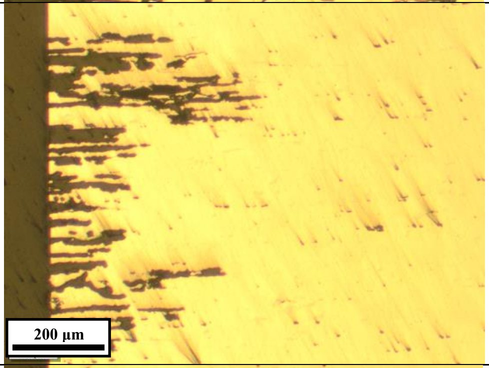
1 x 10^{-5}	**-0.85 V$_{SCE}$**	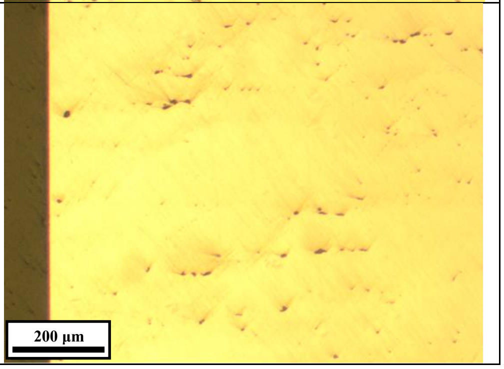

Figure 3.1: Intergranular corrosion damage in NAMLT 65 mg/cm^2 AA5456-H116 following 100 hours' exposure in 0.6 M NaCl at the specified current density.

catalyzes the formation of an aggressive acidified local crack tip chemistry that facilitates the enhanced generation of crack tip H and enables embrittlement in the fracture process zone [15–20]. Intermediate levels of cathodic protection effectively mitigate the anodic dissolution of α and β to disrupt the formation of the occluded, acidified crack tip chemistry [14–16]. Overly cathodic polarization, which may be considered as polarization below -1.1 V_{SCE}, is undesired due to the localized cathodic corrosion that occurs on AA5456-H116 around Al(Mn,Fe,Cr) particles on the alloy surface [21,22]. Potentiostatically-controlled fracture testing has demonstrated up to three orders of magnitude crack growth rate reduction by maintaining an intermediate level of cathodic protection on NAMLT 65 mg/cm^2 AA5456-H116 in 0.6 M NaCl [14,23]. Thus, Al-Mg alloy degradation through IGC / IG-SCC is suppressed at intermediate cathodic potentials more negative than $E_{pit\ (\beta)}$. The efficacy of this potential control raises the possibility that a metal-rich primer (MRP) which can achieve intermediate cathodic potential can protect Al-Mg alloys.

Specifically-designed metal-rich coatings applied to AA5xxx-series alloy surfaces could achieve intermediate cathodic potentials below $E_{pit\ (\beta)}$, which would reduce maintenance costs and improve alloy service life if effective in mitigating IGC and IG-SCC. However, inherent differences exist when utilizing an MRP instead of a potentiostat for potential-based control, such as the necessary galvanic coupling between the anodic particles and the substrate and the increasing area ratio as crack or fissure growth occurs (the MRP is a non-infinite sacrificial anode, unlike a potentiostat). In order to maintain the necessary cathodic protection under these dynamic conditions, the MRP must accomplish stable galvanic coupling, high anodic charge output, and *fast anodic response time* to achieve timely substrate protection against IGC / IG-SCC advance. These capabilities may be understood through assessment of polarizability, which measures the ability of an MRP to sustain a cathodic protection near the open circuit potential (OCP) of the primer following the application of anodic current (such as when crack growth occurs). Pure Zn-rich primer (ZRP) systems (which are not typically considered for Al protection due to the similarity of their open circuit potentials (low ΔOCP) [24,25]) may meet these requirements due to their non-polarizability and high anodic charge output compared to anodic particles such as Mg (OCP of -1.65 V_{SCE} in 0.6 M NaCl) [26–33]. Furthermore, the OCP of pure Zn (-1.09 V_{SCE} in 0.6 M NaCl) lies within an electrode potential range of low IGC/IG-SCC susceptibility for AA5xxx-series alloys (more negative than $E_{pit(\alpha)}$ and $E_{pit(\beta)}$) [3,14], so achievement of this OCP through the use of high Zn loading does not pose a risk for cathodically-driven corrosion or hydrogen embrittlement on aluminum [14,15,34,35]. However, ZRPs have not been critically examined for protection of Al-Mg alloy substrates, and numerous formulation combinations exist to meet different performance criteria.

Two primary types of ZRP exist, organic and inorganic, which both have characteristic advantages and disadvantages in use [36–38]. Depending on the choice of resin, the galvanic protection mechanism is often maximized through the Zn particle loading of 83-91% weight concentration, which enables thorough Zn particle connectivity while maintaining primer adhesion and quality of spray application [36,39]. For inorganic Zn-rich primer (IOZRP) formulations, performance in moderate to aggressive marine atmospheric conditions (as pertinent to coastal oil pipelines and offshore drilling platforms) is enhanced by their insensitivity to UV degradation and high temperatures (up to 400°C) [37]. Due in part to a unique curing process involving the natural formation of a Zn silicate cement matrix, IOZRP systems typically exhibit better initial corrosion protection, toughness, and abrasion resistance than organic resin-based Zn-rich primer systems (OZRP) [36]. IOZRPs are also characteristically brittle due to the lack of flexible organic resin, and inadequate curing to bond the Zn particles to the substrate can result in increased risk of flaking [36,40]. In contrast, OZRPs are less sensitive to moisture or surface preparation, have been shown to offer moderate cathodic protection on steel substrates for longer periods of time than IOZRP [41], and are known for their durable substrate adhesion and flexibility to enable greater versatility in coating application procedures. However, due to their resin type, OZRPs are affected by temperature, with either low or high temperatures negatively affecting optimal primer application, and they have poor resistance to UV degradation, which necessitates the use of a topcoat in service that may stifle the degree of achieved galvanic protection [32,42]. Previous work on ZRP protection on steel may offer further guidance on ZRP selection and evaluation methods.

Extensive work exists in the literature concerning the galvanic protection of steel that may be utilized to inform the interpretation of ZRP performance on Al-Mg. Baseline evaluations have measured ZRP OCP on steel substrates throughout atmospheric or full immersion exposure for up to 5 years to evaluate the effect of Zn particle concentration, resin type, and ZRP thickness on primer longevity [39,43–45], which have demonstrated that inorganic ethyl silicate ZRPs achieve the highest magnitude of potential control and that thicker ZRPs may perform better due to having greater available Zn quantity [44,45]. A combination of potential- and electrochemical impedance spectroscopy (EIS)-based methods have been utilized to evaluate the mechanisms underlying ZRP performance on steel as well, which may be similarly applied to studying ZRPs on Al [41,46–55]. Nonlinear equivalent circuit fitting of data obtained through as much as 10 years atmospheric exposure has demonstrated an importance of understanding ZRP pore resistance and capacitance on steel, as these metrics are influenced by the primer formulation (resin type, Zn particle volume concentration (PVC), primer thickness, Zn particle size distribution) and contribute to the achievement of protective potentials [41,46,48,56]. The combination of these works thoroughly evidences that the sacrificial anode-based cathodic protection achieved by ZRPs on steel may be logically interpreted based on mixed potential theory, thus these works provide considerable insight and assist the prediction of these primers' performance on Al substrates. These prior works also demonstrate proven evaluation methods that may be adapted, and metrics that may be built upon, to assess ZRP performance for IGC/IG-SCC mitigation.

The effective evaluation of ZRP performance on a less demanding Al substrate (lower ΔOCP (difference between the Al OCP and the Zn OCP), which dictates the conditions for ZRP particle oxidation rate and depletion in non-defected coating scenarios), but in more demanding dynamic galvanic coupling scenarios (increasing cathodic surface area requiring anodic charge output by the ZRP to remain in the passive state), requires a union of previously developed experimental methods to characterize new parameters of importance. Steel applications have a characteristically higher ΔOCP and present a greater driving force for Zn oxidation than would be present in Al alloy applications [44,57,58]. Therefore, Al substrates may subject ZRPs to less aggressive conditions in terms of substrate OCP that may further primer longevity, however the mitigation of phenomena such as IG-SCC requires rapid anodic response to dynamic galvanic coupling conditions. In other words, the application is challenging by an increased area of 5456-H116 created as a function of time as IG-SCC proceeds.

Suppression of IGC *and* IG-SCC presents a more challenging goal than the typical static protection of an underlying substrate against uniform corrosion. Thus, the objective of the present work was to develop a new combination of test methods to evaluate the following metrics pertinent to IGC/IG-SCC mitigation: OCP, magnitude and consistency of anodic charge output, pore resistance, anodic response time (also known as capacitive discharge delay), and polarizability. These evaluations were conducted across a variety of ZRPs, with consideration of secondary barrier effects due to corrosion product formation that may be detrimental to galvanic performance. These metrics and the methods through which they are quantified will be described in the sections to follow. Systematic evaluation of sacrificial anode-based cathodic protection as well as secondary barrier formation established by four commercial ZRPs of varying PVC and resin type on highly sensitized (NAMLT 65 mg/cm^2) 5456-H116 was performed through laboratory accelerated cycle testing and cyclic galvanostatic pulse analysis in 0.6 M NaCl immersion. These analyses set a baseline towards determining key coating attributes necessary to establish effective, long-lasting cathodic protection for IGC / IG-SCC suppression on Al-Mg naval alloys in aggressive marine service environments.

3.1.3 **Material and Methods**

3.1.3.1 ***Materials: 5456-H116 and Zinc-Rich Primers***

A 57-mm thick plate of non-recrystallized 5456-H116 (UNS A95456) plate was exposed in the S-T orientation; the microstructural character and composition are reported elsewhere [18]. Rectangular plates of 1 mm thickness, 72 mm length, and 63 mm width were excised and sensitized to NAMLT 65 mg/cm^2 via heating at 100°C for 14 days [18]. Following alloy sensitization, the samples were sonicated in isopropyl alcohol and dried using static-free absorptive cloth prior to spray-coating the Al surfaces using a spraying distance of 200 to 300 mm and 50% overlap. Luna Innovations, Inc. performed all cold spraying of the selected commercial ZRPs using thoroughly agitated, mixed formulations. As shown in Table 1, three of these commercial ZRPs are products of Sherwin Williams, and the fourth is produced by NCP Coatings in Niles, Michigan. The resins/Zn PVC combinations tested are the following, where the designation for identifying each coating is: inorganic ethyl silicate resin (EthylSil) at Zn PVC of 76% (IOZRP (EthylSil,76%)); organic epoxy polyamide resin (EPA) at Zn PVC of 65% (OZRP (EPA,65%)); organic epoxy resin at Zn PVC of 57% (OZRP (Epoxy,57%)); and organic polyurethane (U) resin at Zn PVC of 83%

(OZRP (U,83%)) (Table 3.I). No pretreatments or topcoats were considered, and all coatings were tested as-received and intact, ie. with no added defects (such as scribes).

Table 3.I: Zn-Rich primer characteristics studied in this system

Code	**Zn-Rich Primer Commercial Name**	**Provider**	**Vehicle**	**PWC (%)**	**PVC (%)**	**Thickness (µm)**	**Particle Diameter (µm)**
IOZRP (EthylSil, 76%)	Zinc Clad® II Plus	SW	Ethyl Silicate	83	76	26.1 ± 9.3	5.0 ± 2.7
OZRP (EPA, 65%)	MIL-DTL-24441/19C Type III F159	SW	Epoxy Polyamide	85	65	47.7 ± 14.6	8.9 ± 6.6
OZRP (U,83%)	N-5751M2 Organic Zinc Rich, Single Component, Moisture Cure Primer	NCP	Polyurethane	90	83	30.5 ± 5.7	6.8 ± 2.3
OZRP (Epoxy, 57%)	CC-M30 Two Component Zinc Rich Epoxy Primer	SW	Epoxy	90	57	53.7 ± 12.1	11.2 ± 6.1

SW = Sherwin Williams, NCP = NCP Coatings, PWC = particle weight concentration in the dry film, PVC = particle volume concentration in the wet mix

3.1.3.2 *Coating Characterization: Zinc Capacity*

Scanning electron microscopy (SEM) and energy dispersive spectroscopy (EDS) were utilized for ZRP imaging and elemental analysis under magnifications of 1000x, spot size of 5 nm, and accelerating voltages of 5 kV at 10^{-7} torr H_2O (to avoid charging). The average Zn particle size was obtained by measuring 100 individual particle cross sections from each coating. This method may underestimate the Zn particle diameter due to the inability to guarantee measurement through the mid-section, however these results enable relative comparison between these ZRPs. Primer thickness values were obtained via 25 vertical thickness measurements on 5 different pristine ZRP cross-sectional areas utilizing the SEM. Cross sections were prepared by polishing with silicon carbide paper to 1200 grit in methanol (to ensure the retention of Zn particles).

Characterization of primer crystalline composition, particle oxidation, and corrosion product formation was achieved using X-Ray Diffraction (XRD), which measured the intensity of crystalline plane diffraction before and after primer exposure. X-Ray Diffraction characterizes crystalline content to a resolution limit of 3-5% volume fraction, with a typical penetration depth of up to 150 μm on Al, depending on the diffraction angle (2Θ) [59,60]. A Cu-Kα source (1.54 nm) was used on a PANalytical X'pert powder XRD with a 40-mA beam accelerated at 45 kV to perform continuous scans from 20° to 120° at a step size of 0.05°. Continual presence of a major Al peak at approximately 44.5º verified that the entirety of each ZRP was being sampled, which enabled normalization of Zn peak intensity. Zn peak intensity was affected by primer thickness, which necessitated such normalization for comparative analysis.

Crystalline as well as amorphous corrosion product identification was carried out using Raman Spectroscopy. Raman measurements were conducted using a 200 mW, 514 nm laser at 50% power under a 20x objective lens through an 1800 l/mm visible grating. Scans were accumulated twice with 15 second exposure time, and Raman shift peaks were characterized based on the RRUFF™ database [26]. Raman spectroscopic analysis complemented XRD findings by identifying oxidation products that formed in quantities less than 3-5 vol. %.

3.1.3.3 *The Accelerated Cycle Test: Anodic Charge Output and Barrier Assessment of Zn-Rich Primers*

The electrochemical characteristics of the candidate coating systems were evaluated under full immersion conditions in a controlled laboratory environment. While a wide variety of more realistic exposures have been conducted on similar ZRP systems on steel, there is a scarcity of such analysis on Al substrates (and no published findings on 5456-H116), as such these accelerated tests offer an experimental baseline [41,44,58]. Electrochemical tests were conducted with a working electrode, saturated calomel reference electrode (SCE) fitted with a Luggin capillary, and a Pt counter electrode, all immersed in 0.6 M NaCl electrolyte in quiescent, ambiently aerated conditions. Electrode potential and current were controlled and monitored with an electrochemical impedance spectroscopy (EIS)-capable potentiostat connected to a three-electrode electrochemical flat cell, as described in detail elsewhere [27,29]. The accelerated cycle test method is a well-proven evaluation of the ability of a primer to provide sacrificial cathodic protection in the presence of a remote cathode (such as an exposed 5456-H116 area at the site of a coating macrodefect) [28,29,31,61]. However, no universal relationship has been established between the number of cycles in a cycle test and coating lifetime in the field. The accelerated cycle test enables the measurement of ZRP OCP, anodic charge output magnitude and consistency, pore resistance, anodic response time, and impedance increase due to secondary barrier formation. The sequence of cycles repeatedly quantifies these metrics over time of exposure in simulated, aggressive galvanic coupling conditions. As shown in Table 3.II, cycle testing specifically consisted of a cyclic repetition of OCP, potentiostatic (PS) EIS about the OCP, and PS hold (at -0.85 V_{SCE}) stages to continuously assess the coating throughout the full immersion exposure. The entirety of one cycle

Table 3.II: The cycle test sequence utilized in the present Zn-rich primer study, where potentiostatic holds were conducted at -0.85 V_{SCE} (the AA5456-H116 open circuit potential).

Cycle	Test Stage	Duration (min)	Time Elapsed at Start of Test Listed (min)
A	OCP	60	0
	Potentiostatic EIS	30	60
	Potentiostatic Hold	10	90
B	OCP	60	100
	Potentiostatic EIS	30	160
	Potentiostatic Hold	20	190
C	OCP	60	210
	Potentiostatic EIS	30	270
	Potentiostatic Hold	40	300
D	OCP	60	340
	Potentiostatic EIS	30	400
	Potentiostatic Hold	60	430
E	OCP	60	490
	Potentiostatic EIS	30	550
	Potentiostatic Hold	120	580
F	OCP	60	700
	Potentiostatic EIS	30	760
	Potentiostatic Hold	240	790
G	OCP	60	1030
	Potentiostatic EIS	30	1090
	Potentiostatic Hold	480	1120
H	OCP	60	1600
	Potentiostatic EIS	30	1660
	Potentiostatic Hold	600	1690
I	OCP	60	2290
	Potentiostatic EIS	30	2350
	Potentiostatic Hold	600	2380
J	OCP	60	2980
	Potentiostatic EIS	30	3040
	Potentiostatic Hold	600	3070
K	OCP	60	3670
	Potentiostatic EIS	30	3730
	Potentiostatic Hold	600	3760
L	OCP	60	4360
	Potentiostatic EIS	30	4420
	Potentiostatic Hold	600	4450
M	OCP	60	5050
	Potentiostatic EIS	30	5110
	Potentiostatic Hold	600	5140
Total			5740

test consisted of 13 OCP/EIS/PS hold cycles (Cycle A through Cycle M) on an intact, macro-defect free, primer-coated AA5456-H116 specimen, which together summed to 76 hours of ZRP exposure at -0.85 V_{SCE}, and 20 hours at the ZRP OCP. This accelerated testing was performed three times for each ZRP for statistical analysis. The cycle test was also performed on bare and epoxy-coated 5456-H116 as an experimental baseline to compare barrier properties of a primer with and without sacrificial Zn particles.

During the OCP stage of the cycle testing, the level and continuity of the galvanic coupling between the ZRP and the sensitized 5456-H116 is evident by measuring the potential of the ZRP-coated 5456-H116 as the working electrode. Where appropriate, the OCP of the system will be referred to as the global galvanic couple potential, which more specifically identifies the coupled potential achieved between the ZRP and the 5456-H116.[a] By mixed potential theory, the magnitude of the galvanic couple potential over a macro-defect will be affected by the capacity of the Zn particles, as well as the exposed surface area ratio between the 5456-H116 and ZRP [41,50]. Thus, these measured OCP values were compared to coupled potentials achieved through Zero Resistance Ammeter (ZRA) analysis over two-hour duration between 5456-H116 and pure Zn at 1:1 surface area ratio in 0.6 M NaCl, where the 5456-H116 served as the working electrode, the Zn as the counter electrode, and a Luggin capillary-fitted SCE served as reference. Electrochemical impedance followed this OCP step during cycle testing to assess both the residual barrier properties of the primer and electrochemical porosity, which utilized frequencies between 10^5 and 10^{-2} Hz at 10 points per decade and an AC amplitude ranging from 30 to 60 mV for the ZRPs (100 mV for

---

[a] The open circuit potential corresponds to the point of equal anodic and cathodic reaction rates such that the total net current is zero. Thus, in a generalized case the OCP refers to the corrosion potential, in which the anodic and cathodic reactions occur on the same working electrode. However, in the galvanic coupling of Zn/5456 the zero-current condition is satisfied by the sum of all cathodic and anodic reactions equaling zero at the galvanic couple potential. This point of equality also corresponds to an OCP value for the system, thus this OCP will be termed the global galvanic protection potential to differentiate from that of the generalized case where necessary for this analysis.

the non-particle-containing epoxy), depending on the primer resin resistivity. Periodic EIS measurements throughout the cycle test provided a means to understand the influence of ZRP design on galvanic performance, as defined first by the OCP metric. During the cycle test, increase in the global galvanic couple potential, which would decrease the effectiveness of the ZRP for IGC/IG-SCC mitigation, may be caused by (1) the loss of Zn capacity due to particle oxidation (measured through comparison of pristine and post-test Zn peak intensity in XRD), (2) the loss of Zn particle connectivity due to corrosion product formation (indirectly evaluated through consideration of both primer impedance (EIS) and the OCP), or (3) the coverage of Zn particle surface area by corrosion product which may act as an ion permeation barrier (quantified through pore resistance measurements (EIS) with time of exposure). Equivalent circuit fitting of the EIS results in terms of a resistive-capacitive (RC) circuit then enabled the quantification of (1) the pore resistance, and (2) the anodic response time, which is the rate of capacitive discharge achieved by each ZRP measured by the delay in a given quantity of voltage output. This metric is representative of the responsivity of the ZRP to changing galvanic coupling conditions, such as the speed at which the ZRP would respond to passivate newly exposed cathodic surface area following crack growth. A worst-case galvanic coupling scenario between a ZRP and a large 5456-H116 area was then simulated through the PS hold step at -0.85 V_{SCE}, which is the OCP of NAMLT 65 mg/cm^2 5456-H116 in 0.6 M NaCl immersion. This step quantified the magnitude of anodic charge output achieved by each ZRP at this aggressive potential, as well as the consistency of the anodic charge output (whether or not a high level of output could be maintained) through consideration of all 13 of the PS hold stages throughout the cycle test. Thus, the metric that remained unevaluated following accelerated cycle testing was the ZRP polarizability.

3.1.3.4 ***Galvanostatic Pulse Testing***

Pristine ZRP panels were subjected to a cyclic series of 20 OCP / galvanostatic pulse steps in 0.6 M NaCl with increasing magnitude of applied anodic current to evaluate ZRP polarizability while simulating abrupt, fresh metal exposure during IGC/IG-SCC. This testing consisted first of a 3-hour OCP step to ensure ZRP activation. Galvanostatic pulses were then held for 10 minutes at each level of applied anodic current with 20 minutes at OCP prior to the next pulse, wherein any depletion or particle deactivation would be evident in the form of increased polarizability (more positive coupled potential value when unperturbed by applied current). To differentiate the galvanostatic pulse results, which will be utilized to quantify polarizability, from the accelerated cycle testing results, the coupled potential (E_{coup}) will be utilized as the descriptor of the ZRP state of performance, since this test simulates increasingly aggressive galvanic coupling surface area ratios. Applied current ranging from 1 nA to 100 μA was applied, as shown schematically in Figure 3.2, to simulate various bare surface areas demanding more anodic current output from the ZRP. These tests were conducted in triplicate, with each test being on a non-defected, unexposed 0.78 cm^2 ZRP area, and the ZRP polarizability was defined by the average applied current which caused the global galvanic potential to increase to values more positive than $E_{pit\,(\beta)}$. Qualitatively, the ZRP polarizability described the ability to maintain E_{coup} values in close proximity to the pure Zn OCP (-1.09 V_{SCE} in 0.6 M NaCl) (optimally), or below $E_{pit\,(\beta)}$, and the affinity to continue maintaining these E_{coup} values despite the application of external anodic current. Thus, low polarizability signifies the robust maintenance of E_{coup} values below $E_{pit\,(\beta)}$, such that high levels of applied

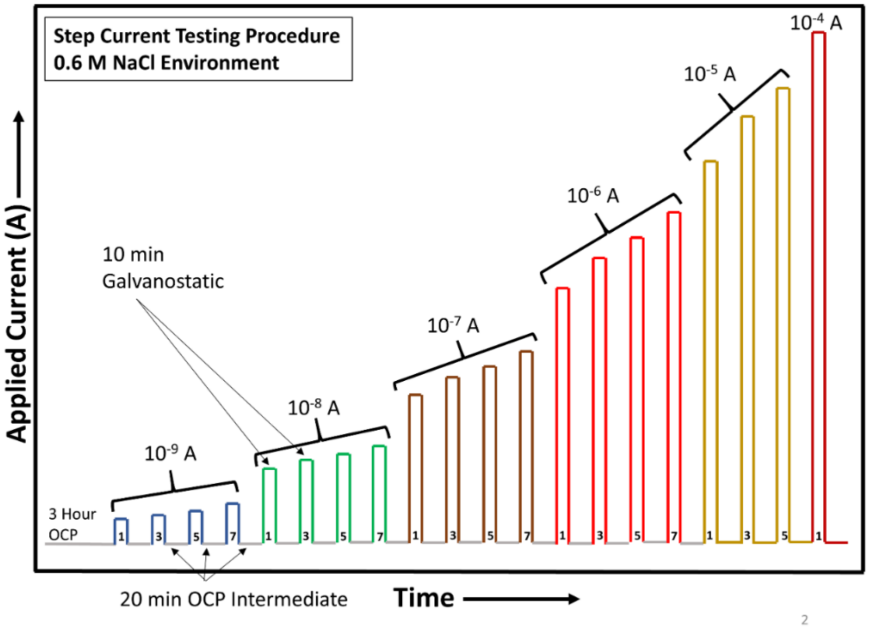

Figure 3.2: The cyclic galvanostatic pulse protocol, with applied pulses ranging from 1 nA to 100 µA for 10- minute durations to assess ZRP anodic response and recovery.

anodic current (exposed 5456-H116 surface area) are necessary to disable the achieved galvanic protection. More highly polarizable ZRPs maintain $E_{coup} < E_{pit\ (\beta)}$ in a smaller range of applied current, thus there is a greater risk of IGC/IG-SCC occurrence due to loss of galvanic protection.

3.1.4 **Results**

3.1.4.1 ***Baseline Assessment to Differentiate Coatings: Average Zinc Particle Size and Primer Thickness***

Baseline assessment utilized EDS elemental mapping on ZRP cross sections to differentiate primer thickness and particle size at 1000x magnification. These characteristic differences are shown in Table 3.I and Figure 3.3 for each ZRP. All Zn particles were roughly spherical in the ZRPs considered here. The differences in primer thickness mirrored differences in particle diameter, with the OZRP (Epoxy,57%) having the largest average thickness and average Zn particle diameter (53.7 ± 12.1 μm thickness and 11.2 ± 6.1 μm diameter), followed by OZRP (EPA,65%) (47.7 ± 14.7 μm thickness and 8.9 ± 6.7 μm diameter), OZRP (U,83%) (30.5 ± 5.7 μm thickness and 6.8 ± 2.3 μm diameter), and IOZRP (EthylSil,76%) (26.1 ± 9.4 μm thickness and 5.0 ± 2.7 μm diameter) (Table 3.I). These ZRPs were not mechanically tested in the present study.[b] Select EDS elemental imaging highlights the difference in resin type between these organic and inorganic ZRPs (Figure 3.4). Figure 3.4a demonstrates the roughly spherical Zn particles individually

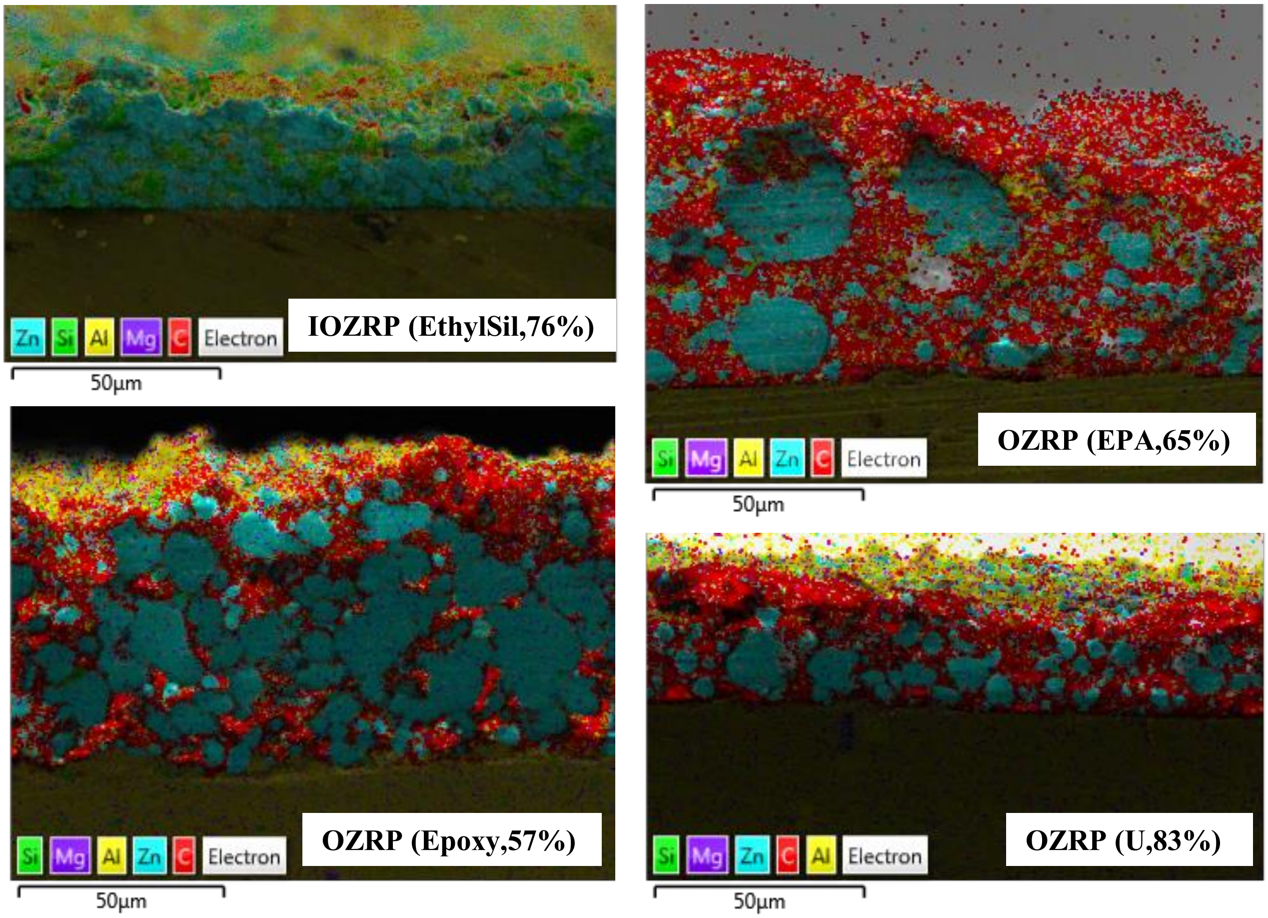

---

[b] The IOZRP (EthylSil,76%) was especially brittle in sample sectioning and handling, and flaking occurred regardless of curing time (up to 1 year). This brittle nature suggests that the Zn curing process, which is known to promote Zn particle reactions with steel surfaces to enhance primer adhesion [37], has no such influence on the surface of the 5456-H116. This flaking behavior was not exhibited by the OZRPs, which showed good adhesion in sectioning and sample handling.

Figure 3.3:Cross sectional EDS elemental analysis of the four candidate Zn-rich primers prior to cycle testing on 5456-H116, NAMLT 65 mg/cm^2, demonstrating the characteristic differences in thickness and Zn particle size for each.

dispersed in OZRP (EPA,65%), which is characteristic of all of the OZRPs in this study. A major differentiating characteristic of the IOZRP (EthylSil,76%) is shown in Figure 3.4b; this primer has low resin resistivity by way of its unique curing process, which forms a Zn silicate cement [37]. The compilation of the characteristic differences between the candidate ZRPs is schematically illustrated in Figure 3.5.

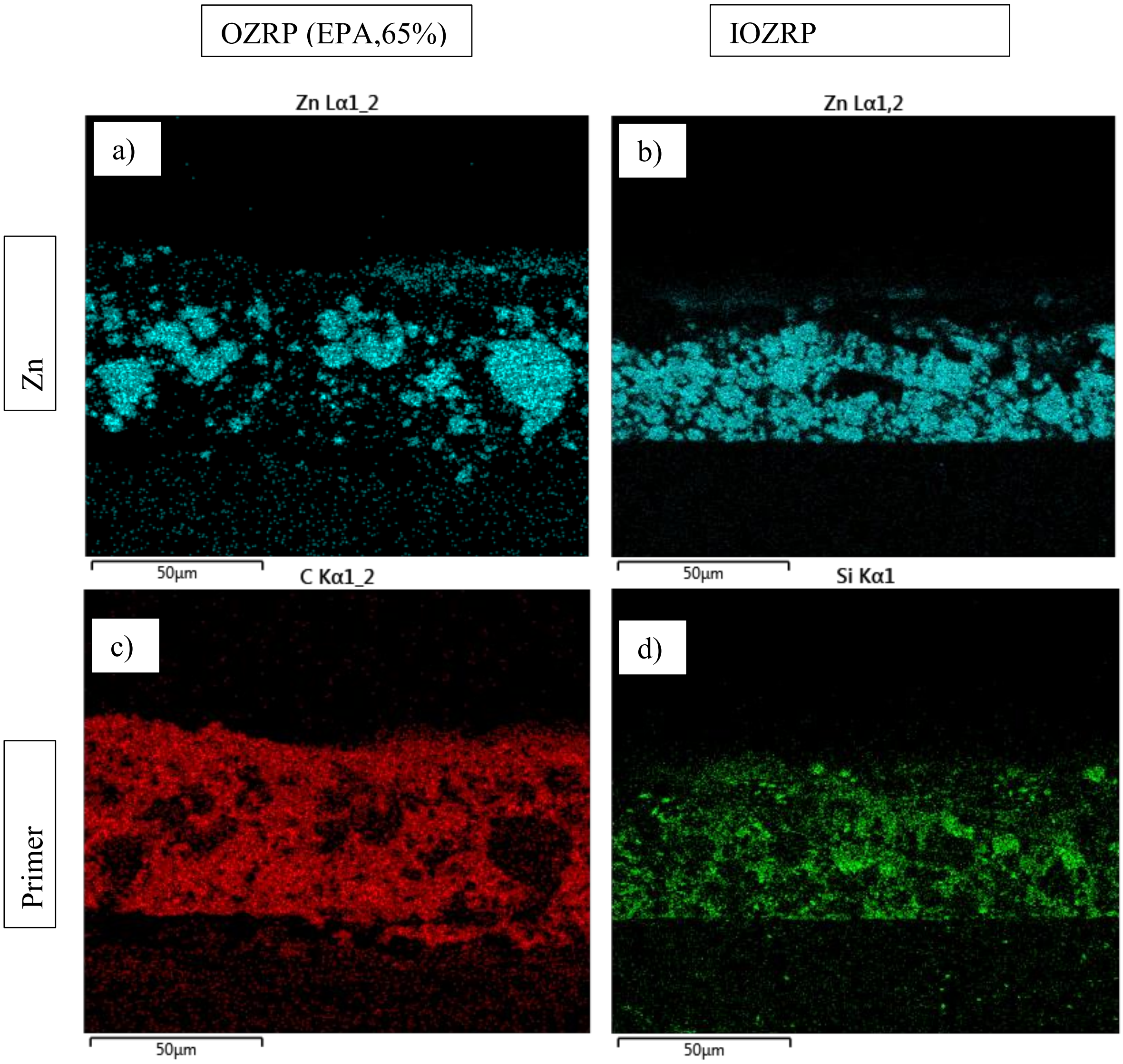

*Figure 3.4:Select element EDS analysis on unexposed primers displaying the Zn distribution for OZRP(EPA,65%) **(a)** and IOZRP(EthylSil,76%) **(b)**, as well as the differences between the organic epoxy polyamide resin (carbon image, **(c)** and the inorganic ethyl silicate (silicon image, **d**). Note the closely connected Zn content in **(b)**, which correlates with the unique curing known to occur in IOZRP (EthylSil,76%), compared to the individual Zn particles that remain in **(a)** for OZRP (EPA,65%).*

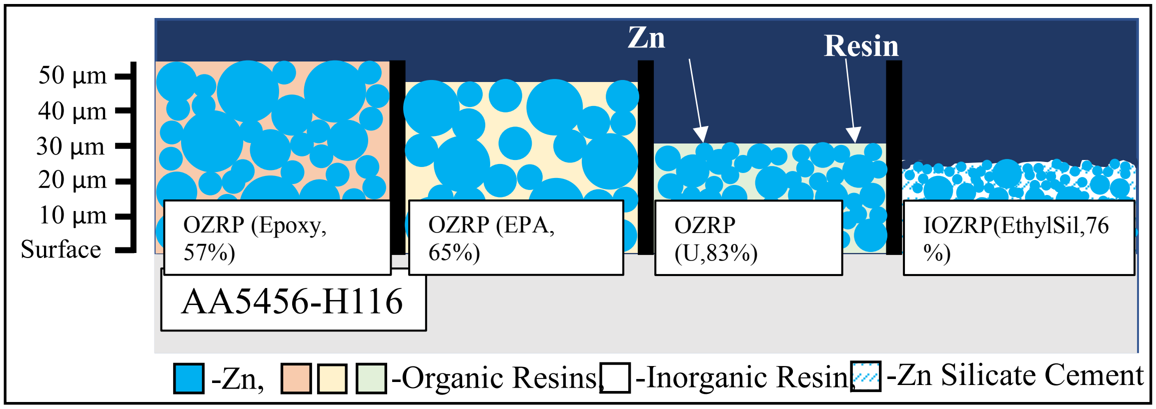

Figure 3.5:Schematic illustrating the differences between the candidate ZRPs based on average primer thickness, average particle diameter variation, resin type, as well as characteristic curing effects. The schematic demonstrates the differences between these ZRPs based on results from EDS statistical analyses of primer cross sections. Primer thickness and particle diameter drawn to scale.

The chemical identities of all crystalline components within the candidate ZRPs were investigated through XRD analysis before and after cycle testing. Zinc and Al were identified in all ZRP spectra, and post-exposure XRD analysis following the cycle test in 0.6 M NaCl identified residual elemental Zn and the corrosion product Simonkolleite ($Zn_5(OH)_8Cl_2\cdot H_2O$) (Figure 3.6). Reference XRD spectra for pure Zn, NAMLT 65 mg/cm^2 5456-H116, and Simonkolleite are shown in Figure 3.6, which together identify all peaks observed on these ZRPs before and after cycle testing.

3.1.4.2 *Global Galvanic Protection Capability Established Throughout Cycle Testing*

Subjecting the ZRPs to 13 PS Hold stages at -0.85 V_{SCE} for a total of 76 hours (Table 3.II) resulted in coating degradation through Zn oxidation in some of the particles; the magnitude of this degradation varied between primers.[c] This degradation in crystalline, metallic Zn content as measured by XRD as well as the average established OCP is illustrated in Figure 3.7 for each ZRP

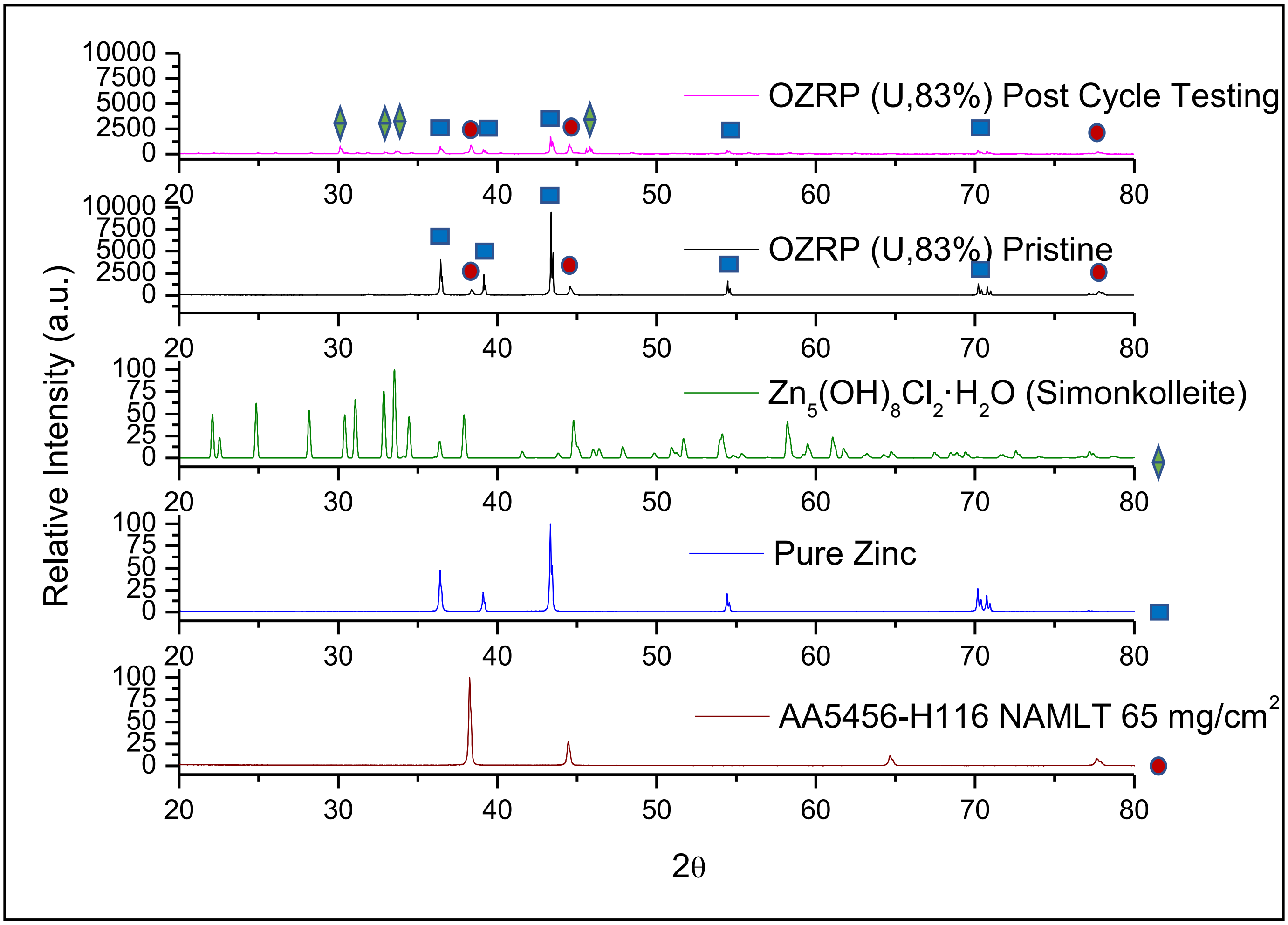

Figure 3.6:Reference XRD spectra for NAMLT 65 mg/cm^2 5456-H116, pure Zinc, and the corrosion product Simonkolleite, all of which appear in the post-cycle testing Zn-rich primer XRD spectra, such as that of OZRP (U,83%) illustrated here. No corrosion products were identified via XRD on any of the pristine ZRPs. The Al peak at 44.5° appeared with the greatest intensity in all ZRP spectra, and therefore was used for Zn peak intensity normalization.

---

[c] A series of cycle tests was also completed with the same overall duration but with PS Hold stages at -0.70 V_{SCE}. In all specimens these conditions resulted in incomplete ZRP depletion as well as primer decohesion, which inhibited post-exposure characterization.

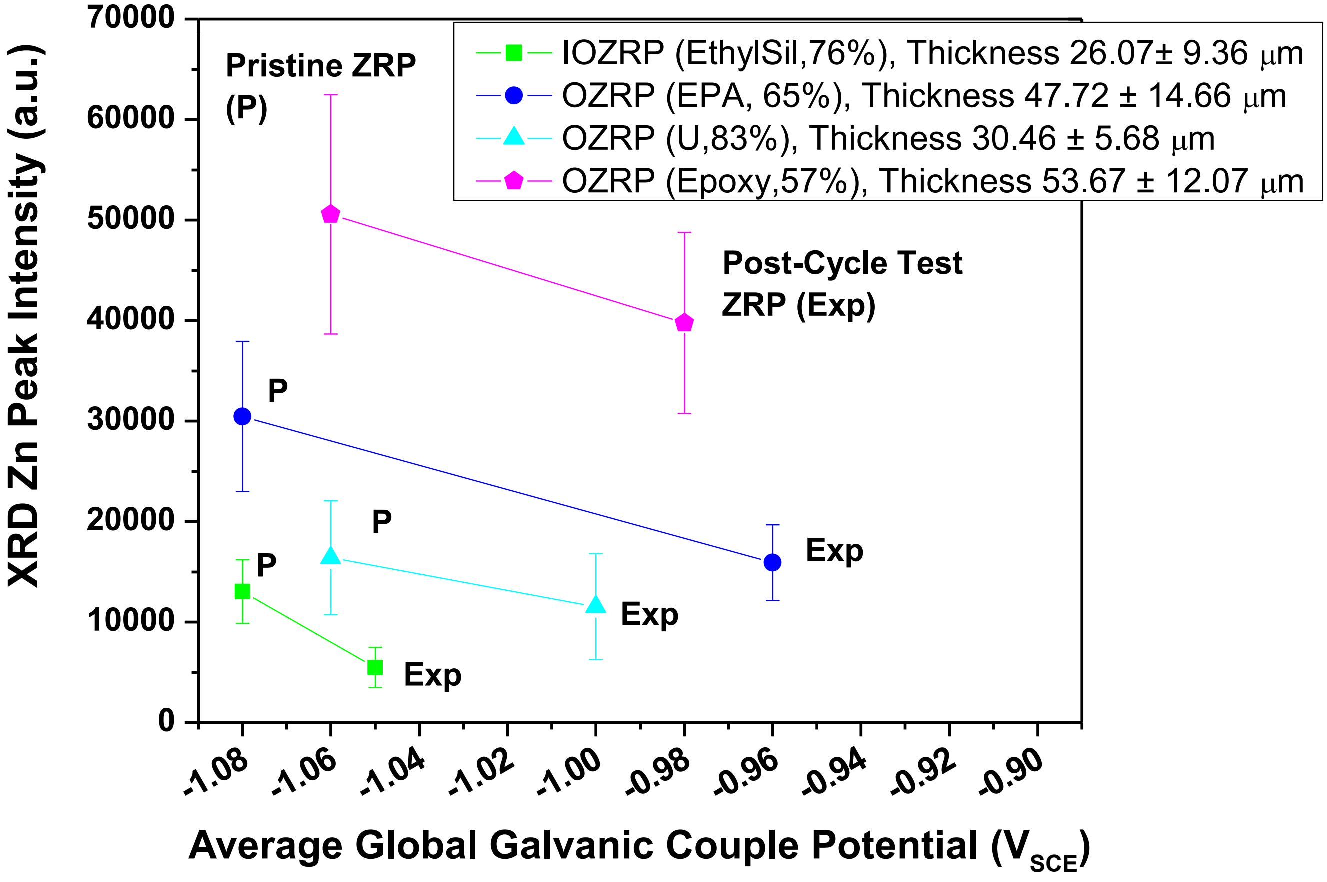

Figure 3.7:The XRD crystalline intensity of each ZRP before and after cycle testing in 0.6 M NaCl, with respect to the average established global galvanic couple potential. As the crystalline Zn content decreases in intensity, the ZRP OCP increases in proximity to that of the 5456-H116 substrate (-0.85 V_{SCE}).

both before and after cycle testing in 0.6 M NaCl. The XRD Zn peak intensity increases with increasing Zn quantity per unit area of ZRP, which is a function of Zn PVC and primer thickness (Table 3.I). Figure 3.8 contains a graphical example of the cycle test results for IOZRP (EthylSil,76%) and OZRP (EPA,65%). These periodic potential measurements during each accelerated testing cycle demonstrate the ZRP-coated 5456-H116 global galvanic protection potential becoming more positive with respect to time during the OCP (OCP/PS EIS) stages of each cycle (A (Cycle 1) through M (Cycle 13), on bottom) as Zn is depleted. The magnitude of the established global galvanic protection potential values (ZRP OCP in the figure) is shown comparatively with the pure Zn OCP in 0.6 M NaCl (dashed blue horizontal line, -1.09 V_{SCE}). The activation period for each ZRP, which involves primer wetting and ion ingress, is indicated by the initial potential drop in Figure 3.9. A ZRP is considered activated here at the point of the most negative established

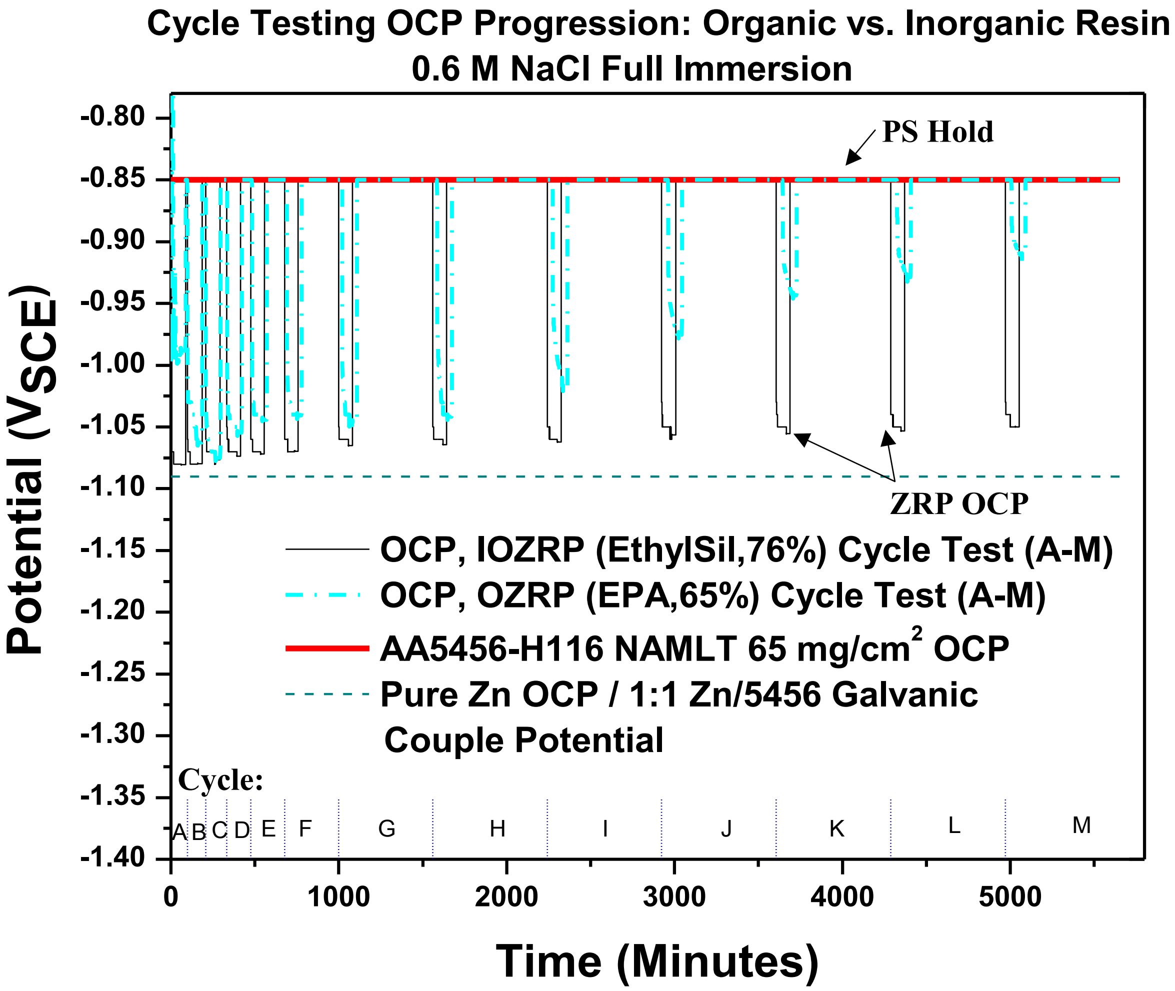

Figure 3.8:Graphical representation of the global galvanic protection potential results for each ZRP, showing the potentiostatic hold steps at the 5456-H116 OCP of -0.85 V_{SCE} as well as the

intermittent OCP steps to assess the ZRP protective state. Direct comparison is made between IOZRP (EthylSil,76%) and OZRP (EPA,65%).

OCP during cycle testing. The OCP trends demonstrated in Figure 3.9 illustrate that the IOZRP (EthylSil,76%) was the only ZRP to consistently show near instant activation upon exposure to 0.6 M NaCl and established the most negative protective potentials overall throughout cycle testing, in agreement with prior work on a steel substrate [44]. The OZRP (U,83%) and the OZRP (Epoxy,57%) required as much as 7-10 hours to activate in 0.6 M NaCl, with OZRP (U,83%) achieving the second most negative and OZRP (Epoxy,57%) achieving the third most negative OCP values (Figure 3.9). The OZRP (EPA,65%) required approximately 3 hours activation time, and achieved the least protective potentials by Cycle M with the largest standard deviation (Figure 3.9, OCP range achieved upon completion of cycle testing shown in Table 3.III). Figure 3.10 reports the cumulative anodic charge output associated with Zn oxidation for IOZRP (EthylSil,76%) (3.10a) and OZRP (Epoxy,57%) (3.10b). The cumulative charge output is calculated through integration of the current output with respect to time, giving the charge, followed by the summation of the charge for each prior and the current cycle. Significant differences are observed. Figure 3.10c illustrates the cumulative anodic charge output for each ZRP throughout cycle testing, which provides evidence for ZRP anodic charge capacity available for protection of exposed 5456-H116. These data illustrate that OZRP (Epoxy,57%) consistently output the highest anodic charge density during the cycle test, followed by IOZRP (EthylSil,76%), OZRP (U,83%), and OZRP (EPA,65%). The differences in activation time and the anodic charge output achieved by each ZRP warrants further analysis into secondary barrier impedance, sacrificial oxidation, and porosity properties.

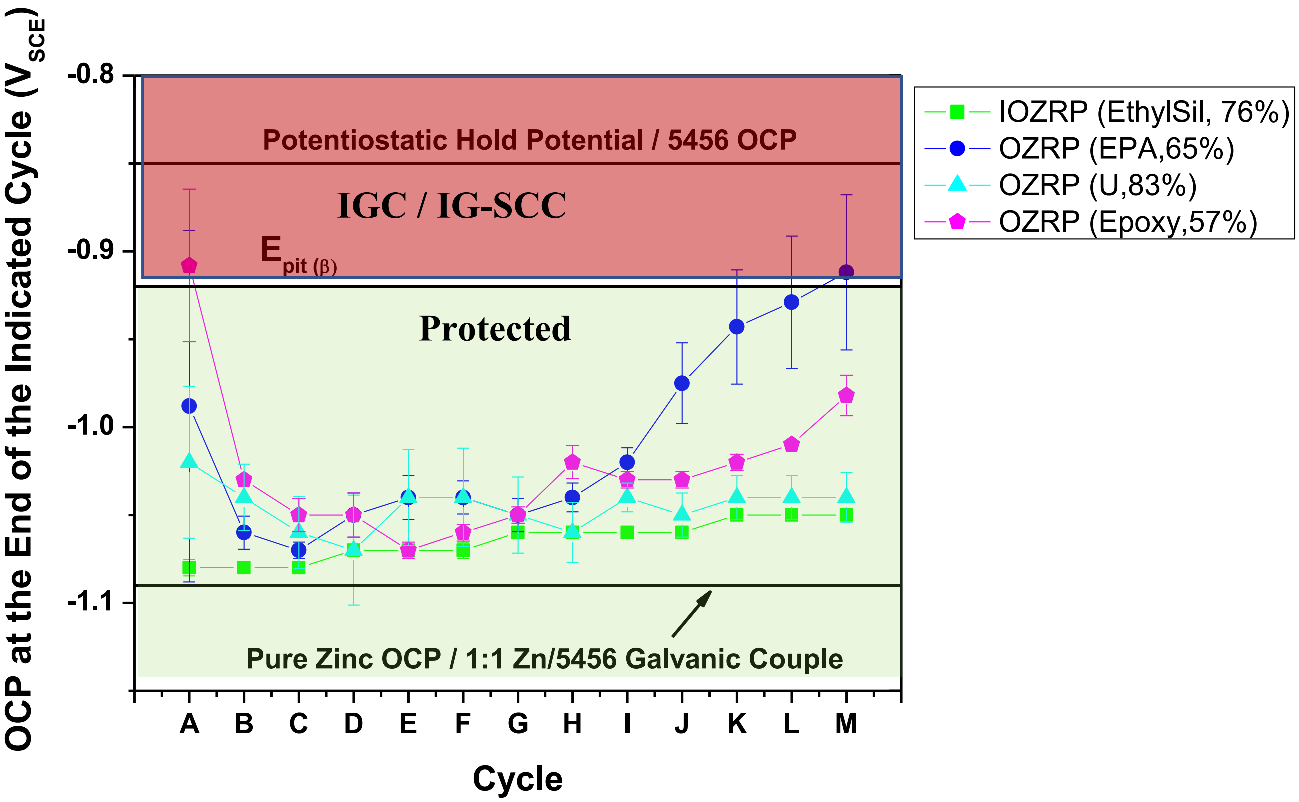

Figure 3.9:The increasingly positive coupled OCP established per cycle (Cycles A – M) during the OCP stages at -0.85 V_{SCE} of the cycle test in 0.6 M NaCl.

Table 3.III: Zn-Rich Primer Charge Capacities and Cathodic Protection Performance

Zn-Rich Primer	**Theoretical Anodic Q from ZRP (C/cm^2)***	**Maximum Anodic Q Output (C/cm^2) by End of Cycle Test****	**ACU by End of Cycle Test*** **	**Max. XRD Depletion at End of Cycle Test**	**Initial Activated OCP**	**OCP Upon Completion of the Cycle Test**
IOZRP (EthylSil,76%)	41.7	4.5	10.7%	58%	-1.08 ± 0.01 V_{SCE}	-1.05 ± 0.02 V_{SCE}
OZRP (EPA, 65%)	64.9	0.6	1.0%	45%	-1.08 ± 0.02 V_{SCE}	-0.91 ± 0.10 V_{SCE}
OZRP (U,83%)	53.2	3.3	6.2%	29%	-1.06 ± 0.03 V_{SCE}	-1.01 ± 0.03 V_{SCE}
OZRP (Epoxy,57%)	64.4	6.7	10.4%	16%	-1.06 ± 0.02 V_{SCE}	-0.98 ± 0.03 V_{SCE}

Q = charge, C = Coulombs, XRD = X-Ray Diffraction, OCP = open circuit potential, Activated OCP = stabilized OCP following immersion and sufficient coating wetting, ZRP = Zn-rich primer, ACU = anodic charge usage

*Based on Zn particle volume concentration and coating thickness
** Maximum anodic charge output calculated by integrating the cumulative maximum anodic current output achieved during one cycle testing with respect to the total duration of the PS hold stages of the cycle test
*** Not designed for universal usage, is a test-and time of exposure-dependent value; calculated by dividing the max. anodic Q by the theoretical anodic Q

3.1.4.3 *Barrier Properties Throughout Electrochemical Cycle Testing*

An important question pertaining to primer performance is the presence of effective residual barrier properties, which were assessed via PS EIS (about the primer OCP) intermittently throughout cycle testing to monitor impedance and pore resistance progression. Figure 3.11 shows the Bode Magnitude impedance response for each intact ZRP as well as for bare and epoxy-

a)

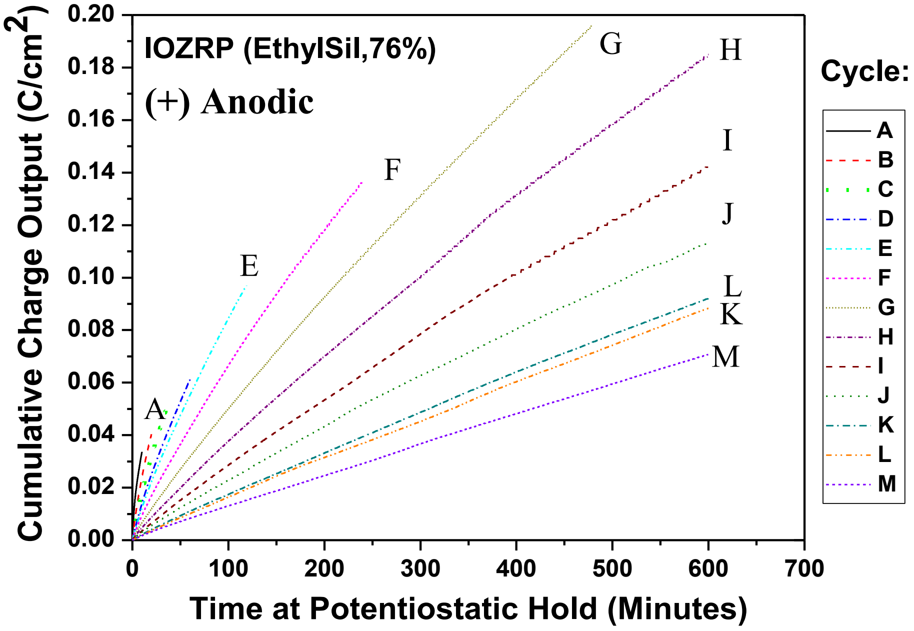

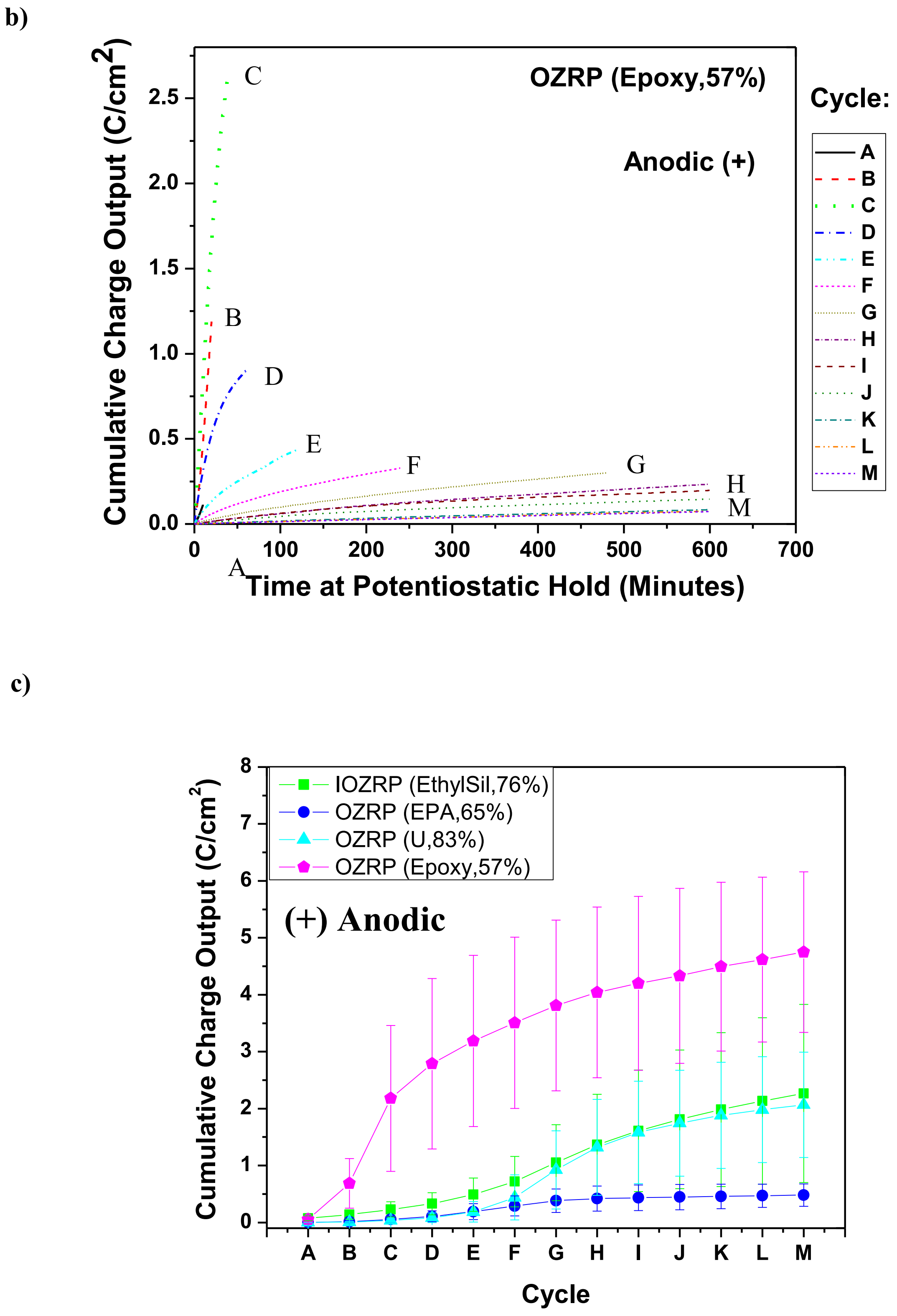

Figure 3.10:The progression of cumulative anodic charge output per cycle (Cycles A – M) during the PS Hold stages at -0.85 V_{SCE} of the cycle test in 0.6 M NaCl for IOZRP (EthylSil,76%)

***(a)** and OZRP (Epoxy,57%) **(b)**. The charge density output per cycle as well as the standard deviation for all of the candidate ZRPs is summarized in **(c)**.*

coated 5456-H116 (Cycles A-M). Directional trends in ZRP impedance are illustrated on these plots by arrows correlated to the most relevant testing cycles (A-M). Previous EIS analyses on MRPs have concluded that assessment of coating impedance at the lowest measured frequency (0.01 Hz here) accurately represents overall conductive/resistive properties of the coating with time of exposure [26–29,32,61], and illustrates vital differences between these ZRPs in terms of overall barrier properties which contribute to the inhibition of corrosion reactions on 5456-H116 [50,54,56]. Figure 3.12 demonstrates these low frequency impedance modulus ($Z_{0.01\ \mathrm{Hz}}$) trends, where full ZRP activation may be considered as the point where the minimum $Z_{0.01\ \mathrm{Hz}}$ is reached. The recovery in impedance is thought to be due to corrosion product formation in ZRPs that blocks pore space [41,50,56]. While the formation of a high impedance secondary barrier may be beneficial for corrosion prevention when no macro-defects are present in the ZRP, such impedance increase may resist galvanic performance by reducing Zn particle connectivity and/or covering Zn surface area to reduce anodic charge output, and thus is detrimental to IG-SCC mitigation purposes. The IOZRP (EthylSil,76%) experiences only impedance increase (Figure 3.12). The OZRP (EPA,65%) has the most variable impedance, though by Cycles B through M this ZRP maintains the highest $Z_{0.01\ \mathrm{Hz}}$ overall. The OZRP (U,83%) has the highest $Z_{0.01\ \mathrm{Hz}}$ at $3\times10^6\ \Omega\text{-cm}^2$, though it experiences the most significant $Z_{0.01\ \mathrm{Hz}}$ loss of two orders of magnitude upon activation (Cycles B through G) with only minor recovery (Figure 3.12). The OZRP (Epoxy,57%) trend is similar to that of the epoxy-coated 5456-H116, though the non-particle containing epoxy exhibits approximately three orders of magnitude higher $Z_{0.01\ \mathrm{Hz}}$ in Cycles D through M (Figure 3.12). The determination of defect area through use of methods such as the breakpoint frequency or saddle point frequency [46,48,62–64] could not be conducted due to the lack of consistent presence of these points in the Bode phase angle dataset.

3.1.4.4 *Coating Depletion and Corrosion Product Identification*

The depletion of Zn particle was assessed through comparison of XRD Zn peak intensities following normalization to the highest Al peak at approximately 44.5°, which originates from the 5456-H116 substrate. Depletion analysis considered the cycle test in which the maximum experimental anodic charge output was achieved for each ZRP (Table 3.III). Following the completion of cycle testing, IOZRP (EthylSil,76%) demonstrated 58% average Zn peak intensity loss, followed by OZRP (EPA,65%) (45% loss), OZRP (U,83%) (29% loss), and OZRP (Epoxy,57%) (16% loss), as shown in Table 3.III. The influence of this crystalline, metallic Zn depletion was then considered in terms of the theoretical anodic charge capacity of each ZRP, as reported in Table 3.III. The theoretical anodic charge output was calculated from the average primer thickness (Table 3.I), the density of Zn (Table 3.IV), the primer Zn particle volume concentration (PVC, Table 3.I), and the exchange of two electrons necessary for Zn oxidation. For comparison, the total experimental anodic current output exhibited by each ZRP during cycle testing was computed by summing the anodic current output from each stage of PS hold at -0.85 V_{SCE} (Figure 3.10c, Table 3.III). The fraction of experimental to theoretical anodic charge output demonstrated the anodic charge usage (ACU) of each ZRP achieved during the cycle test, which was: 10.7% (IOZRP (EthylSil,76%)), 10.4% (OZRP (Epoxy,57%)), 6.2% (OZRP (U,83%)), and 1.0% (OZRP (EPA,65%)) of the total available (Table 3.III). Therefore, these primers have considerable protective capacity remaining following the cycle test, indicating that a considerable reservoir of buried Zn

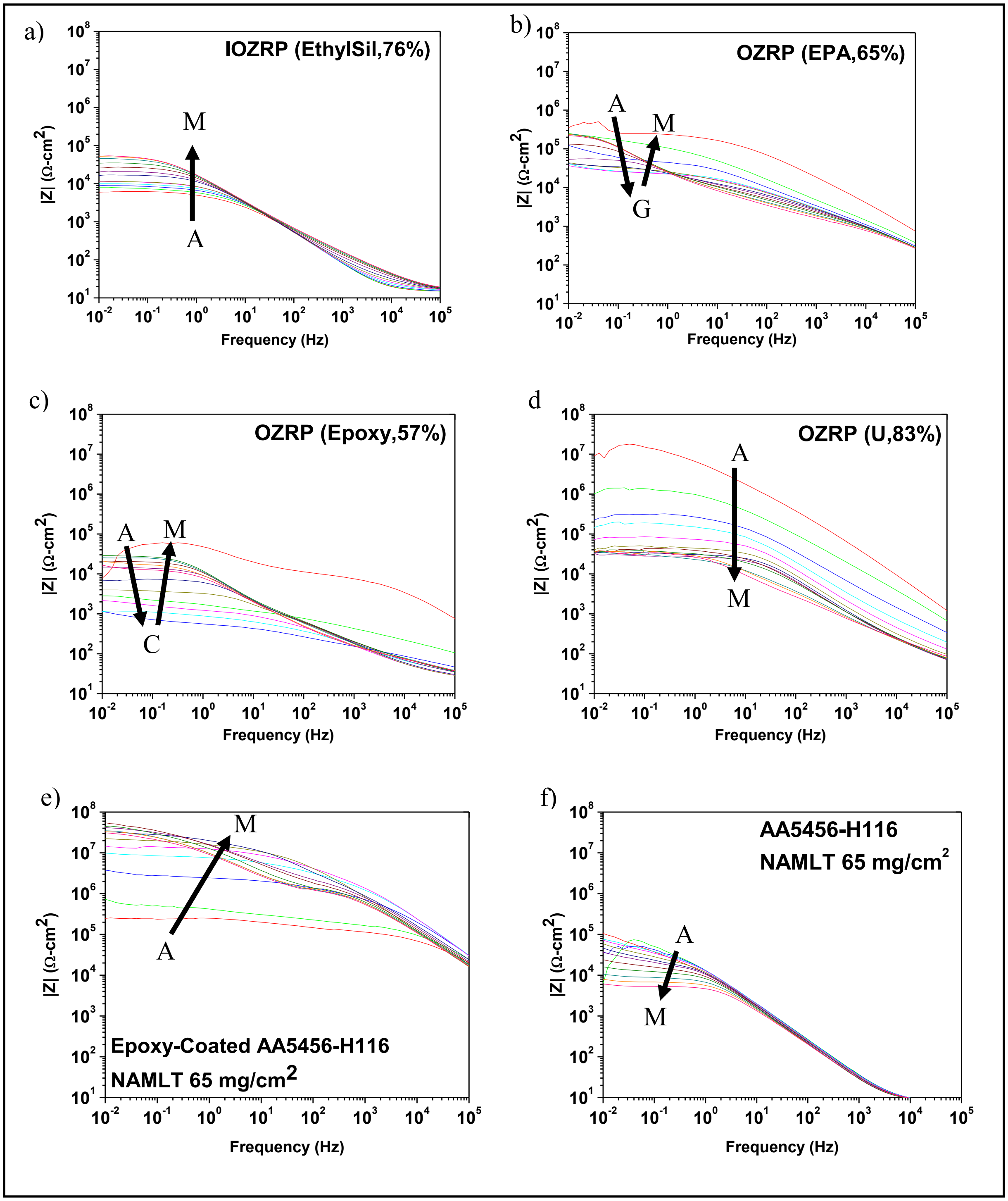

Figure 3.11: EIS Bode Magnitude plots showing results for each ZRP in 0.6 M NaCl, as well as for bare and epoxy-coated, highly sensitized 5456-H116 as reference. With time of exposure at -0.85 V_{SCE}, loss of impedance typically occurs during primer activation followed by increase in impedance by corrosion product formation.

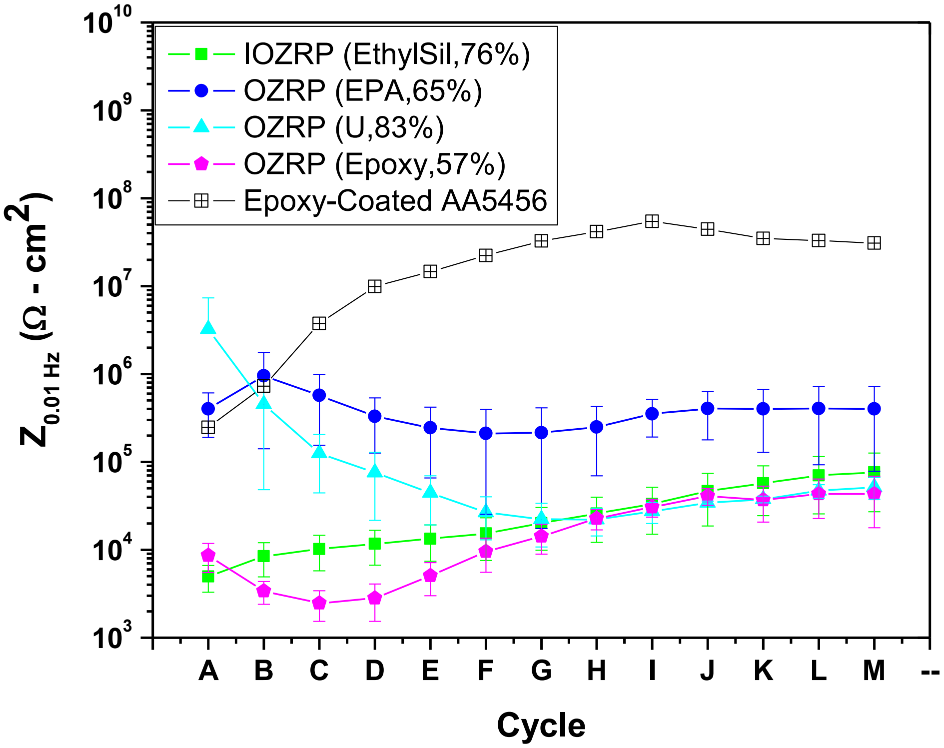

Figure 3.12:Average impedance modulus at 0.01 Hz for each ZRP throughout cycle testing in 0.6 M NaCl, with standard deviations for each to demonstrate variabilities in coating performance.

Table 3.IV: Elemental Molar and Corrosion Product Volumes Potentially Produced per Mole of Zn^{2+}

Element/Compound	Specific Density*	Volume Produced/mole Zn^{2+}
Zn	7.1 g/cm^3	9.1 cm^3
ZnO (Zincite)	5.5 g/cm^3	14.6 cm^3
$Zn(CO)_3$ (Smithsonite)	4.4 g/cm^3	33.6 cm^3
$Zn(OH)_2$ (Wulfingite)	3.0 g/cm^3	32.6 cm^3
$Zn_5(OH)_8Cl_2{\cdot}H_2O$ (Simonkolleite)	3.2 g/cm^3	35.4 cm^3

*Densities obtained from the WebMineral Database remains available for local galvanic protection should a defect develop to expose an isolated Zn particle.

As demonstrated in Figure 3.13, the cycle testing exposure in full immersion caused considerable corrosion product formation to occur on these ZRPs. The Raman spectra shown in

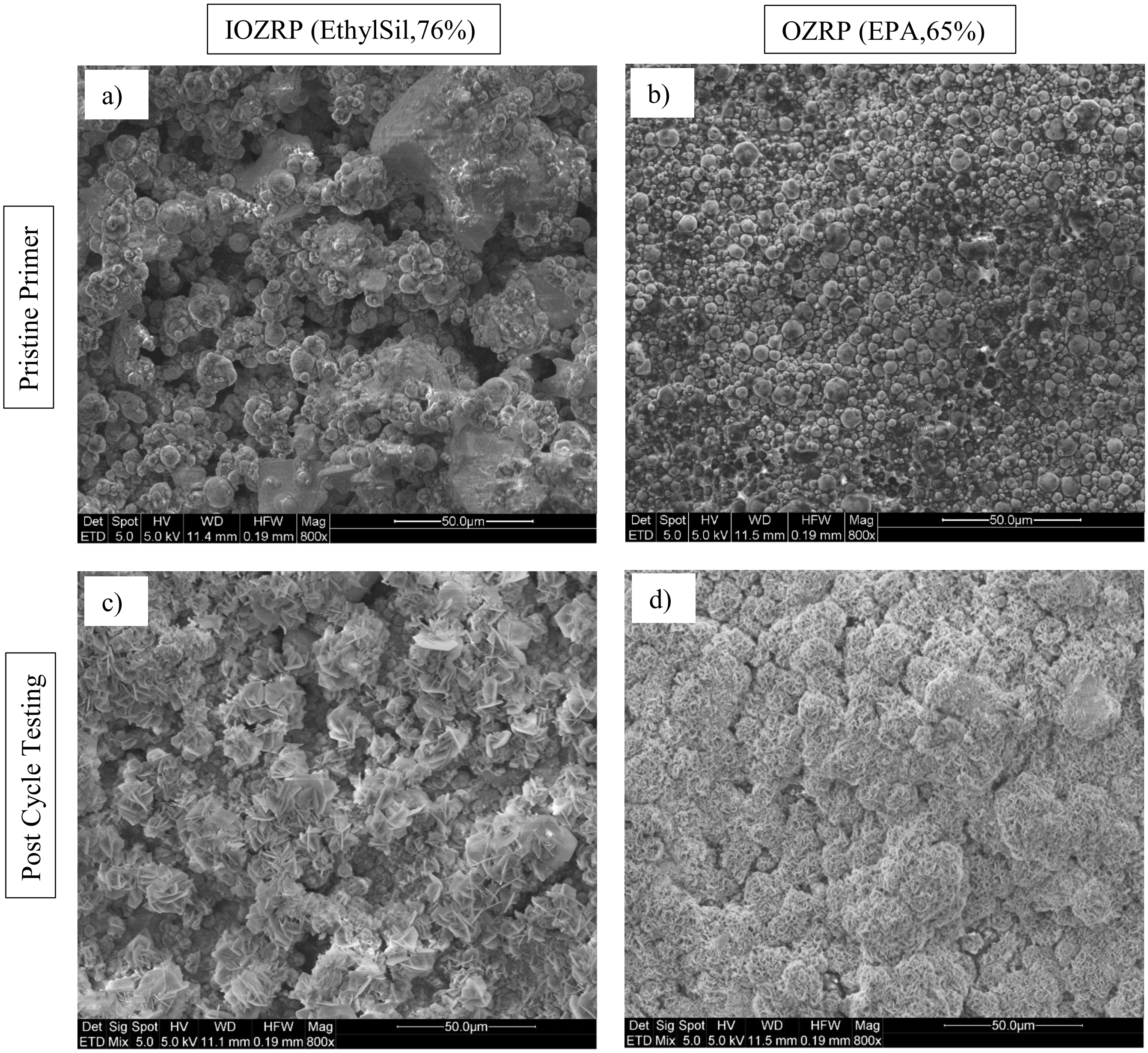

Figure 3.13:Unexposed, pristine primer surfaces ***(a,b)*** *as well as corrosion product coverage following cycle testing in IOZRP (EthylSil,76%)* ***(c)*** *and OZRP(EPA,65%)* ***(d)****, visually demonstrating the difference in coating porosities. The OZRP (EPA,65%) formed the highest impedance secondary barrier upon completion of cycle testing, and the IOZRP (EthylSil,76%) formed the second highest impedance barrier.*

Figure 3.14 for the examples of IOZRP (EthylSil,76%) and OZRP (EPA,65%) illustrate that four corrosion products were identified post-cycle test: ZnO (Zincite), $Zn(OH)_2$ (Wulfingite), $Zn(CO)_3$ (Smithsonite), and $Zn_5(OH)_8Cl_2$•H_2O (Simonkolleite). These corrosion products are common in saline environments on ZRPs subjected to field exposure and contribute to secondary barrier formation [36,51,65,66]. The thickness of corrosion product coverage formed during cycle testing is evident in the Backscatter Electron (BSE) micrographs on post-cycle testing ZRP cross sections shown in Figure 3.15, with Zn corrosion products having lower brightness due to lower average

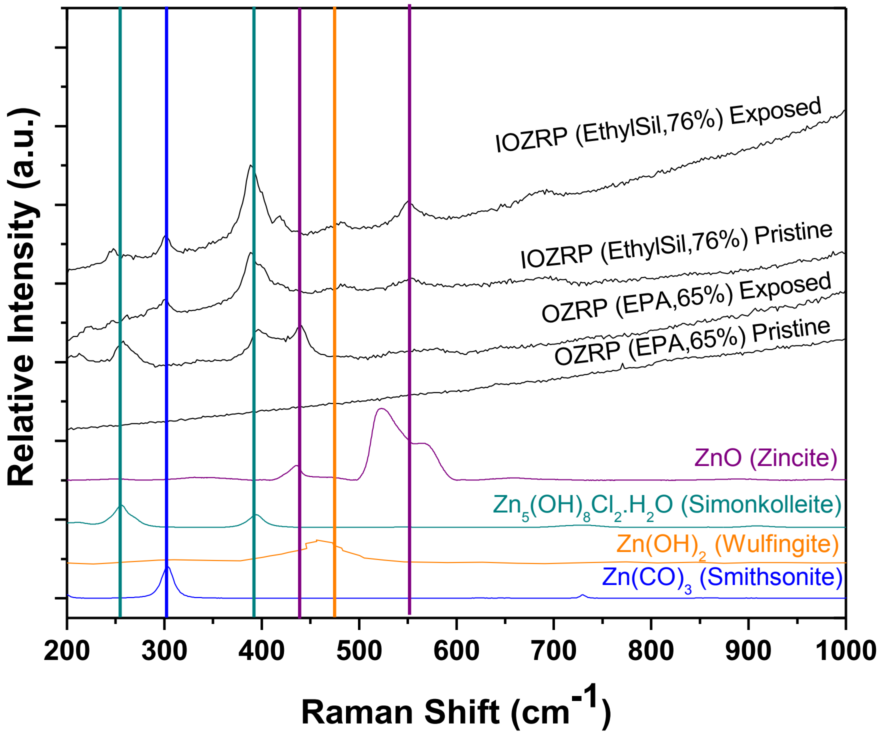

Figure 3.14:Raman spectroscopic analysis identifying corrosion products formed in 0.6 M NaCl during cycle testing of IOZRP (EthylSil,76%) and OZRP (EPA,65%). Reference spectra were acquired from the RRUFF™ database, except for the $Zn(OH)_2$ spectrum, which was acquired from literature [65]. IOZRP (EthylSil,76%) was the only ZRP to have significant corrosion product volumes in pristine condition, and was the only ZRP to form all four identified corrosion products.

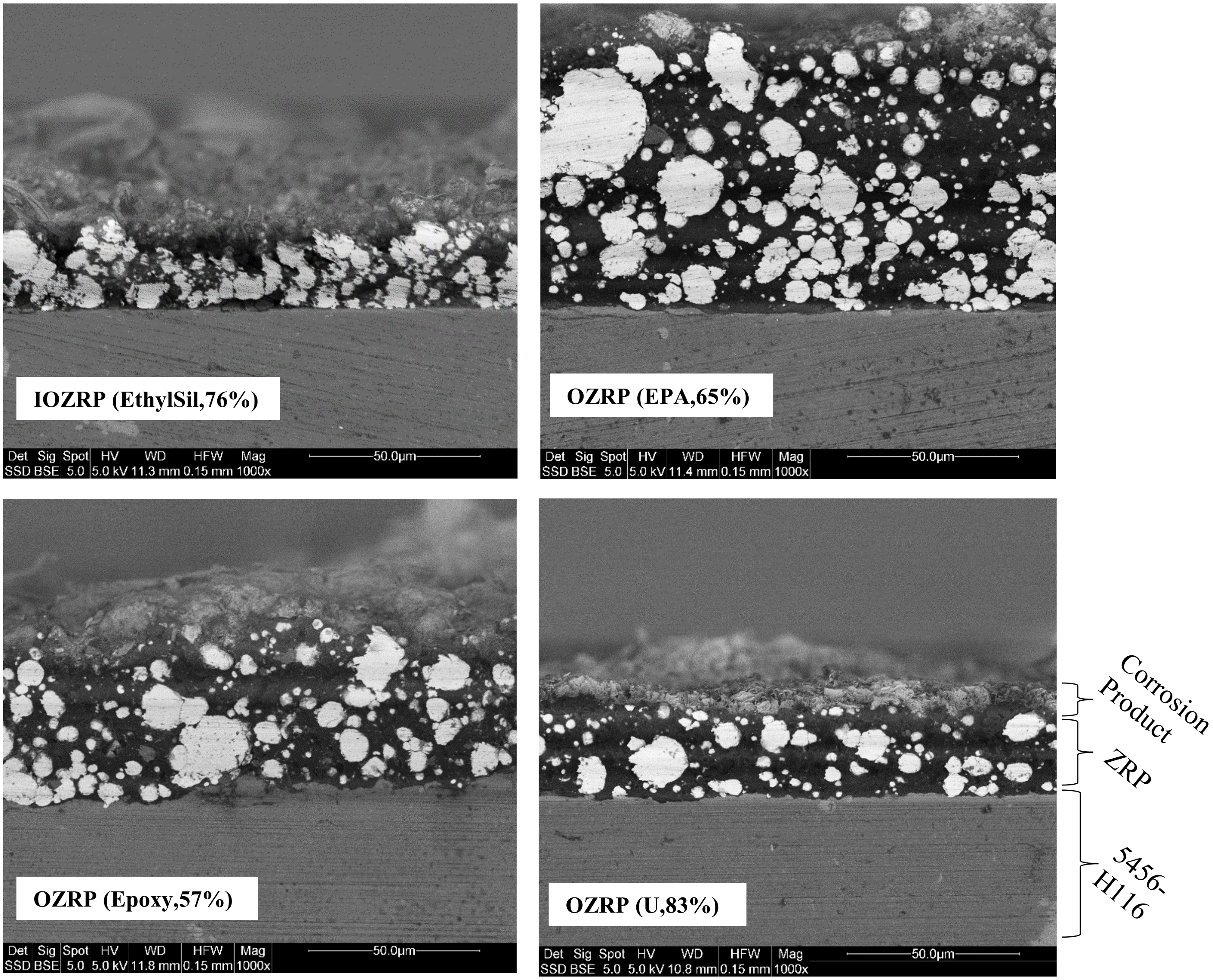

Figure 3.15:Post-cycle test cross sectional backscatter electron micrographs for each ZRP, demonstrating the continued presence of non-porous Zn particles following 76 hours of coating exposure at -0.85 V_{SCE}. The corrosion products formed on each ZRP are visible as a light gray layer atop the intact Zn particles and resin.

atomic weight than the pure Zn particles (Table 3.IV). Specifically, IOZRP (EthylSil,76%) was the only ZRP that showed initial corrosion product content in the pristine primer, having Zincite, Wulfingite, Smithsonite, as well as Simonkolleite present (Figure 3.14). Following exposure, all OZRPs developed Zincite and Simonkolleite peaks.

3.1.4.5 *Galvanostatic Pulse Testing to Evaluate Zinc-Rich Primer Anodic Response*

Each ZRP was subjected to galvanostatic pulse testing utilizing the procedure outlined in Figure 3.2 to evaluate the polarizability of the primer under increasingly aggressive, simulated galvanic coupling conditions where bare Al is created, such as through crack advance. Examples of the raw results of these tests are shown in Figure 3.16 for OZRP (Epoxy,57%) (3.16a) and IOZRP (EthylSil,76%) (3.16b). These data demonstrate that each primer has a critical level of applied current which causes sufficient loss of polarization control such that E_{coup} becomes more positive than $E_{pit\,(\beta)}$.[d] Through averaging the E_{coup} values achieved during each galvanostatic pulse (only the data obtained while the external current was applied) to obtain one representative E_{coup} value per pulse, the polarizability of these ZRPs may be evaluated, as shown in Figure 3.17. From Figure 3.17, the critical current (CC) at which E_{coup} exceeds $E_{pit\,(\beta)}$ will be utilized as a metric for the relative comparison of ZRP polarizabilities. These trends demonstrate that the IOZRP (EthylSil,76%) and the OZRP (Epoxy,57%) are the least polarizable, sustaining $E_{coup} < E_{pit\,(\beta)}$ until CC = 1×10^{-4} A (1.3×10^{-4} A/cm^2) and 1×10^{-5} A (1.3×10^{-5} A/cm^2), respectively. The OZRP (EPA,65%) and OZRP (U,83%) are the most polarizable ZRPs, with CC = 1×10^{-7} A (1.3×10^{-7}

---

[d] It is worth noting that the intermediate OCP steps demonstrate that the ZRP OCP consistently returns to a potential between -1.10 V_{SCE} and -1.05 V_{SCE}, which supports the fact that this test method only evaluates polarizability and does not cause noticeable primer depletion that would skew the results.

A/cm^2) and 3x10^{-6} A (3.8x10^{-6} A/cm^2) (Figure 3.17). The aspects of ZRP design which drive these polarizability trends will be discussed below.

a)

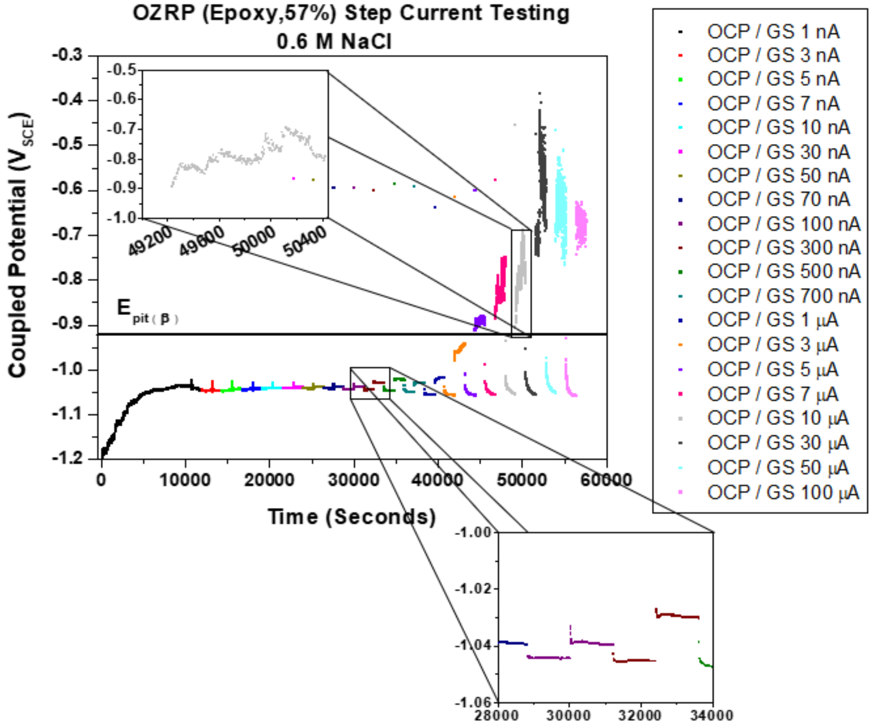

b)

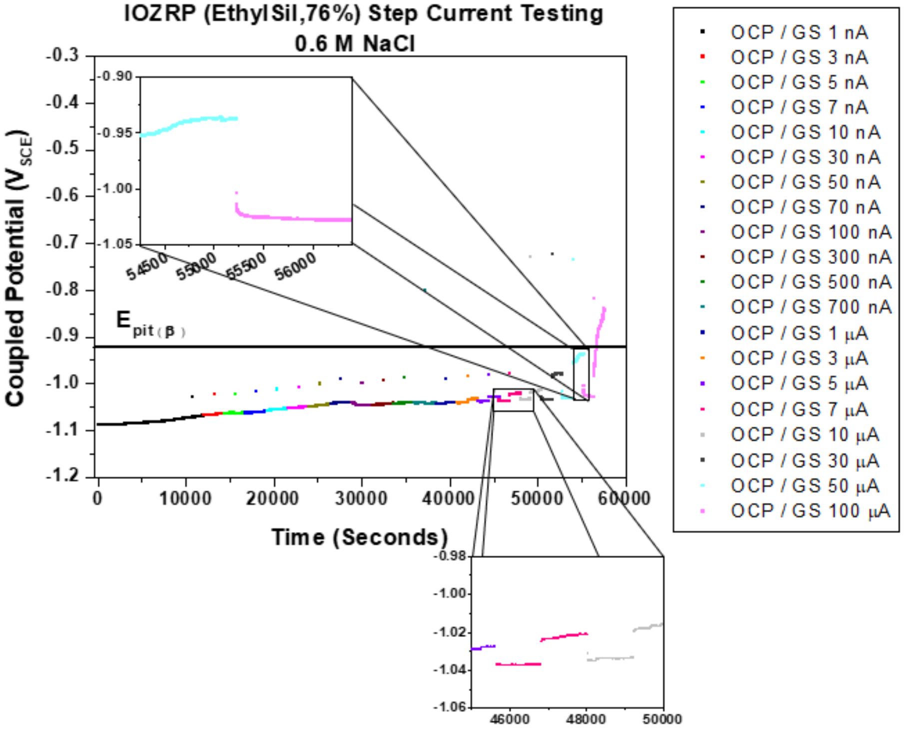

Figure 3.16:Coupled potential of ***(a)*** *OZRP (Epoxy,57%) and* ***(b)*** *IOZRP (EthylSil,76%) throughout the galvanostatic pulse series with applied anodic current ranging from 1 nA to 100 μA. The polarizability of each ZRP is evident by the amount of applied anodic current necessary to cause an increase in coupled potential above $E_{pit\,(\beta)}$. GS refers to the 10-minute galvanostatic pulse following the 20-minute OCP step.*

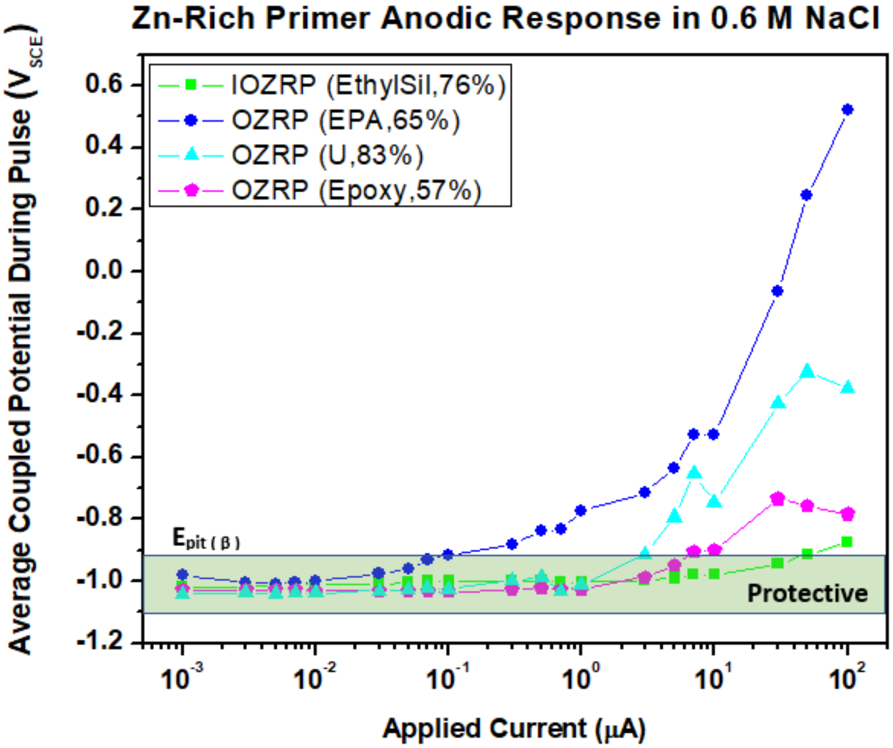

Figure 3.17:Average coupled potential values and overall polarizability of each ZRP following triplicate galvanostatic pulse test series, each on fresh ZRP specimens in 0.6 M NaCl. The entirety of the dataset for each pulse was averaged to obtain the datapoints shown, which demonstrate that the IOZRP (EthylSil,76%) and OZRP (Epoxy,57%) are the least polarizable.

3.1.5 **Discussion**

The combination of accelerated cycle and galvanostatic pulse testing demonstrated a variety of distinctive coating metrics that may assist the optimization of coating design for IGC or IG-SCC mitigation on Al-Mg alloys. Specifically, parameters such as (1) anodic charge output and ACU, (2) pore resistance and polarizability, (3) anodic response time, as well as the (4) secondary barrier impedance will be systematically assessed to elucidate the factors that contribute to optimized ZRP galvanic protection performance for IGC / IG-SCC mitigation. The ZRP rankings based on these metrics as well as physical coating characteristics are summarized in Table 3.V, which will be explained in the sections to follow.

Table 3.V: Compilation of Zinc-Rich Primer Characteristic and Performance Rankings*

Metric	**IOZRP(EthylSil,76%)**	**OZRP(EPA,65%)**	**OZRP(U,83%)**	**OZRP(Epoxy,57%)**
Primer Thickness	4	2	3	1
Zinc Particle Diameter	4	2	3	1
OCP – Cycle Testing	1	4	2	3
XRD Intensity Loss	1	2	3	4
Max. Total Anodic Charge Output	2	4	3	1
Polarizability (CC)	1	4	3	2
Anodic Charge Usage	1	4	3	2
Anodic Response Time	4	1	3	2
Avg. Pore Resistance After Cycle G	3/4	1	2	3/4
Secondary Barrier Impedance in Cycle M	2	1	3	4

*1 = largest (primer thickness, particle diameter, XRD loss, max anodic charge output, CC, ACU, anodic response time), or the most negative (OCP)

3.1.5.1 *Zinc-Rich Primer Anodic Charge Output and Anodic Charge Usage*

The ACU metric collectively characterizes the physical ZRP characteristics such as Zn loading, permeability, and theoretical anodic charge capacity with the magnitude of Zn galvanic coupling and continuity of Zn particle exposure/connectivity throughout testing. Through such collective representation of ZRP attributes, the ACU yields predictions that correlate well with ZRP polarizability and galvanic protection performance. For example, the IOZRP (EthylSil,76%) has the lowest theoretical capacity (41.7 C/cm^2) but exhibits the highest anodic charge output (4.5 C/cm^2) during cycle testing (Table 3.III). This galvanic performance achieved the most negative OCP in Cycle M (-1.05 V_{SCE}) and the highest ACU of 10.7% (Table 3.III). Subsequently, the IOZRP (EthylSil,76%) was also the least polarizable ZRP (highest CC, Figure 3.17). The OZRP (Epoxy,57%) achieved the second highest ACU of 10.4% and was the second least polarizable (Figure 3.17, Table 3.III, see Table 3.V summary). Similarly, one may initially assume that the magnitude of anodic charge output for each ZRP would correlate with the magnitude of achieved OCP, which would make OCP another indicator of ZRP polarizability. However, these results demonstrate that neither the anodic charge output nor the OCP correlate consistently with polarizability (Table 3.V). For example, OZRP (U,83%) achieved an average of 3 mV_{SCE} more negative OCP in Cycle M than OZRP (Epoxy,57%) (Table 3.I), yet OZRP (U,83%) was more polarizable (lower CC, Figure 3.17). Also, the OZRP (Epoxy,57%) achieved 2.2 C/cm^2 greater anodic charge output than IOZRP (EthylSil,76%) during cycle testing, yet the IOZRP was less polarizable (highest CC, Figure 3.17). These comparisons demonstrate that ZRP polarizability cannot be predicted from achieved OCP during cycle testing or experimental anodic charge output. However, the ACU metric does demonstrate consistent correlation (Table 3.V). This metric consists of a culmination of ZRP performance attributes that must be differentiated to understand mechanisms underlying enhanced galvanic protection performance. Based on related literature findings and the present results, ACU is affected most by the pore resistance associated with anodic charge output for galvanic protection for a given Zn PVC, which may be further understood through equivalent circuit modeling [51,54,56,73].

3.1.5.2 ***Zinc-Rich Primer Pore Resistance and Relative Coating Porosity***

For a given Zn PVC, resin- and particle-related porosity directly affect the amount of Zn surface area exposed to the electrochemical environment, and Zn particle connectivity (percolation) is dependent on Zn loading, all of which may influence the primer ACU, the cathodic potential that is established, and the ZRP polarizability [36,39]. This relationship may be understood further through consideration of the ZRP pore resistance (R_{pore}). The R_{pore} value for these ZRPs throughout the cycle test may be quantified through EIS equivalent electrical circuit fitting of the Bode magnitude (Figure 3.11) and phase angle data. An example of this fitting is shown in Figure 3.18 with the respective equivalent electrical circuit consisting of 2 constant phase elements (CPE), with R_{soln} held constant at 25 Ω. The resulting R_{pore} values derived from this theoretical circuit analysis are illustrated in Figure 3.19. Following the stabilization of the R_{pore} behavior in these ZRPs following Cycle G, these analyses demonstrate that high ACU is

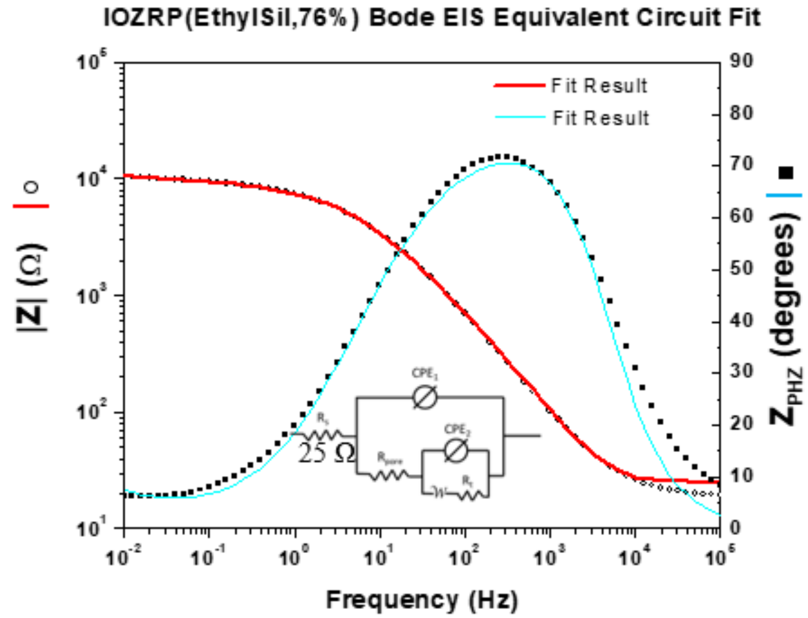

Figure 3.18:Experimental EIS data versus equivalent circuit fit for IOZRP (EthylSil,76%) for one cycle of the accelerated cycle testing conducted in 0.6 M NaCl. The fit utilized R_{soln} = 25.00 Ω (held constant for all fits), R_{ct} = 9.43x10^3 Ω, R_{pore} = 148.30 Ω, CPE_1 = 1.37x10^{-6} S·s^n, n = 0.61, CPE_2 = 13.44x10^{-6} S·s^m, m = 1.0, W = 2.4x10^{-3} S√s.

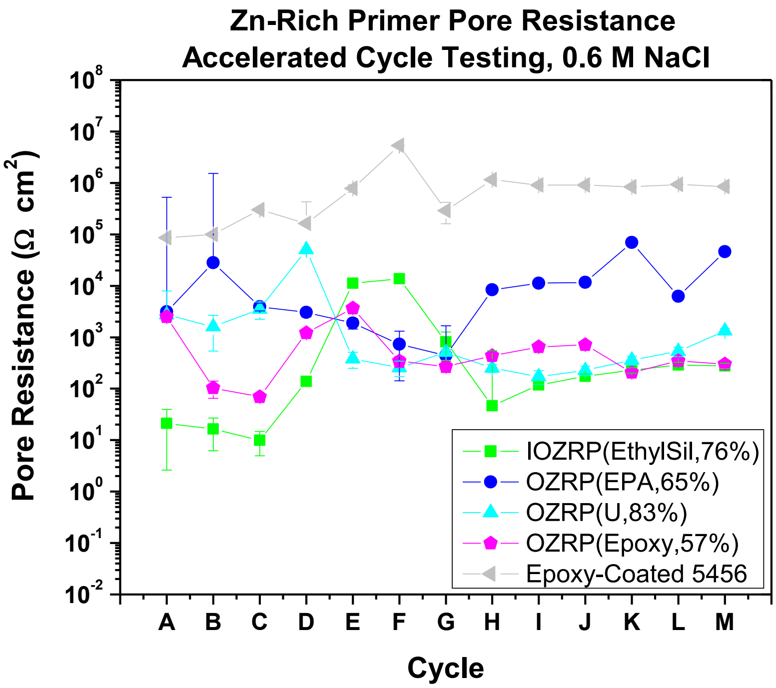

Figure 3.19:Pore resistance according to equivalent circuit fitting of the Bode impedance data measured following each cycle of accelerated cycle testing in 0.6 M NaCl.

supported by low R_{pore}. This trend is evaluated further in Figure 3.20, which demonstrates that OZRP(EPA,65%) experiences a sudden halt in anodic charge output and increase in R_{pore}, suspected to be due to corrosion product formation and Zn particle decoupling. The other ZRPs continue to output more anodic charge generally through the achievement of lower R_{pore} values (Figure 3.20). Following coating activation to reduce R_{pore}, both the IOZRP (EthylSil,76%) and the OZRP (Epoxy,57%) experience R_{pore} increase during Cycles C-E of the cycle test, but are uniquely able to reestablish lower R_{pore}. As the pore resistance is related to the capability for a coating to deliver anodic charge, the charge delay time must be assessed to understand the effect of R_{pore} on ZRP response.

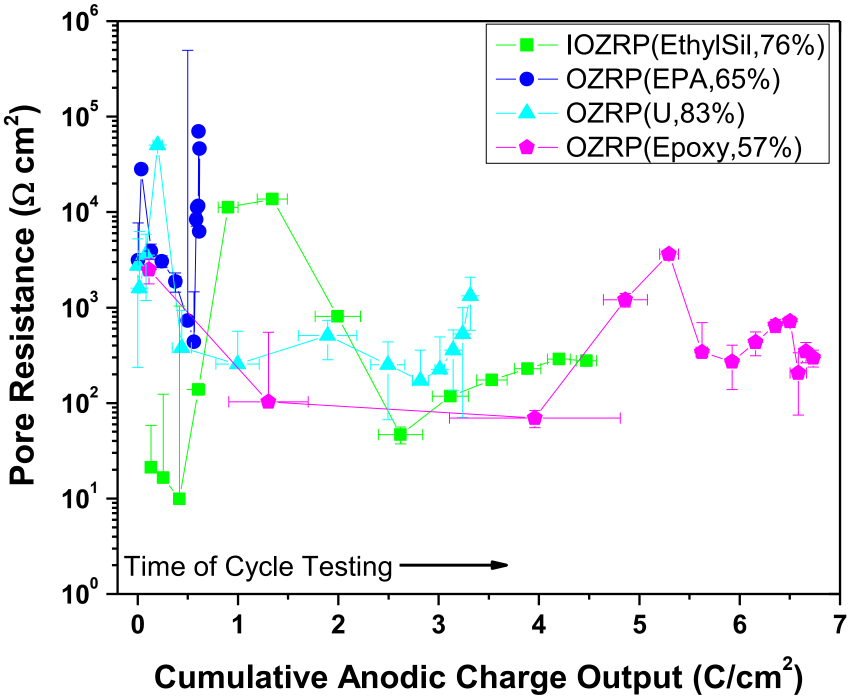

Figure 3.20:Pore resistance as resolved through EIS equivalent circuit fitting with respect to total anodic charge output achieved during the PS hold stages of the accelerated cycle test, demonstrating increased anodic charge usage when low pore resistance is present.

3.1.5.3 ***Resistor-Capacitor Time Constant and Zinc-Rich Primer Anodic Response Time***

The anodic response of each ZRP considered here may be understood in terms of a resistive-capacitive equivalent electrical circuit, which behaves according to the following relationship in terms of capacitive discharge time:

$$V(t) = 1 - V_o e^{-t/\tau} \qquad \text{Equation 3.1}$$

where τ is the circuit time constant, computed through multiplying $R_{pore} \cdot C_{coat}$ [74]. Physically, the polarization behavior for newly immersed Zn, OZRP (Epoxy,57%), and epoxy-coated 5456-H116 can be seen to follow this relationship in Figure 3.21 (however, note the differences in scale as

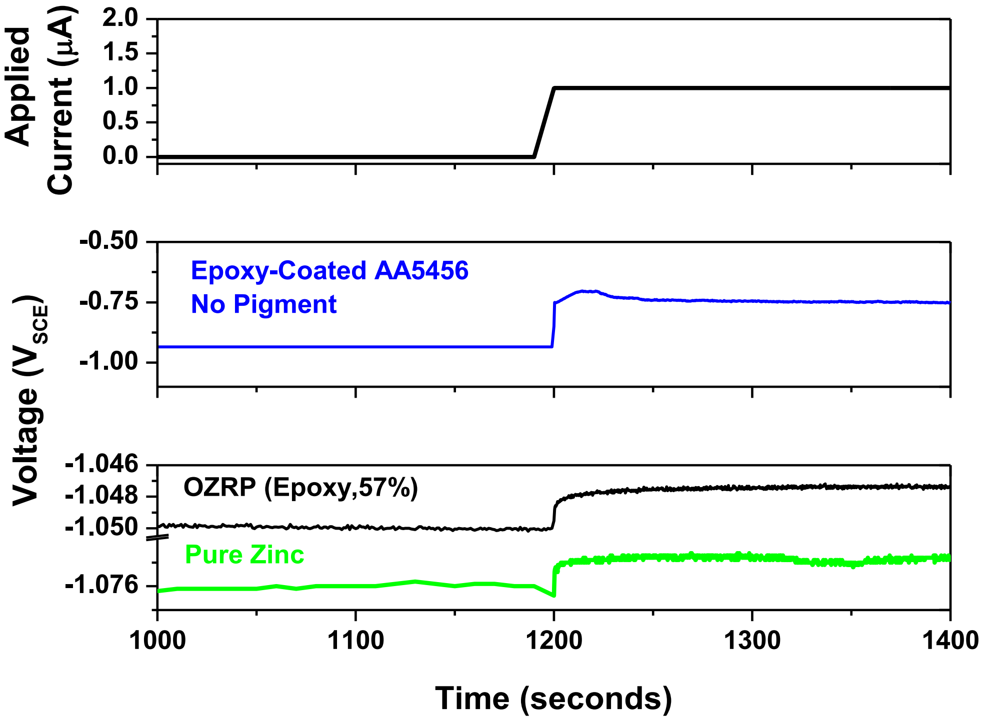

Figure 3.21:The RC circuit relationship dictating the natural anodic response upon the application of an anodic current perturbation (note the differences in scale).

polarizability changes, though the nature of the anodic response is the same). To understand the resistive-capacitive (RC) response of each ZRP in more detail, the equivalent circuit modeling of the EIS data (Figure 3.11) is used to obtain the time constant and discharge delay, which are directly related to ZRP design and may further inform the mechanisms underlying ZRP polarizability [75]. To perform this analysis, the constant phase element representative of the coating (CPE_1, Figure 3.18) was converted to capacitance (C_{coat}) using the relationship proposed by Hsu and Mansfeld [64]:

$$C_{coat} = Y_o(\omega''_{max})^{n-1} \qquad \text{Equation 3.2}$$

where Y_o is the admittance (1/ |Z''|) at 1 radian/s (~ 0.159 Hz), ω_{max}'' is the frequency where the maximum of the imaginary impedance (Z'') occurs, and *n* is the power law constant for the CPE. Calculation of the RC time constant (τ) utilized the R_{pore} values shown in Figures 3.19 and 3.20 and the coating capacitance determined from Equation 3.2. Longer-term ZRP performance is of particular interest and allowed for consideration of more stable trends, therefore the τ values obtained in Cycles G through M were averaged to yield the following averages: IOZRP (EthylSil,76%) has the lowest $\tau_{average}$ at 0.03 sec, followed by OZRP (U,83%) ($\tau_{average}$ = 0.07 sec), OZRP (Epoxy,57%) ($\tau_{average}$ = 0.16 sec), and lastly OZRP (EPA,65%) ($\tau_{average}$ = 1.78 sec) (Table 3.V). Through use of Equation 3.1, these $\tau_{average}$ values may be utilized to determine ZRP anodic response time (capacitive discharge delay), as shown in Figure 3.22. These results are insightful to understand the ZRP polarizability evidenced through galvanostatic pulse testing (Figure 3.17) together with ACU (Table 3.III).

Despite similar ACU achieved throughout cycle testing in IOZRP (EthylSil,76%) and OZRP (Epoxy,57%) (10.7% and 10.4%), the reduced polarizability of IOZRP (EthylSil,76%) may be explained by this ZRP achieving half an order of magnitude faster anodic discharge time than OZRP (Epoxy,57%) (Figure 3.22, Table 3.V). The OZRP (U,83%), which achieves the second fastest anodic discharge time, achieved a considerably lower ACU in comparison to the less polarizable OZRP (Epoxy,57%) (6.2% versus 10.4%, Table 3.III), which explains the increased polarizability of OZRP (U,83%) (Figure 3.17). The OZRP (EPA,65%) achieves the lowest ACU and the greatest delay in anodic discharge, which supports this ZRP high polarizability. These trends suggest that low pore resistance enables more rapid anodic response time. Fast anodic response time coupled with high anodic charge output then favors low polarizability in these ZRPs.

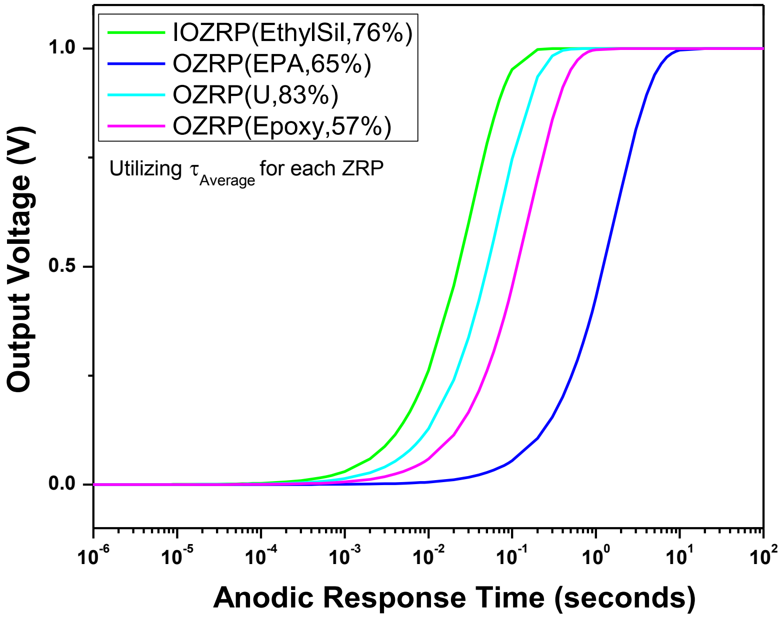

Figure 3.22:The time-dependent voltage discharge relation representative of each ZRP formulation based on the average RC time constant achieved during accelerated cycle testing, demonstrating differences in anodic response time for each primer upon the application of an anodic current perturbation.

However, one more phenomenon remains to be considered, which will affect R_{pore} significantly: corrosion product buildup. Comparison between the RC response of newly immersed ZRP (Figure 3.21) and the long-term experimental polarizability results (Figure 3.16 (blown up portions)) for these ZRPs suggest that corrosion product formation and spalling phenomena may also have an effect on polarization behavior as Zn surface area becomes covered or newly exposed. Further consideration of corrosion product effects will enlighten the understanding of polarizability trends.

3.1.5.4 *Zn-Rich Primer Oxidation: Secondary Barrier Formation*

To understand and predict the stability of intermediate cathodic potential achieved over extended time in service, the mechanism and effect of secondary barrier formation must also be assessed for each ZRP formulation. A major factor contributing to the formation of secondary barrier properties, and thus the eventual cessation of the galvanic protection functionality, is the type of corrosion product that forms for a given amount of primer porosity. As more voluminous corrosion product forms following Zn particle oxidation, there is increasing risk that Zn particle connectivity will decrease as these particles are forced apart, which may reduce galvanic performance. As illustrated in Table 3.IV, if equimolar fractions of available Zn particle were oxidized and distributed between the corrosion products formed on the OZRPs and the IOZRP (EthylSil,76%) throughout cycle testing, the IOZRP would have 16.1% greater volume of Zn corrosion product formation per mole of Zn^{2+} due to the additional presence of Smithsonite and Wulfingite. However, as can be seen in Figure 3.12, the IOZRP (EthylSil,76%) maintains relatively intermediate secondary barrier impedance by Cycle M. In contrast, the OZRP(EPA,65%) achieves high secondary barrier impedance by Cycle M (Figure 3.12), and the OCP achieved by this ZRP rises to the most positive average values (Figure 3.9), suggesting that corrosion product formation has the most influence on Zn particle connectivity in this ZRP (Table 3.V). The culmination of these analyses demonstrate that the maintenance of low pore resistance, high anodic charge output, and low anodic response time enable ZRPs to achieve optimal galvanic protection (Table 3.V). Coatings with these qualities will be most likely to effectively mitigate IGC / IG-SCC in aggressive marine service conditions.

3.1.6 **Conclusion**

Reduction in service life of Al-Mg components due to IGC and IG-SCC can be avoided through use of cathodic protection involving a ZRP. Mitigation of IG-SCC growth via a ZRP is challenging due to near instantaneous increase in 5456 area to protect during crack growth, thus an increasing demand on the ZRP performance. This work developed a new set of criteria to evaluate the ability of ZRPs to provide substrate protection against IG-SCC. The following conclusions were established.

- The candidate ZRPs were able to achieve global galvanic protection potentials below $E_{pit\,(\beta)}$, as required for effective IGC / IG-SCC mitigation on 5456-H116.
- As time of accelerated cycle testing increased, the ability to achieve a highly protective potential relative to $E_{pit\,(\beta)}$ decreased in the ZRPs, with the rate of decrease depending on the ZRP design.
- Potentiostatic hold sequences during cycle testing demonstrated that anodic charge usage in the candidate ZRPs depended on the pore resistance of the coating.
- Equivalent electrical circuit modeling of cycle testing EIS data demonstrated that the ZRPs with low pore resistance achieved faster anodic response time.

- Galvanostatic pulse testing to simulate dynamic 5456-H116 area creation demonstrated that the ZRPs with high anodic charge usage and low pore resistance in full immersion 0.6 M NaCl testing were also the least polarizable (having the highest critical current threshold past which coupled potentials exceeded $E_{pit\ (\beta)}$).

Competing Interests

These authors declare no competing financial or personal interests.

Data Availability Statement

Raw data obtained during this study are available in an open data repository, which can be accessed at the DOI 10.17605/OSF.IO/TJUZD.

3.1.7 References Cited

[1] N.J.H. Holroyd, G.M. Scamans, Environmental Degradation of Marine Aluminum Alloys—Past, Present, and Future, Corrosion. 72 (2016). doi:10.5006/1927.

[2] R.B. Niederberger, J.L. Basil, G.T. Bedford, Corrosion and Stress Corrosion of 5000-Series Al Alloys in Marine Environments, Corrosion. 22 (1966) 68–73. doi:10.5006/0010-9312-22.3.68.

[3] M.L.C. Lim, R.G. Kelly, J.R. Scully, Overview of Intergranular Corrosion Mechanisms, Phenomenological Observations, and Modeling of AA5083, Corrosion. 72 (2016). doi:10.5006/1818.

[4] W.J. Golumbfskie, K.T. Tran, J.M. Noland, R. Park, D.J. Stiles, G. Grogan, C. Wong, Survey of detection, mitigation, and repair technologies to address problems caused by sensitization of Al-Mg alloys on navy ships, Corrosion. 72 (2016) 314–328. doi:10.5006/1916.

[5] N.J.H. Holroyd, G.M. Scamans, The Role of Magnesium During Environment-Sensitive Fracture of Aluminium Alloys, Scr. Metall. Mater. 19 (1985) 945–946.

[6] D.R. Baer, C.F. Windisch, M.H. Engelhard, M.J. Danielson, R.H. Jones, J.S. Vetrano, Influence of Mg on the corrosion of Al, J. Vac. Sci. Technol. a-Vacuum Surfaces Film. 18 (2000) 131–136. doi:10.1116/1.582129.

[7] R.H. Jones, The Influence of Hydrogen on the Stress-Corrosion Cracking of Low-Strength Al-Mg Alloys, J. Miner. Met. Mater. 55 (2003) 42–46. doi:10.1007/s11837-003-0225-5.

[8] Standard Test Method for Determining the Susceptibility to Intergranular Corrosion of 5XXX Series Aluminum Alloys by Mass Loss After Exposure to Nitric Acid (NAMLT Test) 1, Annu. B. ASTM Stand. i (2004) 5–7. doi:10.1520/G0067-04.2.

[9] M.A. Steiner, S.R. Agnew, Modeling sensitization of Al–Mg alloys via β-phase precipitation kinetics, Scr. Mater. 102 (2015) 55–58. doi:10.1016/j.scriptamat.2015.02.012.

[10] M.A. Steiner, S.R. Agnew, Predictive sensitization modeling for AA5xxx aluminum alloys including non-isothermal cases, Corrosion. 72 (2016) 169–176. doi:10.5006/1675.

[11] D. Mizuno, R.G. Kelly, Galvanically Induced Intergranular Corrosion of AA5083-H131 Under Atmospheric Exposure Conditions: Part 1—Experimental Characterization, Corrosion. 69 (2013) 580–592. doi:10.5006/0812.

[12] E.C. Cormack, The Effect of Sensitization on the Stress Corrosion Cracking of Aluminum Alloy 5456, Naval Postgraduate School, 2012.

[13] R. Zhang, S.P. Knight, R.L. Holtz, R. Goswami, C.H.J. Davies, N. Birbilis, A survey of sensitization in 5xxx series aluminum alloys, Corrosion. 72 (2016) 144–159. doi:10.5006/1787.

[14] M.E. McMahon, J.R. Scully, J.T. Burns, Mitigation of intergranular stress corrosion cracking in Al-Mg by electrochemical potential control, J. Miner. Met. Mater. 69 (2017) 1389–1397. doi:10.1007/s11837-017-2362-2.

[15] C.B. Crane, R.. Kelly, R.P. Gangloff, Crack chemistry control of intergranular stress corrosion cracking in sensitized Al-Mg, Corrosion. 72 (2016) 242–263. doi:10.5006/1852.

[16] C.B. Crane, R.P. Gangloff, Stress corrosion cracking of Al-Mg alloy 5083 sensitized at low temperature, Corrosion. 72 (2016) 221–241. doi:10.5006/1766.

[17] R.H. Jones, D.R. Baer, M.J. Danielson, J.S. Vetrano, Role of Mg in the stress corrosion cracking of an Al-Mg alloy, Metall. Mater. Trans. A. 32 (2001) 1699–1711. doi:10.1007/s11661-001-0148-0.

[18] M.E. McMahon, P.J. Steiner, A.B. Lass, J.T. Burns, The effect of temper and composition on intergranular stress corrosion cracking in Al-Mg alloys, Corrosion. 73 (2017) 347–361. doi:10.5006/2317.

[19] C. Taylor, J.R. Scully, R.G. Kelly, R. Lillard, M. Neurock, T. Lookman, M. Francis, Atomistic inquiries into the effect of hydrogen on metals, (2010).

[20] J.R. Scully, G.A. Young, S. Smith, Hydrogen Embrittlement of Aluminum and Aluminum-Based Alloys, in: R.P. Gangloff, B.P. Somerday (Eds.), Gaseous Hydrog. Embrittlement Met. Energy Technol., 1st ed., Woodhead Publishing Limited, Cambridge, UK, 2012: pp. 707–768.

[21] A. Aballe, M. Bethencourt, F.J. Botana, M.J. Cano, M. Marcos, Localized alkaline corrosion of alloy AA5083 in neutral 3.5% NaCl solution, Corros. Sci. 43 (2001) 1657–1674. doi:10.1016/S0010-938X(00)00166-9.

[22] M.E. McMahon, J.R. Scully, J.T. Burns, The effect of potential on stress corrosion cracking in a highly sensitized Al-Mg alloy, Mater. Sci. Eng. A, Draft. (2019).

[23] M.E. McMahon, J.R. Scully, J.T. Burns, Erratum to: Mitigation of Intergranular Stress Corrosion Cracking in Al–Mg by Electrochemical Potential Control, J. Miner. Met. Mater. 69 (2017) 1724–1726. doi:10.1007/s11837-017-2432-5.

[24] P. Plagemann, J. Weise, A. Zockoll, Zinc-magnesium-pigment rich coatings for corrosion protection of aluminum alloys, Prog. Org. Coatings. 76 (2013) 616–625. doi:10.1016/j.porgcoat.2012.12.001.

[25] C. Matzdorf, W. Nickerson, Aluminum alloy coated pigments and corrosion-resistant coatings, 8,277,688, 2012. doi:10.1016/j.(73).

[26] R.J. Santucci Jr., B. Kannan, J.R. Scully, Electrochemical diagnostic cycle testing on magnesium and magnesium oxide-pigmented primers on 2024-T351, Corrosion. 74 (2017) 96–111. doi:10.5006/2547.

[27] A.D. King, B. Kannan, J.R. Scully, Environmental degradation of a mg-rich primer in selected field and laboratory environments: Part 1-without a topcoat, Corrosion. 70 (2014) 512–535. doi:10.5006/0988.

[28] B. Kannan, J.R. Scully, Performance of a magnesium-rich primer on pretreated AA2024-T351 in selected laboratory and field environments: Conversion coating pretreatments, Corrosion. 72 (2016) 1363–1384. doi:10.5006/2187.

[29] A.D. King, J.R. Scully, Sacrificial anode-based galvanic and barrier corrosion protection of 2024-T351 by a Mg-rich primer and development of test methods for remaining life assessment, Corrosion. 67 (2011) 1–22. doi:10.5006/1.3590330.

[30] A.D. King, J.S. Lee, J.R. Scully, Finite Element Analysis of the Galvanic Couple Current and Potential Distribution between Mg and 2024-T351 in a Mg Rich Primer Configuration, J. Electrochem. Soc. 163 (2016) C342–C356. doi:10.1149/2.0171607jes.

[31] R.J. Santucci, B. Kannan, W. Abbott, J.R. Scully, Magnesium and Magnesium Oxide Primer on AA2024-T351: Assessment of Field Performance, Corrosion. 73 (2017) 1196–1201. doi:10.5006/2545.

[32] A.D. King, B. Kannan, J.R. Scully, Environmental degradation of a mg-rich primer in selected field and laboratory environments: Part 2-primer and topcoat, Corrosion. 70 (2014) 536–557. doi:10.5006/0989.

[33] A.D. King, N. Birbilis, J.R. Scully, Accurate electrochemical measurement of magnesium corrosion rates; A combined impedance, mass-loss and hydrogen collection study, Electrochim. Acta. 121 (2014) 394–406. doi:10.1016/j.electacta.2013.12.124.

[34] M.S. Han, S. Ko, S.H. Kim, S.K. Jang, S.J. Kim, Optimization of corrosion protection potential for stress corrosion cracking and hydrogen embrittlement of 5083-H112 alloy in seawater, Met. Mater. Int. 14 (2008) 203–211. doi:10.3365/met.mat.2008.04.203.

[35] J.W. Watson, Y.Z. Shen, M. Meshii, Effect of cathodic charging on the mechanical properties of aluminum, Metall. Mater. Trans. A. 19 (1988) 2299–2304. doi:10.1007/BF02645053.

[36] X.G. Zhang, Corrosion and Electrochemistry of Zinc, 1st ed., Plenum Press, New York, 1996.

[37] G. Parashar, D. Srivastava, P. Kumar, Ethyl silicate binders for high performance coatings, Prog. Org. Coatings. 42 (2001) 1–14. doi:10.1016/S0300-9440(01)00128-X.

[38] Z.W.J. Wicks, F.N. Jones, S.P. Pappas, D.A. Wicks, Organic Coatings: Science and Technology, 3rd ed., John Wiley & Sons, Inc., Hoboken, NJ, 2007.

[39] F. Theiler, The rust preventing mechanism of zinc dust paints, Corros. Sci. 14 (1974). doi:10.1016/0010-938X(74)90001-8.

[40] L. Zhang, A. Ma, J. Jiang, D. Song, J. Chen, D. Yang, Anti-corrosion performance of waterborne Zn-rich coating with modified silicon-based vehicle and lamellar Zn (Al) pigments, Prog. Nat. Sci. Mater. Int. 22 (2012) 326–333. doi:10.1016/j.pnsc.2012.07.001.

[41] J. Feliu S., M. Morcillo, S. Feliu, Deterioration of cathodic protection action of zinc-rich paint coatings in atmospheric exposure, Corrosion. 57 (2001) 591–597. doi:10.5006/1.3290386.

[42] B. Hafford, W.E. Pepper, T.B. Lloyd, Zinc Dust and Zinc Powder, 1st ed., International Lead Zinc Research Organization, New York, 1982.

[43] O.Ø. Knudsen, U. Steinsmo, M. Bjordal, S. Nijjer, Accelerated Testing : Correlation between four accelerated tests and five tears of offshore field testing, JPCL. (2001) 52–56.

[44] O.Ø. Knudsen, U. Steinsmo, M. Bjordal, Zinc-rich primers - Test performance and electrochemical properties, Prog. Org. Coatings. 54 (2005) 224–229. doi:10.1016/j.porgcoat.2005.06.009.

[45] O.Ø. Knudsen, J.I. Skar, Cathodic Disbonding of Epoxy Coatings - Effect of Test Parameters, Nace Int. (2008) 1–10.

[46] F. Mansfeld, C.H. Tsai, Determination of coating deterioration with EIS. I. Basic relationships, Corrosion. 47 (1991) 958–963. doi:10.5006/1.3585209.

[47] R.A. Armas, C.A. Gervasi, A. di Sarli, S.G. Real, J.R. Vilche, Zinc-rinch paints on steels in artificial seawater by electrochemical impedance spectroscopy, Corrosion. 48 (1992) 379–383. doi:10.5006/1.3315948.

[48] C.H. Tsai, F. Mansfeld, Determination of coating deterioration with EIS: Part II. Development of a method for field testing of protective coatings, Corrosion. 49 (1993) 726–737. doi:10.5006/1.3316106.

[49] C.M. Abreu, M. Izquierdo, M. Keddam, X.R. Nóvoa, H. Takenouti, Electrochemical behaviour of zinc-rich epoxy paints in 3% NaCl solution, Electrochim. Acta. 41 (1996) 2405–2415. doi:10.1016/0013-4686(96)00021-7.

[50] S.J. Feliu, R. Barajas, J.M. Bastidas, M. Morcillo, S. Feliu, Study of Protection Mechanisms of Zinc-Rich Paints by Electrochemical Impedance Spectroscopy, Electrochem. Impedance Anal. Ans Interpret. ASTM STP 1188. (1993) 438–449. doi:10.1520/STP18084S.

[51] H. Marchebois, C. Savall, J. Bernard, S. Touzain, Electrochemical behavior of zinc-rich powder coatings in artificial sea water, Electrochim. Acta. 49 (2004) 2945–2954. doi:10.1016/j.electacta.2004.01.053.

[52] S. Shreepathi, P. Bajaj, B.P. Mallik, Electrochemical impedance spectroscopy investigations of epoxy zinc rich coatings: Role of Zn content on corrosion protection mechanism, Electrochim. Acta. 55 (2010) 5129–5134. doi:10.1016/j.electacta.2010.04.018.

[53] N. Hammouda, H. Chadli, G. Guillemot, K. Belmokre, The Corrosion Protection Behaviour of Zinc Rich Epoxy Paint in 3% NaCl Solution, Adv. Chem. Eng. Sci. 01 (2011) 51–60. doi:10.4236/aces.2011.12009.

[54] J.R. Vilche, E.C. Bucharsky, C.A. Giúdice, Application of EIS and SEM to evaluate the influence of pigment shape and content in ZRP formulations on the corrosion prevention of naval steel, Corros. Sci. 44 (2002) 1287–1309. doi:10.1016/S0010-938X(01)00144-5.

[55] D. Pereira, J.D. Scantlebury, M.G.S. Ferreira, M.E. Almeida, The application of electrochemical measurements to the study and behaviour of zinc-rich coatings, Corros. Sci. 30 (1990) 1135–1147. doi:10.1016/0010-938X(90)90061-9.

[56] V. Barranco, S. Feliu, S. Feliu, EIS study of the corrosion behaviour of zinc-based coatings on steel in quiescent 3% NaCl solution. Part 1: Directly exposed coatings, Corros. Sci. 46 (2004) 2203–2220. doi:10.1016/j.corsci.2003.09.032.

[57] R.A. Francis, Inorganic Zinc Silicate Coatings - The Early Days Part II: The Morgan Whyalla Pipeline, in: R.A. Francis (Ed.), Inorg. Zinc Coatings Hist. Chem. Prop. Appl. Altern., 2nd ed., The Australasian Corrosion Association Incorporated, Victoria, 2013: pp.

18–23.

[58] M.D. Danford, D.W. Walsh, M.J. Mendrek, The Corrosion Protection of 2219-T87 Aluminum by Organic and Inorganic Zinc-Rich Primers, 1995.

[59] R. Castaing, Electron Probe Microanalysis, in: L. Marton, M. Claire (Eds.), Adv. Electron. Electron Phys., Academic Press, 1960: pp. 317–386.

[60] P. Zavalij, V. Pecharsky, Fundamentals of Powder Diffraction and Structural Characterization of Materials, 2nd ed., Springer, New York, 2009.

[61] B. Kannan, A.D. King, J.R. Scully, Effect of pretreatments on Alloy 2024-T351 corrosion protection by magnesium-rich, nonchromium primer (MgRP): Laboratory characterization in full immersion, Corrosion. 71 (2015) 1093–1109. doi:10.5006/1700.

[62] H.P. Hack, J.R. Scully, Defect Area Determination of Organic Coated Steels in Seawater Using the Breakpoint Frequency Method, J. Electrochem. Soc. 138 (1991) 33. doi:10.1149/1.2085574.

[63] R. Hirayama, S. Haruyama, Electrochemical impedance for degraded coated steel having pores, Corrosion. 47 (1991) 952–958. doi:10.5006/1.3585208.

[64] C.H. Hsu, F. Mansfeld, Technical Note: Concerning the Conversion of the Constant Phase Element Parameter Y 0 into a Capacitance, Corrosion. 57 (2001) 747–748. doi:10.5006/1.3280607.

[65] P. Colomban, S. Cherifi, G. Despert, Raman identification of corrosion products on automotive galvanized steel sheets, J. Raman Spectrosc. 39 (2008) 881–886. doi:10.1002/jrs.1927.

[66] M.E. McMahon, R.J. Santucci Jr., J.R. Scully, Advanced Chemical Stability Diagrams to Predict the Formation of Complex Zinc Compounds in Chloride Environment, Sci. Rep. (n.d.).

[67] B.R. Hinderliter, K.N. Allahar, G.P. Bierwagen, D.E. Tallman, S.G. Croll, Water sorption and diffusional properties of a cured epoxy resin measured using alternating ionic liquids/aqueous electrolytes in electrochemical impedance spectroscopy, J. Coatings Technol. Res. 5 (2008) 431–438. doi:10.1007/s11998-008-9107-7.

[68] C. Moreno, S. Hernández, J.. Santana, J.G. Guzmán, R.. Souto, S. González, Characterization of water uptake by organic coatings used for the corrosion protection of steel as determined from capacitance measurements, Int. J. Electrochem. Sci. 7 (2012) 8444–8457.

[69] G.R. Newill, James F.; McKnight, Steven H.; Hoppel, Christopher P.R.; Cooper, Effects of Coatings on Moisture Absorption in Composite Materials, 1999.

[70] M. Dornbusch, S. Kirsch, C. Henzel, C. Deschamps, S. Overmeyer, K. Cox, M. Wiedow, U. Tromsdorf, M. Dargatz, U. Meisenburg, Characterization of the water uptake and electrolyte uptake of organic coatings and the consequences by means of electrochemical impedance spectroscopy and UV-vis spectroscopy, Prog. Org. Coatings. 89 (2015) 332–343. doi:10.1016/j.porgcoat.2015.03.016.

[71] S. Ahmadi, Adobe conservation: Evaluation of Silicone and Acrylic consolidants, Queen's University, 2008. http://qspace.library.queensu.ca/handle/1974/1523.

[72] G.D. Semchenko, V.T. Zagoskii, G.P. Telegin, A refractory ceramic with ethyl silicate binder, Refract. Ind. Ceram. 22 (1981) 531–535. doi:10.1007/BF01406898.

[73] H. Marchebois, S. Joiret, C. Savall, J. Bernard, S. Touzain, Characterization of zinc-rich powder coatings by EIS and Raman spectroscopy, Surf. Coatings Technol. 157 (2002) 151–161. doi:10.1016/S0257-8972(02)00147-0.

[74] J.W. Nilsson, S.A. Riedel, Electric Circuits, 6th ed., Prentice-Hall, Inc., Upper Saddle River, 1999.
[75] Q. Wang, The role of zinc particle size and loading in cathodic protection efficiency, Virginia Commonwealth University, 2012.

CHAPTER 4

Zinc-Rich Primer-Based IG-SCC Mitigation on Highly Sensitized AA5456-H116

4.1 Mitigation of Intergranular Cracking in Al-Mg Alloys via Zn-Based Electrode Potential Control in Sodium Chloride Solution

M. E. McMahon,[1,2] J. R. Scully,[1] and J. T. Burns[1]

Center for Electrochemical Science and Engineering, Department of Materials Science and Engineering, University of Virginia, Charlottesville, VA 22904, USA

[1]395 McCormick Rd., Department of Materials Science and Engineering, University of Virginia, Charlottesville, VA 22904, USA

[2]Corresponding author email: mm5kn@virginia.edu.

4.1.1 Abstract

Mitigation of the initiation and propagation of intergranular stress corrosion cracking (IG-SCC) in a single edge notch tensile specimen is achieved through use of various Zn-based anodes on highly sensitized Al-Mg alloy AA5456-H116. Slow rising displacement tests in NaCl solution demonstrate the efficacy of cathodic protection through galvanic coupling with pure Zn or an inorganic Zn-rich primer (IOZRP), as well as through spray-coating the fracture specimen with the IOZRP (with various widths of exposed substrate about the Mode I crack path). These tests were conducted in either 0.60 or 5.45 M NaCl. In all cases, the IG-SCC mitigation performance correlates with the measured coupled potentials, which was corroborated with fixed potential results (via potentiostat). Furthermore, galvanic coupling was able to halt actively propagating IG-SCC (K of 10 MPa√m in 0.60 M NaCl); specifically, the crack growth rate was decreased by three orders of magnitude following the application of cathodic protection. This high level of mitigation is achieved via a potentiostat, coupling with a pure Zn anode (with an exposed area as low as 0.03 cm^2 (1 Zn: 110 5456 surface area ratio)), and by coupling with the IOZRP (with an exposed area

as low as 0.67 cm^2 (67 primer: 350 5456 surface area ratio)). Results are interpreted within the context of a coupled anodic dissolution-hydrogen embrittlement model developed previously.

4.1.2 **Introduction**

AA5xxx-series alloys such as AA5456-H116 are increasingly used in marine superstructures due to their high strength-to-weight ratio and general corrosion resistance.[1] The needed strength is achieved via solid solution strengthening with a supersaturation of 5 wt.% Mg. However, prolonged exposure to in-service temperatures as low as 40°C can lead to precipitation of β phase (Al_3Mg_2) on the grain boundaries due to Mg segregation.[2–6] This process is termed sensitization and is often quantified by the ASTM G-67 Nitric Acid Mass Loss Test (NAMLT).[7] The β phase is highly anodic to the Al-matrix, and in the presence of aggressive (e.g. aqueous chloride) environments extensive dissolution of this phase can lead to severe intergranular corrosion (IGC) and stress corrosion cracking (IG-SCC).[8–10] The NAMLT value is a rough proxy for IG-SCC susceptibility in Al-Mg alloys; specifically, Al-Mg alloys are considered resistant at NAMLT < 15 mg/cm^2, intermediate at 15 – 25 mg/cm^2, and susceptible at > 25 mg/cm^2.[7,8] Following sufficiently long service life, NAMLT values may reach 65 – 70 mg/cm^2 in low temperature exposure. The IG-SCC behavior is hypothesized to be governed by a coupled anodic dissolution-H embrittlement process. Dissolution of the β phase (and possibly the Al matrix) catalyzes the formation of an aggressive high [Cl^-] and acidified local crack tip chemistry, both of which facilitate the enhanced generation of crack tip H. Atomic H can be adsorbed on the crack tip surface and absorbed into the matrix where the local hydrostatic stresses will drive diffusion of the H to the fracture process zone causing embrittlement.[11–16] The hydrogen-based mechanism has been validated by experiment as well as modeling under a recent extension of the hydrogen enhanced decohesion (HEDE) hypothesis to the Al-Mg system.[12,14] Applied potential during cracking is important in this model because corrosion of β and Al matrix exhibit strong dependency on potential and solution chemistry.

Mitigation of IG-SCC has been demonstrated in recent work using intermediate levels of cathodic polarization in aggressive saline environments.[11,12,15] This suppression was observed for sensitized AA5083-H131 (NAMLT $\leq$ 40 mg/cm^2) and AA5456-H116 (NAMLT 65 mg/cm^2) tested in 0.60 M NaCl.[11,12,15] Intermediate levels of cathodic polarization were proven to be effective on NAMLT 65 mg/cm^2 AA5456-H116 in saturated (5.45 M) NaCl, and in 2.00 M and saturated (5.00 M) $MgCl_2$, though mitigation was less potent than in the 0.60 M NaCl environment.[15] Mitigation of IG-SCC is hypothesized to be due to the lowering of the crack tip potential below the critical pitting potentials to suppress β as well as α breakdown (i.e. in 5.45 M NaCl, $E_{pit\ (\beta)} = -1.02$ Volts versus saturated calomel electrode (V_{SCE}) and $E_{pit\ (\alpha)} = -0.85\ V_{SCE}$[15]), which inhibits the development of an aggressive crack tip chemistry thus retarding the generation of embrittling H.[11,12,15,17] The variation in the level of mitigation for various bulk environments was found to scale with the corresponding changes in the β and α breakdown potentials in closely correlated environments.[15]

These results motivate study into engineering-relevant methods of providing effective cathodic protection on naval Al superstructures; one such method is the use of sacrificial coatings. Specifically, Zn-based sacrificial coating systems have been selected for this study due to their ability to polarize to intermediate cathodic potentials, the high magnitude of anodic charge output, and the relatively low self-corrosion rate observed in these systems in prior work.[18–23] Naval Al superstructures contain complex geometries and operate in harsh service conditions, as such coating systems will inevitably experience defects (e.g. mechanical damage, environmental degradation, imperfect system installation, etc.). To address this there are three fundamental requirements for service-ready cathodic protection systems: (1) the sacrificial anodic coating must be able to polarize the crack tip despite macro-defects in the coating and for various component/crack geometries, (2) the ability to quickly couple the external potential with the crack tip potential to electrochemically respond to changes in the crack tip conditions, suppress aggressive occluded chemistry formation, and mitigate IG-SCC, and (3) long-term endurance in aggressive saline environments.

The objective of the current study is to assess the ability of Zn-rich primers to enable rapid mitigation of IG-SCC as well as long term mitigation across a range of stress intensity, alloy/anode ratios, and environments through various engineering-relevant methods. The electrochemical characteristics of a Zn-based coating system will be established and initial evaluation of the efficacy of inhibiting IG-SCC via coatings-based galvanic coupling and spray-coating will be conducted via fracture mechanics-based testing in 0.60 M NaCl and 5.45 M NaCl. Results will evaluate the efficacy and limitations of mitigating IG-SCC via this Zn-rich primer system, as well as providing insight into the importance of primer design on cathodic protection performance in environmental fracture scenarios.

4.1.3 **Experimental Procedures**

4.1.3.1 ***Material and Mechanical Loading***

The composition, metallography, and mechanical properties of the non-recrystallized, 5.7 cm-thick AA5456-H116 material lot utilized in this study are described elsewhere.[14] All 5456 material was sensitized to NAMLT 65 mg/cm^2 through heat treatment at 373 K for 336 hours, which constitutes extensive (≥95%) grain boundary β coverage.[12,14] Linear elastic fracture mechanics (LEFM) testing was performed on S-L oriented single edge notch tensile (SENT) specimens with a gauge width of 17.33 mm and thickness of 6.62 mm. Isolated tests were also performed on thicker SENT samples with gauge width of 12.70 mm and thickness of 12.80 mm. Two types of LEFM testing were performed: constant stress intensity (K) (10 MPa√m) and slow rising displacement. Electrical discharge machined notches of 1.46 mm and 4.80 mm depth centered in the gauge section were used for the constant K and slow rising displacement tests, respectively. All samples were fatigue pre-cracked using a decreasing stress intensity range (ΔK) protocol ($R = 0.1$, frequency = 8 Hz) in laboratory air to a notch plus crack depth of 2.75 mm (constant K) and 5.30 mm (slow rising displacement), with the final maximum stress intensity being 3.5 MPa√m. The slow rising displacement tests were conducted at an initial rate of 0.25 MPa√m/hr from a K of 2.0 MPa√m following a 1-34 hour hold at K = 1.0 MPa√m in full immersion to ensure anode activation (achieving the most negative expected coupled potential based on the Zn:5456 surface area ratio (SAR)). Constant K testing consisted of a K ramp at 0.25 MPa√m/hr from a K value of 2.0 to 10.0 MPa√m under protective potential (-1.1 V_{SCE}), after which the K was held constant at 10.0 ± 0.3 MPa√m as the electrochemical conditions were varied. Prior slow rising displacement results for AA5456 in 0.6 M NaCl demonstrate that a K of 10.0 MPa√m is well above the IG-SCC threshold at -0.8 V_{SCE}, as such the effect of varying galvanic coupling conditions on the IG-SCC growth rates could be examined at this stress intensity.[24] Crack extension was monitored with ~0.5 µm resolution via the direct current potential difference (dcPD) method, the details of which are described elsewhere.[14,25] Resolved crack growth related solely to plasticity effects at the crack tip were subtracted from all da/dt versus K data presented in this work; as such all reported data represents real crack growth. Data analysis utilized Ramberg Osgood constants derived from compression testing stress strain curves to calculate the total elastic-plastic stress intensity (K_J) via

J-integral plastic corrections; details of the underlying fundamentals and application of this method are provided elsewhere.[26]

4.1.3.2 *Environment and Anode/Coating Details*

The environment (either 0.60 or 5.45 M (saturated) NaCl) was maintained in a 200-mL acrylic cell fastened about the SENT sample, with electrolyte flowing at 20 mL/min from a 2.0 L reservoir in ambiently aerated conditions at room temperature.

The effect of galvanic coupling on the IG-SCC behavior was investigated in two ways: (1) connecting anodes to the LEFM sample through a zero-resistance ammeter (ZRA), or (2) directly spray-depositing a coating onto AA5456-H116. These experimental scenarios are graphically illustrated in Figure 4.1. For the first case, the 5456 was galvanically coupled to either pure Zn anodes or Zn-rich primer (ZRP) panels (Figure 4.1a). When ZRA was utilized the anodes were separated from the bulk 0.60 M or 5.45 M NaCl environment via a Pyrex[e] Buchner Funnel fitted with a 3-5 μm pore diameter fritted glass disk, which allowed slow solution flow but mitigated Zn^{2+} ion dispersion thus isolating the role of galvanic protection from chemical effects (Figure 4.1a). The 99.95% pure Zn anodes were cold mounted in epoxy and electrically connected to a ZRA via perfluoroalkoxy alkane (PFA)-insulated Cu wire. The ZRP coated panels, consisting of NAMLT 65 mg/cm^2 AA5456 (in the S-T orientation), were spray-coated with the ZRP. These panels were electrically connected by PFA-insulated Cu wire on the uncoated panel face. Exposed 5456 surfaces and ZRP edges were covered in lacquer to expose only the ZRP surface area during immersion (Figure 4.1a).

---

[e] Trade Name

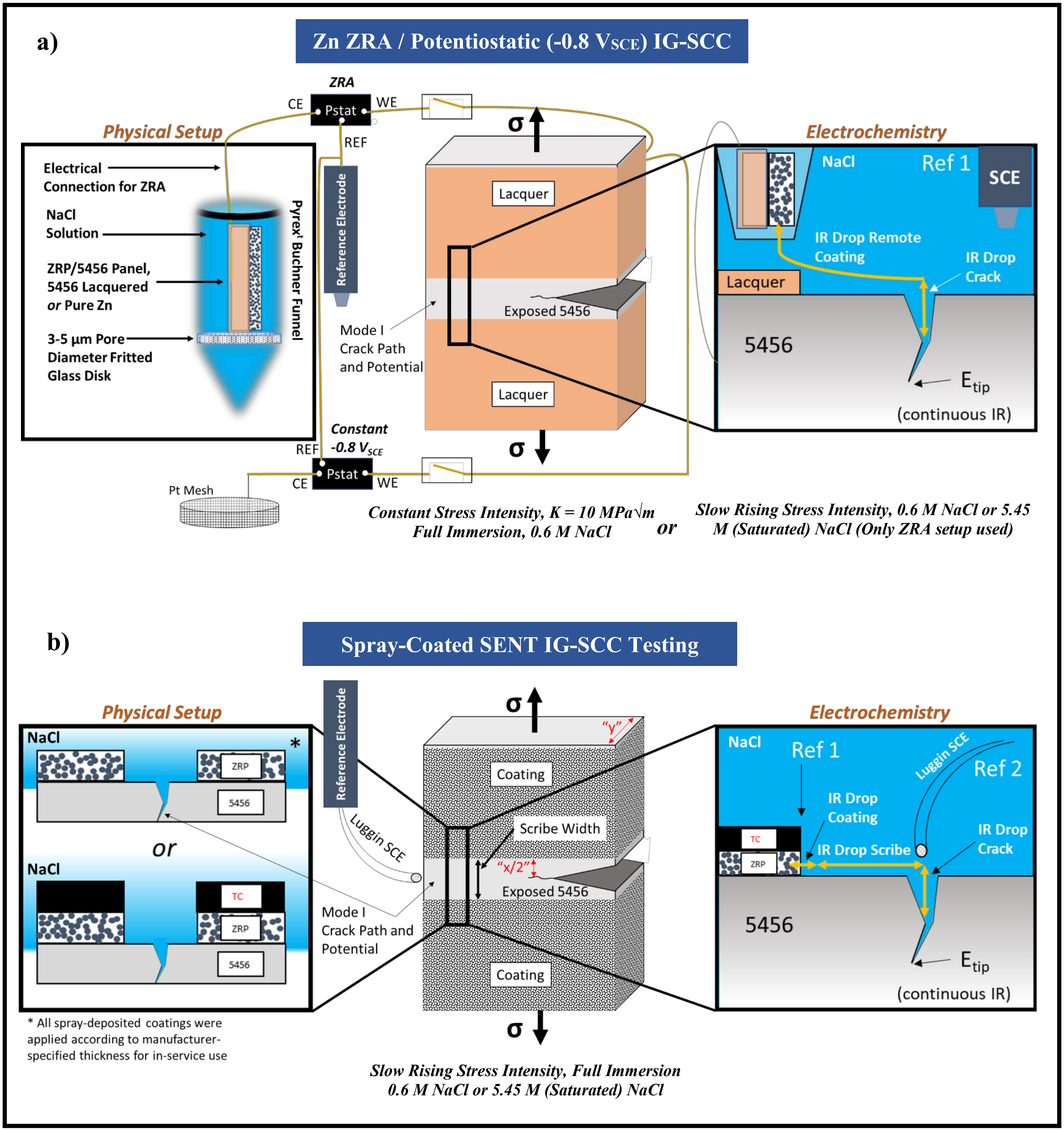
a)
Zn ZRA / Potentiostatic (-0.8 V$_{SCE}$) IG-SCC
Physical Setup
Electrical Connection for ZRA
NaCl Solution
ZRP/5456 Panel, 5456 Lacquered or Pure Zn
3-5 µm Pore Diameter Fritted Glass Disk
Pyrex® Buchner Funnel
ZRA
CE
Pstat
WE
REF
Reference Electrode
σ
Lacquer
Exposed 5456
Mode I Crack Path and Potential
Lacquer
σ
Constant -0.8 V$_{SCE}$
REF
CE
Pstat
WE
Pt Mesh
Electrochemistry
NaCl
Ref 1
SCE
IR Drop Remote Coating
IR Drop Crack
Lacquer
5456
E$_{tip}$
(continuous IR)
Constant Stress Intensity, K = 10 MPa√m
Full Immersion, 0.6 M NaCl
or
Slow Rising Stress Intensity, 0.6 M NaCl or 5.45 M (Saturated) NaCl (Only ZRA setup used)
b)
Spray-Coated SENT IG-SCC Testing
Physical Setup
NaCl
*
ZRP
5456
or
NaCl
TC
ZRP
5456
* All spray-deposited coatings were applied according to manufacturer-specified thickness for in-service use
Reference Electrode
Luggin SCE
Mode I Crack Path and Potential
σ
"y"
Coating
Scribe Width
"x/2"
Exposed 5456
Coating
σ
Electrochemistry
NaCl
Ref 1
Luggin SCE
Ref 2
IR Drop Coating
TC
ZRP
IR Drop Scribe
IR Drop Crack
5456
E$_{tip}$
(continuous IR)
Slow Rising Stress Intensity, Full Immersion
0.6 M NaCl or 5.45 M (Saturated) NaCl

Figure 4.1: Schematics detailing the LEFM testing setup utilized in the present work. The scenario in (a) demonstrates the ZRA setup used to galvanically couple 5456 to either pure Zn or a ZRP in a fritted funnel to isolate galvanic effects, which was utilized both in slow rising displacement and constant K = 10 MPa√m testing. In scenario (b) the LEFM sample is spray-coated with a protective coating (ZRP, ethyl silicate resin (no Zn pigment), or IOZRP + topcoat) to create a galvanic couple directly on the 5456 specimen surface, which utilized slow rising displacement to evaluate the IG-SCC mitigation ability of these sacrificial anodes in 0.60 M or 5.45 M NaCl. Of note is that the IR drop crack will operate down the sides of the crack flank, not down the crack mouth as it may seem to appear above.

Increased engineering relevance was achieved by spray-depositing a ZRP directly onto the LEFM sample before performing the fracture testing in the NaCl environments, as is graphically illustrated in Figure 4.1b. In these cases, the entire sample was coated except for a region (termed scribe) that was centered on the Mode I crack path and had widths ranging from 0.3 mm to 15.0 ("x" in Figure 4.1b, or the width of exposed 5456 substrate about the Mode I crack path). The effect of crack geometry was assessed through replicate tests on ZRP-coated LEFM samples having thickness of 12.80 mm instead of 6.60 mm ("y" in Figure 4.1b). The effect of adding a topcoat (TC, Figure 4.1b) to the ZRP was demonstrated through addition of the Sherwin Williams Macropoxy 646 Fast Cure Epoxy with 0.3 and 5.0 mm scribe widths. Prior work suggests that limiting the bulk surface area of 5456 on a bare sample can cathodically limit the IG-SCC susceptibility, independent of a coupled galvanic benefit.[27,28] As such, two LEFM samples were coated with an ethyl silicate resin (containing no Zn pigment) with the minimum scribe width of 0.3 mm and tested in slow rising displacement in 0.60 M and 5.45 M NaCl to decouple galvanic and cathodic limitation effects.[f]

---

[f] Masking cathode area is a critical test of whether IG-SCC is inhibited by lack of cathode surface or galvanic coupling. If the pigment-free coating blocked cathode sites sufficiently to limit anodic current at the crack tip, IG-SCC would be suppressed.

Two ZRPs were utilized in this study: (1) Sherwin Williams Zn Clad® II Plus, which is an inorganic Zn-rich primer (referred to in this study as the IOZRP), and (2) Sherwin Williams F159 Epoxy Polyamide (organic) Zn-Rich Primer (referred to as OZRP). The IOZRP consists of an inorganic ethyl silicate resin with 76 vol.% (83 wt.%) Zn loading and a $ZnCl_2$-containing accelerator additive to promote the formation of a low resistivity Zn silicate cement.[29] Prior work demonstrated through galvanostatic pulse methods that the IOZRP is exceptionally non-polarizable (requiring a high applied anodic current density before the anodic potential achieved is no longer protective on 5456) and exhibits rapid response time in comparison to select organic ZRPs.[18] The low polarizability (relative proximity of the coupled current and potential to that of the pure Zn/5456 galvanic couple) of the IOZRP is demonstrated in potentiodynamic plots in Figure 4.2 (0.6 M NaCl) and Figure 4.3 (5.45 M NaCl) relative to pure Zn in 0.6 M NaCl. Alternately, the OZRP used in this study (epoxy polyamide resin having 85 wt.%, 65 vol.% Zn pigment content) was the most polarizable ZRP candidate comparatively studied in previous work.[18] The high polarizability of the OZRP causes a more positive galvanically coupled potential and lower coupled current density when connected with 5456, as illustrated in Figures 4.2 and 4.3. The IOZRP performance is evaluated in the current work under a wide range of testing scenarios to evaluate the efficacy of achieved IG-SCC mitigation, while the OZRP performance was assessed only in select testing situations for relative comparison. The topcoat was selectively utilized on the IOZRP to assess the effect on IG-SCC mitigation performance in 5.45 M NaCl. Spray coating of the ethyl silicate resin, IOZRP, IOZRP + topcoat, and OZRP was conducted by LUNA Innovations Inc. according to manufacturer specifications.

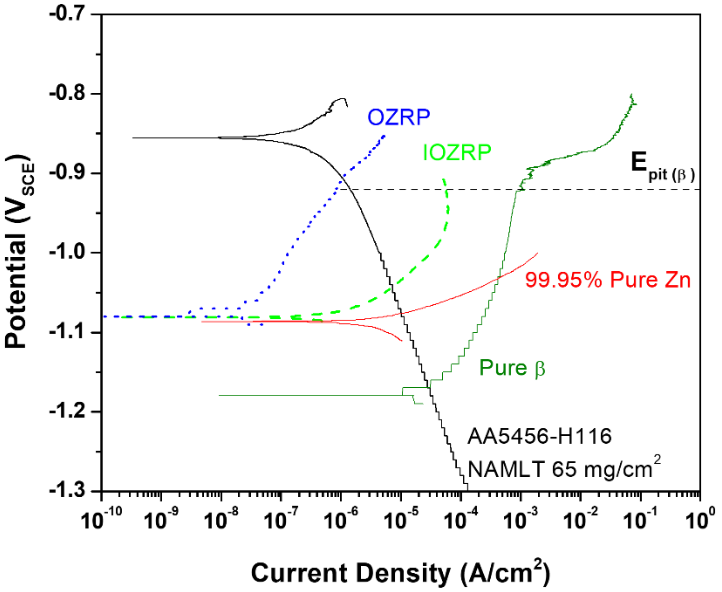

Figure 4.2: Theoretical galvanic couple potentials and current densities for the IOZRP, OZRP, and pure Zn with 5456 in 0.6 M NaCl. All Zn-rich primer potentiodynamic analyses were completed following 10 hours at OCP to allow for primer activation. The tested β phase area was ≈0.0078 cm^2, whilst all other potentiodynamic scans were conducted on 0.78 cm^2 areas (ie. 5456, ZRPs, Zn). Established coupled potentials more negative than $E_{pit(\beta)}$ (-0.92 V_{SCE}) theoretically yield the most effective cathodic protection for the 5456 substrate.

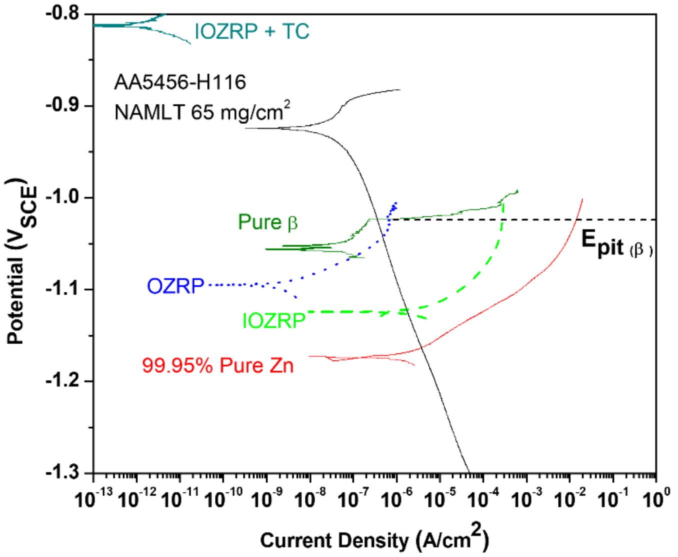

Figure 4.3: Theoretical galvanic couple potentials and current densities for the OZRP, IOZRP, IOZRP+TC, and pure Zn with 5456 in 5.45 M NaCl. All Zn-rich primer potentiodynamic analyses were completed following 10 hours at OCP to allow for primer activation. The tested β phase area was ≈0.0078 cm^2, whilst all other potentiodynamic scans were conducted on 0.78 cm^2 areas (ie. 5456, ZRPs, Zn). Established coupled potentials more negative than $E_{pit(\beta)}$ (-1.02

V_{SCE}) theoretically yield the most effective cathodic protection for the 5456 substrate. Note the extension in the x-axis to lower magnitudes of current density.

4.1.3.3 *Electrochemical Monitoring and Testing Philosophy*

The aim of the current testing is to evaluate the ability of potential control to (1) mitigate the onset of IG-SCC and (2) suppress actively growing IG-SCC through use of finite Zn-based anodes. Prior efforts demonstrated that cathodic polarization can mitigate the onset and growth of cracking with a near-infinite anode (potentiostat-based control).[12,15] Therefore, the slow rising displacement testing conducted here approaches greater engineering relevance by evaluating objective (1), or the ability of Zn-based anodes to mitigate the *onset* of IG-SCC. These evaluations will assess finite anode performance under increasingly aggressive saline, stress intensity, and geometrical conditions. This evaluation is conducted via application of the Zn anodes in various geometries and conditions from the onset of crack initiation and growth testing, with stress intensity slowly increased in either 0.60 M or 5.45 M NaCl (illustrated in Figure 4.1).

The initial measurement of cathodic protection in the slow rising displacement tests utilizes two electrochemical setups. In instances of galvanic coupling, the ZRA method utilizes a potentiostat to monitor both coupled current and potential, where the 5456 SENT is the working electrode, the Zn-based anode is utilized as the counter electrode, and an SCE is the reference electrode. As shown in Figure 4.1a, in ZRA the 5456 LEFM sample is the WE, thus the measurement of negative current means that the 5456 is the cathode. When considering LEFM samples spray-coated with the ZRP, the coupled current between the 5456 and the ZRP can no longer be accurately measured, and platinum mesh serves as the counter electrode with the ZRP/5456 SENT serving as the working electrode. The accurate measurement of the coupled potential is then of the utmost importance, so the SCE is fitted with a Luggin capillary placed along the Mode I crack path on the SENT (Figure 4.1b). The Ohmic (ie. IR) voltage drop effects which will influence these measurements are outlined in Figure 4.1, and will be evaluated in further detail in the Results and Discussion.[g]

The finite anode IG-SCC mitigation performance is then examined in more aggressive crack tip conditions by assessing objective (2), or the ability to suppress *actively growing* IG-SCC through use of finite Zn-based anodes (e.g. pure Zn or ZRP coated panels). Suppressing active crack growth is a greater challenge than mitigating SCC from the start of the testing due to need for the potential (and subsequently the associated occluded site chemistry development and ensuing hydrogen production) at the crack tip to be altered in order to impact a change in crack velocity. To assess the ability to halt active crack advance, the constant stress intensity tests are performed under conditions where literature suggests the development of an aggressive acidified crack tip environment has already occurred.[11] As such, this testing is performed at a constant post-threshold K of 10.0 ± 0.3 MPa√m with the sample polarized to -0.8 V_{SCE} where a crack will be actively growing. Subsequently, the polarization is alternated between -0.8 V_{SCE} and cathodic polarizations via either potentiostat control or coupling with pure Zn or IOZRP (Figure 4.1a). These tests thus examine the efficacy of cathodic polarization-based mitigation of a growing crack with an established aggressive crack tip chemistry.

The methods utilized to quantify the change in crack tip velocity upon applied cathodic polarization, as well as the reproducibility of these effects, are complex and thus warrant further discussion. Steady state, fast SCC (crack growth rate $\approx 1 \times 10^{-3}$ mm/s) is first achieved during

---

[g] It is worth emphasizing here that the IR voltage drop down the crack will occur both down the crack flanks and down the crack mouth, but the major effect will be that which occurs down the crack flanks for the current ZRP-coated LEFM sample geometry. The Figure 1 schematics demonstrating this IR voltage drop effect in the crack should not be mistaken to show this effect arising only from the crack mouth.

constant K = 10 MPa√m tests by potentiostatically applying -0.8 V_{SCE}, followed by a cathodic polarization being applied (via the potentiostat or the galvanic coupling). The impact of the applied polarization is evaluated by the subsequent changes in the crack growth rate. For the potentiostat-controlled polarizations, the floating-ground mode is used with the LEFM sample (grounded by the sample grips) serving as the working electrode and platinized mesh as the counter electrode (Figure 4.1a). Coupling with Zn or IOZRP panels is achieved via the ZRA mode of a second floating-ground potentiostat, where either a pure Zn anode or IOZRP panels functioned as the counter electrode (Figure 4.1a). Utilizing this experimental setup, the ability to interrupt SCC growth was assessed via alternating polarization. For each LEFM sample, the polarization was alternated between -0.8 V_{SCE} controlled with a potentiostat and a cathodic polarization (via either the potentiostat or coupling with the Zn or IOZRP) 15 times. These 15 cycles were broken into 3 different sets of 5 cycles. Each set started with fast crack growth at -0.8 V_{SCE} (optimally ≈1 mm IG-SCC crack growth to start the set) which forms an altered and aggressive crack chemistry, then switched between cathodic polarizations where crack growth rate was reduced and the -0.8 V_{SCE} (0.5 mm crack growth for the 2-5th potential holds), followed by a final 5 hour hold at the cathodic polarization. A constant cathodic polarization level/method was used for cycling within each set; however, different sets invoked different levels/methods of cathodic polarization.

For sets investigating potentiostatic control, cathodic polarizations of -0.9 V_{SCE}, -1.0 V_{SCE}, -1.1 V_{SCE} were used. For coupling with a pure Zn anode, Zn surface areas of 3.00, 0.30, and 0.03 cm^2; prior evaluation demonstrated that these ratios achieve coupled potentials of -1.10, -1.05, and -1.02 V_{SCE}, respectively, in 0.6 M NaCl. These surface areas corresponded to initial Zn: 5456 SARs of 6:5, 1:11, and 1:96. For the IOZRP-controlled cathodic protection, initial surface areas of 12.00, 2.70, and 0.67 cm^2 were used; prior evaluation demonstrated expected coupled potentials of -1.06, -1.03, and -0.98 V_{SCE} (these levels are steady state and may vary with long times of exposure due to activation and depletion (e.g. the loss of available anodic charge due to Zn pigment dissolution)). These surface areas corresponded to initial ZRP: 5456 SARs of 5:1, 1:1, and 1:5. As the crack length increased through the duration of each set, these ratios would increase slightly in favor of the 5456. Each set utilized pristine (or new) IOZRP panels. An initial test at K = 10 MPa√m and constant potentiostatically-applied potential of -0.8 V_{SCE} validated the use of the freely rotating K solution for the SENT geometry[30] out to the crack length/sample width ratio (a/w) of 0.8 ($a \approx 14$ mm); this was further validated via the observed consistency in the da/dt values during the -0.8 V_{SCE} segments independent of the crack length.

The anodic response behavior and successively achieved potentials of the pure Zn, IOZRP, and OZRP were further assessed via a test that challenges the ability of the finite anode to protect new bare Al (thus simulating a crack tip) in electrochemical flat cells in saturated (5.45 M) NaCl. Using ZRA, pure Zn (0.1 cm^2) or ZRP (4.90 cm^2) served as the counter electrode while a 4.90 cm^2 area of NAMLT 65 mg/cm^2 5456 served as the working electrode. These area ratios were chosen to achieve the same initial coupled potential of -1.10 V_{SCE} in the pure Zn and IOZRP cases. To simulate the addition of a new, unpassivated defect, a freshly polished (1200 grit) rectangular prism of NAMLT 65 mg/cm^2 5456 having exposed surface area of 5.36 cm^2 was electrically connected via PFA-insulated Cu wire to the primary 5456 working electrode (4.90 cm^2) and was periodically immersed and removed from the NaCl solution in fixed time intervals.

Potentiodynamic polarization analyses (Figures 4.2 and 4.3) were conducted on intact, non-defected coatings on NAMLT 65 mg/cm^2 5456, as well as 99.95% pure Zn, pure β phase, and bare NAMLT 65 mg/cm^2 5456. These tests were carried out in electrochemical flat cells in 0.6 M NaCl or 5.45 M NaCl at 0.167 mV/sec with platinum mesh serving as the counter electrode and an SCE fitted with a Luggen capillary as reference in ambient, non-deaerated conditions.

4.1.4 **Results**

4.1.4.1 ***Mitigating the Onset of Crack Growth via Engineering Relevant Methods – 0.60 M NaCl***

The first issue addressed is whether the onset of IG-SCC can be suppressed by potential-controlled cathodic protection provided by Zn-based anodes having different attributes. Prior work demonstrated IG-SCC is fully inhibited (e.g., no cracking occurs) when the potential is held at -0.90 V_{SCE}, -1.00 V_{SCE}, and -1.10 V_{SCE} via a potentiostat during full immersion in 0.6 M NaCl.[15,24] As illustrated in Figure 4.4, coupling with finite Zn-based anodes achieves comparable levels of IG-SCC mitigation and the behavior scales with the resulting measured coupled potential. Specifically, galvanic coupling with 0.03 cm^2 of pure Zn (SAR of 1 Zn: 80 5456, E_{couple} = -1.01 V_{SCE}) and spray-coating with IOZRP (scribe width 0.3 mm, E_{couple} = -1.05 V_{SCE}) both suppressed initiation and growth of IG-SCC completely. Coupling with the IOZRP panel (1 IOZRP: 5 5456 initial SAR) resulted in reduced IG-SCC susceptibility. However, there was still a modest amount of IG-SCC (4.8 mm achieved upon reaching K = 20.0 MPa√m) observed with a threshold stress intensity (K_{TH}) of 9.0 MPa√m. The fact that there was cracking for the IOZRP panel where there was an E_{couple} of -0.96 V_{SCE}, is inconsistent with the behavior observed during the potentiostat-controlled testing where no cracking was observed at potentials cathodic to -0.9 V_{SCE}. Also reported in Figure 4.4 are the results from the sample spray-coated with the inorganic ethyl silicate resin without Zn pigment and with 0.3 mm scribe distance. The IG-SCC that occurs in this test demonstrates that simply covering the 5456 surface with a coating that restricts the available cathodic area does not mitigate IG-SCC (E_{couple} = -0.84 V_{SCE} (i.e., the same potential as the bare 5456 open circuit potential in 0.6 M NaCl), K_{TH} = 6.0 MPa√m). This suggests that the reduction in IG-SCC susceptibility observed for the IOZRP coated sample can be solely attributed to galvanic coupling with the Zn pigment.

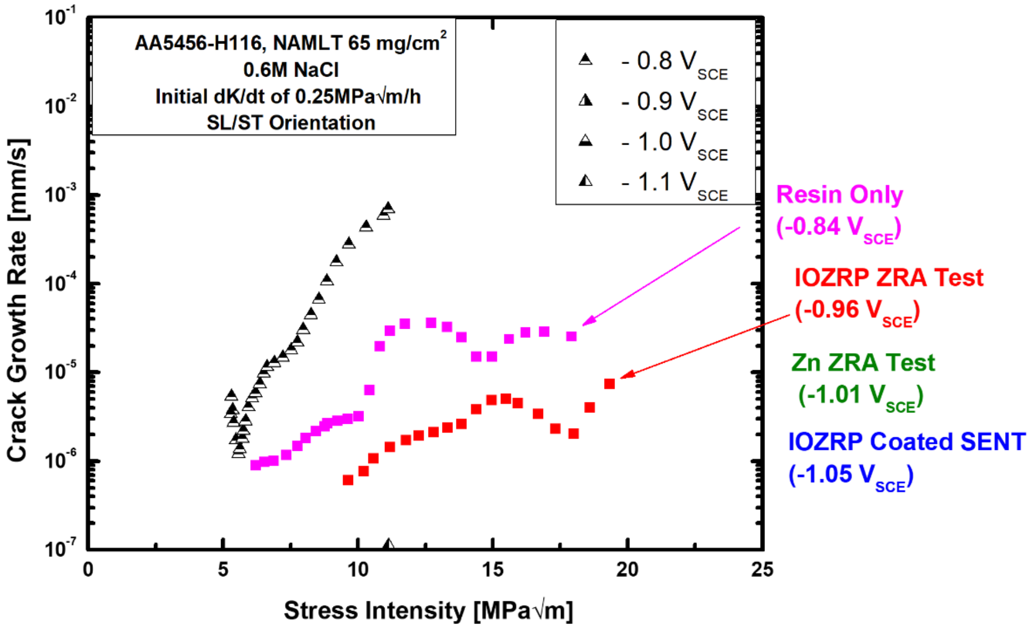

Figure 4.4: Slow rising displacement fracture testing results demonstrating the achieved IG-SCC mitigation in 5456, NAMLT 65 mg/cm^2 through use of (1) spray-coated ethyl silicate resin containing no Zn pigment; (2) galvanic coupling (ZRA) with pure Zn (initial SAR of 1 Zn : 80 5456) (no cracking occurred); (3) galvanic coupling with the IOZRP (1 IOZRP : 5 5456 initial surface area ratio); and (4) spray-coated IOZRP (scribe width 0.3 mm) (no cracking occurred) in 0.6 M NaCl. Results are compared to previously reported, potentiostat-based IG-SCC mitigation (shown in the legend).[15,24] No cracking occurred at potentiostatically-driven -0.90 V_{SCE}, -1.00 V_{SCE}, or -1.10 V_{SCE}.

4.1.4.2 *Mitigating the Onset of Crack Growth via Engineering Relevant Methods – 5.45 M NaCl*

The same slow rising displacement tests conducted in 0.6 M NaCl were performed in more aggressive 5.45 M NaCl full immersion; this effort has two goals. First, to determine if the ability of Zn-based anodes to mitigate the onset of IG-SCC is appreciably decreased with increased chloride content as previous work suggests.[15] Second, prior potentiostat-controlled testing demonstrated that the IG-SCC is retarded but not fully inhibited in this solution (Figure 4.5, see legend), suggesting that this is a more severe test of the cathodic protection performance for the different Zn-based anodes.[15] Several noteworthy findings are shown in Figure 4.5. First, the ZRA couple with pure Zn (initial SAR of 1 Zn to 20 5456, E_{couple} = -1.06 V_{SCE}) and IOZRP (initial SAR of 1 IOZRP: 5 5456, E_{couple} = -1.01 V_{SCE}), as well as spray-coating with IOZRP (E_{couple} = -1.14 V_{SCE} with 0.3 mm scribe) all significantly reduced the IG-SCC susceptibility. Specifically, K_{TH} values increased from 2 MPa√m at -0.8 V_{SCE} (potentiostatically applied) to 11, 13, and 16 MPa√m, respectively. Second, samples spray-coated with the inorganic ethyl silicate resin *without* Zn pigment content (scribe width 0.3 mm, E_{couple} = -0.92 V_{SCE}) and with the OZRP containing Zn pigment (scribe width 0.3 mm, E_{couple} = -0.90 V_{SCE}) demonstrated little reduction in IG-SCC susceptibility. Specifically, both exhibited K_{TH} values of 3 MPa√m. The former demonstrates that there is no apparent cathodic limitation of the cracking behavior brought about solely due to coverage of the 5456 surface by the inorganic resin. The latter results confirm prior work that suggests that the more polarizable OZRP is unable to reduce the potential on the surface of the 5456 specimen and thus cannot mitigate IG-SCC.[18] This result is supported by the potentiodynamic plot in Figure 4.3, wherein the OZRP coupled potential lies near $E_{pit\,(\beta)}$ and could enable high IG-SCC susceptibility if polarized to slightly more positive potentials (which indeed occurred in the slow rising displacement test). Third, the IG-SCC mitigation behavior correlated well with the measured E_{couple} for each of the samples compared to potentiostatic IG-SCC results, demonstrating that the potentials more negative than $E_{pit\,(\beta)}$ continue to suppress IG-SCC when utilizing Zn-based anodes. This is supported by the results in Figure 4.6 showing a

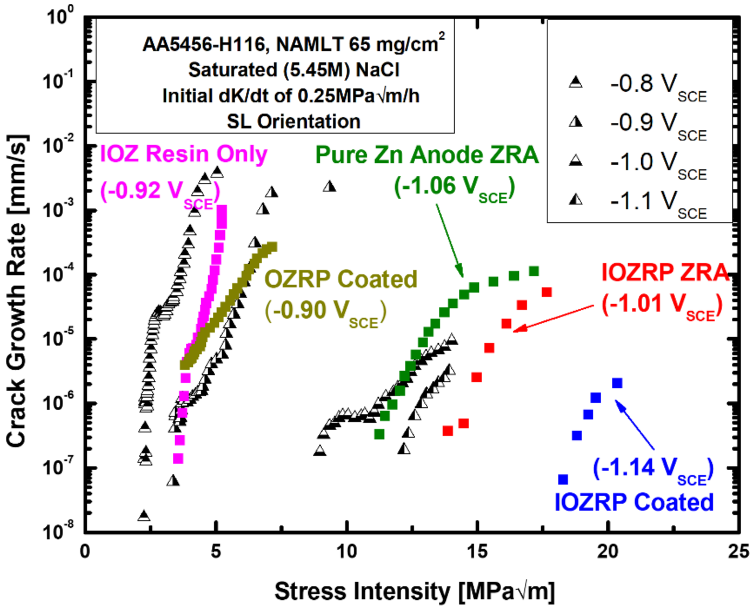

Figure 4.5: Slow rising displacement fracture testing results demonstrating the achieved IG-SCC mitigation in 5456, NAMLT 65 mg/cm^2 through use of (1) spray-coated ethyl silicate resin containing no anodic pigment; (2) galvanic coupling (ZRA) with pure Zn (initial surface area ratio of 1 Zn to 20 5456); (3) galvanic coupling with the IOZRP (1 IOZRP : 5 5456 initial surface area ratio); (4) spray-coated IOZRP (scribe width 0.3 mm); and (5) spray-coated OZRP (scribe width 0.3 mm) in saturated (5.45) M NaCl. Results are compared to previously reported, potentiostat-based IG-SCC mitigation, as detailed in the legend.[15]

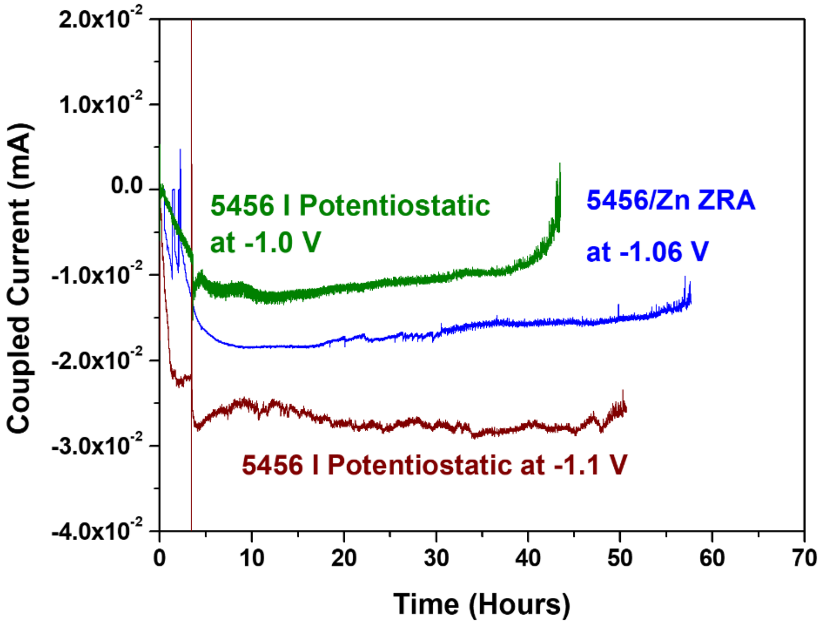

Figure 4.6: Established current trends throughout slow rising displacement testing in 5.45 M NaCl, demonstrating the equivalence of achieved currents between potentiostatic control and ZRA with pure Zn.

good correlation between the coupled current observed during potentiostat-controlled tests at -1.0 and -1.1 V_{SCE} and a Zn-based anode ZRA test with E_{couple} equal to -1.06 V_{SCE}.[h]

The results for the spray-deposited IOZRP with a 0.3 mm scribe in Figure 4.5 are encouraging for engineering application, however it is prudent to examine if the IOZRP has sufficient ability to distribute current to enable protection across wider scribes (e.g. Is there sufficient throwing power?). The IG-SCC growth rate behavior (in 5.45 M NaCl) for IOZRP-coated LEFM specimens with scribe widths of 0.3, 5.0, 10.0, and 15.0 mm are shown in Figure 4.7. The E_{couple} values were -1.14 V_{SCE} (0.3 mm scribe, K_{TH} = 16 MPa√m), -1.10 V_{SCE} (5.0 mm scribe, K_{TH} = 12 MPa√m), -1.08 V_{SCE} (10.0 mm scribe, K_{TH} = 10 MPa√m), and -1.07 V_{SCE} (15.0 mm scribe, K_{TH} = 8 MPa√m) upon completion of the slow rising displacement tests. The ability to maintain these intermediately cathodic potentials reaffirms the low polarizability of the IOZRP (Figure 4.3). As the scribe width was increased from 0.3 mm to 15.0 mm, the surface area of available IOZRP (and the overall quantity of available Zn pigment) was decreased, meaning that the SAR increasingly favored the 5456 such that the achieved potential became mildly more positive. The IG-SCC susceptibility decreased as the measured E_{couple} values became more negative and correlated well with the potentiostatic controlled results.

Maintaining IG-SCC inhibition at scribe widths up to 15 mm strongly demonstrates that the IOZRP coating has sufficient throwing power to (1) polarize the entirety of the crack flanks,

---

[h] This comparison is convincing. When galvanically coupling pure Zn and 5456 using the ZRA, the impedance of the glass frit between the two electrodes is not a factor that introduces sufficient IR voltage drop. Thus, there is no change in the coupled potential between the Zn and 5456 due to the presence of the glass frit. Therefore, a direct comparison with the potentiostatic controlled tests is justified.

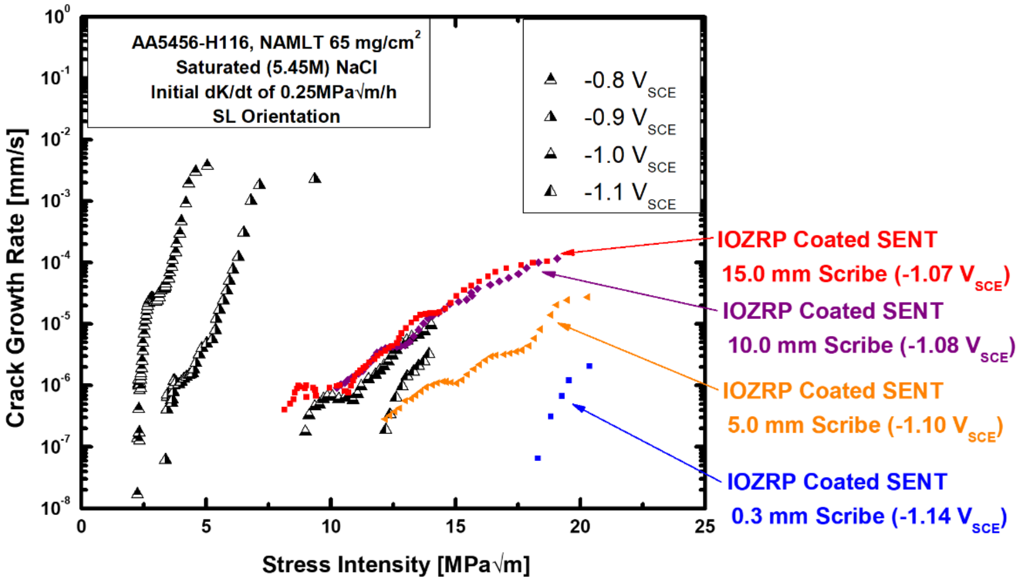

Figure 4.7: Slow rising displacement fracture testing results demonstrating the effect of increasing scribe width on achieved IG-SCC mitigation via spray-coated IOZRP on 5456 in 5.45 M NaCl. Results are compared to previously reported, potentiostat-based IG-SCC mitigation.[15]

and (2) to overcome any IR voltage drop from the crack flanks to the crack tip at the center of a 6.60 mm thick sample. Thus, the electrochemical attributes of the primer impact the crack tip electrochemical processes that govern the proposed coupled anodic dissolution/H-embrittlement damage mechanism.[11,12] It is worthwhile to further investigate (2) to determine if the Zn-based galvanic coupling can provide the same level of protection for a thicker sample (e.g. 'y' in Figure 4.1b increases) which would induce a higher IR voltage drop from the crack flanks to the tip at the center of the specimen. As such, slow rising displacement testing in 5.45 M NaCl was performed on 12.80 mm thick LEFM samples (termed "thick section LEFM samples") galvanically coupled via a ZRA with pure Zn or spray-coated with the IOZRP (scribe widths of 5 and 10 mm). Figure 4.8 illustrates that IG-SCC mitigation is achieved on the thick section LEFM samples for both pure Zn ZRA as well as for spray-deposited IOZRP. These results correlate well with the potentiostatic results on the 6.60 mm thick SENT, suggesting only a minor effect of increasing

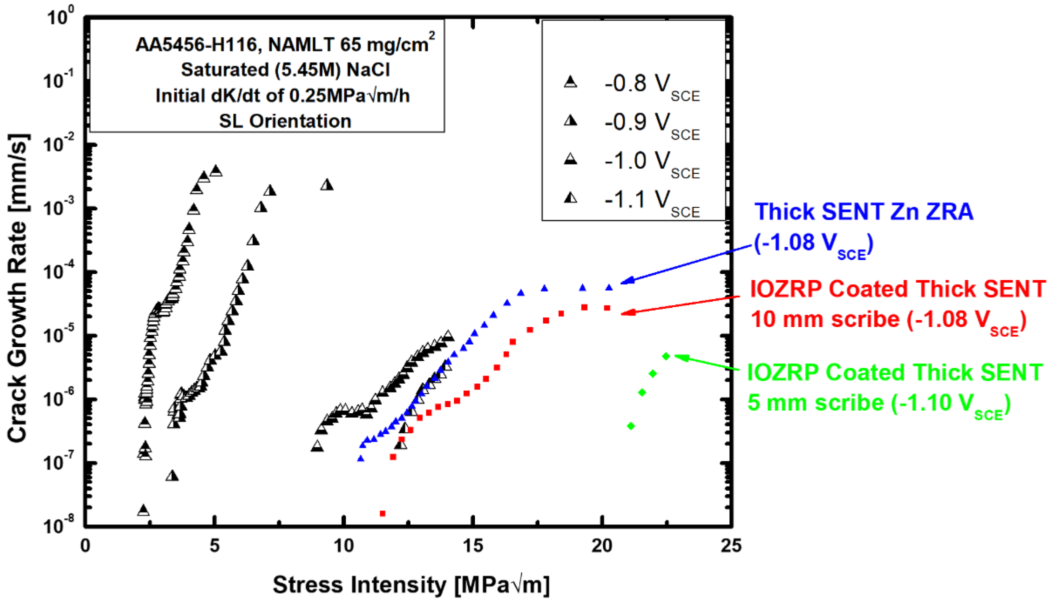

Figure 4.8: Slow rising displacement results demonstrating the effect of increased crack wake thickness on achievable IG-SCC mitigation via finite Zn anodes. The results of galvanic coupling with pure Zn (initial surface area ratio of 33 Zn to 10000 5456) as well as increasing scribe width on spray-coated IOZRP are demonstrated on a thick section 5456 LEFM sample (12.80 mm thickness) in 5.45 M NaCl. Results are compared to previously reported, potentiostat-based IG-SCC mitigation from testing done on 5456 LEFM samples with thickness of 6.60 mm.[15]

the crack wake cross sectional thickness. Rather, the main impact seems to be the increase in exposed 5456 surface area to increase the coupled potential. Specifically, galvanic coupling with pure Zn (initial SAR of 33 Zn: 10000 5456) achieved -1.08 V_{SCE} and a comparable K_{TH} of 11 MPa√m, and the spray-deposited IOZRP also demonstrated IG-SCC mitigation in accordance with the achieved potential (-1.10 V_{SCE} with 5.0 mm scribe, K_{TH} = 20 MPa√m, and -1.08 V_{SCE} with 10.0 mm scribe, K_{TH} = 13 MPa√m) (Figure 4.8).

Lastly, for engineering applications it is possible that the ZRP may be covered by an epoxy topcoat (TC), or some other mission specific coating. To understand the effect of the added topcoat on the IOZRP polarizability, this coating combination was first assessed in non-defected form in 5.45 M NaCl via potentiodynamic polarization, as shown in Figure 4.3 for comparison to the

IOZRP, OZRP, and pure Zn. These results demonstrate that the topcoat significantly increases the IOZRP polarizability when no macro-defects (such as a scribe) are present in the coating. Specifically, the open circuit potential of the IOZRP is increased from -1.13 V_{SCE} to -0.82 V_{SCE} in 5.45 M NaCl once the epoxy topcoat is present. However, in an environmental fracture scenario where crack initiation has occurred, a macro-defect in the primer/TC system could enable more effective sacrificial anode-based cathodic protection. As such, LEFM specimens (6.60 mm thickness) were spray-coated with IOZRP followed by an epoxy topcoat, after which the samples were tested with scribe widths of 0.3 and 5.0 mm in 5.45 M NaCl. Despite the scribe defect to expose a cross-section of the underlying IOZRP (Figure 4.1b), Figure 4.9 illustrates that the topcoat reduces the inhibiting effect of the IOZRP (K_{TH} = 3 MPa√m in both cases). This is likely due to the vast reduction in the exposed IOZRP surface area to only the cross-sectional edge (illustrated in Figure 4.1b, IOZRP + TC scenario), which causes the coupled potential to increase substantially to the 5456 OCP (-0.88 V_{SCE}). As expected, severe IG-SCC occurs at these potentials.

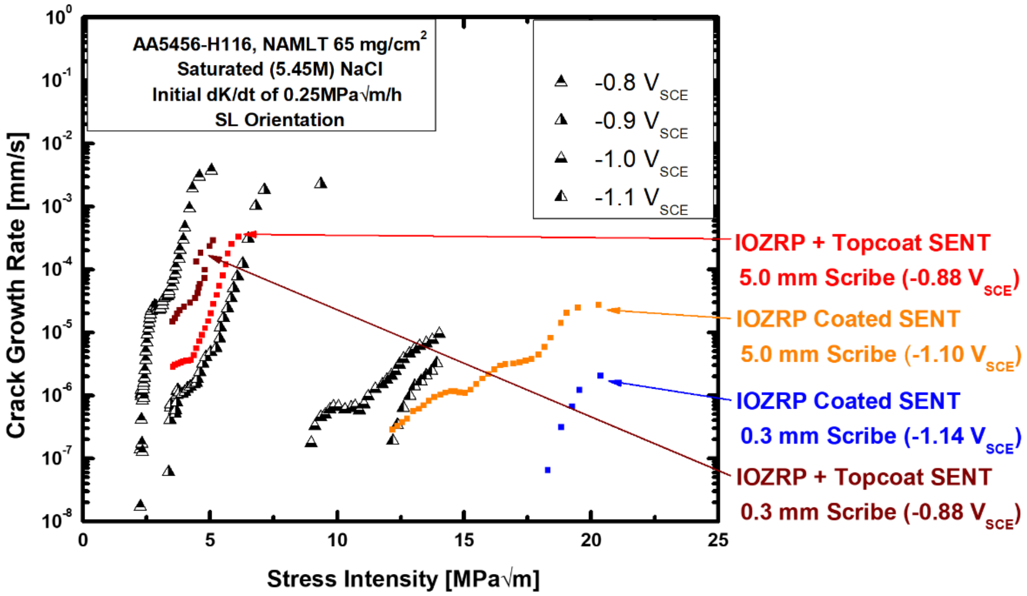

Figure 4.9: Slow rising displacement results demonstrating the effect of a topcoat on the IG-SCC mitigation performance of the spray-coated IOZRP on 5456, NAMLT 65 mg/cm^2 in 5.45 M NaCl.

Results are compared to previously reported, potentiostat-based IG-SCC mitigation as well as to the spray-coated IOZRP specimens having the same scribe and crack wake geometry but no topcoat.[15]

These results demonstrate that, due to the increased polarizability of the IOZRP + TC system, the substrate OCP will be sensed rather than the slightly more positive potential measured when no scribe was present (Figure 4.3). Regardless, both scenarios enable aggressive IG-SCC. Up to 34 hours of activation time was allotted to the 0.3 mm IOZRP + TC test to ensure activation of the primer beneath the TC, during which spikes in the coupled potential experienced in the scribe were evident (as measured by a Luggin probe, Figure 4.1b), presumably as Zn pigments were contacted when electrolyte penetrated the scribed interface. However, the spikes of protective potential were short-lived, with scarcely any occurring after 15 hours of exposure in 5.45 M NaCl. These results are shown in comparison to the non-topcoated IOZRP and OZRP coupled potential results in Figure 4.10.

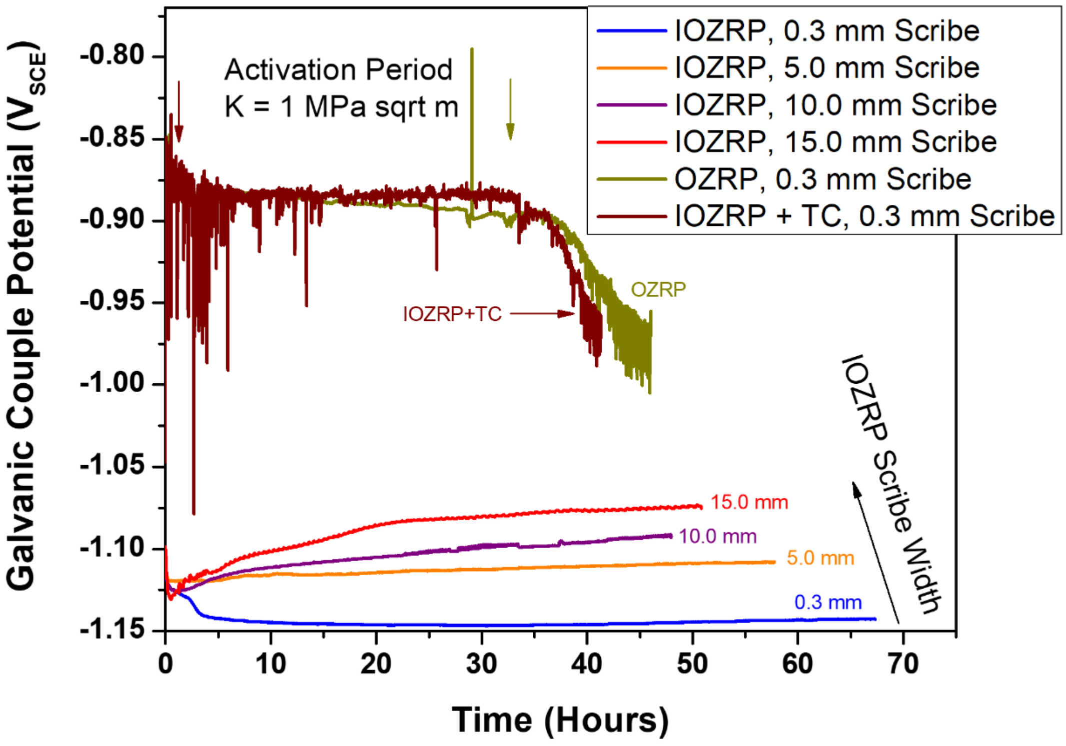

Figure 4.10: The galvanic couple potential established between NAMLT 65 mg/cm^2 5456 and the selected spray-coated metal rich primers during SCC testing in 5.45 M NaCl. This plot demonstrates the effect of increasing scribe width on the coupled potential achieved by the IOZRP, as well as the degradation in the galvanic protection of this primer when a topcoat is applied. The more polarizable OZRP was also tested with a 0.3 mm scribe, which performed similarly to the IOZRP + TC in 5.45 M NaCl. The almost 1.5 day activation period given to the OZRP and IOZRP + TC is shown on the plot, after which the slow rising displacement test was initiated and IG-SCC advance propagated through the LEFM width in approximately 10 hours.

4.1.4.3 *Active Crack Growth Suppression at Constant K = 10 MPa√m via Zn Anodes*

The second issue addressed in this paper is whether an already established aggressive crack tip chemistry associated with rapid IG-SCC growth can be altered sufficiently to retard crack growth via sacrificial anode-based cathodic protection provided by Zn-based systems. In this scenario, the efficacy of cathodic protection will depend on the ability to supply the necessary current to achieve adequate cathodic potentials, which depends on the bulk solution chemistry, the ratio of galvanically coupled surface areas, the resistance associated with any binding resin that may be present, the response time and polarizability associated with the specific pigment loading/resin combination, and the transient increase in surface area at the crack tip.[18,31–33] The cathodic potentials and corresponding current density must alter the crack chemistry and reduce hydrogen production and uptake in order to limit hydrogen transport to the fracture zone.[11] Arguably this process starts upon achieving a sufficiently cathodic local potential and current density on the crack flank and possibly the crack tip.

4.1.4.4 *Simulated Crack Growth Response Observed in Zn-Based Anodes*

To begin to understand these influences, anodic response testing was performed in 5.45 M NaCl and is reported in Figure 4.11. Through 5 iterations of roughly doubling the coupled bare 5456 surface area (to vaguely simulate the exposure of new 5456 surface area via crack growth) a pure Zn anode of 0.1 cm^2 coupled to 4.90 cm^2 5456 (Zn: 5456 SAR of 1:49 initially, rising to 1:102 when simulating crack growth) generally maintains a cathodic polarization below $E_{pit(\beta)}$ (-1.02 V_{SCE}, as needed to ensure mitigation of IG-SCC [15]). A decrease in the effective charge output with further iterations results in degradation in the level of the achieved cathodic polarization (Figure 4.11a). When 4.90 cm^2 5456 was coupled with 4.90 cm^2 of IOZRP (initial ZRP: 5456 SAR of 1:1, rising to ~ 1:2 following the 5456 addition) to achieve the same initial E_{couple} of -1.10 V_{SCE}, the results demonstrated an initially comparable performance to the pure Zn anode (Figure 4.11b). With further iterations, the effective charge output decreased and the ability to maintain cathodic potentials below $E_{pit(\beta)}$ was compromised. Specifically, by the fourth iteration the coating was unable to maintain control of a protective potential, though with time the IOZRP did reestablish potential below $E_{pit(\beta)}$ while still coupled to the 10.26 cm^2 5456 area. Lastly, the more polarizable[18] (Figure 4.3) OZRP was evaluated with the same SAR as in the IOZRP testing, which demonstrated two major differences. First, the 4.90 cm^2 OZRP achieves 150 mV_{SCE} more positive of a galvanic couple potential with 5456 compared to the IOZRP (-0.95 V_{SCE} vs. -1.10 V_{SCE}). Second, upon doubling the galvanically coupled 5456 area, the cathodic protection achieved by the OZRP is completely disabled with no recovery prior to restoring the 1 OZRP: 1 5456 coupled SAR (Figure 4.11c). These data are supported by Figure 4.3 as well as prior work that demonstrates the higher polarizability of the OZRP in 0.6 M NaCl.[18] This analysis was purposefully performed in an aggressive environment and with bare surface exposures that greatly exceed what would be a)

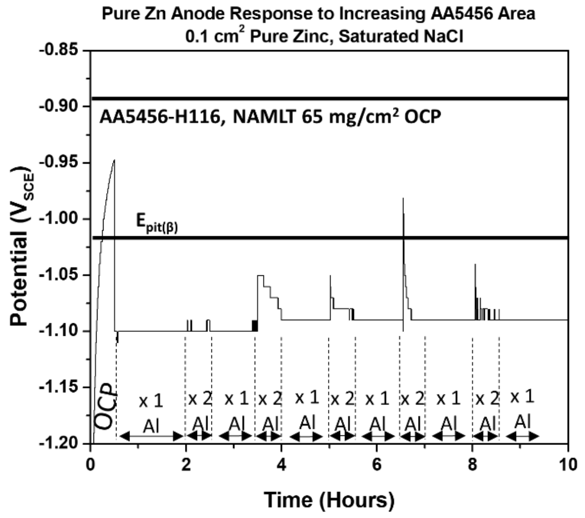
Pure Zn Anode Response to Increasing AA5456 Area
0.1 cm^2 Pure Zinc, Saturated NaCl
AA5456-H116, NAMLT 65 mg/cm^2 OCP
$E_{pit(\beta)}$
Potential (V_{SCE})
-0.85
-0.90
-0.95
-1.00
-1.05
-1.10
-1.15
-1.20
OCP
x 1 Al
x 2 Al
x 1 Al
x 2 Al
x 1 Al
x 2 Al
x 1 Al
x 2 Al
x 1 Al
x 2 Al
x 1 Al
0
2
4
6
8
10
Time (Hours)

b)

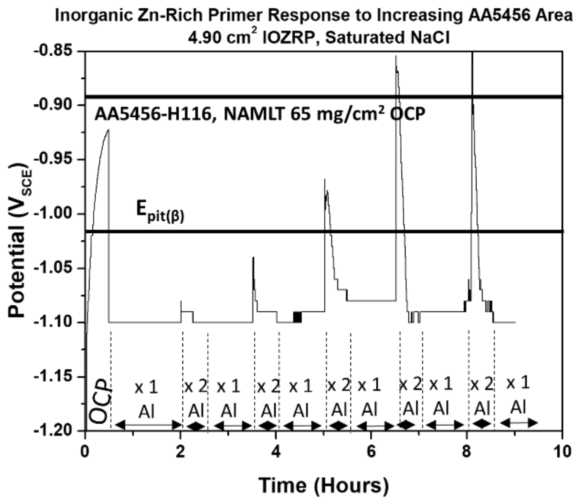
Inorganic Zn-Rich Primer Response to Increasing AA5456 Area
4.90 cm^2 IOZRP, Saturated NaCl
AA5456-H116, NAMLT 65 mg/cm^2 OCP
$E_{pit(\beta)}$
Potential (V_{SCE})
-0.85
-0.90
-0.95
-1.00
-1.05
-1.10
-1.15
-1.20
OCP
x 1 Al
x 2 Al
x 1 Al
x 2 Al
x 1 Al
x 2 Al
x 1 Al
x 2 Al
x 1 Al
x 2 Al
x 1 Al
0
2
4
6
8
10
Time (Hours)

c)

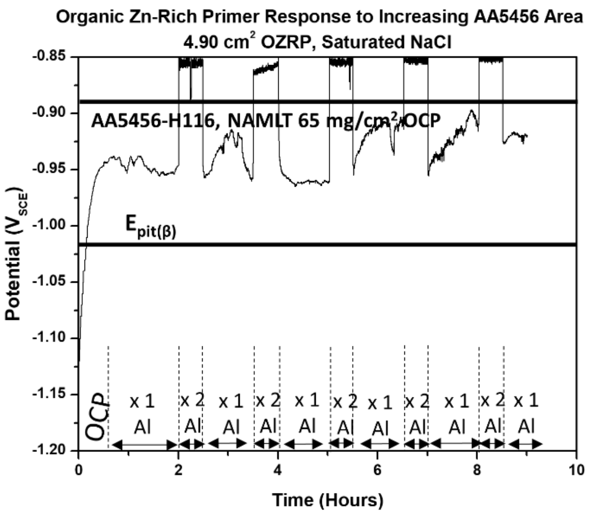
Organic Zn-Rich Primer Response to Increasing AA5456 Area
4.90 cm^2 OZRP, Saturated NaCl
AA5456-H116, NAMLT 65 mg/cm^2 OCP
$E_{pit(\beta)}$
Potential (V_{SCE})
-0.85
-0.90
-0.95
-1.00
-1.05
-1.10
-1.15
-1.20
OCP
x 1 Al
x 2 Al
x 1 Al
x 2 Al
x 1 Al
x 2 Al
x 1 Al
x 2 Al
x 1 Al
x 2 Al
x 1 Al
0
2
4
6
8
10
Time (Hours)

*Figure 4.11: Anodic response testing results demonstrating the coupled potential response of **(a)** 0.1 cm^2 pure Zn, **(b)** 4.90 cm^2 IOZRP, and **(c)** 4.90 cm^2 OZRP to simulate crack growth achieved through increasing the 5456 area from 4.90 cm^2 (x1) to 10.26 cm^2 (x2). These results demonstrate the high polarizability of the OZRP relative to the IOZRP, as well as the possible performance limitations of these finite anodes in aggressive conditions.*

encountered at real crack growth rates in 5456. This aggressive test enabled differentiation of the performance of the three Zn-based anodes and suggests limitations that may arise in IG-SCC mitigation through coupling with metal-rich primers. These results justified evaluation using conditions that are more relevant to engineering scenarios.

4.1.4.5 ***IG-SCC Mitigation via Intermittent Galvanic Coupling***

The results of LEFM testing in 0.6 M NaCl at a constant K of 10 MPa√m where the electrochemical conditions are alternated between potentiostat-based polarization at -0.8 V_{SCE}, and cathodic polarization via either potentiostat control, or ZRA coupled to pure Zn or IOZRP panels are shown in Figures 4.12-4.14. At a K of 10 MPa√m and -0.8 V_{SCE}, fast IG-SCC occurs with a corresponding aggressive (low pH and high [Cl-]) crack chemistry.[11] The effect of potentiostat-controlled alternation of polarization between -0.8 V_{SCE} and either -0.9 (Cycles 1-5), -1.0 (Cycles 11-15), or -1.1 (Cycles 6-10) V_{SCE} is shown in Figure 12; the dashed lines indicate the time points of the polarization changes. There are three important aspects of these data. First, there is a rapid decrease in growth rate by up to three orders of magnitude following the application of the cathodic polarization across the 15 cycles. This is summarized in Table 4.I, where the amount of crack extension (Δa) and the time (Δt) between each data point gathered after the change in polarization is reported. For example, the row “1.0 to 1.1” presents data for the crack extension that occurs between the application of the applied potential and the subsequent (first) data point collected (Δa_{0-}

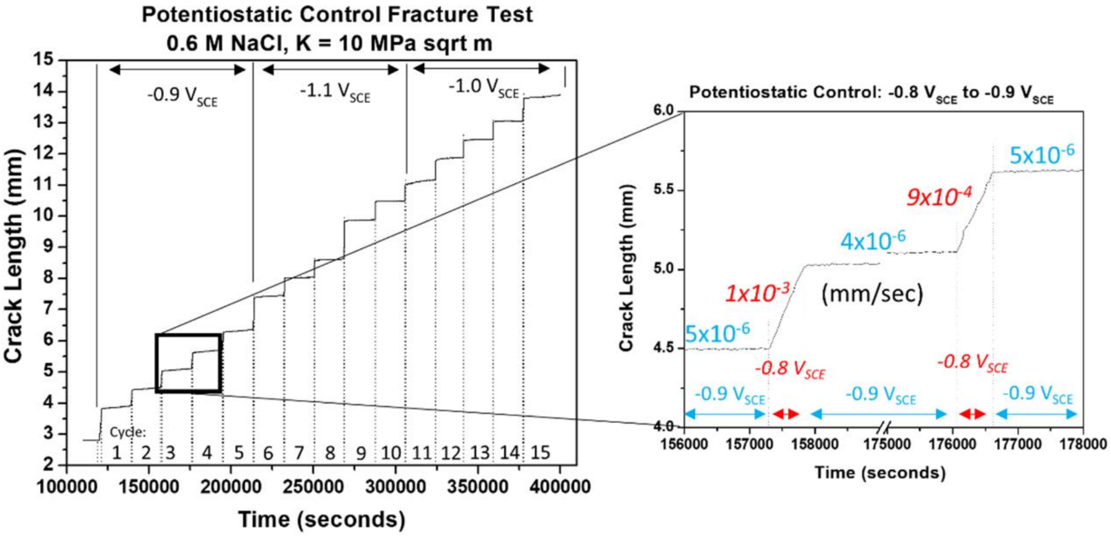

Figure 4.12: Testing based on potentiostat control at K = 10 MPa√m in 0.6 M NaCl, demonstrating the ability to mitigate IG-SCC with potentials as positive as -0.9 V_{SCE} utilizing near-infinite cathode. The zoomed-in portion demonstrates crack growth rates during hysteresis for Cycles 3 and 4.

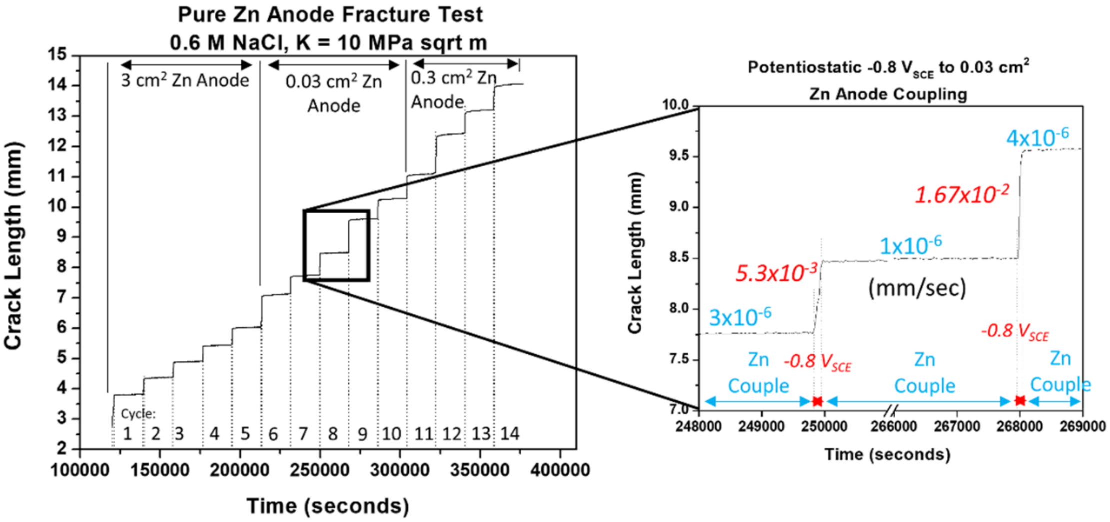

Figure 4.13: Testing based on galvanic coupling with pure Zn at K = 10 MPa√m in 0.6 M NaCl, demonstrating the ability to mitigate IG-SCC with Zn surface area as low as 0.03 cm^2. The zoomed-in portion demonstrates crack growth rates achieved during hysteresis for Cycles 8 and 9.

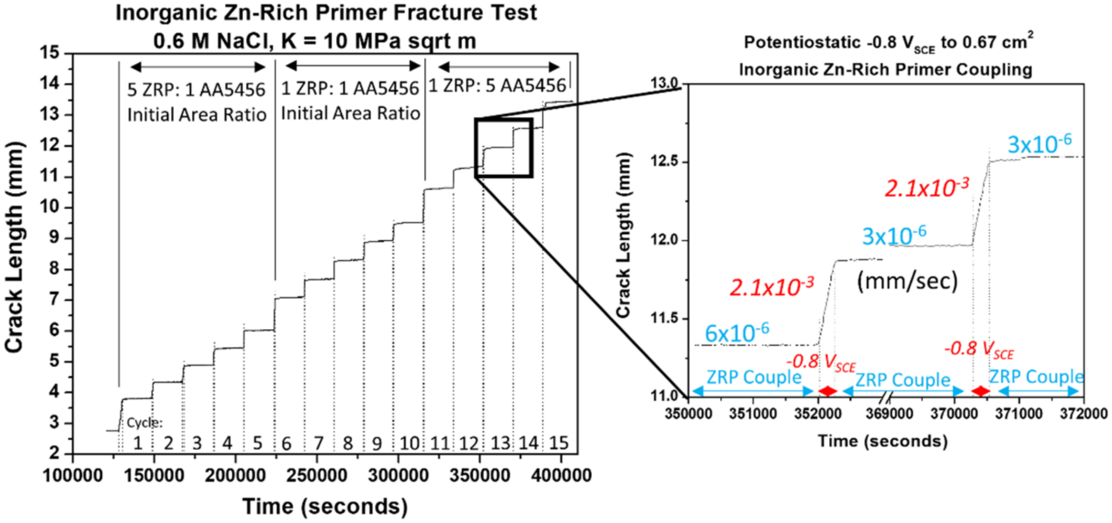

Figure 4.14: Testing based on galvanic coupling with IOZRP at K = 10 MPa√m in 0.6 M NaCl, demonstrating the ability to mitigate IG-SCC with IOZRP area as low as 0.67 cm^2 (Cycle 15). The zoomed-in portion demonstrates crack growth rates achieved during hysteresis for Cycles 13 and 14.

$_1$), likewise "1.1 to 1.2" is the crack extension ($\Delta a_{1\text{-}2}$) in between the first and second data points collected, etc. While the time increment (Δt) between data collection is typically ≈30 seconds, there is some variability thus the exact times are also listed in Table 4.I. Furthermore, to enable a comparative analysis between any transient occurring immediately following the application of the protective potential (e.g. between 1.0 and 1.1), an average value of the crack extension that occurred between each of the first through fourth data points is also reported (e.g. $\Delta a_{Avg1\text{-}4} = (\Delta a_{1\text{-}2} + \Delta a_{2\text{-}3} + \Delta a_{3\text{-}4})/3$). These results are plotted in Figure 4.15 for the IOZRP ZRA test, and similar trends are observed for the potentiostat and pure Zn ZRA tests. There are several noteworthy findings. First, the Δa values are vastly reduced within the first ≈30 second period following applied cathodic protection; specifically, for most cases (39/44 of the test stages conducted between the potentiostat-, pure Zn-, and IOZRP-based tests) the $\Delta a_{0\text{-}1}$ is below 0.065 mm whereas the average Δa during the -0.8 V_{SCE} period is 0.101 mm. Second, in most cases the $\Delta a_{0\text{-}1}$ is

Table 4.I : IG-SCC mitigation delay analysis, constant K = 10 MPa√m testing in 0.6 M NaCl

Data Point Relative to Polarization Change	IG-SCC Mitigation Transients					
	Potentiostat		Pure Zn ZRA		IOZRP ZRA	
	Δa (mm)	Δt (sec)	Δa (mm)	Δt (sec)	Δa (mm)	Δt (sec)
1.0 to 1.1	0.0120	23.1	0.0251	11.0	0.0018	14.9
1.1 to 1.2	0.0000	35.7	0.0000	32.6	0.0000	18.5
1.1 to 1.4 Avg	0.0001		0.0037		0.0073	
2.0 to 2.1	0.0037	60.5	0.0140	16.8	0.0098	18.7
2.1 to 2.2	0.0053	35.6	0.0008	32.6	0.0000	32.6
2.1 to 2.4 Avg	0.0049		0.0004		0.0021	
3.0 to 3.1	0.0124	22.7	0.0000	13.6	0.0138	21
3.1 to 3.2	0.0059	35.7	0.0087	32.6	0.0000	32.7
3.1 to 3.4 Avg	0.0034		0.0033		0.0036	
4.0 to 4.1	0.0131	21.2	0.0056	18.8	0.0004	20.7
4.1 to 4.2	0.0000	35.7	0.0029	65.2	0.0072	32.6
4.1 to 4.4 Avg	0.0018		0.0034		0.0045	
5.0 to 5.1	0.0266	21.7	0.0034	18.5	0.0000	20.4
5.1 to 5.2	0.0000	35.6	0.0038	32.6	0.0000	32.6
5.1 to 5.4 Avg	0.0005		0.0053		0.0026	
6.0 to 6.1	0.0100	16.5	0.0061	20.3	0.0031	18.5
6.1 to 6.2	0.0000	35.7	0.0003	32.6	0.0045	32.6
6.1 to 6.4 Avg	0.0037		0.0028		0.0042	
7.0 to 7.1	0.0198	20.7	0.0617	21.1	0.0168	25.4
7.1 to 7.2	0.0011	35.7	0.0017	32.6	0.0032	32.6
7.1 to 7.4 Avg	0.0017		0.0015		0.0013	
8.0 to 8.1	0.0335	23.1	0.0785	21.3	0.0171	20.8
8.1 to 8.2	0.0042	35.7	0.0000	32.6	0.0023	32.6
8.1 to 8.4 Avg	0.0024		0.0018		0.0023	
9.0 to 9.1	0.0648	57.1	0.0225	16.6	0.0246	17.2
9.1 to 9.2	0.0000	35.7	0.0040	32.6	0.0096	65.2
9.1 to 9.4 Avg	0.0024		0.0013		0.0047	
10.0 to 10.1	0.0200	21.3	0.1393	18.3	0.0089	22.9
10.1 to 10.2	0.0000	35.6	0.0000	32.6	0.0045	32.6
10.1 to 10.4 Avg	0.0010		0.0020		0.0024	
11.0 to 11.1	0.0267	22.6	0.1268	23.7	0.0377	20.6
11.1 to 11.2	0.0000	32.6	0.0317	32.6	0.0022	32.6
11.1 to 11.4 Avg	0.0015		0.0165		0.0025	
12.0 to 12.1	0.0446	32.9	0.0475	22.7	0.0429	16.7
12.1 to 12.2	0.0000	32.6	0.0793	32.6	0.0000	32.6
12.1 to 12.4 Avg	0.0055		0.0554		0.0107	
13.0 to 13.1	0.0546	20.8	0.0411	22.6	0.0280	15.6
13.1 to 13.2	0.0000	32.6	0.0589	32.6	0.0060	32.6
13.1 to 13.4 Avg	0.0006		0.0392		0.0026	
14.0 to 14.1	0.0549	23.0	0.0504	20.3	0.0341	18.6
14.1 to 14.2	0.0000	32.6	0.0526	32.6	0.0006	32.6
14.1 to 14.2 Avg	0.0018		0.0574		0.0035	
15.0 to 15.1	0.1400	20.2	Valid K Solution Limit Reached		0.1766	23.0
15.1 to 15.2	0.0493	32.6			0.0028	32.6
15.1 to 15.4 Avg	0.0235				0.0030	

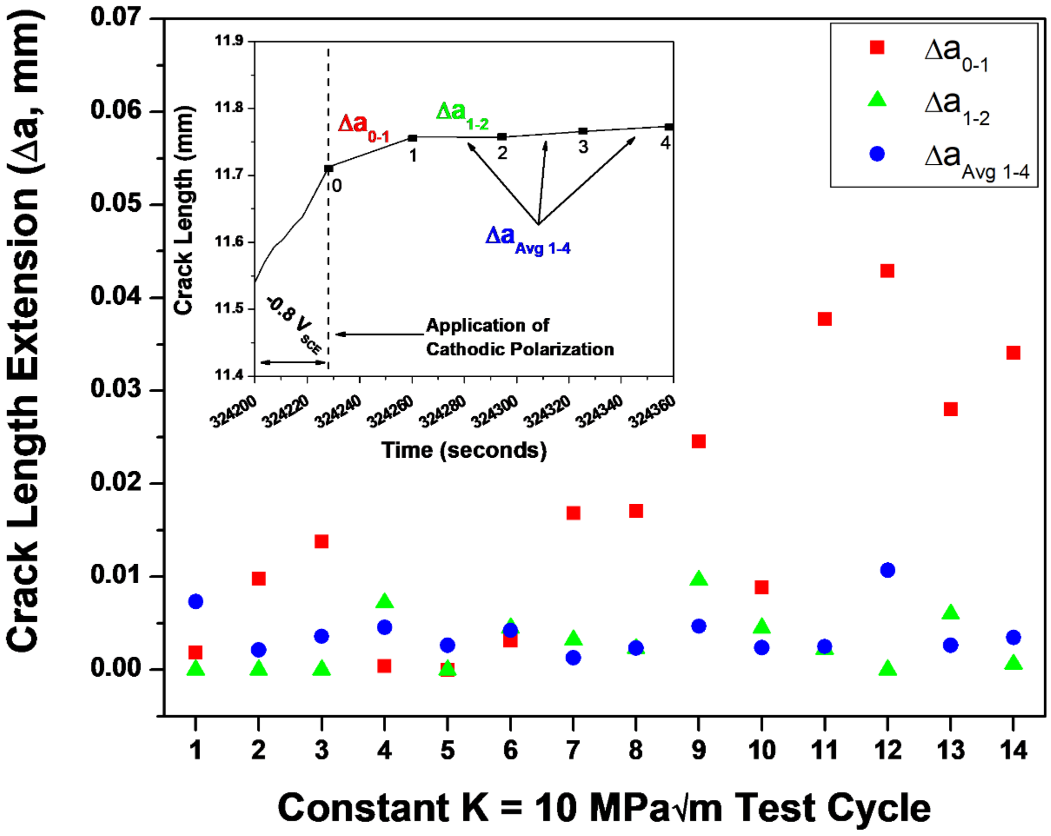

Figure 4.15: Crack length extension versus test cycle (one -0.8 V_{SCE} *period followed by a cathodically polarized period) analysis for the constant K = 10 MPa√m LEFM test utilizing IOZRP ZRA with AA5456-H116, demonstrating the IG-SCC mitigation time transient that was observed in these ZRA/potentiostat-controlled tests (full IG-SCC mitigation often observed within one data point following applied cathodic polarization). The inset details the origin of the Δa values, as well as demonstrates an example of an IG-SCC mitigation time transient dataset.*

considerably higher than the $\Delta a_{Avg1\text{-}4}$ which suggests that despite the vast reduction in crack extension, there is still a time transient period required to reach the full level of inhibition. Third, generally the $\Delta a_{1\text{-}2}$ is similar to the $\Delta a_{Avg1\text{-}4}$ which suggests that the full level of inhibition is almost achieved by the time the second data point is collected. While this general observation is true there are instances where $\Delta a_{1\text{-}2}$ exceeds $\Delta a_{Avg1\text{-}4}$, which suggests a longer transient period to achieve the full level of inhibition. Finally, coupling the analysis above with the Δt values listed in Table 4.I demonstrates that on average the full level of inhibition is not immediate but will generally occur

(2/3 of the time) within 30 seconds of the application of the protective potential. Of note, there were several instances (e.g. 14 of 44 cycles) where complete mitigation required 65-130 seconds, and one instance where 581 seconds was required (cycle 12, pure Zn ZRA).

The rapid decrease in crack growth rate upon application of potentiostat-based cathodic polarization is highlighted in the inset figure in Figure 4.12 (growth rates (da/dt) are given above the trend lines in mm/s), where cracking at -0.8 V_{SCE} exhibits da/dt of ≈$1x10^{-3}$ mm/s but upon cathodic polarization (dashed lines) the crack growth rate decreases to ≈$5x10^{-6}$ mm/s (Figure 4.12). The mean and standard deviation of the crack growth rates achieved at -0.8 V_{SCE} and during cathodic polarization for each set of 5 cycles are detailed in Table 4.II. These results demonstrate that such large and immediate changes in the da/dt behavior are realized for each level of cathodic polarization, as shown numerically in Table 4.II and graphically in Figure 4.12. This result is consistent with prior work that demonstrated in 0.6 M NaCl bulk solutions that similar levels of IG-SCC mitigation were observed at -0.9, -1.0, and -1.1 V_{SCE} during slow rising displacement.[15]

Table 4.II: Crack growth rate results following constant K = 10 MPa√m testing in 0.6 M NaCl

Test at K = 10 MPa√m	**Fast Crack Growth Rate Distribution at -0.8 V_{SCE}**					
	Set 1: Cycles 1-5		Set 2: Cycles 6-10		Set 3: Cycles 11-15	
	Mean (mm/sec)	Standard Deviation (mm/sec)	Mean (mm/sec)	Standard Deviation (mm/sec)	Mean (mm/sec)	Standard Deviation (mm/sec)
Potentiostat	9.0 x 10^{-4}	1.1 x 10^{-4}	4.7 x 10^{-3}	3.3 x 10^{-3}	3.9 x 10^{-3}	4.6 x 10^{-4}
Pure Zn	1.4 x 10^{-3}	4.7 x 10^{-4}	6.1 x 10^{-3}	5.3 x 10^{-3}	5.3 x 10^{-3}	1.0 x 10^{-3}
IOZRP	7.4 x 10^{-4}	3.0 x 10^{-4}	2.7 x 10^{-3}	5.7 x 10^{-4}	2.5 x 10^{-3}	8.5 x 10^{-4}
	Crack Growth Rate Distribution Under Cathodic Protection					
Potentiostat	4.4 x 10^{-6}	4.9 x 10^{-7}	2.0 x 10^{-6}	6.6 x 10^{-7}	3.5 x 10^{-6}	2.7 x 10^{-6}
Pure Zn	2.0 x 10^{-6}	0.0	3.0 x 10^{-6}	1.1 x 10^{-6}	5.0 x 10^{-6}	7.1 x 10^{-7}
IOZRP	1.4 x 10^{-6}	4.9 x 10^{-7}	2.8 x 10^{-6}	4.0 x 10^{-7}	4.2 x 10^{-6}	1.5 x 10^{-6}

Mean crack growth rates achieved under cathodic polarization via potentiostat varied by ≈2-fold (2.4×10^{-6} to 4.0×10^{-6} mm/sec), and those achieved at -0.8 V_{SCE} varied by ≈5-fold across all 15 cycles (9.0×10^{-4} to 4.7×10^{-3} mm/sec) (Table 4.II).

Results of testing where LEFM specimens were alternated between -0.8 V_{SCE} and polarization via galvanic coupling with a pure Zn anode are shown in Figure 4.13 for surface areas of 3.00, 0.03, and 0.30 cm^2. Following electrode stabilization, a pure Zn surface area of 3.00 cm^2 achieved coupled potentials in the range -1.05 to -1.12 V_{SCE} (6 Zn: 5 5456 SAR at the initiation of the set, rising to 1:1 by the end) (Cycles 1-5). To set a lower bound, this surface area was decreased in Set 2 (Cycles 6-10) to 0.03 cm^2 (initial Zn: 5456 SAR of 1:96 rising to 1:110 by the end of Cycle 10 due to crack extension), which achieved coupled potentials in the range of -1.02 to -1.05 V_{SCE}. In Set 3, coupling with the intermediate Zn surface area of 0.30 cm^2 (initial Zn: 5456 SAR of 1:11, rising to 1:12 by the end of the set) (Cycles 11-14) achieved coupled potentials of -1.02 to -1.04 V_{SCE}. Cycle 15 occurred after the SENT K solution limit of 14 mm crack length and was removed from the data, though it showed similar results as the previous cycles. The mean crack growth rate variation across all 15 cycles was ≈5-fold at -0.8 V_{SCE} (1.4×10^{-3} to 6.4×10^{-3} mm/sec) and ≈2.5-fold during the pure Zn ZRA (2.0×10^{-6} to 5.0×10^{-6} mm/sec), as was seen under potentiostat-based control (Table 4.II). Critically, these results demonstrate that galvanic coupling (even with very unfavorable SAR) can be equally efficient at mitigating a growing crack as potentiostat-based cathodic protection (Figures 4.4 and 4.12) in bulk 0.6 M NaCl environment.

Results of testing where LEFM specimens were polarized via galvanic coupling with the IOZRP are shown in Figure 4.14 for initial surface areas of 12.00, 2.70, and 0.67 cm^2. In Set 1, coupling with 12.00 cm^2 IOZRP (initial IOZRP: 5456 SAR of 5:1, rising to 120:29 by the set completion) achieved coupled potentials in the range -1.05 to -1.01 V_{SCE}. Set 2 utilized decreased

IOZRP surface area of 2.70 cm^2 (initial IOZRP: 5456 SAR of 1:1, rising to 9:11 by the set completion), which achieved potentials in the same range as achieved in Set 1. In Set 3, the smallest IOZRP surface area of 0.67 cm^2 (initial IOZRP: 5456 SAR of 1:5, rising to 67:350 by the end of the set) maintained coupled potentials ranging from -1.04 V_{SCE} to -0.96 V_{SCE}. Crack growth rate decreases of up to three orders of magnitude were again observed following the applied cathodic polarization via coupling with the IOZRP. Mean crack growth rate variation was again ≈5-fold at -0.8 V_{SCE} (7.4 x 10^{-4} to 2.7 x 10^{-3} mm/sec) and ≈2.5-fold during the IOZRP ZRA (1.4 x 10^{-6} to 4.2 x 10^{-6} mm/sec) (Table 4.I). The repeatability of these encouraging results was observed even for the lowest ZRP: 5456 SAR (Cycle 15). Critically, these results also demonstrate that galvanic coupling with non-polarizable Zn primers (even with very unfavorable SAR) can be equally efficient at mitigating a growing crack.

4.1.5 **Discussion**

These results demonstrate mitigation of IG-SCC via cathodic protection that is applied in three ways: (1) nominally infinite anode (e.g. potentiostat), (2) finite sacrificial anode (e.g. ZRA coupled to pure Zn), and (3) finite anode embedded in a high access impedance (e.g. ZRA coupled or spray-deposited ZRPs) (Figures 4.1, 4.2, and 4.3). Each of these methods of IG-SCC mitigation demonstrated the ability to suppress the onset of environmentally-assisted cracking as well as to arrest actively propagating IG-SCC. In both situations, suppression of aggressive crack chemistry formation is required, with the former involving the initial formation of the chemistry, and the latter involving the modification of the already existing aggressive chemistry. The systematic set of experimental results in this paper provide a basis to discuss the mechanism by which mitigation occurs and comment on the implications of this work in the context of engineering applications.

4.1.5.1 *Correlation of IG-SCC Mitigation with the Coupled Potential*

The data show a clear correlation between the established coupled potential and achieved IG-SCC mitigation in NAMLT 65 mg/cm^2 5456, regardless of the means of achieving the potential. To understand the effect that applied cathodic polarization has at the crack tip to achieve such mitigation, the IG-SCC mechanism must be reviewed. Prior work demonstrated that the electrochemical stability of the α Al matrix and the β phase control the occluded chemistry formation at the crack tip, which directly influences the H production due to the local development of an enhanced H overpotential.[11,12,15] Cation production by anodic dissolution increases exponentially at the β breakdown potential (-0.92 V_{SCE} in 0.6 M NaCl (Figure 4.2), and -1.02 V_{SCE} in 5.45 M NaCl (Figure 4.3)), and cation hydrolysis then leads to crack tip acidification. Enhanced hydrogen production is enabled by acidification. The formation of local acidified conditions promotes Cl^- ingress for charge balance, and the presence of the Cl^- species causes oxide rupture to destabilize the α Al matrix.[34,35] Furthermore, ohmic potential drop down the crack wake/flanks creates conditions for development of greater overpotentials for hydrogen production.[11] If more H is produced then more H can be adsorbed on the surface and absorbed into the alloy matrix and is thus available to diffuse to the high tensile hydrostatic stress field in the fracture process zone. To achieve IG-SCC mitigation, application of intermediate cathodic polarization to the crack tip promotes passivity of the α Al matrix and the β phase. Since the cations would not be generated in this case, there is no driving force for the hydrolysis that governs acidification and Cl^- ingress. As such, the chemistry changes and the hydrogen overpotential decreases, which limits the H-content available for embrittlement in the fracture process zone. Critically, this work demonstrates that mitigation of IG-SCC in sensitized 5456 will occur at intermediate cathodic potentials, regardless of whether a potentiostat, pure Zn anode, or IOZRP is used. Thus, galvanic coupling with low polarizability, finite Zn anodes may achieve sufficient current output to first overcome the Ohmic voltage drop sources on the crack wake/flanks, then to affect the crack tip potential to effectively arrest the aforementioned processes which lead to aggressive hydrogen generation. The success of these Zn-based systems to overcome these factors and achieve IG-SCC mitigation has significant implications for in-service use, and merits further discussion.

Upon galvanic coupling, the finite nature of pure Zn and ZRP anodes raises the possibility that the effective anodic current output available from these systems is insufficient to distribute an intermediate cathodic potential to the crack tip and mitigate IG-SCC, especially in comparison to a potentiostat. Mixed potential theory dictates that the actual true potential experienced at the crack tip (E_{tip}) will be affected by various Ohmic (i.e. IR) voltage drop sources:

$$E_{tip\,(\sum IR\ Sources)} = E_{Primer\,(IR\ Free)} + IR_{Crack} + IR_{Scribe} + IR_{Coating} \quad \text{Equation 4.1}$$

These IR voltage drop sources and physical locations are graphically illustrated in Figure 4.1, and schematically depicted according to mixed potential theory in Figure 4.16. Figure 4.16 demonstrates how these IR voltage drop sources influence the galvanic couple potential to drive the crack tip potential towards more positive values (promoting higher IG-SCC susceptibility, especially if the crack tip potential increases towards $E_{pit\,(\beta)}$).

The effect of solution resistance may be substantially greater in atmospheric conditions, which will be introduced below in the Discussion.[27] Quantitative modeling in 0.6 M NaCl showed modest IR_{crack} effects on E_{tip} in Al-Mg having similar crack geometry and orientation, such as at applied potential of -0.730 V_{SCE} (E_{tip} = -0.817 V_{SCE}) and -1.020 V_{SCE} (E_{tip} = -1.050 V_{SCE}).[11] These results demonstrate that a difference of 30-87 mV should be expected between E_{tip} and E_{primer} due solely to the IR_{Crack} effects.[11] The present results corroborate these findings when comparing the

IG-SCC mitigation achieved by the spray-deposited IOZRP on the normal and thick section LEFM samples, which yielded similar IG-SCC severities for a constant scribe width (Figures 4.7 and 4.8). The remaining IR voltage drop sources, which have not been totally quantified, would presumably exist within the ZRP itself (due mostly to the high access impedance) ($IR_{Coating}$) and in the aqueous solution along the scribe (IR_{Scribe}). The nature of the present findings lends further understanding to these IR voltage drop effects in the context of IG-SCC mitigation via Zn-based anodes.

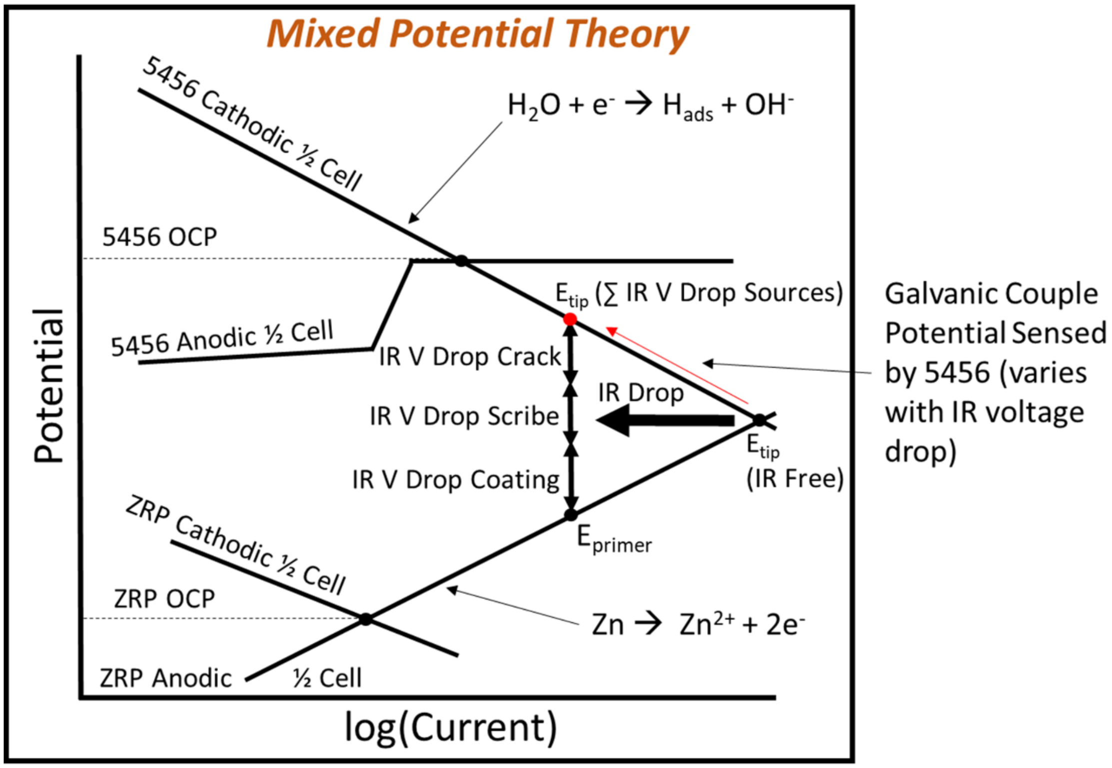

Figure 4.16: Schematic depicting the additive IR voltage drop effects on the spray-coated LEFM sample according to mixed potential theory, wherein the IR voltage drop promotes more positive crack tip potentials and thus more severe IG-SCC in the presence of a Zn-based galvanic couple with 5456.

4.1.5.2 *Experimental Insights on Ohmic Voltage Drop Effects on Zn-Based IG-SCC Mitigation*

The present results show that the achieved potential as measured by the Luggin-fitted SCE at the SENT mid-section typically achieved the expected IG-SCC mitigation based on a 30-87 mV$_{SCE}$ (or less) potential difference at the crack tip, as compared to that achieved via potentiostat. Considering first the ZRA results, which were meant to isolate only the galvanic effect (limiting Zn^{2+} dissolution into the bulk solution), the application of -1.06 V$_{SCE}$ via pure Zn ZRA in 5.45 M NaCl (Figure 4.5) achieved K_{TH} of 11.0 MPa√m, which lies between the potentiostatically-applied -1.0 V$_{SCE}$ (K_{TH} = 8.0 MPa√m) and -1.1 V$_{SCE}$ (K_{TH} = 12.0 MPa√m) results. The application of -1.01 V$_{SCE}$ in 0.6 M NaCl via the pure Zn ZRA (Figure 4.4) completely arrested IG-SCC, which would be expected from the -0.9 V$_{SCE}$ and the -1.0 V$_{SCE}$ results obtained via potentiostat. However, the ZRA tests did not always match this trend; for example, in 0.6 M NaCl the IOZRP ZRA (E_{couple} = -0.96 V$_{SCE}$) allowed crack growth to occur, despite the lack of crack growth upon application of -0.90 V$_{SCE}$ via potentiostat (Figure 4.4). On the other hand, in 5.45 M NaCl, the IOZRP ZRA (E_{couple} = -1.01 V$_{SCE}$) achieved more effective IG-SCC mitigation than, for instance, potentiostat-based polarization at -1.10 V$_{SCE}$ (Figure 4.5). The cause for these deviations when using a ZRA is not entirely clear. Correlation of the coupled current showed logical trends over long periods when comparing potentiostat-based polarization and pure Zn ZRA (Figure 4.6), however the coupled current did not match based on the established potential when comparing with IOZRP galvanic couples based on similar exposed 5456 area. With extended exposure time, the cathodic (negative) current measured on the 5456 surface (ZRA with IOZRP) would increase in value (approach zero) above that expected for the established potential.

The spray-coated IOZRP results further inform on the impact of the IR voltage drop effects. Through consideration of scribe widths up to 15.0 mm, the achieved potential continued to track well with the potentiostat-based IG-SCC mitigation results, exhibiting ≤ 130-87 mV variance between the potential measured in the SENT mid-section and the presumed crack tip potential based on the measured IG-SCC severity (Figure 4.7). Increasing the scribe width in 5 mm increments increased the coupled potential by +0.01 to +0.04 V_{SCE}, which demonstrates the robust nature of the low polarizability in the IOZRP. Furthermore, the IOZRP continued to successfully mitigate IG-SCC in the thick section LEFM samples (thickness 12.80 mm) with scribe width of up to 10 mm, despite more than doubling the crack wake thickness. For example, at the 10 mm scribe width, the IOZRP achieved the same coupled potential at the SENT mid-section (-1.08 V_{SCE}, Figures 4.7 and 4.8) regardless of the crack wake thickness, which achieved comparable IG-SCC mitigation. In the case of the 5 mm scribe width tests conducted on these two SENT geometries, the IG-SCC severity was noticeably reduced in the thick section IG-SCC test. These findings suggest a negligible increase in IR voltage drop down the crack wake with increased crack size, supporting the finding that crack geometry has little deleterious effect on the IOZRP IG-SCC mitigation performance.

4.1.5.3 ***Potential Induced Modification of Aggressive Growth Crack Tip Environments***

A key factor dictating the ability to mitigate IG-SCC in service is also the speed of mitigation of a growing crack where an aggressive chemistry has already formed. The current results strongly suggest that the crack tip may be effectively polarized through engineering-relevant cathodic protection methods to suppress fast crack growth by mitigating IG-SCC. While the suppression occurs quickly, there is a transient time period before the full level of inhibition is realized (Figure 4.15 and Table 4.1). Typically, this transient is less than ≈30 seconds, but can extend to 581 seconds. Mechanistic evaluation of the cause for this delay will provide insight into the mechanics of IG-SCC and the effect of cathodic polarization.

The IG-SCC mitigation time transient could be due to (1) a delay in achieving the polarization of the crack tip upon application of the external potential, (2) continued cracking through a H-charged region ahead of the crack tip, and/or (3) delay in crack tip chemistry de-acidification. Since the potential shift is limited by double layer charging, it is expected that there will be very limited delay in the crack tip polarization, as such (1) is unlikely.[36] Prior to applying intermediate cathodic polarization at constant K = 10 MPa√m, IG-SCC was driven at ~$1.00\text{x}10^{-3}$ mm/sec to achieve from 0.5 to 1.0 mm of crack growth. As such, the mitigation time transient could be associated with the time needed to crack through the H-charged region ahead of the crack tip (e.g. (2)). Assuming a da/dt of $1.00\text{x}10^{-3}$ mm/sec and hydrogen diffusivity of $1.40\text{x}10^{-10}$ cm^2/sec (as measured for 5083-H131[37]), a moving line source analysis[38,39] predicts that the hydrogen charged zone would extend 0.1 micrometer ahead of the moving crack. This value is well below the typical $\Delta a_{0\text{-}1}$ (Table 4.I). Furthermore, assuming that the crack continues to propagate at $1.00\text{x}10^{-3}$ mm/sec through the H charged zone, then it would only require ~0.1 second to crack through this region. This simplified scenario suggests that the IG-SCC mitigation delay is not due to cracking through a H-charged region.

The above analysis suggests that the mitigation time transient is likely due to a delay in the alteration of the crack tip chemistry (e.g. (3)). As such it is reasonable to consider the electrochemical processes that occur after the application of the cathodic polarization. Recall that the rate of cracking is hypothesized to be governed by the flux of H at the crack tip, which is described by the overpotential for H production. This value is dependent on the potential at the crack tip and the local crack tip chemistry (e.g. overpotential increases with increasingly acidic pH and, to a lesser extent, increasing [Cl-]). Cathodic polarization that shifts the potential *at the crack tip* to below the β (and matrix) breakdown potential would (1) decrease dissolution, thus drastically reduce the cation production rate, and (2) consume protons along the entire crack flank and tip where the potential is sensed. The acidification of the crack tip is caused by hydrolysis of cations, as such the reduction in the cation production rate and the consumption of the protons along the crack flank will result in a less acidic crack tip condition. Furthermore, at these conditions there will be less driving force for the ingress of anions to maintain charge neutrality, as such the crack tip [Cl-] will also be reduced. While the modification of the crack tip potential will be nearly simultaneous with the application of the external potential (e.g. (1)), the resulting chemistry changes will likely have a time dependence. The quantification of the time required for these changes is beyond the scope of this effort. However, it is reasonably hypothesized that the observed IG-SCC mitigation time transient is associated with the time required to adjust the crack tip chemistry to a less acidic and lower [Cl-] environment.

4.1.5.4 *Implications to Engineering Applications*

These findings provide considerable insight into the potential use of ZRP systems for IG-SCC mitigation in naval service. Critically, the IOZRP has been demonstrated to successfully mitigate IG-SCC with scribe width of up to 15 mm, and based on the demonstrated trends (Figure 4.7), even larger defects sizes may be possible to protect with this coating (these were outside the scope of the present work due to the chosen SENT/environmental cell dimensions). Crack geometry has negligible effect on the IOZRP performance; rather, the amount of exposed Al area seems the most influential, as this factor will impact the magnitude of coupled potential achieved by the ZRP. These results also demonstrate that a conventional, high impedance topcoat cannot be applied if

IG-SCC mitigation is the purpose of the IOZRP (Figures 4.3, 4.9, and 4.10). Use of the OZRP, which was demonstrated to be more polarizable than the IOZRP in 0.6 M NaCl (Figure 4.2) and in 5.45 M NaCl (Figures 4.3 and 4.5), also demonstrates that all ZRP systems are not the same, despite similarities in Zn loading. For the same 0.3 mm scribe in 5.45 M NaCl, spray coating with the IOZRP achieved vastly different IG-SCC mitigation than the OZRP (which provided no protection (Figure 4.5)). These results begin to highlight ZRP performance characteristics that must be carefully considered for IG-SCC mitigation purposes.

The IOZRP considered in the present work is a relatively brittle coating that can be difficult to apply and requires specific humidity conditions for proper adhesion, especially on substrates other than steel.[18,29] When choosing or designing coatings with more desirable physical qualities, performance attributes such as polarizability must be critically considered for IG-SCC mitigation. Prior work demonstrated that the IOZRP was the least polarizable of four commercial ZRP candidates evaluated in 0.6 M NaCl.[18] However, other organic ZRP systems exist commercially that may offer better adhesion and flexibility on 5456 than the IOZRP, with only slight decreases in polarizability that may achieve similar IG-SCC mitigation.[18] Thus, the present findings lay the foundation for the employment of ZRP systems on naval Al-Mg components in aggressive marine conditions, and demonstrate the importance of purposeful ZRP selection and design for IG-SCC mitigation.

4.1.5.5 ***Future Work: Zn-Rich Primer Performance in Atmospheric Conditions***

The current work is conducted solely in full immersion conditions where the electrolyte continuously connects the crack tip to the sacrificial cathodic protection system. However, for more accurate simulation of marine naval service conditions, atmospheric wet/dry and thin film environments must be considered wherein the ZRP may become electrochemically disconnected from the crack tip, or the electrolyte layer thickness may limit the anodic current output from the ZRP.[27] More IG-SCC susceptible Al-Mg alloys such as AA5083-H131 should also be considered, as these alloys are used for both the hull and superstructure of vessels such as the Littoral Combat Ship where the entire range of immersion conditions will be experienced. Future work will consider ZRP performance on alloys such as 5083-H131 in a wide range of immersion conditions such as misting and thin film that more accurately simulate marine naval service, and which will more realistically demonstrate the efficacy of low polarizability ZRP systems for IG-SCC mitigation.

4.1.6 **Conclusions**

The mitigation of IG-SCC was achieved in highly sensitized (NAMLT 65 mg/cm^2) AA5456-H116 via potentiostat, pure Zn anode- and IOZRP-based galvanic coupling, as well as IOZRP spray coating in NaCl full immersion. Fracture mitigation was demonstrated by continual application of these cathodic protection methods during slow rising displacement in 0.60 M and 5.45 M NaCl, as well as in intermittent application while at constant post threshold K of 10 MPa√m in 0.60 M NaCl. These evaluations yielded the following conclusions:

- IG-SCC mitigation correlated with achieved potential regardless of whether a potentiostat, pure Zn anode, or ZRP was utilized to achieve the potential.
- ZRP polarizability became increasingly vital to cathodic protection performance with increasingly aggressive testing conditions (salinity, primer defect size, crack size, etc.).
  - Increasing the scribe width from 0.3 mm to 15.0 mm, and/or increasing fracture specimen thickness from 6.60 mm to 12.80 mm, had incremental effect on the spray-deposited

IOZRP performance in 5.45 M NaCl due to the low polarizability of the IOZRP, and in all cases intermediate cathodic potentials were still achieved to mitigate IG-SCC.

  - Spray-coating with the more polarizable OZRP, with the minimal defect size of 0.3 mm, was ineffective for IG-SCC mitigation in 5.45 M NaCl.

- The use of an epoxy topcoat on the IOZRP masked the majority of the exposed IOZRP area, rendering this high performance ZRP system ineffective for IG-SCC mitigation.
- At constant K = 10 MPa√m, the crack growth rate decreased in rate by up to three orders of magnitude upon application of a cathodic potential.
- At constant K = 10 MPa√m, the effective IG-SCC mitigation performance of pure Zn was validated to the surface area ratio of 1 Zn: 110 5456, as well as in the IOZRP to the ratio of 67 ZRP: 350 5456 in 0.6 M NaCl.

4.1.7 References

1. Holroyd, N.J.H., and G.M. Scamans, *Corrosion* 72 (2016).
2. Holroyd, N.J.H., and G.M. Scamans, *Scr. Metall. Mater.* 19 (1985): pp. 945–946.
3. Gupta, R. k., R. Zhang, C. h. j. Davies, and N. Birbilis, *Corrosion* 69 (2013): pp. 1081–1087.
4. Zhang, R., S.P. Knight, R.L. Holtz, R. Goswami, C.H.J. Davies, and N. Birbilis, *Corrosion* 72 (2016): pp. 144–159.
5. Steiner, M.A., and S.R. Agnew, *Corrosion* 72 (2016): pp. 169–176.
6. Steiner, M.A., and S.R. Agnew, *Scr. Mater.* 102 (2015): pp. 55–58.
7. ASTM, “ASTM: G67-04 Standard Test Method for Determining the Susceptibility to Intergranular Corrosion of 5XXX Series Aluminum Alloys by Mass Loss After Exposure to Nitric Acid (NAMLT Test)” (West Conshocken, PA: ASTM International, 2004).
8. Lim, M.L.C., R.G. Kelly, and J.R. Scully, *Corrosion* 72 (2016).
9. Lim, M.L.C., R. Matthews, M. Oja, R. Tryon, R.G. Kelly, and J.R. Scully, *Mater. Des.* 96 (2016): pp. 131–142.
10. Seifi, M., N.J.H. Holroyd, and J.J. Lewandowski, *Corrosion* 72 (2016): pp. 264–283.
11. Crane, C.B., R.. Kelly, and R.P. Gangloff, *Corrosion* 72 (2016): pp. 242–263.
12. Crane, C.B., and R.P. Gangloff, *Corrosion* 72 (2016): pp. 221–241.
13. Jones, R.H., D.R. Baer, M.J. Danielson, and J.S. Vetrano, *Metall. Mater. Trans. A* 32

(2001): pp. 1699–1711.
14. McMahon, M.E., P.J. Steiner, A.B. Lass, and J.T. Burns, *Corrosion* 73 (2017): pp. 347–361.
15. McMahon, M.E., J.R. Scully, and J.T. Burns, *J. Miner. Met. Mater.* 69 (2017): pp. 1389–1397.
16. McMahon, M.E., P.J. Steiner, A.B. Lass, and J.T. Burns, *Corrosion* 73 (2017): pp. 713–723.
17. Watson, J.W., Y.Z. Shen, and M. Meshii, *Metall. Mater. Trans. A* 19 (1988): pp. 2299–2304.
18. McMahon, M.E., J.T. Burns, and J.R. Scully, *Prog. Org. Coatings* (2019). In Review.
19. Knudsen, O.Ø., U. Steinsmo, M. Bjordal, and S. Nijjer, *JPCL* (2001): pp. 52–56.
20. Koul, M.G., A. Sheetz, P. Ault, J. Repp, and A. Whitfield, *Corrosion* 70 (2014): pp. 337–350.
21. Knudsen, O.Ø., U. Steinsmo, and M. Bjordal, *Prog. Org. Coatings* 54 (2005): pp. 224–229.
22. Feliu S., J., M. Morcillo, and S. Feliu, *Corrosion* 57 (2001): pp. 591–597.
23. Thomas, S., N. Birbilis, M.S. Venkatraman, and I.S. Cole, *Corrosion* 68 (2012): pp. 015009-1-015009-9.
24. McMahon, M.E., J.R. Scully, and J.T. Burns, *J. Miner. Met. Mater.* 69 (2017): pp. 1724–1726.
25. Gangloff, R.P., D.C. Slavik, S. Piascik, and R.H. Van Stone, "Direct Current Electrical Potential Measurement of the Growth of Small Cracks," in Small-Crack Test Methods, eds. J.M. Larsen, and J.E. Allison (Philadelphia, PA: American Society for Testing and Materials, 1992), pp. 116–168.
26. Gangloff, R., H. Ha, J. Burns, and J. Scully, *Metall. Mater. Trans. A* 45 (2014): pp. 3814–3834.
27. Steiner, P., and J. Burns, *Corrosion* 74 (2018): p. 1117-1131.
28. Khullar, P., J. V. Badilla, and R.G. Kelly, *Corrosion* 72 (2016): pp. 1223–1225.
29. Parashar, G., D. Srivastava, and P. Kumar, *Prog. Org. Coatings* 42 (2001): pp. 1–14.
30. Tada, H., P.C. Paris, and G.R. Irwin, *The Stress Analysis of Cracks Handbook* (St. Louis, MO: Paris Productions Incorporated, 1985).
31. King, A.D., and J.R. Scully, *Corrosion* 67 (2011): pp. 1–22.
32. King, A.D., J.S. Lee, and J.R. Scully, *J. Electrochem. Soc.* 163 (2016): pp. C342–C356.
33. King, A.D., B. Kannan, and J.R. Scully, *Corrosion* 70 (2014): pp. 512–535.
34. Natishan, P.M., W.E.O. Grady, E. Mccafferty, and D.E. Ramaker, *J. Electrochem. Soc.* 146 (1999): pp. 1737–1740.
35. McCafferty, E., *Corros. Sci.* 37 (1995): pp. 481–492.
36. Van dr Linden, B., H. Terryn, and J. Vereecken, *J. Appl. Electrochem.* 20 (1990): pp. 798–803.
37. Ai, J.-H., M.L.C. Lim, and J.R. Scully, *Corrosion* 69 (2013): pp. 1225–1239.
38. Scully, J.R., G.A. Young, and S. Smith, "Hydrogen Embrittlement of Aluminum and Aluminum-Based Alloys," in Gaseous Hydrog. Embrittlement Met. Energy Technol., eds. R.P. Gangloff, and B.P. Somerday, 1st ed. (Cambridge, UK: Woodhead Publishing Limited, 2012), pp. 707–768.
39. Young, G.A., and J.R. Scully, "Hydrogen Production, Absorption and Transport During Environment Assisted Cracking of an Al-Zn-Mg-(Cu) Alloy in Humid Air," in Int. Conf.

Hydrog. Eff. Mater. Behav. Corros. Deform. Interact., eds. Moody, Ricker, Was, Jones, Thompson, and Moran (2002), pp. 893–907.

CHAPTER 5

Potential Secondary Chemical Protection Effects of Bulk Chemistry Zn2+ Content on IG-SCC Severity in Al-Mg

5.1 Advanced Chemical Stability Diagrams to Predict the Formation of Complex Zinc Compounds in Chloride Environment

M. E. McMahon [ǂ, *], R. J. Santucci Jr. [ǂ], and J. R. Scully[ǂ]

[ǂ] Center for Electrochemical Science and Engineering, Department of Materials Science and Engineering, University of Virginia, Charlottesville, VA 22904
[*] Corresponding author. E-mail: mm5kn@virginia.edu

Key words: Thermodynamics, zinc, corrosion product, nanoparticles, modeling

5.1.1 Abstract

A chemical stability map is advanced by incorporating ion complexation, solubility, and chemical trajectories to predict ZnO, $Zn(OH)_2$, $Zn(CO_3)$, $ZnCl_2$, $Zn_5(CO_3)_2(OH)_6$, and $Zn_5(OH)_8Cl_2 \cdot H_2O$ precipitation as a function of the total Zn content and pH of an NaCl solution. These calculations demonstrate equilibrium stability of solid Zn products often not considered while tracking the consumed and produced aqueous Zn ion species concentrations through chemical trajectories. The effect of Cl-based ligand formation is incorporated into these stability predictions, enabling enhanced appreciation for the local corrosion conditions experienced at the Zn surface. The present work also extends the chemical stability diagram derivations by incorporating a Gibbs-Thompson curvature relation to predict the effect of nanoscale precipitate phase formation on species solubility. These calculations demonstrate with the ZnO system that solubility is a strong function of nanoscale curvature (ie. nanoparticle radius). Additionally, the complexation of Cl^- with Zn^{2+} is demonstrated to compete with the formation of solid phases, making precipitation more difficult. These complex thermodynamic predictions of equilibrium Zn corrosion product precipitation correlate well with experimental results for Zn corrosion in full and alternate NaCl immersion. The demonstrated thermodynamic prediction methods have far-

reaching utility in a variety of fields requiring nanoscale, semiconductor, and/or structural materials.

5.1.2 Introduction

Chemical stability predictions inform decisions in the corrosion engineering, chemical engineering, geology, soil science, energy, and biomedical fields. These technological fields increasingly demand the accurate understanding of chemical system progression in increasingly complex conditions.[1–5] Classical thermodynamic predictions of metal stability, environmental degradation, and eventual corrosion product formation have undergone extensive experimental verification since Marcel Pourbaix's original derivation of E-pH (chemical stability) diagrams,[2–7] however little work exists which actively aims to further develop Pourbaix's prediction methods. Recent work by Santucci et. al [8] added to Pourbaix's chemical stability diagram method by developing chemical trajectory expressions which track the progression of available ion content in the global system with respect to pH. The equilibrium metal (M) ion concentration ($[M^{n+}]$) and pH conditions necessary for M-compound formation, as well as the changes in those conditions upon dissolution of the M-compound were graphically depicted in these improved chemical stability diagrams. The ionic concentration and pH trajectory trends were validated through analysis of the work of Plagemann et. al,[9] Lin et. al,[10] and Xu et. al [11] concerning previously published yet not fully explained experimental findings, wherein customized chemical stability diagrams produced thermodynamic predictions that answered open questions remaining from the interpretation of purely empirical experimental results.[8] However, these analyses required equilibrium stability calculation for relatively simple oxidation products whose precipitation could be predicted based on known chemical potentials. More complex corroding systems that have considerable engineering relevance have yet to be fully assessed through chemical stability prediction, as the necessary chemical potential data for such systems are not necessarily known. Thus, these methods must be expanded in breadth, complexity, and accuracy.

One element of increasing societal importance for materials science and engineering is Zinc (Zn), which has been historically used in the design of brass alloys and for sacrificial corrosion protection. Corrosion in the Zn system has been thoroughly studied due to the importance of this metal for cathodic protection of steel,[12] however formation of many typical and important Zn corrosion products are only qualitatively understood due to the complexity of their makeup.[13] Today, Zn is also used in a wider variety of applications such as hazard management, biomedical applications such as drug delivery and antibiotics, as well as in electronics and data storage.[14–20] Depending on the application, either metallic Zn or a specific Zn corrosion product may be desired, for which the development of accurate stability / precipitation prediction methods would be beneficial and may inform product development for long-term use.

The complex makeup of many of the zinc compounds requires advancements in the derivation of expressions which track the evolution of total Zn concentration ($[\mathrm{Zn}]_{\mathrm{Tot}}$) in tandem with pH as these compounds react electrochemically to achieve equilibrium in the aqueous phase. Complexities arise due to proton transfer reactions (as with Zn^{2+} + OH^- and CO_3^{2-} + H^+) and complexation reactions (as with Zn^{2+} + Cl^-). Therefore, the present work will quantify and predict corrosion product formation within the Zn system through thermodynamically-derived chemical stability diagrams based on known solubility constants that have not been broadly considered.[21] The derivation will include complexation effects due to chloride, hydroxide, and carbonate species as a function of bulk chemistry. Lastly, surface effects due to precipitated solid phase curvature will be incorporated into the method through utilizing a Gibbs-Thompson relation, which will predict the required conditions for spherical ZnO nanoparticle formation as a function of radius.

5.1.3 Theory / Calculations

This work utilized recently developed solubility relations [21] to derive chemical stability diagrams that encompass the spectrum of experimentally observed Zn corrosion products that form in non-sulfate-containing marine environment. These corrosion products include Zincite (ZnO), Wulfingite ($Zn(OH)_2$, (amorphous as well as epsilon phase)), Smithsonite ($Zn(CO_3)$), Zinc Chloride ($ZnCl_2$), Simonkolleite ($Zn_5(OH)_8Cl_2 \cdot H_2O$), and Zinc Hydroxycarbonate ($Zn_5(CO_3)_2(OH)_6$).[12,13] Previous work demonstrated the utility of chemical stability diagrams when derived based on thermodynamic chemical potential data, which enabled the stability prediction of relatively simple reaction products such as $Mg(OH)_2$ or Li_2CO_3.[8,22] In the Zn system, however, the presence of complex corrosion products such as Simonkolleite and Zinc Hydroxycarbonate require an expansion on the previously demonstrated methods, as the chemical potentials for these complex products are not known or easily determined.[12]

5.1.3.1 *Construction of Equilibrium Chemical Stability Boundaries: Bulk Formation*

Baseline thermodynamic predictions in the present work neglected Cl^- complexation effects, and so the calculation of each aqueous Zn ion's stability was necessary. Lange's Handbook of Chemistry provided stability constant values for the range of Zn ion species present in chloride-based, non-sulfate-containing saline environment.[22] These data were utilized to create predominance diagrams for the Zn system, which demonstrated that three zones of ion predominance generally occur: Zn^{2+} (pH 9.0 and lower), $Zn(OH)_2^0$ (pH 9.0 to pH 13.0), and $Zn(OH)_4^{2-}$ (pH 13.0 and higher).[6,12,22] Zinc predominance diagrams are common in the literature, especially when considering nanoparticle formulation, and are useful to determine available ion content within an electrochemical system as a function of pH.[23–25] These predominance results based on the Lange constants, which demonstrated $Zn(OH)_2^0$ stability in the central pH region, were compared with previous work by Pourbaix, which computed a different set of aqueous Zn ions thought at the time to be dominant ($HZnO_2^-$ was most stable in the central pH region).[6] These comparisons showed good correlation between the models, and demonstrated that, with self-consistent use of a given thermodynamic database, use of a certain ion for rederivation of stability products (K_{sp}) is not necessary to yield consistent predictions. Corrosion product reactions were then rederived with respect to Zn^{2+}, $Zn(OH)_3^-$ (chosen to enable the stability prediction of $Zn(OH)_2$ (s)), and $Zn(OH)_4^{2-}$, creating three reactions and three K_{sp} values for each corrosion product which, when summed together, produce each equilibrium compound stability boundary line across the entire pH range (for situations where ion complexation effects due to Cl^- are not considered). These K_{sp} values are shown with respect to each predominant ion in Table 5.I. For example, in the case of the amorphous $Zn(OH)_2$ reaction equilibrium can be established through the following routes:

(Alkaline) $$Zn(OH)_2\ (s) = Zn^{2+}\ (aq) + 2OH^-\ (aq) \quad \text{Equation 5.1}$$

(Near-Neutral) $$Zn(OH)_2\ (s) + OH^-\ (aq) = Zn(OH)_3^-\ (aq) \quad \text{Equation 5.2}$$

(Acidc) $$Zn(OH)_2\ (s) + 2OH^-\ (aq) = Zn(OH)_4^{2-}\ (aq) \quad \text{Equation 5.3}$$

Utilizing these reactions, the solubility relation can be determined based on the K_{sp} constants in Table 1, such as for Equation 1:

$$log(K_{sp}) = log\left(\frac{(Zn^{2+})(OH^-)^2}{Zn(OH)_2}\right) = -15.42 \qquad \text{Equation 5.4}$$

Derivation of the three chemical stability equations, one with respect to each predominant aqueous Zn ion, when summed produced a solubility-based chemical stability diagram for $Zn(OH)_2$ (am) based on the assumption that free dominant Zn_{aq} ion availability is not limiting (always present in greater quantities than necessary for equilibrium corrosion product precipitation). The method of calculating these equilibria follows fundamental solubility relations, which can be found in previous work and elsewhere.[8,22] The method of calculation and the exact solubility relations utilized to construct the chemical equilibrium diagrams are provided in detail in the Supplemental Material (Section 5.1.11).

Table 5.I : Zn-based solid corrosion product equilibrium stability constants, K_{sp}, and formation ratio with respect to predominance zone. *a* = # of available Zn cations required, *b* = # of available OH^- species required, and *c* = # of CO_3^{2-} species required for corrosion product formation. K_{SP} values are determined with respect to the dissolution of the compound to Zn^{2+}, Cl^-, CO_3^{2-}, and OH^-.

Corrosion Product		log(Solubility Product (K_{sp})) for Each Ion Predominance Zone			Species Formation Ratio
		Zn^{2+}	$Zn(OH)_3^-$	$Zn(OH)_2^{2-}$	a : b : c
ZnO	Zincite	-16.65	-2.51	1.01	1 : 2 : 0
$Zn(OH)_2$ (amorphous)	Wulfingite (am)	-15.42	-1.28	-2.24	1 : 2 : 0
$Zn(OH)_2$ (epsilon)	Wulfingite (ε)	-17.04	-2.90	-1.62	1 : 2 : 0
$Zn(CO_3)$	Smithsonite	-10.92	3.22	6.74	1 : 0 : 1
$Zn_5(CO_3)_2(OH)_6$	Zinc Hydroxycarbonate	-77.60	-6.90	10.70	5 : 6 : 2
$Zn_5(OH)_8Cl_2 \cdot H_2O$	Simonkolleite	-73.80	-3.10	14.50	5 : 8 : 0

In the presence of complexing species such as chloride, however, the necessary Zn_{aq} content required for unhindered corrosion product precipitation may not always exist, as these ligands compete for the use of this cation content through ligand formation (such as formation of $ZnCl^+$, $ZnCl_3^-$, etc.). To account for this complexation competition, available, dominant Zn_{aq} content was quantified for each ion predominance zone across the pH spectrum to quantify the "actual" solubility of each corrosion product. In this treatment, the actual solubility of Zn-compounds was calculated with respect to free Zn^{2+} by determining the actual $[Zn^{2+}]$ as a function of pH and $[Cl^-]$. The specific stability constants, or β values, shown in Table 5.II, were used to determine the ratio of each Zn-based ion present in solution to the total aqueous Zn concentration, $[Zn_{Tot}]$. The derivation of this aqueous Zn ion availability equation is provided in the Electronic Supplemental Material. These equations were utilized to quantify the ratio of free Zn^{2+} ion content to the total aqueous Zn concentration for the Zn^{2+} ion. Since the Zn^{2+} requirement for corrosion product equilibrium was calculated from equations like Equation 5.4, the total Zn_{aq} content required for corrosion product formation could be determined from this ratio. Chemical stability diagrams were then reconstructed to incorporate complexation competition in this way, enabling these diagrams to predict bulk Zn corrosion product formation under more rigorous solubility conditions for the marine environment of interest.

Table 5.II : Zn-based aqueous ion specific stability product constants, β, calculated based on formation from Zn^{2+}.

Zn-L Ion Species	**log(Stability Product (β))** $\boldsymbol{\beta = \frac{[Zn(L)_x^{2-xl}]}{[Zn^{2+}][L^{l-}]^x}}$
$Zn(OH)^+$	4.40
$Zn(OH)_2^0$	11.30
$Zn(OH)_3^-$	14.14
$Zn(OH)_4^{2-}$	17.66
$ZnCl^+$	0.43
$ZnCl_2$	0.61
$ZnCl_3^-$	0.53
$ZnCl_4^{2-}$	0.20

5.1.3.2 *Construction of Equilibrium Chemical Stability Boundaries: Nanoscale Formation*

The size scale of the corrosion product formation was also evaluated by incorporating the Gibbs-Thompson curvature relation into the chemical stability trend equations. For this purpose, use of chemical potential was necessary instead of solubility, as has been practiced in previous work,[6,8] which enabled the differentiation of the bulk chemical potential from the curvature-dependent chemical potential for the corrosion product of interest:

$$\mu_{\text{curve}}\,(\text{convex}) = \mu_{\text{bulk}} + \frac{2\gamma\Omega}{r} \qquad \text{Equation 5.5}$$

where γ = interfacial energy (J/m^2), Ω = molar volume (m^3/mol), and r = radius of the nanosphere (m). As γ and Ω can be experimentally and mathematically understood, the effect of curvature on corrosion product stability may then be assessed at the nanoscale. This derivation is conducted with respect to a spherical case, but these relations may be derived to consider more general curvature geometries also. In the case of the ZnO dissolution reaction in the Zn^{2+} predominance zone,

$$ZnO + H_2O = Zn^{2+} + 2OH^- \qquad \text{Equation 5.6}$$

for example, the incorporation of the surface curvature would affect the ZnO chemical potential component of the overall solubility relation:

$$log\left(\frac{[Zn^{2+}][OH^-]^2}{1}\right) = \frac{-\left((\mu_{Zn\,2+} + 2\mu_{OH-}) - \left(\mu_{H2O} + \mu_{bulk\;ZnO} + \frac{2\gamma\Omega}{r}\right)\right)}{2.303\;RT} \qquad \text{Equation 5.7}$$

where R is the ideal gas constant (J/mol K) and T is temperature (K). The γ_{ZnO} value of 3.55 J/m^2 was obtained from theoretical modeling literature (which does not incorporate the environment, but is a suitable baseline to evaluate trends in stability) and describes the assumedly relaxed lattice state on the (111) ZnO surface,[26] which enabled the calculation of a nanoscale ZnO chemical stability diagram. Use of this relation enables the derivation of chemical stability based on both "actual" solubility and surface curvature to enable thermodynamic prediction of the Zn ion concentration and pH boundaries for ZnO nanostructure formation and dissolution.

5.1.3.3 *Construction of Chemical Trajectory Trends*

The derivation of the chemical trajectory relations required unique expressions for each corrosion product or group of corrosion products having a specific and unique elemental ratio. To first quantify the ratio of produced cations and the corresponding pH change associated with the dissolution of each corrosion product, consider the general Zn reaction for a simple hydroxide:

$$M_a(OH)_b + nH^+ = aM^{n+} + bH_2O \qquad \text{Equation 5.8}$$

where the desired cation (M^{n+}) to H^+ ratio is *a : n* (the relationship between metal ion charge and number of hydrogen ions may require more sophisticated variable assignment in exceedingly complex reactions). Effects on chemical trajectory due to the presence of a pH buffer have been considered and quantified in previous work.[8] After applying the previously developed trajectory expressions to quantify the [M^{n+}] change as a function of pH for the corroding system,[8] the following general chemical trajectory equation is produced:

$$log[M^{n+}] = log\begin{pmatrix} [M^{n+}]_{init} + \frac{a}{b}[10^{-pH_{init}} - 10^{-pH_{inst}}] \\ + \frac{a}{b}[10^{pH_{inst}-14} - 10^{pH_{init}-14}] \end{pmatrix} \qquad \text{Equation 5.9}$$

However, the effects of more complex corrosion product dissolution need to be assessed in the Zn system, in which exist complex elemental ratios that must be accounted for. For instance, take the Simonkolleite ($Zn_5(OH)_8Cl_2 \cdot H_2O$) dissolution reaction:

$$Zn_5OH_8Cl_2 \cdot H_2O = \; 5Zn^{2+} + 8OH^- + 2Cl^- + H_2O \qquad \text{Equation 5.10}$$

In this reaction, the produced cation content must be tracked according to the change in OH^- or H^+ concentration. During complexation competition, the available free OH^- content and its distribution between $Zn(OH)^+$, $Zn(OH)_2^{o}$, $Zn(OH)_3^-$, or $Zn(OH)_4^{2-}$ will be affected by pH (Table 5.II). For that purpose, the fraction of hydroxylation (OH^- consumption to form aqueous OH-based complexes) that occurs for each released M^{n+} may be tracked as *f*:

$$f = \sum d\left[M(OH)_d^{n-d}\right]_{d\in[1,4]} \qquad \text{Equation 5.11}$$

where *d* is the required number of OH^- consumed during hydroxylation and *n* is the charge of the free metal ion. When the given reaction occurs, such as Simonkolleite dissolution, 8 OH^- species are produced as well as 5 Zn^{2+} species (*b* = 8, *a* = 5, *a :b* ratio = 5 : 8). The *a : b* ratio would quantify the chemical system progression ($[Zn]_{tot}$) across the pH range of an M^{n+} - pH diagram without the complication of species complexation; however, the subsequent complexation of OH^- species, according to the *f* function reduces the effective increase in available OH^- content as a function of pH, requiring that Equation 5.11 incorporate such effects to become:

$$log[M^{n+}] = log\left(\begin{gathered}[M^{n+}]_{init} + \frac{a}{b-af}\left[10^{-pH_{init}} - 10^{-pH_{inst}}\right] + \\ \frac{a}{b-af}\left[10^{pH_{inst}-14} - 10^{pH_{init}-14}\right]\end{gathered}\right) \qquad \text{Equation 5.12}$$

Furthermore, the presence of carbonate species must also be quantified to establish the proper trend, as the availability of CO_3^{2-} is also influenced by pH. Consider the dissolution of Zn hydroxycarbonate:

$$Zn_5(CO_3)_2OH_6 = 5Zn^{2+} + 2CO_3^{2-} + 6OH^- \qquad \text{Equation 5.13}$$

For this reaction to occur, the availability of the pH-dependent species CO_3^{2-} is necessary, as can be understood through the following relation:

$$Zn(OH)_f^{2-f} + H_F(CO_3)_c^{-(2-F)} = Zn^{2+} + f\,OH^- + c\,CO_3^{2-} + F\,H^+ \qquad \text{Equation 5.14}$$

where *c* is the required number of CO_3^{2-} species. This combined reliance on hydroxyl and carbonate species availability produces the following chemical trajectory equation to quantify the progression of pH and $[M^+]$ dissolved in solution:

$$log[M^{n+}] = log\begin{pmatrix} [M^{n+}]_{init} + \frac{a}{b+cF-af}[10^{-pH_{init}} - 10^{-pH_{inst}}] + \\ \frac{a}{b+cF-af}[10^{pH_{inst}-14} - 10^{pH_{init}-14}] + \\ \left[\frac{[CO_3^{2-}]_{init}}{b+cF-af}\left(G_{inst}^{CO_3^{2-}} - G_{init}^{CO_3^{2-}}\right)\right] \end{pmatrix} \qquad \text{Equation 5.15}$$

where $G^{CO_3^{2-}}$ quantifies the fraction of available CO_3^{2-} in a similar fashion as Equation 5.11. For the calculation of the remaining chemical trajectories necessary to describe the corroding Zn system, the *a : b : c* ratio for each Zn corrosion product is included in Table 5.I. Together, these trend relations enable the tracking of the available aqueous Zn ion concentration from an initial pH / available CO_3^{2-} condition in consideration OH^- - and Cl^- -based ligand formation.

5.1.4 **Results**

5.1.4.1 ***Ion Predominance and Chemical Stability as a Function of Bulk Environment***

To begin to develop a more inclusive chemical stability diagram for the Zn system, the regions and type of Zn ion species predominance must be understood based on the spectrum of Zn ions known to occur in a given solution. Consider a non-sulfate-containing chloride environment where Zn^{2+} is provided by any dissolution process that may occur during corrosion, drug delivery, Zn-rich coating depletion, oxide degradation, etc. The pertinent ions are listed in Table 5.II. The state of chloride saturation at 5.45 M concentration was first assessed to evaluate predominance, as shown in Figure 5.1. These diagrams are marked by threshold pH values at which a transition in the dominant, aqueous Zn ion species occurs. At this high chloride content, the $ZnCl_4^{2-}$ ion dominates from pH -1.0 to 9.8 followed by $Zn(OH)_2^0$ dominating from pH 9.8 to 10.9, and lastly $Zn(OH)_4^{2-}$ dominates from pH 10.9 to 16.0. Similar Zn ion predominance diagrams have been previously produced in the literature for corrosion analysis at various fixed [Cl^-] or [CO_3^{2-}], many of which utilize the program Medusa-Hydra.[27–31] However, these predominance diagrams are often underutilized and are not typically used to produce even basic chemical stability diagrams. As shown on the right y-axis in Figure 5.1, the coordination of the dominant hydroxide species increases with increasing overall amount of consumed hydroxyl ions (and increasingly alkaline pH). To evaluate the effect of the chloride complexation further, ion predominance was calculated

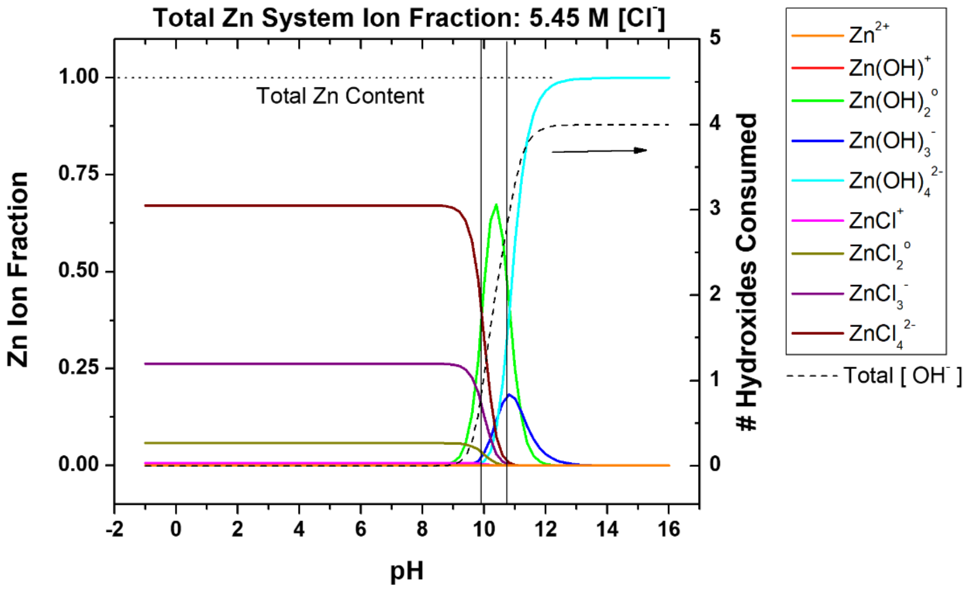

Figure 5.1: Speciation diagram depicting the fractional distribution of various Zn-based species as a function of pH for a given ligand concentration, in this case 5.45 M [Cl^-]. Included is the function (dashed line) which describes the number of OH^- which would be consumed upon the addition of Zn^{2+} to the system, as a function of pH. Transition points are marked by vertical black lines where the dominant aqueous Zn ion identity changes. This system neglects carbonates.

at the dilute condition of 0.06 M, as shown in Figure 5.2. In the substantially reduced presence of Cl^- the Zn^{2+} ion now dominates in the acidic region to a pH of 8.3. However, the neutral and alkaline regions remain unchanged, as transition between these aqueous ion predominance regions remains at a pH of 10.9 and both the $Zn(OH)_2^0$ and $Zn(OH)_4^{2-}$ continue to dominate (Figure 5.2). As can be seen in the total hydroxyl consumption, the chloride content does have some measurable

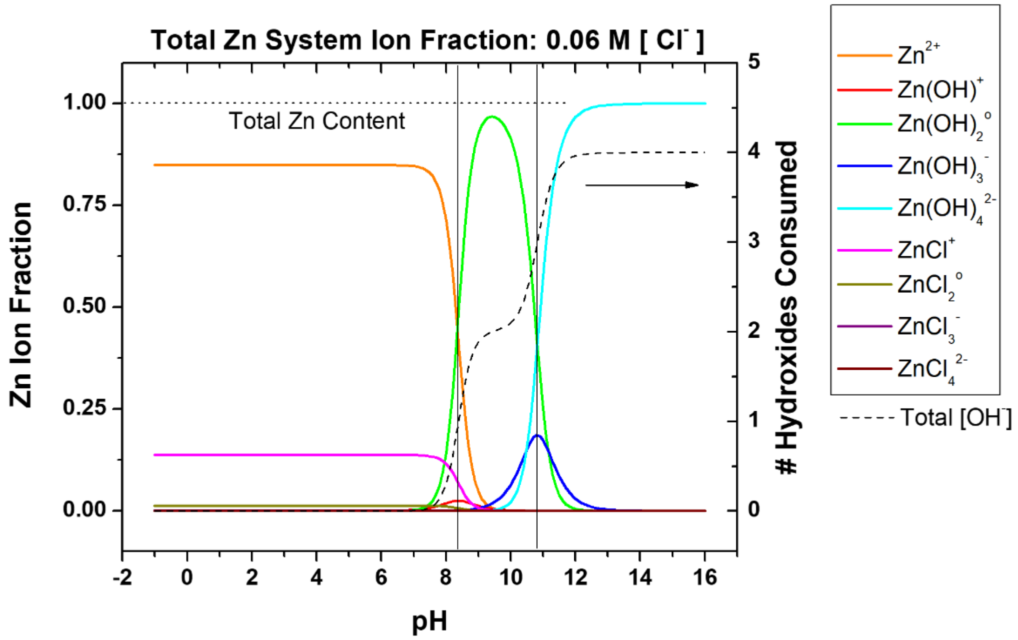

Figure 5.2: Speciation diagram depicting the fractional distribution of various Zn-based species as a function of pH for a given ligand concentration, in this case 0.06 M [Cl^-]. Included is the function (dashed line) which describes the number of OH^- which would be consumed upon the addition of Zn^{2+} to the system, as a function of pH. Transition points are marked by vertical black lines where the dominant aqueous Zn ion identity changes. This system neglects carbonates.

impact on the hydroxide formation at neutral pH. As the more dilute conditions are common and chloride concentrations of approximately 2 M are necessary before the Zn^{2+} ion no longer dominates in the acidic region, the predominant ions pertinent to the dilute scenario will be mainly considered for recalculation of corrosion product solubility relations to derive the chemical stability diagrams.

As a baseline, the Zn chemical stability diagram for saturated chloride conditions (5.45 M) was first developed neglecting Cl^- complexation effects (no limitation on available Zn_{aq} content), as shown in Figure 5.3 zoomed in to focus on the key pH range of 3.0 to 15.0. The exact chemical reactions necessary to construct Figure 5.3, as well as the chemical stability diagrams to follow, can be found in the Supplemental Material (Section 5.1.11). Analyses of solid Zn corrosion product stability with respect to pH are present in the literature for simple Zn-based corrosion products, but not for complex products such as $Zn_5(CO_3)_2(OH)_8$ and $Zn_5(OH)_8Cl_2\cdot H_2O$.[6,32] At these high chloride concentrations for a fixed dissolved carbonate content of 5 mM, $Zn(CO_3)$ is the most readily formed corrosion product from pH 4.0 to 7.8, followed by $Zn_5(CO_3)_2(OH)_8$ from a pH of 7.8 to 10.8, and lastly $Zn(OH)_2$ (epsilon) from pH 10.2 to 15.0. These corrosion products require small Zn concentrations to form under these conditions, with the lowest requirement being approximately $8\text{x}10^{-9}$ M and $6\text{x}10^{-8}$ M Zn_{aq} for $Zn_5(CO_3)_2(OH)_8$ and $Zn(OH)_2$ / $Zn(CO_3)_2$ at pH 9.2, respectively. However, the condition of plentiful free Zn^{2+} content for corrosion product formation is unlikely, and free Zn^{2+} ion limited conditions must be quantified to more accurately predict corrosion product formation.

5.1.4.2 ***Chemical Stability as a Function of Bulk Environment and Complexation Competition***

For the same saturated chloride (5.45 M) condition, the Zn chemical stability diagram was then recalculated to include the effects of ion complexation, as shown in Figure 5.4. Also included

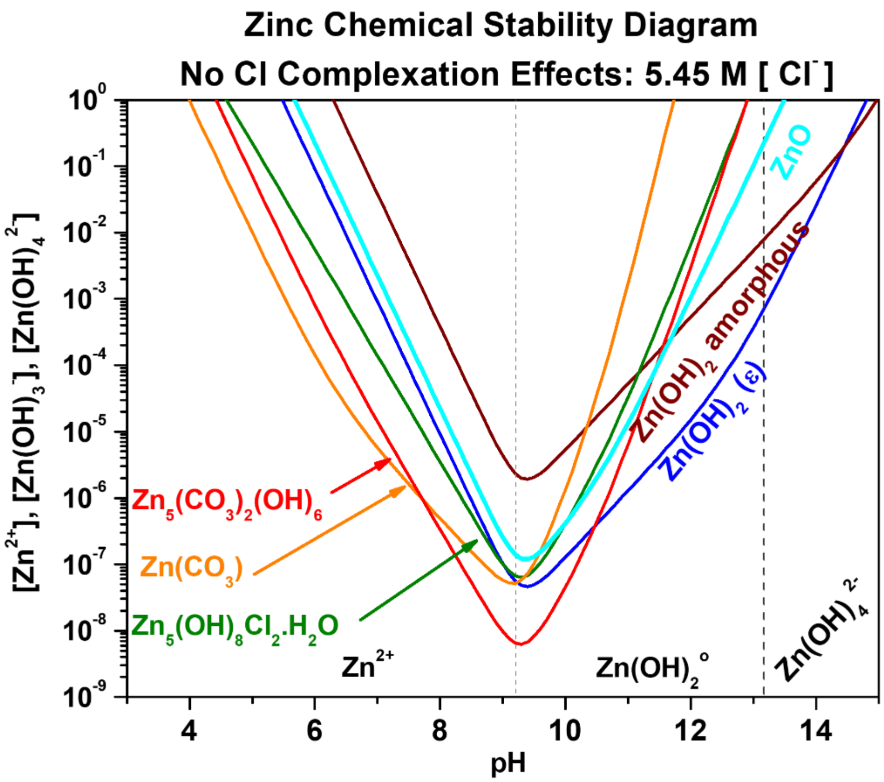

Figure 5.3: Chemical stability diagram for the Zn-Water system. Relevant species are given for exposure in a Cl$^-$ (5.45 M) and CO_3^{2-} (5.00 mM) containing environment. This diagram does not include the effect of ligand complexation due to the presence of Cl$^-$.

in Figure 5.4 are the chemical trajectories (M^{n+}, pH) to track the $[Zn_{tot}]$ progression of the system from an initial pH of 7 if Zn^{2+} were added to the solution via dissolution of the various compounds. Separate trajectory lines are necessary for each elemental ratio required to form the associated corrosion products (Table 5.I), thus the line color for the trajectories matches that of the associated corrosion product equilibrium stability line. For example, the orange chemical trajectory corresponds to the orange equilibrium chemical stability curve for $Zn(CO_3)$, which has the unique $a : b : c$ of 1:0:1 (Table 5.I). A unique case exists for $Zn(OH)_2$ and ZnO, since both have $a : b : c$ of 1:2:0 (Table 5.I), thus the single chemical trajectory associated with the chemical stability curves for $Zn(OH)_2$ and ZnO is shown in black. The point of intersection between these chemical trajectories and the relevant equilibrium stability line has been circled to indicate the total aqueous

Zn concentration and pH required for equilibration of each corrosion product. It is recognized that the equilibrium conditions may be met for the formation of a more stable compound upon the dissolution of a less stable compound, resulting in compound transformation over time. As can be readily observed in Figure 5.4, the inclusion of complexation effects due to Cl^- and OH^- on corrosion product stability causes an increase in the required total aqueous Zn content of two orders of magnitude to reach and establish equilibrium, and the chemical stability trends all shift towards

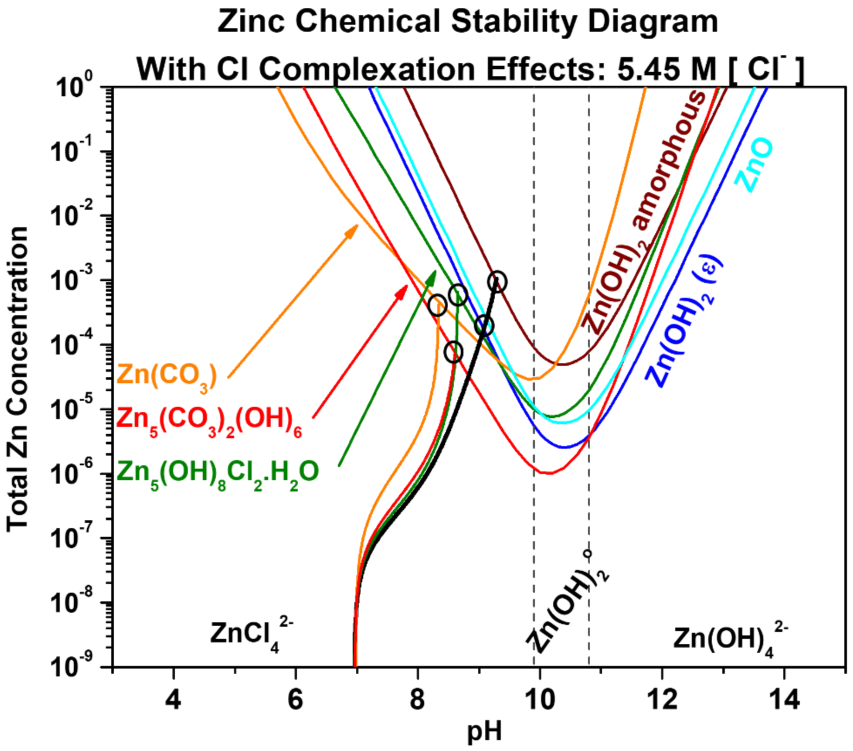

Figure 5.4: Chemical stability diagram for the Zn-Water system. Relevant species are given for exposure in a Cl^- (5.45 M) and CO_3^{2-} (5.00 mM) containing environment. This diagram includes the effect of ligand complexation with Cl^- on the stability of the zinc compounds. Included are chemical dissolution trajectories which describe how the solution chemistry progresses after assuming some initial condition (pH = 7, $[Zn_{tot}] = 10^{-8}$) to a final equilibrium condition (where the trajectory line intersects an equilibrium line). The trajectory line color matches that of the compound being tracked with respect to concentration and pH (black corresponds to the trajectory line involving both $Zn(OH)_2$ and ZnO due to the expense of their trajectory being the same (Table 5.I)). Note the incorporation of ligand complexation effects due to the presence of Cl^-.

more alkaline pH values. Chemical stability diagrams for the Zn system that incorporate ligand complexation effects exist sparingly in the literature, such as in Tay et. al,[32] which considers only OH^- complexation effects on aqueous Zn ion availability. However, no Zn stability diagrams exist to predict the complexity of corrosion products shown here, nor do any works consider Cl^- and OH^- complexation in a CO_3^{2-} - containing environment, and none exist which also track such a complex system state via chemical trajectories. As shown in Figure 5.4, $Zn(CO_3)_2$ remains the most readily formed corrosion product from pH 6.0 to 7.8 when Cl^- complexation is considered, followed by $Zn_5(CO_3)_2(OH)_8$ from a pH of 7.8 to 10.8, and lastly $Zn(OH)_2$ (epsilon) from pH 10.2 to 13.7. At the point of least Zn content requirement for formation at pH 10.2, $Zn_5(CO_3)_2(OH)_6$ and $Zn(OH)_2$ (epsilon) require approximately $1x10^{-6}$ M and $2x10^{-6}$ M [Zn_{Tot}]. The chemical trajectories for each corrosion product are relatively similar despite considerable differences in elemental ratios required to form the range of products.

The effect of the chloride content and complexation was then re-evaluated by recalculating the chemical stability diagram for a dilute chloride concentration of 0.06 M at fixed dissolved carbonate concentration of 5 mM, as shown in Figure 5.5. The first readily observed changes in the chemical stability trends are that the ZnO and $Zn(OH)_2$ trends flatten in the neutral region, and the minima in zinc ion concentration required to reach equilibrium of the carbonate- / chloride-containing corrosion products shift towards pH of ~ 8.5. Under these dilute chloride conditions these minima also decrease the Zn ion requirement for equilibrium by half an order of magnitude. The combination of these changes causes intersection of the $Zn_5(CO_3)_2(OH)_6$ and $Zn(OH)_2$ (epsilon) stability curves with the chemical trajectory trends near their minima, suggesting that formation of these phases may occur at increasingly lower [Zn_{tot}] until an initial pH of approximately 8 in the bulk system.

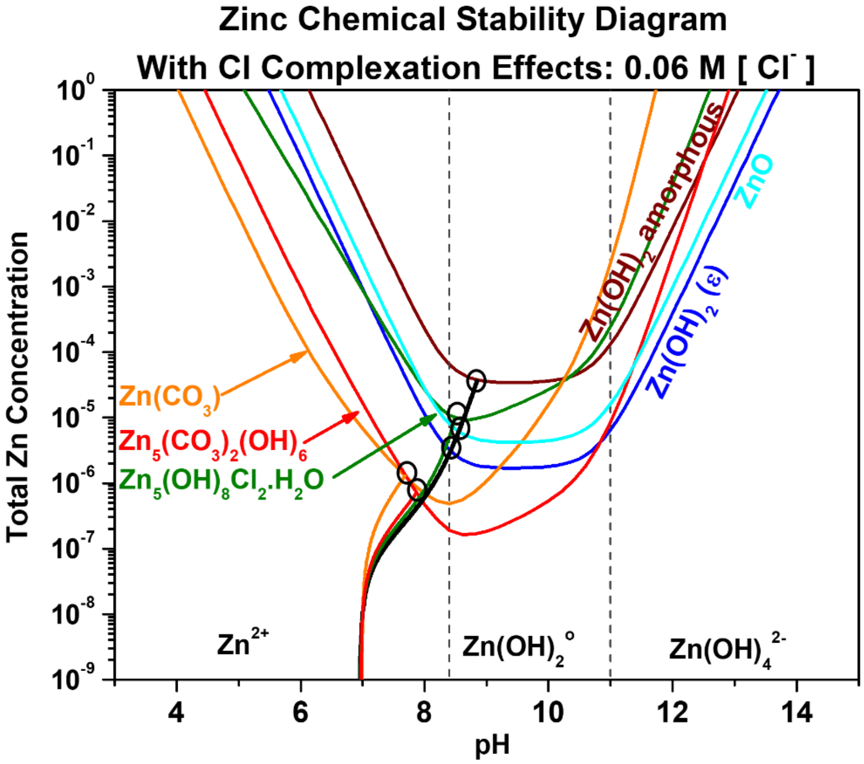

Figure 5.5: Chemical stability diagram for the Zn-Water system. Relevant species are given for exposure in a Cl^- (0.06 M) and CO_3^{2-} (5 mM) containing environment. This diagram includes the effect of ligand complexation on the stability of the zinc compounds. Included are chemical dissolution trajectories which describe how the solution chemistry progresses to some initial condition (pH = 7, $[Zn_{tot}] = 10^{-8}$) to a final equilibrium condition (where the trajectory intersects an equilibrium line). The trajectory line color matches that of the compound being tracked with respect to concentration and pH (black corresponds to both $Zn(OH)_2$ and ZnO due to the expense of their trajectory being the same (Table 5.I)).

5.1.4.3 *Chemical Stability as a Function of Complexation and Curvature*

Nanoparticles of ZnO are being increasingly utilized in the biomedical, corrosion engineering, and energy sectors, and their formulation can be both dangerous due to high reactivity and costly.[33,34] For this reason, ZnO has been thoroughly studied in terms of production pathways, quality, and the effects of different production methods on particle size and surface reactivity/energy.[28] One theoretical study found that the surface energy of ZnO on the relaxed

(111) plane at 298 K remains relatively constant at 3.55 J/m^2,[26] which we utilized here to evaluate the Zn_{aq} requirement for ZnO nanoparticle equilibrium as a function of radius, Zn^{2+} and pH. This Gibbs-Thompson-based chemical stability prediction is shown in Figure 5.6, demonstrating the increase in the required [Zn_{Tot}] for ZnO nanoparticle equilibration at increasingly small radii. Specifically, a ZnO nanoparticle with radius of 4 nm at pH 9.5 is soluble at roughly four orders of magnitude greater [Zn_{Tot}] in the bulk solution than is a nanoparticle having radius of 30 nm, and therefore is less thermodynamically stable. As the ZnO surface energy is fixed here at a value theoretically calculated in vacuum, the effect of utilizing a different γ value was evaluated in Figure 5.7. These predictions demonstrate that there is an observable effect on the equilibrium requirement for ZnO nanoparticles in terms of [Zn_{Tot}] and pH conditions by changing γ from 3.55 J/m^2 to 1.00 J/m^2, however this effect only exists at radii less than 1 micrometer (10^{-6} m). These findings are comparable to experimental findings present in the literature, as will be explored in the Discussion.

5.1.5 **Discussion**

Zinc remains a consistently utilized metal today, with ever diversifying applications pertaining to health, biotechnology, and energy. With these diverse needs comes the demand to understand Zn corrosion and the formation of specific oxidation products in changing electrochemical conditions and saline environments, as these changes may be either beneficial or detrimental to component performance. In studies on Zn-rich primers (ZRPs), for instance, not only are certain products such as $Zn_5(CO_3)_2(OH)_6$ known to be more passivating and protective than others,[13] but each corrosion product will also have a characteristic volume increase associated

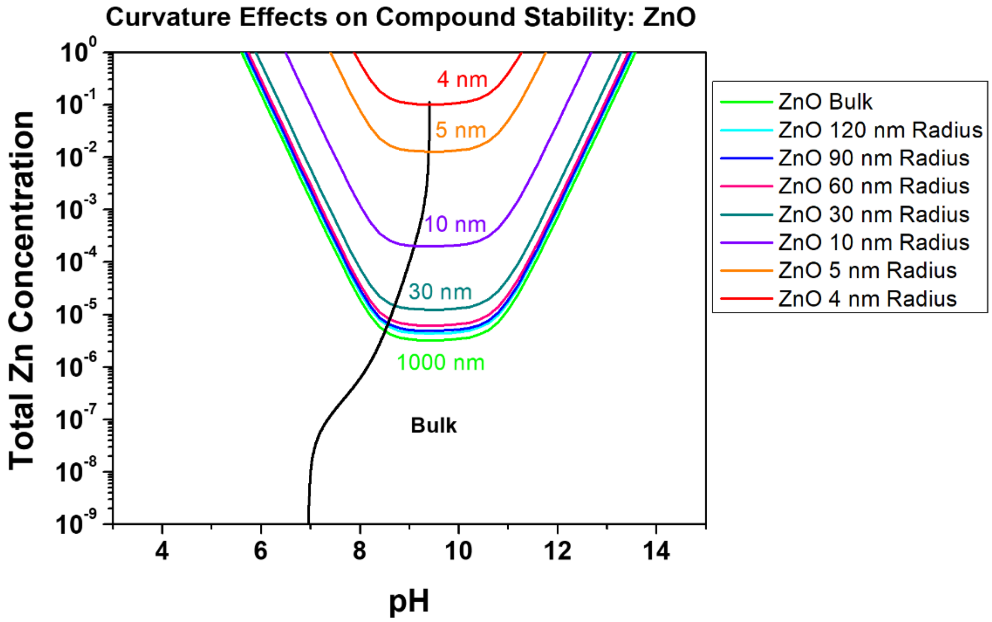

Figure 5.6: Chemical stability diagram for ZnO at various particle radii at the nanometer scale, illustrating the effect of surface curvature on the stability ($[Zn_{Tot}]$, pH) phase field at a constant surface energy of 3.55 J/m^2 [26]. Included in the solid black line is the chemical trajectory trend for a starting pH of 7, $[Zn_{Tot}] = 10^{-8}$. This thermodynamic calculation assumes a constant temperature of 298 K and spherical capillarity effects on a (111), relaxed lattice ZnO surface condition. A $[Cl^-]$ of 0.06 M is considered here.

with its formation that is known to affect coating porosity, Zn pigment connectivity, and the electrolyte ingress necessary for pigment activation to achieve effective corrosion protection on vital alloys such as steel.[13,35–41] Comparison of the present modeling results with experimental findings on Zn in the literature will enlighten the reader as to the accuracy and utility of these new developments to advance the scope of the chemical stability diagram. Furthermore, comparison will be drawn from the wide spectrum of literature on ZnO nanoparticle formation[19,28,34,42] to discuss the potential for utilizing the Gibbs-Thompson rederivation of the ZnO chemical stability diagram.

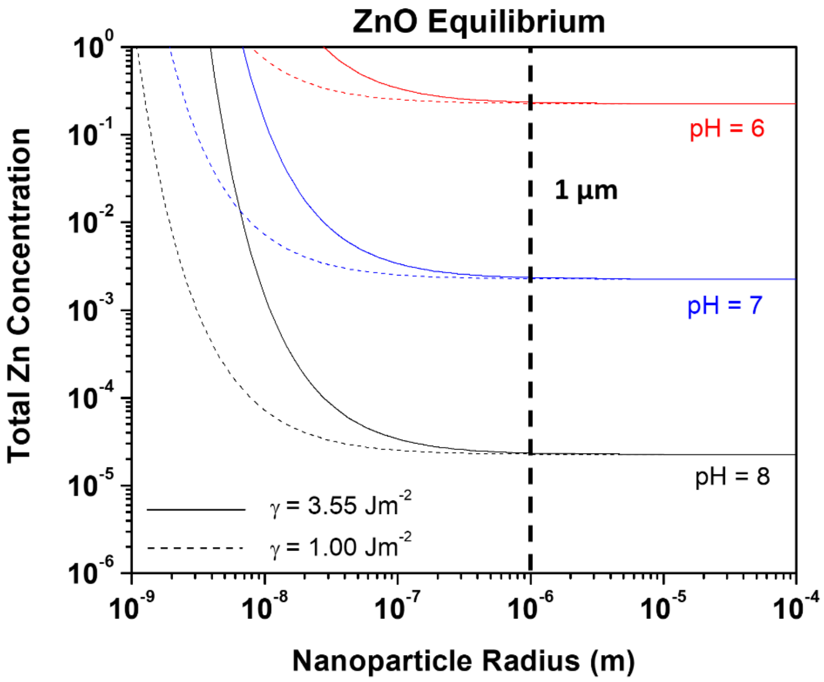

Figure 5.7: Line plot demonstrating the effect of ZnO particle radius on the equilibrium $[Zn_{Aq}]_{Tot}$ *stability requirement. The effect of varying surface energy is given by the trends produced for the two different surface energy values (Equation 5.5).*

In order to validate the utility of the presently developed chemical stability diagram methods, a thorough literature review will first demonstrate notable experimental results and trends for the pure Zn system. Experimental studies demonstrate that Zn corrosion is largely dictated by anionic surface chemistry and bulk pH conditions, and that reaction kinetics play a significant role only in select situations, which suggests that chemical stability diagrams could be a valuable predictive tool when accurately applied to the Zn system.[12,27,43,44] At pH lower than 5.0 or higher than 13.5, little to no corrosion product formation typically occurs on Zn.[12,45] At more intermediate pH values, experimental results have shown that Zn easily forms carbonate species, as dictated by the absorption and presence of CO_3^{2-} in the electrolyte.[13,43] These findings on pure Zn agree with alternate immersion studies on ZRPs, which find an increasing presence of CO_3-containing Zn corrosion product formation with increased drying time (and thus increasing concentration of dissolved CO_3^{2-} in the surface film).[13,35] Ohtsuka and Matsuda demonstrated through use of in-situ Raman spectroscopy that ZnO and $Zn(OH)_2$ (epsilon) readily form on the Zn surface during dry air exposure, and as the relative humidity (RH) is increased to 75% $Zn_5(CO_3)_2(OH)_6$ also forms.[35] At continuous RH of 80% or more, only $Zn_5(OH)_8Cl_2 \cdot H_2O$ and aqueous $ZnCl_2^0$ formation occur on the Zn surface.[35] When drying cycles are introduced intermittent to the establishment of 88% RH, a combination of ZnO, $Zn_5(CO_3)_2(OH)_6$, $Zn_5(OH)_8Cl_2 \cdot H_2O$, and aqueous $ZnCl_2^0$ are found on the Zn surface, with the amount of $Zn_5(CO_3)_2(OH)_6$ increasing as greater drying to wetting ratio was allowed.[35] Mouanga et. al and Ligier et. al also demonstrated that $Zn_5(CO_3)_2(OH)_6$ and $Zn_5(OH)_8Cl_2 \cdot H_2O$ were the major corrosion products formed on pure Zn following atmospheric exposure in dilute chloride, which is supported in the literature by the known transformation of $Zn(OH)_2$ / ZnO to these more complex products as a function of dissolved carbonate content.[13,46] In agreement with these proposed mechanisms, Marchebois et. al demonstrated that the formation of ZnO occurs quickly on pure Zn in full simulated seawater immersion, followed by the formation of increasing amounts of $Zn_5(OH)_8Cl_2 \cdot H_2O$ with time.[38] The presently developed Zn chemical stability diagrams predict the majority of these experimental results and demonstrate strong utility for the thermodynamically-dictated Zn system.

Chemical stability diagrams are based on thermodynamic stability and cannot communicate the influence of kinetics in the formation of Zn corrosion products. However, cross comparison of these diagrams with the extensive experimental evidence present in the literature can suggest the utility of these diagrams where stability, rather than kinetics, is dominant, and can infer where the electrochemical kinetics may be necessary to obtain the equilibrium Zn concentration. Figure 5.5 demonstrates that during dilute chloride immersion of the Zn surface, the formation of any Zn corrosion products outside of the pH value range of 4.5 to 13.5 would require 1 or more moles of aqueous Zn content. The low probability of such a high Zn ion concentration being present agrees with the experimental findings showing that little to no corrosion product forms outside the pH range of 5.0 to 13.5.[45] In dilute alkalinity, such as in the conditions which may occur where low RH is present, Figure 5 predicts the formation of $Zn(OH)_2$ (epsilon) followed by ZnO. This prediction is in agreement with Ohtsuka and Matsuda.[35] However, the dominance of ZnO formation with increasing exposure time suggests that $Zn(OH)_2$ (epsilon) is affected more by kinetic limitations such that ZnO is more readily formed. Additionally, it is possible that the assumed thermodynamic variables utilized here may not accurately reflect experiment, as the conventional chemical potential for NiO was recently revisited using first-principle modelling.[7] When RH < 80% is present, $Zn_5(CO_3)_2(OH)_6$ coexists with ZnO and $Zn(OH)_2$ in the presence of NaCl salt, which directly agrees with Figure 5.5 at pH of 10.7 or less. The acidification of the chloride solution to achieve pH less than 10.1 would agree with the known effects of atmospheric CO_2 aqueous absorption to form carbonic acid, known on a large scale as the ocean acidification process.[47] When utilizing the chemical trajectory trends from the example starting condition of pH 7.0, the $Zn(OH)_2$ (epsilon)/ZnO formation (solid black trajectory line) would begin at more alkaline pH (8.30 / 8.55) than the formation of $Zn_5(CO_3)_2(OH)_6$ (solid red trajectory line) (pH 8.00). Given a condition of sufficient wetting to increase [Cl^-], the $Zn(OH)_2$ (epsilon), ZnO, and $Zn_5(CO_3)_2(OH)_6$ trends would shift slightly towards more alkaline values and $Zn_5(OH)_8Cl_2 \cdot H_2O$ formation would more readily occur (Figure 5.4). These trends are also in agreement with the results of Ohtsuka and Matsuda, wherein increased RH caused the stabilization of aqueous $ZnCl_2^0$ and $Zn_5(OH)_8Cl_2 \cdot H_2O$ in the thin film.[35] As illustrated in Figure 5.1, aqueous $ZnCl_x$ species predominate at pH 9.8 or less in conditions of high [Cl^-], and in saturated NaCl conditions Figure 5.4 would predict that $Zn_5(OH)_8Cl_2 \cdot H_2O$ stability would be reached prior to

$Zn(OH)_2$ (epsilon) / ZnO equilibration at pH 9.0 or less. Specifically, recalculation of these ion predominance relations demonstrates that aqueous $ZnCl_2^0$ is the most abundant species when [Cl^-] is between 0.7 M and 1.2 M.

The thermodynamic predictions presented here also correlate well with long-term, controlled atmospheric exposure results on pure Zn where the [Cl^-] and/or [CO_3^{2-}] were limited. Qu et. al deposited dilute amounts of NaCl on the Zn surface and held 80% RH using purified water vapor and air for 25 hours, which resulted in the formation of ZnO and $Zn_5(OH)_8Cl_2 \cdot H_2O$.[48] Svensson and Johansson performed similar experiments on pure Zn but for 420 hours at 70% RH, and only $Zn_5(OH)_8Cl_2 \cdot H_2O$ was observed through X-Ray Diffraction regardless of the amount of NaCl deposited on the Zn surface prior to exposure.[49] In light of the known transformation of ZnO / $Zn(OH)_2$ with increasing exposure time, these results agree well with Figure 4.5 for the initial pH of 7 due to the lack of carbonate species introduced during these experiments. Specifically, these thermodynamic predictions would dictate that ZnO would begin to form at pH of 8.5 and [Zn_{aq}] of $6x10^{-6}$ M, while $Zn_5(OH)_8Cl_2 \cdot H_2O$ formation would require higher concentration, [Zn_{aq}] of $1x10^{-5}$ M, at pH 8.5. In the case of Svensson and Johansson, additional salt deposition at 75% RH would increase [Cl^-] towards saturation, which would explain the dominance of the $Zn_5(OH)_8Cl_2 \cdot H_2O$ formation; as [Cl^-] increases, $Zn_5(OH)_8Cl_2 \cdot H_2O$ becomes more stable than ZnO at pH below 10.0 as seen in the high [Cl^-] case of Figure 5.4.[49] Ligier et. al evaluated pure Zn corrosion product formation following exposure to simulated atmospheric electrolytes containing $5x10^{-3}$ M $NaHCO_3$/ $1x10^{-3}$ H_2O_2 and $2x10^{-1}$ M NaCl/ $5x10^{-3}$ $NaHCO_3$/$1x10^{-3}$ M H_2O_2 for 4 days, and demonstrated that the amount of $Zn_5(CO_3)_2(OH)_6$ formed on Zn depends on the [Cl^-] concentration, as $Zn_5(OH)_8Cl_2 \cdot H_2O$ formation quickly dominates.[13] These results do not correlate well with the dilute [Cl^-] or saturated [Cl^-] prediction shown in Figures 5.4 and 5.5 for an initial pH of 7, suggesting that kinetic limitations may have more effect in $Zn_5(CO_3)_2(OH)_6$ than in $Zn_5(OH)_8Cl_2{\cdot}H_2O$ formation; perhaps with a difference in CO_3^{2-} / Cl^- diffusivity. None of the aforementioned atmospheric exposures resulted in the formation of $Zn(CO_3)_2$, despite this corrosion product being the most stable from pH 4.0 to 7.7 in dilute chloride and from pH 5.7 to 7.8 in saturated chloride conditions (Figures 5.4 and 5.5). However, the 13-16 year marine exposures conducted on pure Zn by de la Fuente et al. demonstrate ZnO, $Zn(CO_3)_2$, and $Zn_5(OH)_8Cl_2{\cdot}H_2O$ formation, suggesting that either the previous experiments did not reach sufficiently low pH or that $Zn(CO_3)_2$ has slow formation kinetics.[50]

The present diagrams focus solely on a chloride-based saline environment with equilibrium carbonate concentration of 5 mM (adjustable to consider more dilute cases), which does not include the effects of impurities present in the electrolyte such as sulfur, less common corrosion product formation, or changing temperature (all calculations done at 25°C) (for more detail on the assumptions see the Supplemental Material (Section 5.1.11)). However, further advancement of these diagrams to incorporate such effects will prove useful for predicting Zn corrosion in unique settings, such as for the design of effective cathodic protection systems. Modern developments in the use of ZnO have produced a much wider spectrum of uses for this material, however, in which the chemical stability diagram based on the Gibbs-Thompson rederivation may also prove useful to predict performance.

Zinc oxide has the unique duality of a large direct band gap and the ability to form nanostructures, making the applications for this material far-reaching: ranging from drug delivery and cancer therapy to piezoelectric power generation and spintronics.[28] Considerable research has been dedicated to expanding the growth and production procedures as well as to discover new applications for ZnO, especially when used in the form of nanoparticles and nanorods.[28,32,42] Such research is motivated by the strong tunability of the size, shape, and morphology of ZnO crystals in solutions such as $ZnAc_2$.[28,32] Specifically, in this solution the ZnO size, density, growth uniformity, and crystal morphology may be tuned via control of the $ZnAc_2$ concentration and the solution pH through addition or subtraction of NH_4OH.[28] Despite the typical use of organic solutions to contain the ZnO formation reactions, common ZnO growth trends exist that enable correlation with the present thermodynamic analysis in aqueous Cl-based environment.

Figure 5.6 demonstrates the concept of the curvature-dependent chemical stability diagram derivation in NaCl for comparison to the bulk thermodynamic predictions shown in Figures 5.3-5.5, demonstrating that as much as 5 orders of magnitude increase in aqueous Zn concentration is necessary for ZnO to be thermodynamically stable in Cl-containing environment at increasing nanoscale size, from the bulk (greater than 1 micrometer) to 4 nm particle radius. These predictions also demonstrate that the dependence of ZnO solubility on surface curvature is greater than the effect of $[Cl^-]$ complexation, which is supported by the results of ZnO synthesis studies utilizing various ZnO precipitation methods in non-chloride-containing solutions. Moazzen et. al observed that the average ZnO nanoparticle size produced in Zn acetate dihydrate + sodium hydroxide solution increased as the ratio of Zn acetate dihydrate to sodium hydroxide was decreased from 1:1 (20 nm ZnO particle size) to 1:4 (36 nm ZnO particle size).[51] When hydrothermally growing ZnO nanorods in Zn acetate and ammonia, Tay et. al observed increasingly smaller, denser ZnO nanorods forming as the Zn acetate concentration was increased for a given concentration of ammonia following three hours at 370 K.[32] Tay et. al utilized curvature relations based in nucleation theory as well as a basic Zn chemical stability diagram prediction to support and explain these findings, which arrived at similar conclusions as seen here.[32] Recent work in lead-based systems has demonstrated utility of curvature-based solubility relationships for determining nanoparticle formation as well.[52] These results also illuminate the effect of surface energy on the stability of capillary-affected surfaces. Figure 5.7 illustrates that larger concentrations of aqueous Zn are indeed for surfaces with higher surface energy. The curvature-dependent derivation illustrated here may easily be expanded to offer further insight into mechanisms underlying ZnO growth in more favorable and economically viable media (out of the scope of the present work), especially as the solubility constants necessary for such mathematical constructs are increasingly available for the Zn species of interest to ZnO growth.[21,22,53,54]

5.1.6 Conclusion

The chemical stability diagram concept has been advanced within the present work to encompass (1) "actual" solubility through accounting for all known species complexes; (2) chemical trajectories based on complex elemental ratios and present species which predict pH and M^{n+} conditions where specific corrosion products are expected to be in equilibrium with specific compounds, as well as the M^{n+} and pH ranges where these products are soluble, and (3) the dependence of solubility on surface curvature relevant to the prediction of nanoscale growth and morphology. The utility of this method was demonstrated for the corroding Zn system on the bulk scale, and for the ZnO system at the nanoscale in NaCl environment. These thermodynamic bulk scale predictions correlate well with experiment for the Zn system in NaCl, and suggest that the chemical stability diagram method should continue to be advanced for more accurate understanding of reaction trends in technologically relevant metals and corrosion systems.

Acknowledgements

The authors are grateful for the financial support and contribution of the United States Office of Naval Research [Award # N000141512491] under the direction of Dr. Airan Perez, the United

States Office of the Undersecretary of Defense Corrosion University Pilot Program [Award # FA7000-14-2-0010] under the direction of Mr. Daniel Dunmire, and the National Science Foundation [Award # NSF DMR #1309999].

Data Availability Statement

All thermodynamic constants utilized in the present work may be found in raw form in the references provided, or derived from the raw form using methods described in the Electronic Supplemental Material. Calculations generated during this study are available in an open access data repository, which can be accessed at DOI 10.17605/OSF.IO/Y39U6.

Author Contributions

All authors contributed to the derivation and construction of these chemical stability diagrams, as well as to the structure and composition of this manuscript. M.E.M provided literature review of Zn corrosion and drafted the paper. R.J.S, Jr. provided literature review of publications utilizing speciation and/or chemical stability methods, created the graphical abstract, and modified the manuscript. J.R.S reviewed, edited, and modified the manuscript.

Competing Interests

The authors declare no competing interests

5.1.7 Supplemental Material

The derivation of ion predominance will be systematically illustrated. The stability of each ion was assessed using stability constants, with respect to Zn^{2+}. For example, for the $Zn(OH)^+$ ion:

$Zn^{2+} + OH^- \rightarrow Zn(OH)^+$ $\quad$ $\log \beta = 4.40$ $\quad$ Equation 5.16

$4.40 = \log \frac{[Zn(OH^+)]}{[Zn^{2+}][OH^-]} = \log [Zn(OH)^+] - \log [Zn^{2+}] - \log [OH^-]$ $\quad$ Equation 5.17

$\boxed{[Zn^{2+}][OH^-] \cdot 10^{4.40} = [Zn(OH)^+]}$ $\quad$ Equation 5.18

These relations were derived for each ion and summated to quantify the total available Zn ion concentration with respect to Zn^{2+} (summation with other stability derivations based on additional predominant ions such as $Zn(OH)_4^{2-}$ yields the same overall results):

$Zn_{total} = [Zn^{2+}] + [Zn(OH)^+] + [Zn(OH)_2^0] + [Zn(OH)_3^-] + [Zn(OH)_4^{2-}] + [ZnCl^+]$
$+ [ZnCl_2^0] + [ZnCl_3^-] + [ZnCl_4^{2-}]$ $\quad$ Equation 5.19

$Zn_{total} = [Zn^{2+}] + [Zn^{2+}][OH^-] \cdot 10^{4.4} + [Zn^{2+}][OH^-]^2 \cdot 10^{11.3} + [Zn^{2+}][OH^-]^3 \cdot 10^{14.14}$
$+ [Zn^{2+}][OH^-]^4 \cdot 10^{17.66} + [Zn^{2+}][Cl^-] \cdot 10^{0.43} + [Zn^{2+}][Cl^-]^2 \cdot 10^{0.61} + [Zn^{2+}][Cl^-]^3 \cdot$
$10^{0.53} + [Zn^{2+}][Cl^-]^4 \cdot 10^{0.20}$ $\quad$ Equation 5.20

$Zn_{total} = [Zn^{2+}] (1 + 10^{pH-14+4.4} + 10^{2pH-28+11.3} + 10^{3pH-42+14.14} + 10^{4pH-56+17.66} +$
$[Cl^-] \cdot 10^{0.43} + [Cl^-]^2 \cdot 10^{0.61} + [Cl^-]^3 \cdot 10^{0.53} + [Cl^-]^4 \cdot 10^{0.20})$ $\quad$ Equation 5.21

$$\boxed{\begin{array}{l} Zn_{total} = [Zn^{2+}] (1 + 10^{pH-9.6} + 10^{2pH-16.7} + 10^{3pH-27.86} + 10^{4pH-38.34} + [Cl^-] \cdot 10^{0.43} \\ + [Cl^-]^2 \cdot 10^{0.61} + [Cl^-]^3 \cdot 10^{0.53} + [Cl^-]^4 \cdot 10^{0.20}) \end{array}} \quad \text{Equation 5.22}$$

Knowing the available total aqueous Zn ion content with respect to Zn^{2+}, the next step is to quantify the corrosion product equilibrium stability, derived here for $Zn(OH)_2$ (amorphous) as an example:

$Zn(OH)_2$ (Amorphous)

With Respect to Zn^{2+}

$\log K = -15.42 = \log[Zn^{2+}] + 2\log[OH^-]$ $\quad$ Equation 5.23
$[Zn^{2+}] = 10^{-15.42 + 28 - 2pH} = 10^{12.58 - 2pH}$ $\quad$ Equation 5.24

$\boxed{10^{12.58 - 2pH} = [Zn^{2+}]}$ $\quad$ Equation 5.25

With Respect to $Zn(OH)_3^-$

$Zn(OH)_2 = Zn^{2+} + 2OH^-$ $\quad$ $\log(K) = -15.42$ $\quad$ Equation 5.26
$Zn^{2+} + 3OH^- = Zn(OH)_3^-$ $\quad$ $\log(K) = 14.14$ $\quad$ Equation 5.27

$Zn(OH)_2 + OH^- = Zn(OH)_3^-$ $\quad$ $\log(K) = -1.28$ $\quad$ Equation 5.28

$-1.28 = \log\frac{[Zn(OH)_3^-]}{[OH^-]} = \log[Zn(OH)_3^-] + pOH$ Equation 5.29

$\boxed{10^{-15.28+pH} = [Zn(OH)_3^-]}$ Equation 5.30

With Respect to $Zn(OH)_4^{2-}$

$Zn(OH)_2 = Zn^{2+} + 2OH^-$ $\log(K) = -15.42$ Equation 5.31
$Zn^{2+} + 4OH^- = Zn(OH)_4^{2-}$ $\log(K) = 17.66$ Equation 5.32

$Zn(OH)_2 + 2OH^- = Zn(OH)_3^-$ $\log(K) = -2.24$ Equation 5.33
$-2.24 = \log\frac{[Zn(OH)_4^{2-}]}{[OH^-]^2} = \log[Zn(OH)_4^{2-}] + 2pOH$ Equation 5.34

$\boxed{10^{-30.24+2pH} = [Zn(OH)_3^-]}$ Equation 5.35

Overall, derivation of the equilibrium solubility of the other corrosion products utilizing this method yielded the following equations, summarized in Table 5.III:

Table 5.III: Equilibrium stability equations derived for each corrosion product

	Equilibrium Stability Equation		
Corrosion Product	**Zn^{2+}**	**$Zn(OH)_3^-$**	**$Zn(OH)_4^{2-}$**
Zinc Hydroxide (am)	$10^{12.58 - 2pH} = [Zn^{2+}]$	$10^{-15.28 + pH} = [Zn(OH)_3^-]$	$10^{-30.24 + 2pH} = [Zn(OH)_4^{2-}]$
Zinc Hydroxide (ε)	$10^{10.96 - 2pH} = [Zn^{2+}]$	$10^{-16.90 + pH} = [Zn(OH)_3^-]$	$10^{-29.62 + 2pH} = [Zn(OH)_4^{2-}]$
Zincite	$10^{11.35 - 2pH} = [Zn^{2+}]$	$10^{-16.51 + pH} = [Zn(OH)_3^-]$	$10^{-26.99 + pH} = [Zn(OH)_4^{2-}]$
Smithsonite	$10^{-10.92 - \log(CO_3 2-)} = [Zn^{2+}]$	$10^{-38.78 + 3pH - \log(CO_3 2-)} = [Zn(OH)_3^-]$	$10^{-49.26 + 4pH - \log(CO_3 2-)} = [Zn(OH)_4^{2-}]$
Hydroxycarbonate	$10^{1.28 - 1.2pH - 0.4\log(CO_3 2-)} = [Zn^{2+}]$	$10^{-26.58 + 1.8pH - 0.4\log(CO_3 2-)} = [Zn(OH)_3^-]$	$10^{-37.06 + 2.8pH - 0.4\log(CO_3 2-)} = [Zn(OH)_4^{2-}]$
Simonkolleite	$10^{7.64 - 1.6pH - 0.4\log(Cl-)} = [Zn^{2+}]$	$10^{-20.22 + 1.4pH - 0.4\log[Cl-]} = [Zn(OH)_3^-]$	$10^{-30.70 + 2.4pH - 0.4\log[Cl-]} = [Zn(OH)_4^{2-}]$

The summation of the three equations determined the equilibrium stability trend across the entirety of the pH range when no ion complexation effects due to Cl^- were considered. When complexation was considered, the available Zn^{2+} content was understood through use of Equation 5.24, which enabled the sole use of the Zn^{2+} relationship to calculate the chemical stability diagram.

Assumptions:

- Concentrations were expressed in molarity here. The importance of species activity is recognized, as activity more accurately describes the reactivity of a species and the thermodynamic stability of its reaction products. The framework used here necessitates the use of molarity, particularly for determining the dissolution trajectory expressions. When concentration is low, the activity is sufficiently well approximated by molarity.

- The authors recognize that many different compounds and aqueous species exist. Some common examples of Zinc-based products were considered here, ranging from simple (ZnO) to complex ($Zn_5(OH)_8Cl_2 \cdot H_2O$) chemical formulae. Certainly other species could be considered and other systems modelled (SO_4-containing, for instance). This work establishes the framework which enables such analysis to be conducted by the reader.
- Only thermodynamically stable phases were considered in the present work. The possibility of forming metastable (or kinetically stable) phases is recognized.
- Ligands were assumed to be in excess of the Zn ion. This allows [Cl^-], for example, to be approximated by the total Cl concentration. This approximation is insufficient when [Zn_{tot}] approaches [Cl_{tot}] (for example, this assumption is valid up to 10^{-2} M [Zn_{tot}] at 2.5 M [Cl^-], see the figure that follows). Generally, solid phases form before this condition is met. However, the graphical abstract was calculated exactly for the aqueous phases only (where solid phases were artificially suppressed/ignored) taking into account the consumption of Cl^- by Zn-Cl complexation. The procedure for this calculation is outlined below:

Equilibrium Calculations When the Ligand is Not in Excess

1. The equilibrium constants were calculated for successive, stepwise chlorination of Zn-Cl complexes, as for $Zn^{2+}/ZnCl^+$, $ZnCl^+/ZnCl_2^0$, $ZnCl_2^0/ZnCl_3^-$, $ZnCl_3^-/ZnCl_4^{2-}$. While these constants were not directly reported here, they are easily calculated by summing the appropriate reactions given in Table 5.II. For each equilibrium, a condition is imposed where each Zn-based species is present in equal concentrations. This allows for the determination of [Cl^-] where this condition is valid.
2. A chloride mass balance is constructed where Cl_{tot} is solved for in terms of Cl^- and all of the Zn-Cl complexes. The concentration of the Zn-Cl complexes is dependent on [Cl^-] (which was just determined for each reaction) and [Zn^{2+}]. [Zn^{2+}] is solved for such that the Cl_{tot} expression is equal to the total chloride concentration in the system (2.5 M in the example of the graphical abstract).
3. A zinc mass balance is constructed for Zn_{tot} as shown in Equation 5.22 above. The Zn_{tot} is solved for such that [Zn^{2+}] is equal to the value determined by the chloride mass balance. Zn_{tot} will depend on [Cl^-] (which is fixed by the equilibrium calculation in step 1) and pH (which is incrementally varied from pH 0 to the pH at which $Zn(OH)_2^0$ dominance occurs).
4. The equilibrium constant for the reaction between $Zn(OH)_2^0$ and each of the Zn-Cl complexes is determined. When the Zn-Cl and $Zn(OH)_2^0$ are set equal then the equilibrium boundary can be calculated with respect to [Cl^-] and pH ([OH^-]). The [Cl^-] can be taken from the equilibrium condition between each successive Zn-Cl species, such that the pH can be calculated where $Zn(OH)_2^0$ become the most dominant species with respect to each Zn-Cl complex.
5. The equilibrium between the Zn-OH complexes can be determined directly from Table 5.II.

The excess ligand assumption:

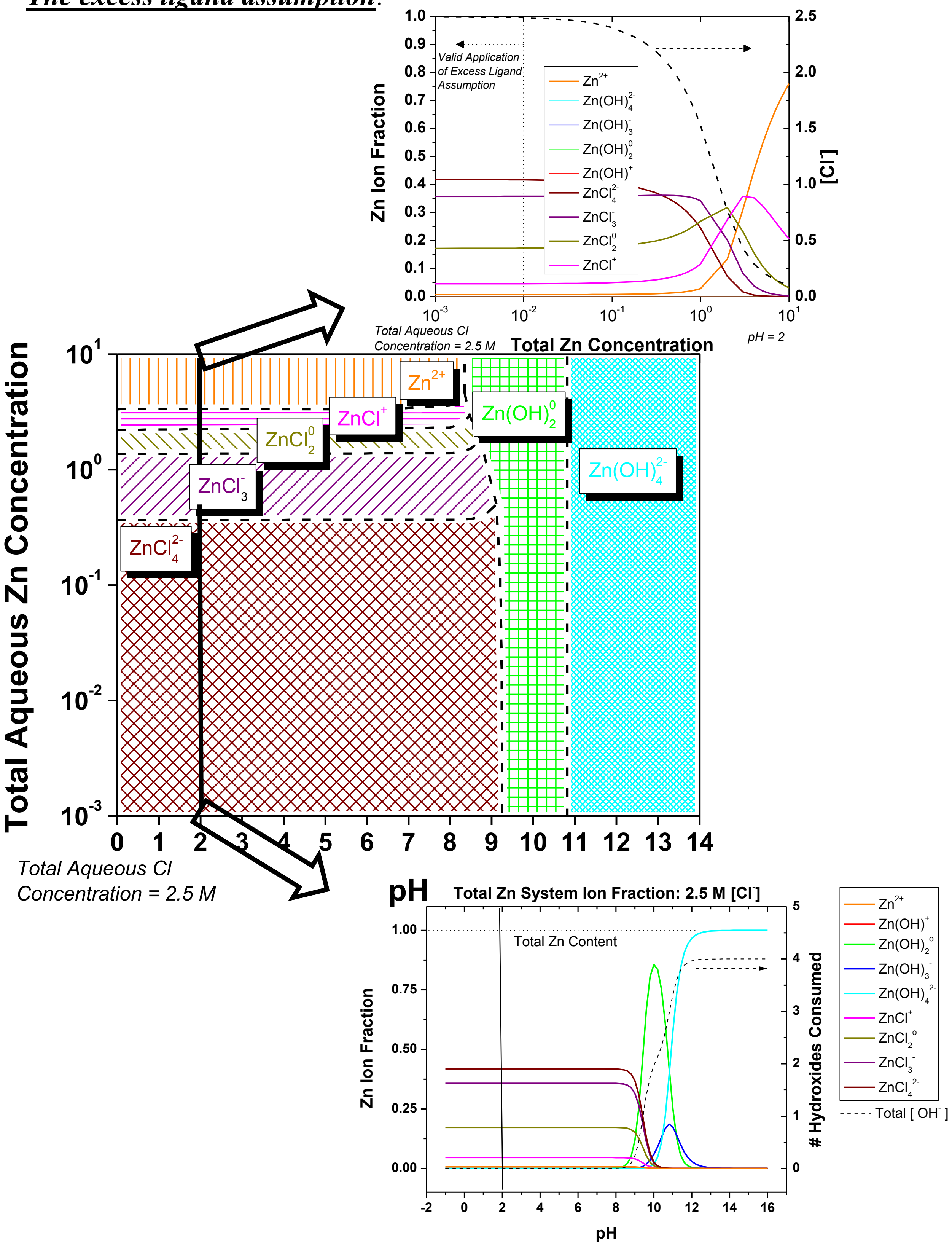

5.1.8 References

1 F. M. Toma, J. K. Cooper, V. Kunzelmann, M. T. McDowell, J. Yu, D. M. Larson, N. J. Borys, C. Abelyan, J. W. Beeman, K. M. Yu, J. Yang, L. Chen, M. R. Shaner, J. Spurgeon, F. A. Houle, K. A. Persson and I. D. Sharp, *Nat. Commun.*, 2016, **7**, 1–11.

2 M. Schuisky and A. Harsta, *J. Electrochem. Soc.*, 1998, **145**, 4234–4239.

3 D. G. Kinniburgh and D. M. Cooper, *Environ. Sci. Technol.*, 2004, **38**, 3641–3648.

4 J. D. Hem, *Int. Assoc. Sci. Hydrol. Bull.*, 1960, **5**, 45–53.

5 H. L. Bohn, R. A. Myer and G. A. O'Connor, in *Soil Chemistry*, John Wiley & Sons, Inc., New York, 3rd edn., 2001, pp. 201–206.

6 M. Pourbaix, *Atlas of Electrochemical Equilibria in Aqueous Solutions*, National Association of Corrosion Engineers, 1974.

7 L. F. Huang, M. J. Hutchison, R. J. Santucci, J. R. Scully and J. M. Rondinelli, *J. Phys. Chem. C*, 2017, **121**, 9782–9789.

8 R. J. Santucci, M. E. McMahon and J. R. Scully, *npj Mater. Degrad.*, 2018, **2**, 1.

9 P. Plagemann, J. Weise and A. Zockoll, *Prog. Org. Coatings*, 2013, **76**, 616–625.

10 J. Lin, D. Battocchi and G. P. Bierwagen, *Corrosion*, 2017, **73**, 408–416.

11 W. Xu, N. Birbilis, G. Sha, Y. Wang, J. E. Daniels, Y. Xiao and M. Ferry, *Nat. Mater.*, 2015, **14**, 1229–1235.

12 X. G. Zhang, *Corrosion and Electrochemistry of Zinc*, Plenum Press, New York, 1st edn., 1996.

13 V. Ligier, M. Wéry, J.-Y. Hihn, J. Faucheu and M. Tachez, *Corros. Sci.*, 1999, **41**, 1139–1164.

14 2013, 1, 1–12.

15 K. S. Suganthi, *Flex. Print. Electron.*, 2018, **3**, 1–11.

16 H. Agarwal, S. Venkat Kumar and S. Rajeshkumar, *Resour. Technol.*, 2017, **3**, 406–413.

17 W. Salem, D. R. Leitner, F. G. Zingl, G. Schratter, R. Prassl, W. Goessler, J. Reidl and S. Schild, *Int. J. Med. Microbiol.*, 2015, **305**, 85–95.

18 P. K. Mishra, H. Mishra, A. Ekielski, S. Talegaonkar and B. Vaidya, *Drug Discov. Today*, 2017, **22**, 1825–1834.

19 A. Król, P. Pomastowski, K. Rafińska, V. Railean-Plugaru and B. Buszewski, *Adv. Colloid Interface Sci.*, 2017, **249**, 37–52.

20 F. Verbakel, S. C. J. Meskers and R. A. J. Janssen, *J. Appl. Phys.*, , DOI:10.1063/1.2794475.

21 S. Hagemann, *Entwicklung eines thermodynamischen Modells für Zink, Blei und Cadmium in salinaren Lösungen*, Gesellschaft für Anlagen- und Reaktorsicherheit (GRS) mbH, Berlin, 1st edn., 2012.

22 G. S. James, *Lange's Handbook of Chemistry*, New York, 17th edn., 2017.

23 K. J. Kim, P. B. Kreider, C. Choi, C. H. Chang and H. G. Ahn, *RSC Adv.*, 2013, **3**, 12702–12710.

24 C. H. Choi, J. B. Levin and C. H. Chang, *CrystEngComm*, 2016, **18**, 8645–8652.

25 S. E. A. Sharaf El-Deen, S. I. Moussa, Z. A. Mekawy, M. K. K. Shehata, S. A. Sadeek and H. H. Someda, *Radiochim. Acta*, 2017, **105**, 43–55.

26 C. Tang, M. J. S. Spencer and A. S. Barnard, *Phys. Chem. Chem. Phys.*, 2014, **16**, 22139–22144.

27 S. Thomas, N. Birbilis, M. S. Venkatraman and I. S. Cole, *Corrosion*, 2012, **68**, 015009-1-

015009-9.
28 Z. C. Feng, *Handbook of Zinc Oxide and Related Materials: Volume 1, Materials*, CRC Press, New York, 2013.
29 P. Volovitch, C. Allely and K. Ogle, *Corros. Sci.*, 2009, **51**, 1251–1262.
30 M. Bockelmann, L. Reining, U. Kunz and T. Turek, *Electrochim. Acta*, 2017, **237**, 276–298.
31 S. Thomas, N. Birbilis, M. S. Venkatraman and I. S. Cole, *Corros. Sci.*, 2013, **69**, 11–22.
32 C. B. Tay, S. J. Chua and K. P. Loh, *J. Cryst. Growth*, 2009, **311**, 1278–1284.
33 H. Agarwal, S. Venkat Kumar and S. Rajeshkumar, *Resour. Technol.*, 2017, **3**, 406–413.
34 R. Brayner, S. A. Dahoumane, C. Yéprémian, C. Djediat, M. Meyer, A. Couté and F. Fiévet, *Langmuir*, 2010, **26**, 6522–6528.
35 T. Ohtsuka and M. Matsuda, *Corrosion*, 2003, **59**, 407–413.
36 O. Ø. Knudsen, U. Steinsmo and M. Bjordal, *Prog. Org. Coatings*, 2005, **54**, 224–229.
37 H. Marchebois, S. Joiret, C. Savall, J. Bernard and S. Touzain, *Surf. Coatings Technol.*, 2002, **157**, 151–161.
38 H. Marchebois, C. Savall, J. Bernard and S. Touzain, *Electrochim. Acta*, 2004, **49**, 2945–2954.
39 J. Feliu S., M. Morcillo and S. Feliu, *Corrosion*, 2001, **57**, 591–597.
40 S. J. Feliu, R. Barajas, J. M. Bastidas, M. Morcillo and S. Feliu, *Electrochem. Impedance Anal. ans Interpret. ASTM STP 1188*, 1993, 438–449.
41 E. Diler, B. Rouvellou, S. Rioual, B. Lescop, G. Nguyen Vien and D. Thierry, *Corros. Sci.*, 2014, **87**, 111–117.
42 E. A. Meulenkamp, *J. Phys. Chem. B*, 1998, **102**, 5566–5572.
43 T. E. Graedel, *J. Electrochem. Soc.*, 1989, **136**, 193–203.
44 I. Suzuki, *Corros. Sci.*, 1985, **25**, 1029–1034.
45 B. E. Roetheli, G. L. Cox and W. B. Littreal, *Met. Alloy.*, 1932, **3**, 73–76.
46 M. Mouanga, P. Berçot and J. Y. Rauch, *Corros. Sci.*, 2010, **52**, 3984–3992.
47 S. E. Manahan, *Environmental Chemistry*, CRC Press, New York, 8th edn., 2005.
48 Q. Qu, C. Yan, Y. Wan and C. Cao, *Corros. Sci.*, 2002, **44**, 2789–2803.
49 J. E. Svensson and L. G. Johansson, *Corros. Sci.*, 1993, **34**, 721–740.
50 D. de la Fuente, J. G. Castano and M. Morcillo, *Corros. Sci.*, 2006, **49**, 1420–1436.
51 M. Ali, M. Moazzen, • Seyed, M. Borghei and F. Taleshi, , DOI:10.1007/s13204-012-0147-z.
52 C. Dai, J. Zhao, D. E. Giammar, J. D. Pasteris, X. Zuo and Y. Hu, *ACS Earth Sp. Chem.*, , DOI:10.1021/acsearthspacechem.8b00040.
53 A. E. Martell and R. M. Smith, *Critical Stability Constants*, Plenum Press, New York, 6th edn., 1989.
54 R. Fernandez-Prini, A. H. Harvey and D. A. Palmer, *Aqueous Systems at Elevated Temperatures and Pressures*, Elsevier, New York, 2004.

CONCLUSIONS

The conclusions drawn from this work are the following:

1. Cathodic polarization is similarly effective for IG-SCC mitigation in the 5.0 wt.% Mg-containing AA5456-H116 as in the 4.5 wt.% AA5083-H131, even with sensitization as high as NAMLT 65 mg/cm^2. This protection extends to saline environments having high [Cl$^-$], as well as acidic bulk pH, albeit with reduced potency. Critically, the efficacy of the cathodic polarization for IG-SCC mitigation trends with $E_{pit\ (\alpha)}$ and $E_{pit\ (\beta)}$, which may change with the bulk saline environment.
2. The effective window of applied cathodic polarization in which highly sensitized AA5456-H116 remains passive extends from $E_{pit\ (\beta)}$ to ≈ -1.1 V_{SCE}, which is the approximate threshold where localized cathodic corrosion begins around Al(Mn,Fe,Cr) intermetallic particles. The β phase remains relatively passive at potentials more negative than $E_{pit\ (\beta)}$, not exhibiting amphoteric qualities. Thus, hydrogen evolution occurs primarily through HER on AA5456-H116 at polarization at or more negative than the reversible hydrogen potential at ≈ -1.3 V_{SCE}. However, the SCC susceptibility in this polarization range is low due to the low amount of absorbed hydrogen content per unit area. Chemically-induced crack tip blunting plays a secondary role to resist SCC by decreasing the driving force (stress concentration) for crack advance.
3. Sacrificial pigment choice was evaluated for IG-SCC mitigation purposes on AA5456-H116, where the candidate pigments were Zn, Mg, and Al-Zn. The pure Zn-rich primers provided effective cathodic polarization that was well-maintained in part due to the low self-corrosion rate of Zn. In comparison, the Mg pigment did not maintain cathodic polarization for sufficient durations, and the Al-Zn pigment rarely achieved sufficient

cathodic polarization. A hybrid Mg/Al-Zn primer was evaluated that maintained more stable cathodic polarization than pure Mg-based primer, but this primer achieved low anodic charge output and thus was more polarizable than the majority of the candidate Zn-rich primers.

4. Metal-rich primer polarizability was found to be an important metal-rich primer attribute for IG-SCC mitigation because fracture scenarios create increasingly aggressive galvanic coupling conditions. In the case of AA5456-H116, the ability of the primer to maintain coupled potentials below $E_{pit\,(\beta)}$ dictates the primer's IG-SCC mitigation performance, and increasingly low polarizability enables the maintenance of such potentials. Thus, low polarizability translates to effective mitigation in an increasingly diverse range of environmental fracture scenarios. The correlation between polarizability and ZRP IG-SCC mitigation performance is supported by the comparison between the highly effective IOZRP(EthylSil,76%) and the ineffective OZRP(EPA,65%).
5. Polarizability may be quickly quantified via the newly developed galvanostatic pulse method. Zn-rich primers having different resin types and Zn loading are differentiated through this method and accelerated cycle testing to demonstrate that the least polarizable ZRPs consistently maintain high anodic charge output, low pore resistance, and have a low capacitive discharge delay. These primer attributes may be atypical of conventional formulations meant for long-term corrosion prevention, where high impedance and low resin porosity is often desired.
6. At a constant $K = 10\ \mathrm{MPa}\sqrt{\mathrm{m}}$, 1000x reduction in IG-SCC growth rate is demonstrated to occur through use of a potentiostat, pure Zn ZRA, as well as IOZRP ZRA to achieve intermediate cathodic polarization in 0.6 M NaCl. The mitigation was consistently

achieved across a range of intermediate cathodic potentials and galvanically coupled Zn/IOZRP surface areas, thus the critical factor to achieve this crack growth rate reduction was the achievement of the potential, not the source.

7. The least polarizable ZRP of the evaluated candidates, the IOZRP(EthylSil,76%), achieves a high level of IG-SCC mitigation in dilute (0.60 M) as well as saturated (5.45 M) NaCl, with defect width up to 15 mm about the Mode I crack path (likely extending to even larger widths), across a range of crack geometries. The achieved mitigation was similarly effective as that achieved via potentiostat, according to the potential that was achieved. The addition on an epoxy topcoat to the IOZRP significantly increases the polarizability and makes this primer relatively ineffective for IG-SCC mitigation.
8. Secondary chemical protection due to Zn^{2+} may play a role alongside galvanic protection to enable the IG-SCC mitigation observed through spray-depositing ZRPs on AA5456-H116. For a constant [Cl^-] of 0.6 M at -0.9 V_{SCE}, IG-SCC growth rates are considerably reduced in Zn^{2+}-containing bulk solution compared to NaCl. Titration in simulated crack tip solution demonstrates that part of the Zn^{2+} effect may be to reduce crack tip acidification, however further work is needed.
9. Advanced chemical stability modeling methods are developed to predict Zn corrosion product formation at equilibrium in a variety of [Cl^-] conditions. These modeling predictions agree with the results of both atmospheric- and laboratory-based Zn and ZRP exposure, and demonstrate a significant influence of bulk [Cl^-] on overall product stability as well as the required conditions for precipitation.

FUTURE WORK

To briefly summarize, this dissertation has (1) evaluated the window of applied potential in which IG-SCC is effectively mitigated on highly sensitized AA5456-H116, (2) elucidated key Zn-rich primer attributes necessary to most effectively achieve potentials within this window despite aggressive galvanic coupling conditions, as well as developed means through which to evaluate these attributes, in a variety of aggressive conditions, and (3) demonstrated optimal primer performance in IG-SCC mitigation with consideration of both galvanic and secondary chemical effects driving this performance. Based on these findings, the following knowledge gaps remain:

(1) The hypothesized mechanism driving crack tip acidification in Al-Mg alloys, which is predicated on the measured pH decrease that occurs when $MgCl_2$ is titrated into $AlCl_3$ [1,2], should be evaluated in further detail to understand the influence of other species such as potassium, carbonates, and sulfates that may be present in the marine service environment.

(2) Secondary chemical protection effects due to Zn cation content, as well as Zn-based corrosion product formation, must be more thoroughly evaluated to understand potential influences on IG-SCC susceptibility in AA5456 and the more susceptible AA5083, which will inform ZRP selection for marine service conditions

   a. Specifically, the possible influence of bulk Zn cation concentration on the pH, the rate of hydrolysis, and the overall H absorption at the crack tip must be determined

(3) The rate of crack growth mitigation following applied cathodic polarization, as demonstrated in the current work, often occurs within seconds – the cause for the variability in this time transient is important to determine to further the understanding of the IG-SCC mechanism and its rate limiting steps. Secondary chemical protection effects due to the

presence of cations such as Zn on this mitigation time transient in Al-Mg are unknown and should be determined.

(4) When utilizing the spray-deposited IOZRP for IG-SCC mitigation, the addition of the epoxy topcoat drastically increased the primer polarizability. The consideration/ development of porous and conductive topcoat systems which continue to provide UV radiation protection may be beneficial for ZRP-based galvanic protection systems. This combination of coatings may continue to achieve a low capacitive discharge delay as well as high overall conductivity in marine service, unlike classic topcoat/primer combinations.

(5) To more accurately simulate marine service conditions, the efficacy of ZRP-based IG-SCC mitigation must be evaluated on AA5456 as well as AA5083 in atmospheric exposures such as salt fog, misting, and/or thin film to evaluate the effects of electrolyte film thickness, salinity, and electrolyte film continuity. In particular, these conditions may affect the ZRP throwing power, or the ability to polarize the crack tip across large coating defects/ crack dimensions.

(6) The present evaluations were based in simplified NaCl and $MgCl_2$ full immersion conditions to aid the interpretation of the results. The next step in complexity is to assess ZRP-based IG-SCC mitigation in ASTM simulated ocean water, which contains a variety of salt species. Some of these salts buffer the bulk solution pH, which may affect the acidification of the crack tip.

References Cited

[1] M.L.C. Lim, Intergranular Corrosion Propagation in Sensitized Al-Mg Alloys, The University of Virginia, 2016.

[2] C.B. Crane, R.. Kelly, R.P. Gangloff, Crack chemistry control of intergranular stress corrosion cracking in sensitized Al-Mg, Corrosion. 72 (2016) 242–263. doi:10.5006/1852.

APPENDIX I

Comparison of Zn / Al-Zn / Mg-Rich Primer Polarizability

8.1 The Effect of Environment on Metal-Rich Primer Polarizability for The Mitigation of Stress Corrosion Cracking on Highly Sensitized Al-Mg

M. E. McMahon ǂ, *, J. T. Burns*, and J. R. Scully*

* Center for Electrochemical Science and Engineering, Department of Materials Science and Engineering, University of Virginia, Charlottesville, VA 22904

ǂ Corresponding author. E-mail: mm5kn@virginia.edu

Keywords: aluminum alloy, sacrificial protection, cathodic protection, metal-rich primer, polarizability

8.1.1 Abstract

Seven commercial metal-rich primers were evaluated for their polarizability, or ability to maintain protective potential in increasingly aggressive galvanic coupling conditions, as a function of NaCl concentration on highly sensitized AA5456-H116. Galvanostatic pulse and simulated crack growth experiments evaluated the potential efficacy of these sacrificial anodic protection systems for the mitigation of intergranular stress corrosion cracking. These evaluations demonstrated that Zn-rich primers exhibit the least polarizability compared to Al- and Mg-based primers, and that the primers which achieve the lowest anodic charge output in response to changes in galvanic coupling conditions (such as that which would occur during crack growth) are most affected by increasing environmental severity. Specifically, the magnitude of applied current up to which these primers continue to maintain protective coupled potentials decreases as salinity increases, which does not always occur in the primers with the highest magnitude of anodic charge output (Zn-rich primer). Galvanic coupling with pure Zn is likewise demonstrated to be more effective in IG-SCC mitigation compared to coupling with Mg due to the low self-corrosion rate of Zn, compared to the high rate of self-corrosion observed in Mg in 5.45 M NaCl.

8.1.2 Introduction

The Mg supersaturation that affords Al-Mg alloys a high general corrosion resistance, strength-to-weight ratio, and weldability for marine conditions also cripples these alloys over extended service. During the sensitization process, the Mg leaves solid solution to form the anodic intergranular β phase (Al_3Mg_2) in tropical ocean temperatures, rendering these alloys susceptible to both intergranular corrosion (IGC) and intergranular stress corrosion cracking (IG-SCC) under sufficient applied load. Together IGC and IG-SCC have considerably reduced the expected service life of Al-Mg superstructural and hull components on the Littoral Combat Ship and the CG-47 Class Cruiser. The β phase is highly anodic to the matrix thus in aggressive (e.g. aqueous chloride) environments, rapid dissolution occurs and causes severe IGC under static conditions [1] and IG-SCC in the presence of a stress [2,3]. The extent of sensitization is typically quantified by the ASTM G-67 Nitric Acid Mass Loss test (NAMLT) [4], making this metric a rough proxy for IGC / IG-SCC susceptibility. Materials are rated as resistant at NAMLT < 15 mg/cm^2, intermediate at 15 – 25 mg/cm^2, and susceptible at > 25 mg/cm^2 [1,4–7], with long-term sensitization at low temperature often achieving NAMLT values as high as 65-70 mg/cm^2 [8,9].

Susceptibility to IGC and IG-SCC is high in sensitized Al-Mg alloys which are exposed to potentials above the β phase pitting potential ($E_{pit\,(\beta)}$, -0.92 V_{SCE} in 0.6 M NaCl and -1.02 V_{SCE} in 5.45 M NaCl [28,29]) in chloride-containing environments [1,10]. Intergranular corrosion and IG-SCC increase in severity with increasing potential more positive than $E_{pit\,(\beta)}$ [10–12]. The IG-SCC behavior is hypothesized to be governed by a coupled anodic dissolution process (of the β phase and the α matrix), which catalyzes the formation of an aggressive acidified local crack tip chemistry that facilitates the enhanced generation of crack tip H and enables embrittlement in the fracture process zone [13–18]. Thus, Al-Mg alloy degradation through IGC / IG-SCC is suppressed at intermediate cathodic potentials more negative than $E_{pit\,(\beta)}$. The existence of this threshold potential raises the possibility that a metal-rich primer tuned to the proper potential and polarization condition can protect Al-Mg alloys.

A metal-rich coating must accomplish stable galvanic coupling with low self-corrosion and low passivation rates to achieve lasting substrate protection against IGC / IG-SCC in service. Specifically-designed metal-rich coatings applied to 5xxx-series alloy surfaces could provide the optimal galvanic protection through achievement of intermediate cathodic potentials below $E_{pit\,(\beta)}$, which could reduce maintenance costs and improve alloy service life if effective in mitigating IGC and IG-SCC. Pure Zn-based primer systems, which are not typically considered for Al protection due to the close proximity of their open circuit voltages (low ΔOCP) to those of numerous commercial Al alloys [19,20], could meet these requirements due to the protective nature of their OCP, their low polarizability (the ability to maintain protective coupled potentials following the application of increasingly high anodic currents, such as when crack growth occurs to expose fresh Al surface area), as well as their lower self-corrosion rate than that of other candidate pigments such as Mg (OCP of -1.60 V_{SCE} in 0.6 M NaCl). A variety of other metal-rich primers have also been formulated for Al alloy protection however, such as Al- and Mg-based primers, and hybrid alloy pigment systems (such as Al-Zn-In and Zn-Mg) [19–27]. Neither pure Mg-rich primers, Al-rich primers, nor hybrid Al-Mg based primers have been evaluated in the literature for the cathodic protection of highly sensitized AA5456-H116 in simulated marine service conditions.

Previous work evaluated four commercial Zn-rich primers (ZRPs) on highly sensitized AA5456-H116 [28], one having an inorganic matrix and the others having organic matrices. These evaluations demonstrated that the inorganic Zn-rich primer was the least polarizable and thus would have the highest efficacy for IG-SCC mitigation. Subsequently, this ZRP was indeed proven to effectively mitigate IG-SCC in slow rising displacement tests, and this protection remained even with scribe distances of up to 15 mm due to the low polarizability of this system [29]. However, this ZRP can have brittle characteristics and may be difficult to apply to Al substrates (high moisture sensitivity and lack of chemical bonding to Al) [28,30,31]. In service, more robust primer characteristics such as increased flexibility and adhesion may be necessary, which may be attained through use of organic matrix-based metal-rich primers. However, these coating systems may be more polarizable due to the resistive nature of the matrix [28]. Conditions may exist in service where higher coating polarizability is allowable to achieve the necessary sacrificial galvanic protection, though the effect of environment must first be determined to inform the selection of metal-rich primer systems having these attributes.

This research aims to determine the efficacy of Zn-, Al- and Mg-rich primers on highly sensitized (NAMLT 65 mg/cm^2) AA5456-H116 for consideration in aggressive saline service conditions. Systematic evaluation of coating polarizability in three commercial Al/Mg-rich primers and four commercial ZRPs on AA5456-H116 will inform selection and future design of such systems for the purpose of IG-SCC mitigation, and these evaluations will be conducted via galvanostatic pulse and simulated crack growth testing in 0.60 M and 5.45 M NaCl. Galvanic coupling with pure Zn and Mg anodes will then evaluated for IG-SCC mitigation during slow rising displacement testing in 5.45 M NaCl. These analyses will set a baseline towards determining key coating qualities of Al/Mg/Zn – based primers to achieve effective, long-lasting cathodic protection for IG-SCC mitigation on Al-Mg naval alloys in a variety of aggressive marine service environments.

8.1.3 **Test Setup**

8.1.3.1 ***Materials: 5456-H116 and Metal-Rich Primers***

A 57-mm thick plate of non-recrystallized 5456-H116 (UNS A95456) plate was exposed in the S-T orientation; the microstructural character and composition are reported elsewhere [16]. Rectangular plates of 1 mm thickness, 72 mm length, and 63 mm width were excised and sensitized to NAMLT 65 mg/cm^2 via heating at 100°C for 14 days [16]. Following alloy sensitization, the samples were sonicated in isopropyl alcohol and dried using static-free absorptive cloth prior to spray-coating the Al surfaces using a spraying distance of 200 to 300 mm and 50% overlap. Luna Innovations, Inc. performed all cold spraying of the selected commercial metal-rich primers (MRPs) using thoroughly agitated, mixed formulations, with cured primer thicknesses in agreement with manufacturer specifications. As shown in Table 8.1, three of the ZRPs considered here are commercial products of Sherwin Williams, and the fourth is produced by NCP Coatings in Niles, Michigan. All Zn pigment was roughly spherical in the ZRPs considered here. The resins/Zn pigment volume concentrations (PVC) combinations tested are the following, where the designation for identifying each coating is: inorganic ethyl silicate resin (EthylSil) at Zn PVC of 76% (IOZRP (EthylSil,76%)); organic epoxy polyamide resin (EPA) at Zn PVC of 65% (OZRP (EPA,65%)); organic epoxy resin at Zn PVC of 57% (OZRP (Epoxy,57%)); and organic polyurethane (U) resin at Zn PVC of 83% (OZRP (U,83%)) (Table 1). The Al/MgRPs considered here are also shown in Table 8.1. Two of these coatings are products of Randolph Coatings (Chicopee, Massachusetts), where the resin/pigment combination and designation for identifying each coating is: epoxy resin, 27% PVC Al-5wt.% Zn pigment (AlRP(Epoxy,27%)), and epoxy resin, 28% PVC Al-5wt.% Zn pigment + 19% PVC Mg pigment (Al-MgRP(Epoxy,28/19%). (Table 8.1). The Al-based and Mg particles embedded in the primers produced by Randolph Coatings are all roughly spherical. The third epoxy coating is a product of AkzoNobel (Waukegan, Illinois), and the resin/pigment combination and designation for identifying this coating is: epoxy resin, 26% PVC Mg flake pigment (MgRP(Epoxy,26%)) (Table 1). No pretreatments or topcoats were considered, and all coatings were tested as-received and intact, ie. with no added defects (such as scribes).

Table 8.1: Metal-rich primer characteristics studied in this system

Code	**Metal-Rich Primer Commercial Name**	**Provider**	**Vehicle**	**PWC (%)**	**PVC (%)**
IOZRP (EthylSil, 76%)	Zinc Clad® II Plus	SW	Ethyl Silicate	83	76
OZRP (EPA, 65%)	MIL-DTL-24441/19C Type III F159	SW	Epoxy Polyamide	85	65
OZRP (U,83%)	N-5751M2 Organic Zinc Rich, Single Component, Moisture Cure Primer	NCP	Polyurethane	90	83
OZRP (Epoxy, 57%)	CC-M30 Two Component Zinc Rich Epoxy Primer	SW	Epoxy	90	57
AlRP (Epoxy,27%)	LN4841	RC	Epoxy	44	27
Al-MgRP (Epoxy,28/19%)	LN4847	RC	Epoxy	33 (Al-Zn) 14 (Mg)	28 (Al-Zn) 19 (Mg)
MgRP (Epoxy,26%)	Aerodur 2100	AN	Epoxy	40	26

SW = Sherwin Williams, NCP = NCP Coatings, RC = Randolph Coatings, AN = AkzoNobel, PWC = pigment weight concentration in the dry film, PVC = pigment volume concentration in the wet mix

8.1.3.2 *Galvanostatic Pulse Testing*

Pristine MRP panels were subjected to a cyclic series of 20 OCP / galvanostatic pulse steps in 0.60 M NaCl and 5.45 M NaCl with increasing magnitude of applied anodic current to evaluate primer polarizability while simulating abrupt, fresh metal exposure during IGC/IG-SCC. This testing consisted first of a 3-hour OCP step to ensure primer activation. In the case of the Al/MgRPs, extended activation time up to 24 hours was utilized in replicate testing, which achieved similar results as the 3-hour OCP tests. Galvanostatic pulses were then held for 10 minutes at each level of applied anodic current with 20 minutes at OCP prior to the next pulse, wherein any depletion or pigment deactivation would be evident in the form of increased polarizability. Applied current ranging from 1 nA to 100 μA was applied to simulate various bare surface areas demanding more anodic charge output from the MRP. These tests were conducted in triplicate, with each test being on a non-defected, previously unexposed 0.78 cm^2 MRP area. The reported results are averages from the triplicate testing, wherein the coupled potential data obtained during each 10-minute applied galvanostatic pulse period were averaged in each test to achieve one average potential per value of applied current, and the mean of these values between the three tests is reported to provide a conservative prediction of coating galvanic protection performance.

8.1.3.3 *Simulated Crack Growth Testing*

The anodic response and successively achieved potentials of these commercial primers were assessed diagnostically via a test that challenges the ability of the finite anode to protect new bare Al (thus simulating a crack tip) in electrochemical flat cells in saturated (5.45 M) NaCl. Using ZRA, a non-defected MRP plate (4.90 cm^2) served as the counter electrode while a 4.90 cm^2 area of NAMLT 65 mg/cm^2 AA5456 served as the working electrode. To simulate the addition of a new, unpassivated defect, a freshly polished (1200 grit) rectangular prism of NAMLT 65 mg/cm^2 AA5456 having exposed surface area of 5.36 cm^2 was electrically connected via PFA-insulated Cu wire to the primary AA5456 working electrode (4.90 cm^2) and was periodically immersed and removed from the NaCl solution in fixed time intervals. These simulated periods of crack advance challenged the MRP to maintain a protective coupled potential, the ability of which varied between the primers based on the polarizability and magnitude of anodic charge output.

8.1.3.4 *LEFM Testing to Demonstrate the Efficacy of Zn- and Mg-based Galvanic Coupling in IG-SCC Mitigation*

AA5456-H116 (NAMLT 65 mg/cm^2) single edge notch tensile (SENT) specimens having thickness of 6.60 mm and width of 17.30 mm were utilized in slow rising displacement testing in 5.45 M NaCl full immersion environment. Electrical discharge machined notches of 4.80 mm depth centered in the gauge section were used. All samples were fatigue pre-cracked using a decreasing stress intensity range (ΔK) protocol ($R = 0.1$, frequency = 8 Hz) in laboratory air to a notch plus crack depth of 5.30 mm, with the final maximum stress intensity being 3.5 MPa√m. Crack extension was monitored with ~ 0.5 μm resolution via the direct current potential difference (dcPD) method, the details of which are provided elsewhere [16,32]. Resolved crack growth related solely to plasticity effects at the crack tip were subtracted from all da/dt versus K data shown in the present work such that only real crack growth results are shown. Crack growth data analysis utilized Ramberg Osgood constants derived from compression testing stress strain curves to calculate the total elastic-plastic stress intensity (K_J) via J-integral plastic corrections; the underlying fundamentals and application of this method are detailed elsewhere [33].

At room temperature, the environment (0.60 or 5.45 M NaCl) was maintained in a 200-mL acrylic cell fastened about the sample, with ambiently aerated electrolyte flowing at 20 mL/min from a 2.0 L reservoir. The slow rising displacement tests were conducted at an initial rate of 0.25 Mpa√m/hr from a K of 2.0 Mpa√m. The measurement of cathodic protection in the slow rising displacement tests utilized the Zero Resistance Ammeter (ZRA) setup to galvanically couple the Zn or Mg anode to the AA5456-H116 SENT. The ZRA method utilizes a potentiostat to monitor both coupled current and potential, where the AA5456-H116 SENT is the working electrode, a 99.95% pure Zn or 99.9% pure Mg anode is the counter electrode, and an SCE is the reference electrode.

8.1.4 **RESULTS**

8.1.4.1 ***Galvanostatic Pulse Testing***

The results of the galvanostatic pulse testing conducted in 0.60 M NaCl on the seven MRPs are shown in Figure 8.1. To interpret these results, the threshold current (TC) metric will be utilized, which represents the applied current past which the coupled potential established by the

MRP is above $E_{pit\ (\beta)}$. These data comparatively include the results from the four ZRPs in 0.60 M NaCl [28], which demonstrate higher polarizability in all but the OZRP(EPA,65%). Specifically, the TC values for the ZRPs are 30.000 μA (IOZRP(EthylSil,76%)), 8.000 μA (OZRP(Epoxy,57%)), 2.000 μA (OZRP(U,83%)), and 0.100 μA (OZRP(EPA,65%)). In the case of the Al/MgRPs, the TC values in 0.6 M NaCl are 0.200 μA (MgRP(Epoxy,26%)), 0.080 μA (Al-MgRP(Epoxy,28/19%)), and for the AlRP(Epoxy,27%), the coupled potential was never at or more negative than $E_{pit\ (\beta)}$ (TC < 0.001 μA). Thus, the urethane-, epoxy-, and ethyl silicate-based ZRPs maintained protective coupled potentials at applied currents one order of magnitude or greater than those which were tolerated by the OZRP(EPA,65%) or the Al/MgRPs in 0.6 M NaCl.

The same galvanostatic pulse procedures were replicated on fresh MRP specimens in 5.45 M naCl to determine whether salinity affects the characteristic TC value for each primer. Figure 8.2 demonstrates the results of these analyses for the ZRPs, wherein the following average TC values are achieved: 7.000 μA (IOZRP(EthylSil,76%), >100.000 μA (OZRP(Epoxy,57%)), and the OZRP(U,83%) nor the OZRP(EPA,65%) achieved potentials at or more negative than $E_{pit\ (\beta)}$ at any of the applied currents considered (TC < 0.001 μA). In the Al/MgRPs, the MgRP(Epoxy,26%) was the only primer to achieve protective potentials in 5.45 M NaCl during the galvanostatic pulse tests (TC = 0.100 μA) (Figure 8.3). These results are summarized in Table 8.II, demonstrating that the TC value decreases in all of the MRPs except for the OZRP(Epoxy,57%) as the NaCl concentration is increased.

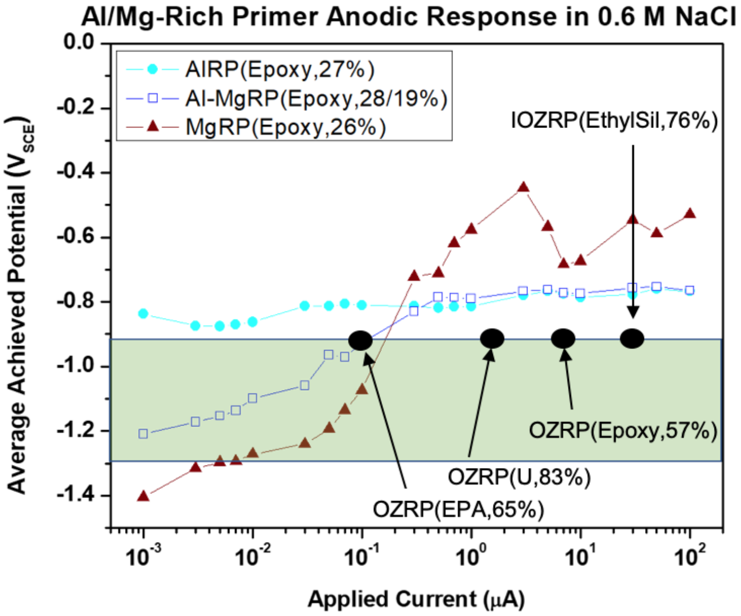

Figure 8.1: Galvanostatic pulse results for the Al/MgRP's, and, shown for comparison, the threshold currents achieved by the ZRPs in 0.6 M NaCl, demonstrating the effective range of applied current in which these primers are able to maintain protective potentials in the cathodic protection window of -1.30 to -0.92 V_{SCE}.

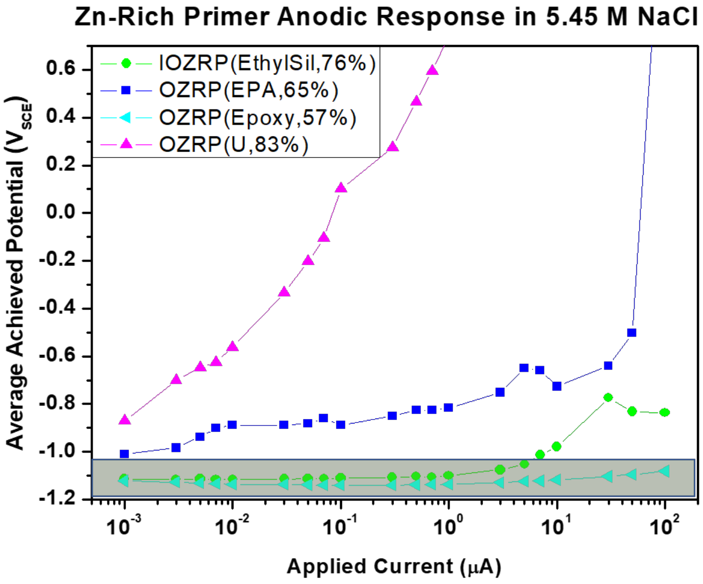

Figure 8.2: Galvanostatic pulse results for the ZRP's in 5.45 M (saturated) NaCl, demonstrating the effective range of applied current in which these primers are able to maintain protective potentials below $E_{pit\,(\beta)}$, -0.92 V_{SCE}.

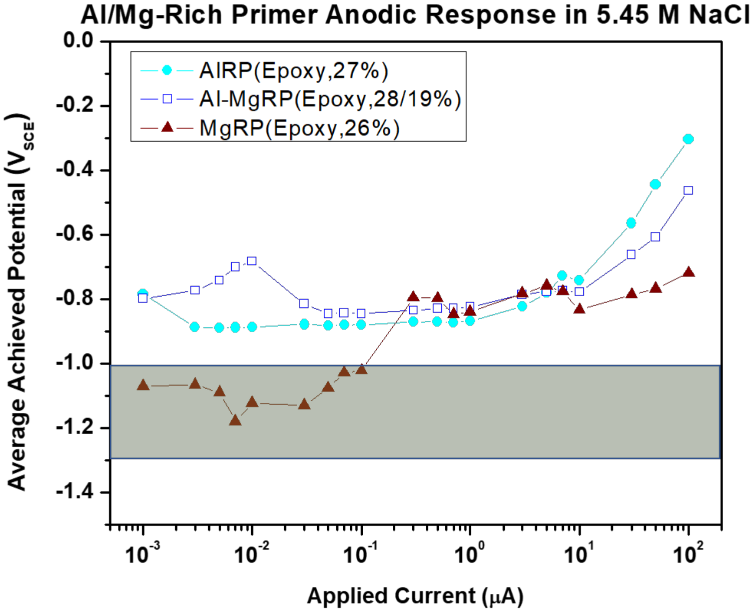

Figure 8.3: Galvanostatic pulse results for the Al/MgRP's in 5.45 M (saturated) NaCl, demonstrating the effective range of applied current in which these primers are able to maintain protective potentials in the cathodic protection window of -1.30 to -1.02 V_{SCE}.

Table 8.II

Metal-Rich Primer	**Threshold Current to Exceed Primer Polarization Resistance**	
	0.60 M NaCl (μA)	**5.45 M NaCl (μA)**
IOZRP (EthylSil,76%)	30.000	7.000
OZRP (EPA,65%)	0.100	< 0.001
OZRP (U,83%)	2.000	< 0.001
OZRP (Epoxy,57%)	8.000	> 100.000
AlRP (Epoxy,27%)	< 0.001	< 0.001
Al-MgRP (Epoxy,28/19%)	0.080	< 0.001
MgRP (Epoxy,26%)	0.200	0.100

8.1.4.2 *Simulated Crack Growth Testing Results*

The galvanostatic pulse analyses demonstrate that increased saline concentration is often deleterious to MRP polarizability, though the galvanostatic pulses do not directly demonstrate the MRP anodic response upon the increase in AA5456-H116 area, which would occur during crack growth. Thus, the simulated crack growth tests are conducted in 5.45 M NaCl full immersion with aggressive crack advance simulated through more than doubling the cathodic AA5456-H116 area, instantaneously. The aggressive nature of the 5.45 M NaCl plus the large magnitude of Al surface area increase assist the differentiation in galvanic protection performance achieved between these MRPs. Several of these datasets are provided from select tests to demonstrate distinct differences in MRP performance. The results from the OZRP(Epoxy,57%) test are illustrated in Figure 5.4, wherein the primer maintains protective potentials below $E_{pit\,(\beta)}$ for the majority of the test despite the sudden increase in AA5456-H116 cathode area (shown as the periods where "1" and "2" are present). The IOZRP(EthylSil,76%) performed similarly to the OZRP(Epoxy,57%), though this ZRP did allow the coupled potential to increase above $E_{pit\,(\beta)}$ in the 4th and 5th repetitions of simulated crack growth before reestablishing potentials below $E_{pit\,(\beta)}$ within 10-15 minutes (all while coupled to the 12.80 cm^2 AA5456-H116 area). This difference in galvanic protection performance agrees with the galvanostatic pulse test results, which concluded that the OZRP(Epoxy,57%) maintained lower polarizability than the IOZRP(EthylSil,76%) in 5.45 M NaCl (Table 2). The same testing procedure was applied to the OZRP(U,83%),

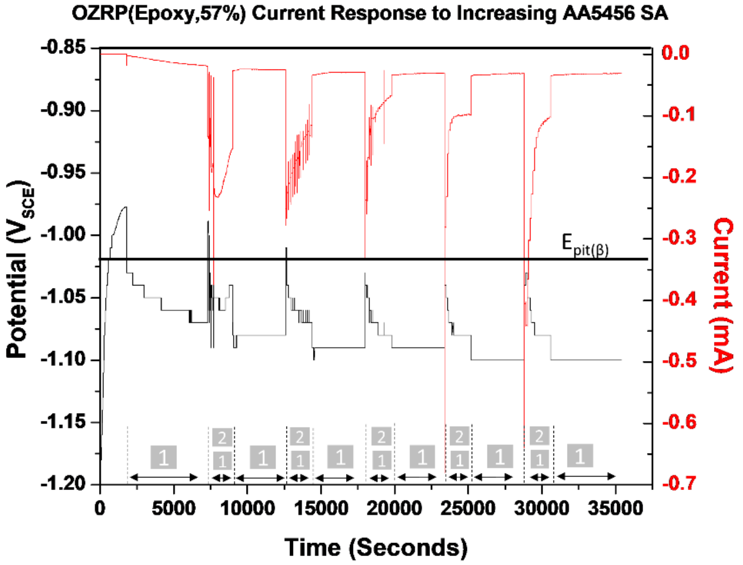

Figure 8.4: Simulated crack growth testing with the OZRP(Epoxy,57%), demonstrating the magnitude of anodic current output and the subsequent coupled potential maintained during the increase in galvanically coupled AA5456-H116 area from 4.90 cm^2 to 10.26 cm^2 in 5.45 M NaCl.

yielding the results shown in Figure 8.5. Uniquely, this ZRP demonstrated rather sporadic galvanic protection, and achieved a very low magnitude of anodic charge output compared to the OZRP(Epoxy,57%). At various points while testing, protective potentials below $E_{pit\ (\beta)}$ were achieved by the OZRP(U,83%), however during the majority of the galvanic coupling test period non-protective potentials were maintained. Lastly, the results of the simulated crack growth testing on the MgRP(Epoxy,26%) are shown in Figure 8.6, wherein the opposite trend is apparent: the galvanic protection is consistently inhibited by the increase in the AA5456-H116 area. The OCP period was increased to 12 hours for the MgRP(Epoxy,26%) to ensure primer activation prior to galvanic coupling, which is not shown in Figure 8.6. The same trend in galvanic protection as achieved by the MgRP(Epoxy,26%), the consistent inhibition of effective galvanic protection, is also representative of the OZRP(EPA,65%), Al-MgRP(Epoxy,28/19%), and AlRP(Epoxy,27%) performance, which aligns with the polarizability results obtained from galvanostatic pulse testing (Table 8.II).

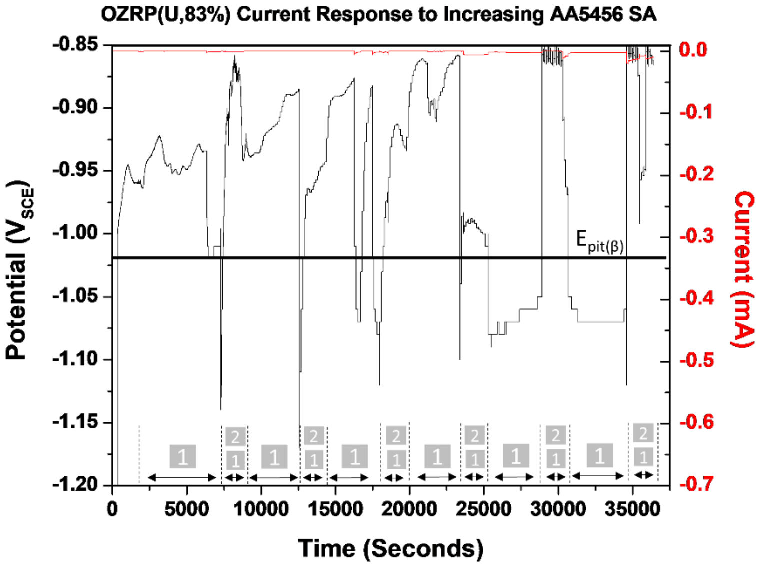

Figure 8.5: Simulated crack growth testing with the OZRP(U,83%), demonstrating the magnitude of anodic current output and the subsequent coupled potential maintained during the increase in galvanically coupled AA5456-H116 area from 4.90 cm^2 to 10.26 cm^2 in 5.45 M NaCl.

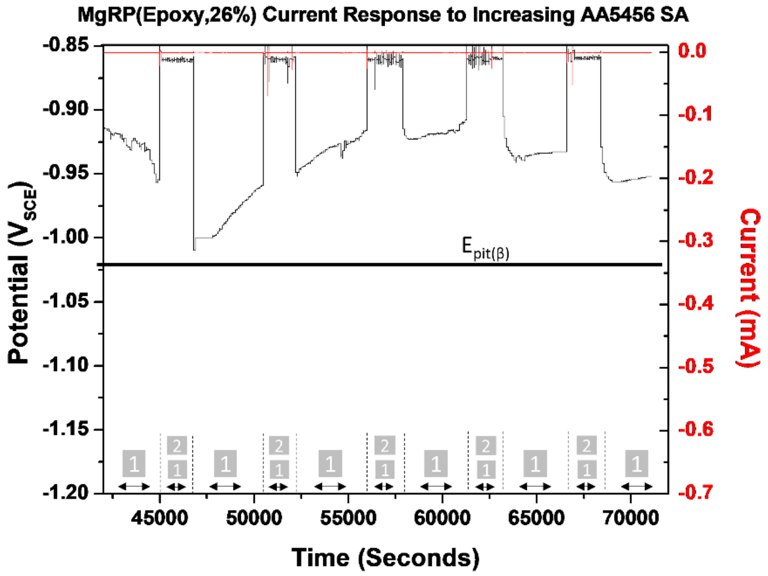

Figure 8.6: Simulated crack growth testing with the MgRP(Epoxy,40%), demonstrating the magnitude of anodic current output and the subsequent coupled potential maintained during the increase in galvanically coupled AA5456-H116 area from 4.90 cm^2 to 10.26 cm^2 in 5.45 M NaCl.

8.1.4.3 *IG-SCC Mitigation as a Function of Galvanically Coupled, Pure Metal Anode Type*

The previous testing demonstrated that Zn-based primers have the lowest polarizability, suggesting that Zn-based anodes may be the more robust source of galvanic protection for IG-SCC mitigation compared to Al- or Mg-based anodes. However, the previous analyses compared MRPs having various metal pigment PVCs, with the Al- and Mg-based MRPs having lower PVC than the ZRPs. Thus, a direct comparison between the IG-SCC mitigation achieved by pure metal anodes, specifically pure Zn and pure Mg, is required to more thoroughly inform the selection of a robust sacrificial protection system for IGC/IG-SCC mitigation in naval service. Slow rising displacement testing was conducted on galvanically-coupled AA5456-H116 with either (1) 0.05 cm^2 pure Mg or (2) 0.03 cm^2 pure Zn, the results of which are shown in Figure 8.7. These crack growth rate versus K data illustrate a significant difference between these evaluations: in the case of the pure Zn galvanic coupling, the achieved IG-SCC follows a relatively consistent trend with increasing stress intensity. The coupled potential results throughout this LEFM test, which are shown in Figure 8.8, suggest the cause: the low self-corrosion rate and consistent achieved coupled potential (-1.07 V_{SCE}) achieve relatively similar IG-SCC mitigation as in the potentiostatic case (-1.0 V_{SCE} and -1.1 V_{SCE}, Figure 8.7). The coupled potential results achieved by the pure Mg/AA5456-H116 galvanic coupling are shown in Figure 8.9, where a new, freshly polished pure Mg anode replaced the original Mg anode whenever the coupled potential rose above $E_{pit\ (\beta)}$ (suggesting Mg passivation due to corrosion product coverage). These results demonstrate the cause for the less consistent IG-SCC trend shown in Figure 8.7; the potential-dependent IG-SCC behavior aligned with the relatively inconsistent coupled potential trend shown in Figure 8.9. This inconsistent trend was the result of fast increase in the Mg/AA5456-H116 coupled potential at several points in the test (surpassing $E_{pit\ (\beta)}$), after which a newly polished Mg anode was quickly installed. Thus, the IG-SCC severity increased as the coupled potential increased, and this loss of effective galvanic protection was more likely to occur while utilizing the pure Mg anode. These results demonstrate that the Mg anode is prone to rapid self-corrosion and loss of effective galvanic control, which is in agreement with the literature [34,35], and suggest that Mg is a less dependable anode for long-term IG-SCC mitigation in aggressive saline conditions.

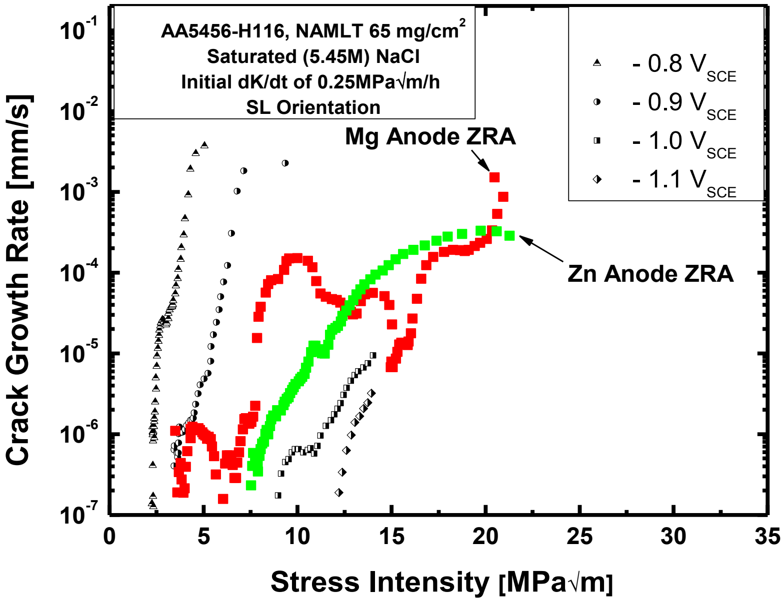

Figure 8.7: LEFM test results demonstrating the magnitude of IG-SCC mitigation achieved by galvanic coupling with either 0.05 cm^2 Mg anode, or with 0.03 cm^2 Zn anode in 5.45 M NaCl.

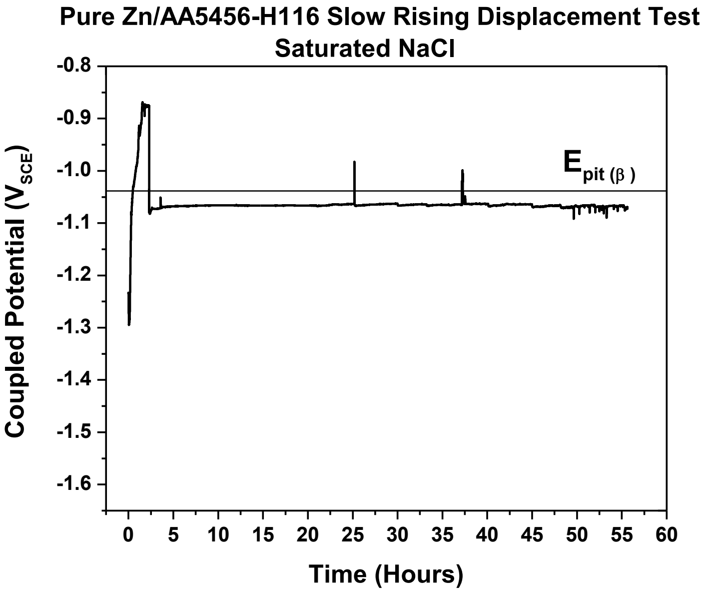

Figure 8.8: Galvanic couple potential results between the pure Zn anode and AA5456-H116 during LEFM testing in 5.45 M NaCl, demonstrating the consistent coupled potentials maintained during the entirety of the test for a similar exposed Zn surface area.

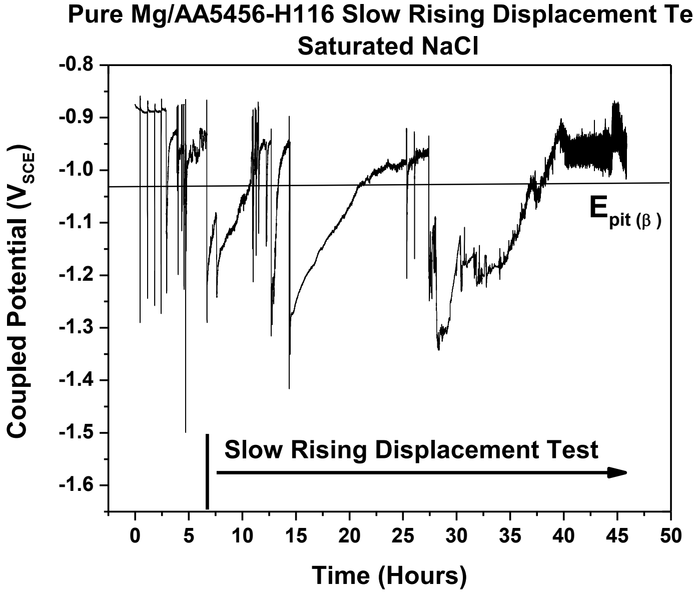

Figure 8.9: Galvanic couple potential results between pure Mg/AA5456-H116 during the LEFM testing in 5.45 M NaCl, demonstrating the relatively rapid corrosion and passivation that occurred on the Mg anode that warranted repeated polishing throughout the test to continue to achieve protective potentials.

8.1.5 **CONCLUSIONS**

A variety of commercial metal-rich primers containing anodic pigments such as Zn, Al, and Mg were surveyed on AA5456-H116 to evaluate primer polarizability via galvanostatic pulse and simulated crack growth tests, which sought to understand the effect of bulk saline environment on the efficacy of these systems for IG-SCC mitigation in naval service. These evaluations were then complemented by LEFM testing based on galvanic coupling with pure Zn and pure Mg, which demonstrated the performance of each anode type in IG-SCC mitigation without the complications of a high impedance resin. The following conclusions were drawn:

1. The galvanostatic pulse and simulated crack growth tests are demonstrated to be complementary testing techniques to evaluate MRP polarizability in various saline environments

2. Metal-rich primer polarizability is increased with increasing NaCl salinity in all but the primers which achieve the highest anodic charge output
3. Zn-rich primers are often the least polarizable sacrificial protection systems when compared to Al- and Mg-based primers, where the combined choice of resin type/pigment PVC are crucial design attributes
4. Zn-based sacrificial protection systems are more likely candidates to achieve effective IG-SCC mitigation due to the low self-corrosion rate and protective OCP value characteristic of Zn

8.2 REFERENCES

[1] M.L.C. Lim, R.G. Kelly, J.R. Scully, Overview of Intergranular Corrosion Mechanisms, Phenomenological Observations, and Modeling of AA5083, Corrosion. 72 (2016). doi:10.5006/1818.

[2] D.R. Baer, C.F. Windisch, M.H. Engelhard, M.J. Danielson, R.H. Jones, J.S. Vetrano, Influence of Mg on the corrosion of Al, J. Vac. Sci. Technol. a-Vacuum Surfaces Film. 18 (2000) 131–136. doi:10.1116/1.582129.

[3] R.H. Jones, The Influence of Hydrogen on the Stress-Corrosion Cracking of Low-Strength Al-Mg Alloys, J. Miner. Met. Mater. 55 (2003) 42–46. doi:10.1007/s11837-003-0225-5.

[4] Standard Test Method for Determining the Susceptibility to Intergranular Corrosion of 5XXX Series Aluminum Alloys by Mass Loss After Exposure to Nitric Acid (NAMLT Test) 1, Annu. B. ASTM Stand. i (2004) 5–7. doi:10.1520/G0067-04.2.

[5] M.A. Steiner, S.R. Agnew, Modeling sensitization of Al–Mg alloys via β-phase precipitation kinetics, Scr. Mater. 102 (2015) 55–58. doi:10.1016/j.scriptamat.2015.02.012.

[6] M.A. Steiner, S.R. Agnew, Predictive sensitization modeling for AA5xxx aluminum alloys including non-isothermal cases, Corrosion. 72 (2016) 169–176. doi:10.5006/1675.

[7] D. Mizuno, R.G. Kelly, Galvanically Induced Intergranular Corrosion of AA5083-H131 Under Atmospheric Exposure Conditions: Part 1—Experimental Characterization, Corrosion. 69 (2013) 580–592. doi:10.5006/0812.

[8] E.C. Cormack, The Effect of Sensitization on the Stress Corrosion Cracking of Aluminum Alloy 5456, Naval Postgraduate School, 2012.

[9] R. Zhang, S.P. Knight, R.L. Holtz, R. Goswami, C.H.J. Davies, N. Birbilis, A survey of sensitization in 5xxx series aluminum alloys, Corrosion. 72 (2016) 144–159. doi:10.5006/1787.

[10] M.E. McMahon, J.R. Scully, J.T. Burns, Mitigation of intergranular stress corrosion

cracking in Al-Mg by electrochemical potential control, J. Miner. Met. Mater. 69 (2017) 1389–1397. doi:10.1007/s11837-017-2362-2.

[11] L. Blohm, Analysis of Galvanic Coupling of AA5XXX-H116 and CDA 706 Utilizing Laboratory, Outdoor, and Accelerated Testing, University of Virginia, 2018.

[12] P. Steiner, J. Burns, Mechanistic Studies of Intergranular Stress Corrosion Cracking in Al-Mg Alloys under Atmospheric Exposure Conditions, Corrosion. (2018) 2853. doi:10.5006/2853.

[13] C.B. Crane, R.. Kelly, R.P. Gangloff, Crack chemistry control of intergranular stress corrosion cracking in sensitized Al-Mg, Corrosion. 72 (2016) 242–263. doi:10.5006/1852.

[14] C.B. Crane, R.P. Gangloff, Stress corrosion cracking of Al-Mg alloy 5083 sensitized at low temperature, Corrosion. 72 (2016) 221–241. doi:10.5006/1766.

[15] R.H. Jones, D.R. Baer, M.J. Danielson, J.S. Vetrano, Role of Mg in the stress corrosion cracking of an Al-Mg alloy, Metall. Mater. Trans. A. 32 (2001) 1699–1711. doi:10.1007/s11661-001-0148-0.

[16] M.E. McMahon, P.J. Steiner, A.B. Lass, J.T. Burns, The effect of temper and composition on intergranular stress corrosion cracking in Al-Mg alloys, Corrosion. 73 (2017) 347–361. doi:10.5006/2317.

[17] C. Taylor, J.R. Scully, R.G. Kelly, R. Lillard, M. Neurock, T. Lookman, M. Francis, Atomistic inquiries into the effect of hydrogen on metals, (2010).

[18] J.R. Scully, G.A. Young, S. Smith, Hydrogen Embrittlement of Aluminum and Aluminum-Based Alloys, in: R.P. Gangloff, B.P. Somerday (Eds.), Gaseous Hydrog. Embrittlement Met. Energy Technol., 1st ed., Woodhead Publishing Limited, Cambridge, UK, 2012: pp. 707–768.

[19] P. Plagemann, J. Weise, A. Zockoll, Zinc-magnesium-pigment rich coatings for corrosion protection of aluminum alloys, Prog. Org. Coatings. 76 (2013) 616–625. doi:10.1016/j.porgcoat.2012.12.001.

[20] C. Matzdorf, W. Nickerson, Aluminum alloy coated pigments and corrosion-resistant coatings, 8,277,688, 2012. doi:10.1016/j.(73).

[21] C. Matzdorf, W. Nickerson, Active Aluminum Rich Coatings, 8,262,938 B2, 2012. doi:10.1074/JBC.274.42.30033.(51).

[22] A.D. King, J.R. Scully, Sacrificial anode-based galvanic and barrier corrosion protection of 2024-T351 by a Mg-rich primer and development of test methods for remaining life assessment, Corrosion. 67 (2011) 1–22. doi:10.5006/1.3590330.

[23] M.E. Nanna, G.P. Bierwagen, Mg-rich coatings: A new paradigm for Cr-free corrosion protection of Al aerospace alloys, J. Coatings Technol. Res. 1 (2004) 69–80. doi:10.1007/s11998-004-0001-7.

[24] M.E. Nanna, G.P. Bierwagen, D. Battocchi, Magnesium Rich Coatings and Coating Systems, US 2007/0128351 A1, 2007. doi:10.1016/j.micromeso.2003.09.025.

[25] F. Presuel-Moreno, M.A. Jakab, N. Tailleart, M. Goldman, J.R. Scully, Corrosion-resistant metallic coatings, Mater. Today. 11 (2008) 14–23. doi:10.1016/S1369-7021(08)70203-7.

[26] A.D. King, J.S. Lee, J.R. Scully, Finite Element Analysis of the Galvanic Couple Current and Potential Distribution between Mg and 2024-T351 in a Mg Rich Primer Configuration, J. Electrochem. Soc. 163 (2016) C342–C356. doi:10.1149/2.0171607jes.

[27] R.J. Santucci, M.E. McMahon, J.R. Scully, Utilization of chemical stability diagrams for improved understanding of electrochemical systems: evolution of solution chemistry

towards equilibrium, Npj Mater. Degrad. 2 (2018) 1. doi:10.1038/s41529-017-0021-2.

[28] M.E. McMahon, J.T. Burns, J.R. Scully, New Criteria for Substrate Protection Against Stress Corrosion Cracking in Al-Mg Alloys Based on Non-Polarizability of Zn-Rich Primers, Prog. Org. Coatings. (2019) In Review.

[29] M.E. McMahon, J.R. Scully, J.T. Burns, Mitigation of Intergranular Cracking in Al-Mg Alloys via Zn-Based Electrode Potential Control in Sodium Chloride Solution, Corrosion. (2019) In Review.

[30] R. Romagnoli, V. Vetere, Anticorrosive Protection by Zinc-Ethyl Silicate Paints. A Review, Corros. Rev. 10 (1992). doi:10.1515/CORRREV.1992.10.3-4.337.

[31] G. Parashar, D. Srivastava, P. Kumar, Ethyl silicate binders for high performance coatings, Prog. Org. Coatings. 42 (2001) 1–14. doi:10.1016/S0300-9440(01)00128-X.

[32] R.P. Gangloff, D.C. Slavik, S. Piascik, R.H. Van Stone, Direct current electrical potential measurement of the growth of small cracks, in: J.M. Larsen, J.E. Allison (Eds.), Small-Crack Test Methods, American Society for Testing and Materials, Philadelphia, PA, 1992: pp. 116–168.

[33] R. Gangloff, H. Ha, J. Burns, J. Scully, Measurement and Modeling of Hydrogen Environment-Assisted Cracking in Monel K-500, Metall. Mater. Trans. A. 45 (2014) 3814–3834.

[34] R.L. Liu, S. Thomas, J.R. Scully, G. Williams, N. Birbilis, An experimental survey of the cathodic activation of metals including Mg, Sc, Gd, La, Al, Sn, Pb, and Ge in dilute chloride solutions of varying pH, Corrosion. 73 (2017) 494–505. doi:10.5006/2282.

[35] A.D. King, N. Birbilis, J.R. Scully, Accurate electrochemical measurement of magnesium corrosion rates; A combined impedance, mass-loss and hydrogen collection study, Electrochim. Acta. 121 (2014) 394–406. doi:10.1016/j.electacta.2013.12.124.

APPENDIX II

Experimental Findings Concerning Zn^{2+} Chemical Protection Effects on IG-SCC Severity in Al-Mg

9.1 Zn^{2+} Influence on Stress Corrosion Cracking Severity in a Highly Sensitized Al-Mg Alloy

M. E. McMahon [ǂ, *], J. T. Burns[*], and J. R. Scully[*]

[*] Center for Electrochemical Science and Engineering, Department of Materials Science and Engineering, University of Virginia, 395 McCormick Rd., Charlottesville, VA 22904
[ǂ] Corresponding author. E-mail: mm5kn@virginia.edu

9.1.1 Abstract

Zn-rich primers are of growing interest for fracture mitigation on Al-Mg alloys, and recent work has demonstrated that a galvanic as well as chemical protection mechanism may drive these primers' performance. The effect of Zn salt species content in the bulk environment on stress corrosion cracking (SCC) severity for a constant potential of -0.9 V_{SCE} was evaluated on NAMLT 65 mg/cm^2 AA5456-H116. LEFM testing demonstrated that, for a constant [Cl^-], the threshold stress intensity for SCC remained relatively the same in these conditions but the SCC growth rate was reduced with increasing stress intensity in the presence of Zn ions. Potentiodynamic analysis in 0.6 M NaCl/0.3 M $ZnCl_2$ demonstrated that $E_{pit\,(\alpha)}$ and $E_{pit\,(\beta)}$ are unchanged by the Zn content, however titration of $ZnCl_2$ into Al-Mg simulated crack tip solution suggests that Zn salt species may reduce crack tip acidification. These results support the combined galvanic and chemical protection that may be achieved through use of Zn-rich primers for IG-SCC mitigation on AA5456-H116.

9.1.2 Introduction

AA5xxx-series (Al-Mg) alloys having greater than 3 wt.% Mg become increasingly susceptible to environmental degradation during the prolonged exposure to 40-50°C typical of naval service [1–3]. During the sensitization process, supersaturated Mg precipitates from solid solution to form the highly anodic intergranular β phase (Al_3Mg_2). Sensitized materials are highly susceptible to localized attack, specifically intergranular corrosion (IGC) and intergranular stress corrosion cracking (IG-SCC) under applied loads well below the alloy yield strength and fracture toughness [4–10]. The density of the intergranular β, which is often estimated via the Nitric Acid Mass Loss Test (NAMLT), is a key factor dictating the alloy susceptibility to the IGC and IG-SCC phenomena [11–16]. Though a point of debate [17,18], the NAMLT value is a common proxy for alloy susceptibility, which is considered low at NAMLT < 15 mg/cm^2, intermediate at NAMLT 15-25 mg/cm^2, and high at NAMLT ≥ 25 mg/cm^2 [19–22].

Sensitization of Al-Mg alloys in naval service has proven difficult to avoid, and IG-SCC of marine structures where residual stress levels can be high is increasingly common [2,23]. Numerous research efforts have confirmed a coupled anodic dissolution (of the β/α-Al matrix) and hydrogen embrittlement mechanism driving IG-SCC [12,13,15,16,18,24–28]. Specifically, localized anodic β phase dissolution at the crack tip provides Al^{3+} and Mg^{2+} cations in the local crack tip chemistry that (1) promote metal cation hydrolysis reactions to form hydrogen, (2) drive Cl^- ingress for charge neutralization, which (3) affects the oxide at the crack tip to enable further α-Al matrix dissolution [24,29,30]. The acidification of the crack tip that occurs through the metal cation hydrolysis reactions enables hydrogen adsorption and diffusion into the fracture process zone, where the hydrogen promotes decohesion of the grain boundary and/or at the interface of the intergranular β particle and the matrix. This mechanism has been recently supported through experimental work in a variety of saline environments and alloy sensitization conditions [16,25,26,28,31,32], and has been theoretically supported through hydrogen-enhanced decohesion modeling [16,25,26].

The dependence of IG-SCC on the reactivity of the β phase enables the successful mitigation of this phenomenon through intermediate cathodic polarization, wherein the β phase and the α-Al matrix may be maintained in a passive state [24,25,27]. Utilizing potentiostatic control, Crane and Gangloff demonstrated increasingly effective IG-SCC mitigation through establishing potentials below the breakdown potential of the α-Al matrix ($E_{pit\ (\alpha)}$), and especially below that of the β phase ($E_{pit\ (\beta)}$) in AA5083-H131 in 0.6 M NaCl [24,25]. McMahon et. al. demonstrated similar levels of mitigation in more highly sensitized AA5456-H116 utilizing a potentiostat as well as Zn-rich primers (ZRPs) when potentials below $E_{pit\ (\alpha)}$ and/or $E_{pit\ (\beta)}$ were achieved [27,33]. Interestingly, spray-deposited ZRPs achieved similar IG-SCC mitigation for a given achieved potential, when compared to the IG-SCC severity achieved under potentiostat-based control [33]. Spray-deposited ZRPs also demonstrated more effective IG-SCC mitigation than that achieved through galvanic coupling with ZRP panels separated by a microporous filter to mitigate Zn^{2+} egress into the bulk saline environment [33]. These results suggest that Zn^{2+}-based secondary chemical protection may have a role in ZRP IG-SCC mitigation performance.

Prior works exist demonstrating significant effects of Zn^{2+} content on corrosion phenomena in aluminum alloys and in steels. Sakairi et al. demonstrated in tap water that the galvanic corrosion of AA3003 is suppressed when Zn^{2+} is incorporated, which is thought to occur by supporting oxide stability [34]. Khedr and Lashien demonstrated that Zn^{2+} concentrations as low as 10^{-8} M in neutral and acidic Cl-containing solutions suppress Al corrosion through surface deposition and electron consumption, however with increasing concentration these non-uniform Zn deposition sites promoted pitting corrosion in the immediate vicinity [35,36]. Numerous studies exist on steels demonstrating that Zn^{2+} content slows anodic and cathodic reactions on the steel surface by depositing layers of corrosion product and/or adsorbing to the alloy surface over extended exposure [37–41]. In sulphuric acid, the presence of Zn cations has been demonstrated to inhibit hydrogen evolution and thus hydrogen embrittlement in iron [42]. In sulfate environment, added Zn content was demonstrated to have the most protective effect to delay the onset of IG-SCC in Type 304 stainless steel by incorporating into the oxide film and promoting passivity [43]. No works exist considering the effects of Zn ion content on environmental fracture in Al, as Zn-based sacrificial protection systems are only recently growing in common use for this purpose.

The aim of the current work is to experimentally determine the impact of Zn^{2+} content in the bulk saline environment on IG-SCC severity in highly sensitized AA5456-H116. These evaluations will consider the effect of Zn content on the (1) critical pitting potentials of the β phase and the α-Al matrix, (2) the crack tip acidification, and (3) the overall IG-SCC mechanism. This baseline will further inform metal-rich primer selection for IG-SCC mitigation purposes in marine applications.

9.1.3 **Experimental Methods**

9.1.3.1 ***Al-Mg Alloy and Sensitization Procedure***

The composition, metallography, and mechanical properties of the unrecrystallized AA5456-H116 material lot utilized in the this study were previously reported [44]. All specimens were obtained from a rolled plate of 5.7 cm thickness and were excised in the S-L orientation. Samples were sensitized at 373 K for 336 hours to achieve the NAMLT value of 65 mg/cm^2, which constitutes intergranular β coverage of 95% or more.

9.1.3.2 ***Mechanical Testing to Evaluate the Effect of Zn^{2+} Content on IG-SCC Severity***

An AA5456-H116 single edge notch tensile (SENT) specimen was excised having gauge thickness of 6.60 mm and width of 17.30 mm, with an electrical discharge machined (EDM) notch placed at the plate and specimen mid-thickness (t/2) with 4.80 mm depth. The specimen was degreased through sonication in acetone, methanol, and deionized water followed by compressed air drying prior to testing. Linear elastic fracture mechanics (LEFM) testing consisted first of a fatigue precracking protocol using a decreasing stress intensity range (ΔK) protocol (R = 0.1, frequency = 8 Hz) in laboratory air to a notch plus crack depth of 5.30 mm, with the final maximum stress intensity being 3.5 MPa√m. The stress corrosion cracking test utilized slow rising displacement with the fatigue pre-cracked SENT fixed in a 200-mL acrylic environmental cell, where 2.72 M $ZnCl_2$ solution was continuously recycled at 20 mL/min from a 2 L reservoir in ambient conditions. The slow rising displacement test was conducted at an initial rate of 0.25 MPa√m/hr from a K of 2.0 MPa√m following a 1 hour hold at K = 1.0 MPa√m in full immersion, and was completed upon specimen failure. Electrochemical conditions were controlled via a floating ground potentiostat by bulk alloy polarization to -0.9 V_{SCE}, which enabled direct comparison to tests run at similar potentials in NaCl environment [27]. Crack extension was monitored with ~0.5 μm resolution via the direct current potential difference (dcPD) method, the details of which are described elsewhere [44,45]. Resolved crack growth related solely to plasticity effects at the crack tip were subtracted the da/dt versus K data [46]; as such all reported data represent real crack growth. Data analysis utilized Ramberg Osgood constants derived from compression testing stress strain curves to calculate the total elastic-plastic stress intensity (K_J) via J-integral plastic corrections; details of the underlying fundamentals and application of this method are provided elsewhere [47].

9.1.3.3 *Electrochemical Evaluation to Determine Zn^{2+} Effects on Crack Tip Conditions*

Electrochemistry analysis first utilized potentiodynamic test methods to determine the effect of Zn content on $E_{pit\ (\alpha)}$ and $E_{pit\ (\beta)}$. These evaluations were conducted in 300 mL electrochemical flat cells where the 5456 or pure β served as the working electrode, platinized mesh served as the counter electrode, and a Saturated Calomel electrode (SCE) served as the reference. All specimens were polished under actively flowing water to 1200 grit surface finish via silicon carbide paper prior to testing. Potentiodynamic scans were conducted starting at ± 0.05 V_{SCE} about the open circuit potential (OCP, stabilized for 30 minutes prior), with ramp rate of 0.167 mV/s at ambient temperature and in ambiently aerated conditions. Test solutions consisted of freshly mixed 5.45 M (saturated) NaCl and 2.72 M $ZnCl_2$.

Titration of $ZnCl_2$ into simulated Al-Mg crack tip solution informed the impact of bulk Zn^{2+} content on crack tip acidification and hydrogen evolution kinetics. Simulated Al-Mg crack tip solution, which was proposed by Crane et al. [24], consists of 2.5 M $AlCl_3$ + 0.11 M $MgCl_2$, with pH ≈ -0.4. The addition of $MgCl_2$ to $AlCl_3$ has been demonstrated to drastically reduce the pH to this negative value, which is hypothesized to promote hydrogen embrittlement [48]. 1 M $ZnCl_2$ solution was titrated into 500 mL of this simulated crack tip solution in 100 μL to 50 mL portions while measuring the pH.

9.1.4 **Results**

9.1.4.1 *Stress Corrosion Cracking Susceptibility in Zn^{2+}-Containing Solution*

The results of the stress corrosion cracking evaluation in 2.72 M $ZnCl_2$ are shown in Figure 9.1 in comparison to previous tests run at applied polarizations of -0.8 V_{SCE} to -1.1 V_{SCE} in 5.45 M NaCl [27]. For a fixed [Cl^-] concentration of 5.45 M, these results demonstrate reduced IG-SCC severity in NAMLT 65 mg/cm^2 AA5456-H116 at -0.9 V_{SCE} in the presence of Zn^{2+} compared to Na^+. Specifically, the two SCC tests at -0.9 V_{SCE} both demonstrate different threshold stress intensities for SCC (K_{TH}) (K_{TH} = 3.5 MPa√m in 0.6 M NaCl, K_{TH} = 9.0 MPa√m in 0.3 M $ZnCl_2$), and the crack growth rates are considerably less in the Zn-containing solution, exhibiting three orders of magnitude reduction at K = 10 MPa√m (2.5x10^{-6} mm/s versus 2.2x10^{-3} mm/s) (Figure 9.1). Analysis of the fracture surface through EDS, as shown in Figure 9.2, demonstrates Zn deposition in the SENT notch area but considerably less Zn on the fracture surface.

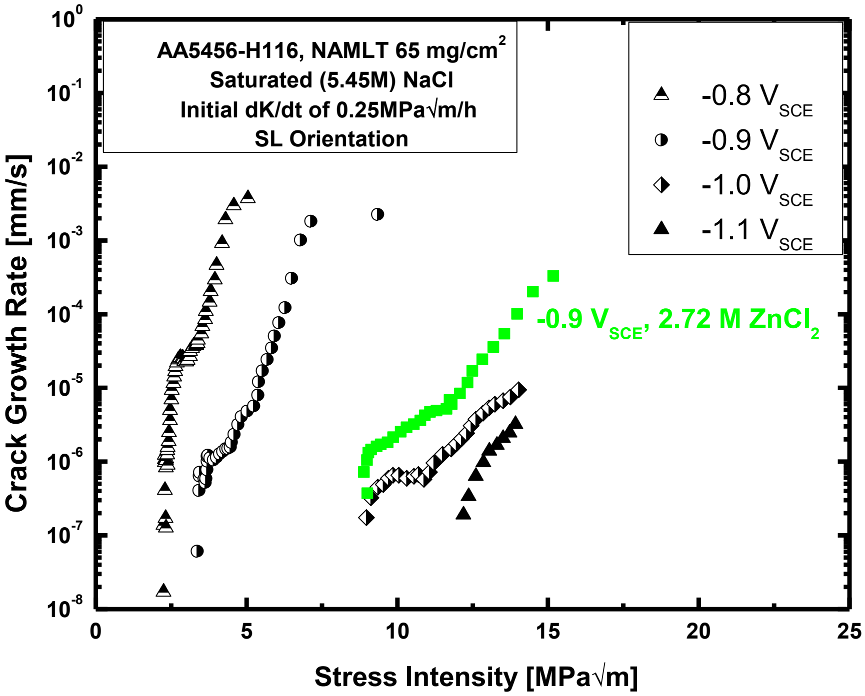

Figure 9.1: LEFM results obtained on NAMLT 65 mg/cm^2 AA5456-H116 during -0.9 V_{SCE} potentiostatic hold in 2.72 M $ZnCl_2$ bulk solution, demonstrating the reduced IG-SCC severity that occurs in comparison to the -0.9 V_{SCE}, 5.45 M NaCl results, despite the constant [Cl^-].

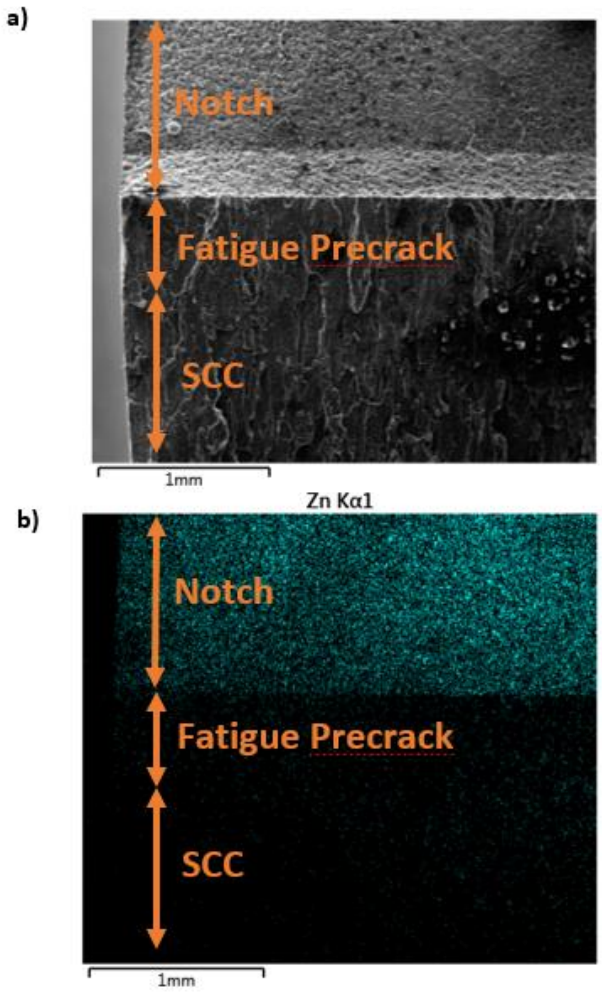

Figure 9.2: Energy dispersive spectroscopy results obtained on the fracture surface of the LEFM specimen following the potentiostatic, -0.9 V_{SCE} test in 2.72 M $ZnCl_2$, demonstrating the predominant Zn content covering the notch area but the reduced coverage observed on the fracture surface. The micrograph of the notch/fracture surface is shown in (a) and the composition map obtained through EDS in (b).

9.1.4.2 *Effect of Zn^{2+} on Critical Pitting Potentials and Simulated Crack Tip Solution Acidity*

The results of the potentiodynamic evaluations on NAMLT 65 mg/cm^2 AA5456-H116 as well as on the pure β phase in 0.6 M NaCl and 0.3 M $ZnCl_2$ are shown in Figure 9.3. These results demonstrate two main takeaways: (1) the pitting potentials for the β phase and the 5456 are not affected by the Zn^{2+} with a fixed [Cl^-]; (2) while the OCP of the 5456 remains relatively unchanged, the β phase OCP is increased roughly 150 mV. Interestingly, the cathodic kinetics are increased on 5456 in 0.3 M $ZnCl_2$ as well, despite considerable Zn-based corrosion product precipitation on the alloy surface. This corrosion product formation occurred during the cathodic polarization scan but not during the anodic scan upwards from the 5456 OCP.

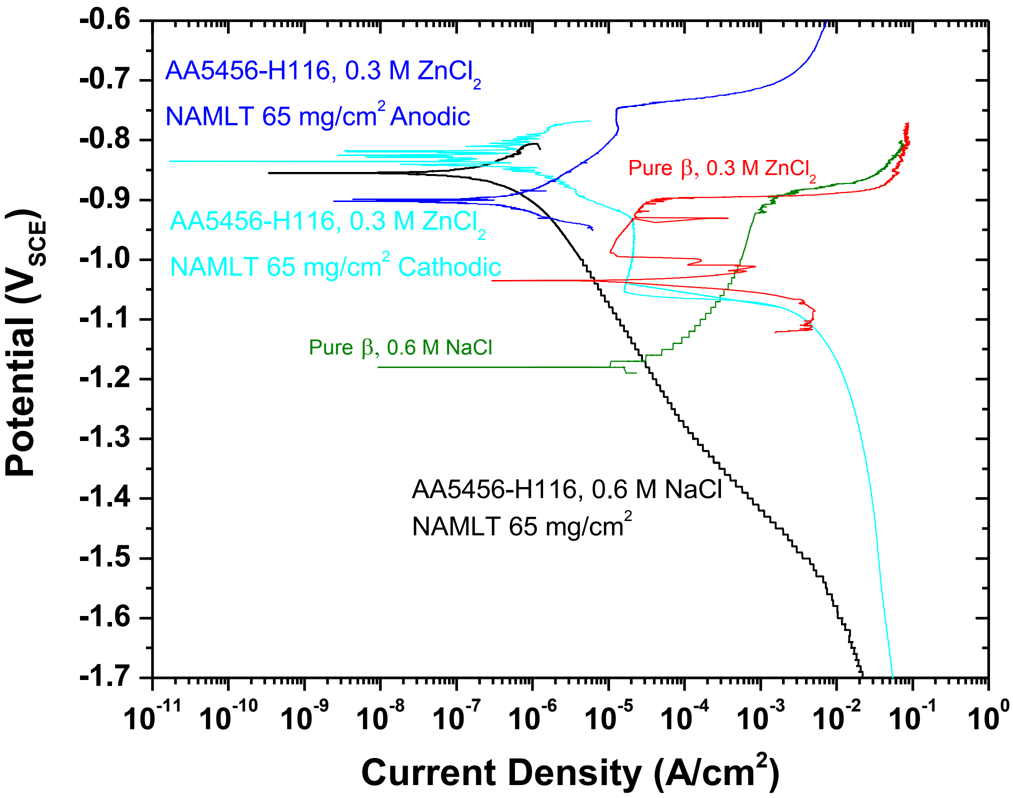

Figure 9.3: Potentiodynamic comparison between the NAMLT 65 mg/cm^2 AA5456-H116/pure β phase electrochemical behavior in 0.6 M NaCl and 0.3 M $ZnCl_2$, demonstrating the negligible impact on the critical pitting potentials when the [Cl^-] concentration is held constant.

The results of the titration of $ZnCl_2$ into simulated crack tip solution are shown in Figure 9.4. These results clearly demonstrate that the addition of Zn content to the Al-Mg crack tip can increase the pH to reduce the acidification. Specifically, the addition of 0.1 M Zn^{2+} increases the simulated crack tip solution pH from -0.38 to 0.74, or more than a 10-fold reduction in hydrogen concentration, and further addition of Zn^{2+} to reach concentrations of 0.5 M or more seems to approach a pH plateau at ≈ 1.5, which would be a two order of magnitude reduction in crack tip hydrogen concentration.

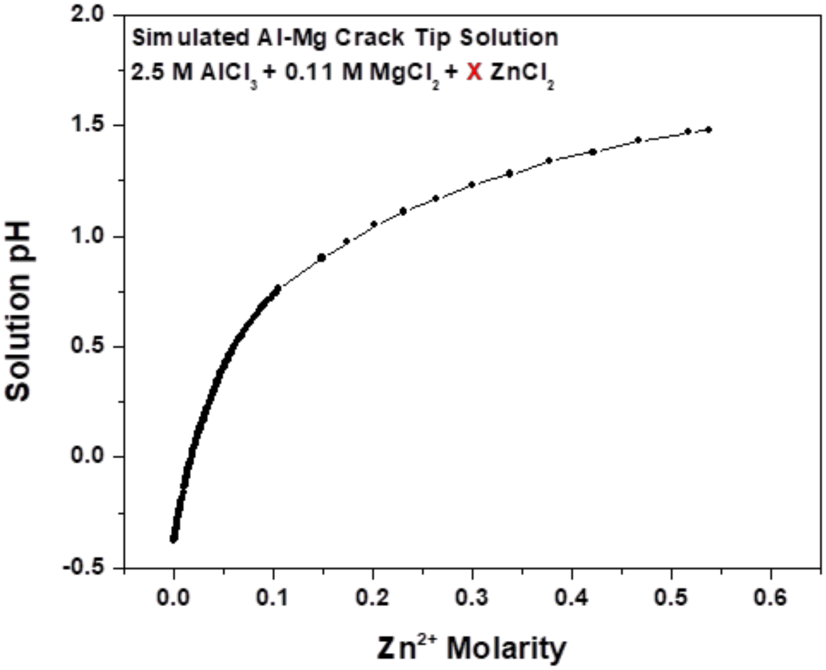

Figure 9.4: Results from the titration of $ZnCl_2$ into simulated Al-Mg crack tip solution (7.7 M Cl^- + 2.5 M Al^{3+} + 0.11 M $MgCl_2$), demonstrating the 10-fold decrease in [H] when 0.1 M Zn^{2+} concentration is introduced.

9.1.5 **Discussion**

There are several ways in which Zn^{2+} content may be speculated to affect the IG-SCC mechanism. These include (1) the alteration of $E_{pit\,(\alpha)}$ and $E_{pit\,(\beta)}$ to change the required crack tip potential for cation dissolution to occur; (2) the coverage of the anodic/cathodic area at the crack tip/in the crack wake to suppress the rate of anodic and cathodic reactions or the adsorption of H; (3) stabilization of the crack tip oxide to inhibit hydrogen adsorption; (4) corrosion product formation to serve as an ion-permeation barrier mitigating Cl^- ingress; and (5) reduction of crack tip acidification. The present results demonstrate that (1) (Figure 9.3) and (2) (Figure 9.2) are not viable, however the remaining options will be discussed in further detail.

9.1.5.1 *Stabilization of the Crack Tip Oxide to Inhibit H Adsorption*

Based on the prior findings on 304 stainless steel, bulk Zn cation content could conceivably promote oxide stability and passivity to affect IG-SCC severity in Al-Mg alloys [43]. At the Al-Mg crack tip, IG-SCC is enabled by β phase dissolution, which then promotes dissolution in the α-Al matrix by driving Cl^- ingress. However, in the situation where Zn^{2+} could incorporate into the oxide to increase stability, the best-case scenario would entail only β phase dissolution at the crack tip. Based on Figure 9.3, the critical pitting potentials are not changed on NAMLT 65 mg/cm^2 AA5456-H116 in Zn-containing saline environment for a constant [Cl^-], therefore the bulk pitting potentials for the α-Al matrix and the β phase should remain at -0.92 V_{SCE} and -1.03 V_{SCE} in 2.72 M $ZnCl_2$ [33]. Though the crack tip solution would differ from the bulk, these potentials would suggest that the potentiostatic -0.90 V_{SCE} conditions maintained throughout the LEFM test were cathodic to $E_{pit\ (\alpha)}$, and if the oxide was stabilized further by the Zn^{2+} content the reduced cation dissolution into the crack tip solution could reduce the quantity of hydrogen produced. However, to be active, this effect would require rapid oxide stabilization and reformation during crack growth since each crack growth event would freshly expose α-Al matrix.

9.1.5.2 *Zn-Based Corrosion Product Barrier Formation Limiting Cl^- Ingress*

Chemical stability modeling as well as corrosion product characterization on pure Zn/ZRPs following atmospheric exposure demonstrate that Zn^{2+} complexes strongly with Cl^- [49]. On the crack wake, the sequestration of Cl^- to form these corrosion products may reduce the severity of oxide rupture and therefore reduce the Al oxidation at the crack tip. If corrosion product were to encircle the crack, this layer could theoretically even serve as an ion selective barrier. However, the fractography following the LEFM test in 2.72 M $ZnCl_2$ demonstrated negligible Zn corrosion product formation on the crack wake or the crack flanks (Figure 9.2), so Cl^- ingress should have been unhindered. Interestingly, the majority of the Zn deposition was in the LEFM specimen EDM notch, and visual assessment demonstrated a white semicircle of corrosion product encircling the center of the notch. In the pH 4.9 bulk $ZnCl_2$ solution conditions, chemical stability modeling demonstrates that any Zn-based corrosion product formation in also metastable [49]. Therefore, the impact of the corrosion product in this LEFM test is considered negligible.

9.1.5.3 ***Reduction of Crack Tip Acidification***

The rapid acidification of the Al-Mg crack tip has been experimentally supported through demonstration of the rapid reduction in pH with only slight addition of $MgCl_2$ to $AlCl_3$ [24,48,50]. Furthermore, Crane et al. demonstrated that IG-SCC occurs in unsensitized Al-Mg when tested in simulated crack tip solution, which is pH $\approx$ -0.40 (Figure 9.4) [24]. These results demonstrate that the crack tip acidity is the primary factor driving IG-SCC, in agreement with SCC phenomena in other alloy systems [51–62], as hydrogen is able to adsorb and diffuse in the fracture process zone to enhance decohesion. The titration results shown in Figure 4 suggest that the presence of Zn^{2+} in the bulk environment may reduce this acidification. Specifically, there is a two order of magnitude reduction in the H concentration achieved through addition of approximately 0.5 M $ZnCl_2$. While these results are compelling and suggest that the reduced IG-SCC behavior is due to less crack tip acidification in the presence of Zn ions, the results still suggest an acidic environment at a pH of 1.5. Speculatively, this acidity would still be sufficient to drive IG-SCC, though separate study would be needed to assess the effect of bulk environment pH on the IG-SCC severity. *In toto*, the effect of aqueous Zn content on the IG-SCC mechanism is likely a combination of synergistic influences, which may include the reduction in acidity as well as stabilization effects on the oxide.

9.1.6 **Conclusions**

The effect of Zn salt species content in the bulk environment on IG-SCC severity for a constant potential of -0.9 V_{SCE} was evaluated on NAMLT 65 mg/cm^2 AA5456-H116. Linear elastic fracture mechanics testing demonstrated that, for a constant [Cl$^-$], K_{TH} nearly tripled in value (3.5 MPa√m to 9.0 MPa√m) in these conditions and the IG-SCC growth rate was reduced by as much as three orders of magnitude with increasing stress intensity in the presence of Zn ions. Potentiodynamic analysis in 0.6 M NaCl/0.3 M $ZnCl_2$ demonstrated that $E_{pit\ (\alpha)}$ and $E_{pit\ (\beta)}$ are unchanged by the Zn content, however titration of $ZnCl_2$ into Al-Mg simulated crack tip solution suggests that Zn salt species may reduce crack tip acidification. These results support the combined galvanic and chemical protection that may be achieved through use of Zn-rich primers for IG-SCC mitigation on AA5456-H116. The effect of Zn content on the IG-SCC mechanism is likely a combination of synergistic influences, which may include the reduction in acidity as well as stabilization effects on the oxide.

9.1.7 **References Cited**

[1] R.B. Niederberger, J.L. Basil, G.T. Bedford, Corrosion and Stress Corrosion of 5000-Series Al Alloys in Marine Environments, Corrosion. 22 (1966) 68–73. doi:doi:10.5006/0010-9312-22.3.68.
[2] N.J.H. Holroyd, G.M. Scamans, Environmental Degradation of Marine Aluminum Alloys—Past, Present, and Future, Corrosion. 72 (2016). doi:10.5006/1927.
[3] E.H. Dix, W.A. Anderson, M.B. Shumaker, Influence of Service Temperature on the

Resistance of Wrought Aluminum-Magnesium Alloys to Corrosion, Corrosion. 15 (1959) 55–62.

[4] A.J. Davenport, Y. Yuan, R. Ambat, B.J. Connolly, M. Strangwood, A. Afseth, G.M. Scamans, Intergranular Corrosion and Stress Corrosion Cracking of Sensitised AA5182, Mater. Sci. Forum. 519–521 (2006) 641–646. doi:10.4028/www.scientific.net/MSF.519-521.641.

[5] R.H. Jones, The Influence of Hydrogen on the Stress-Corrosion Cracking of Low-Strength Al-Mg Alloys, J. Miner. Met. Mater. 55 (2003) 42–46. doi:10.1007/s11837-003-0225-5.

[6] M. Seifi, N.J.H. Holroyd, J.J. Lewandowski, Deformation rate and sensitization effects on environmentally assisted cracking of Al-Mg naval alloys, Corrosion. 72 (2016) 264–283. doi:10.5006/1949.

[7] J.R. Scully, G.A. Young, S. Smith, Hydrogen Embrittlement of Aluminum and Aluminum-Based Alloys, in: R.P. Gangloff, B.P. Somerday (Eds.), Gaseous Hydrog. Embrittlement Met. Energy Technol., 1st ed., Woodhead Publishing Limited, Cambridge, UK, 2012: pp. 707–768.

[8] V.S. Raja, T. Shoji, Stress Corrosion Cracking: Theory and Practice, Woodhead Publishing Limited, Cambridge, UK, 2011.

[9] M.L.C. Lim, R.G. Kelly, J.R. Scully, Overview of Intergranular Corrosion Mechanisms, Phenomenological Observations, and Modeling of AA5083, Corrosion. 72 (2016). doi:10.5006/1818.

[10] N.J.H. Holroyd, G.M. Scamans, The Role of Magnesium During Environment-Sensitive Fracture of Aluminium Alloys, Scr. Metall. Mater. 19 (1985) 945–946.

[11] D.R. Baer, C.F.W. Jr, M.H. Engelhard, M.J. Danielson, R.H. Jones, J.S. Vetrano, Influence of Mg on the corrosion of Al, J. Vac. Sci. Technol. A. 18 (2000) 131–136. doi:10.1116/1.582129.

[12] R.H. Jones, J.S. Vetrano, C.F. Windisch, Stress Corrosion Cracking of Al-Mg and Mg-Al Alloys, Corrosion. 60 (2004) 1144–1154. doi:10.5006/1.3299228.

[13] J.S. Vetrano, R.E. Williford, S.M. Bruemmer, R.H. Jones, Influence of microstructure and thermal history on the corrosion susceptibility of AA 5083, in: Alum. Alloy., 1997.

[14] J. s. Vetrano, M. j. Danielson, D. r. Baer, R. h. Jones, Microchemistry and Microstructural Aspects Leading to Stress Corrosion Cracking in AA5083, in: S.K. Das (Ed.), Automot. Alloy. 1999, John Wiley & Sons, Inc., 2000: pp. 205–210. http://onlinelibrary.wiley.com/doi/10.1002/9781118787601.ch17/summary.

[15] R.H. Jones, D.R. Baer, M.J. Danielson, J.S. Vetrano, Role of Mg in the stress corrosion cracking of an Al-Mg alloy, Metall. Mater. Trans. A. 32 (2001) 1699–1711. doi:10.1007/s11661-001-0148-0.

[16] M.E. McMahon, P.J. Steiner, A.B. Lass, J.T. Burns, The effect of temper and composition on the stress corrosion cracking of Al-Mg alloys, Corrosion. 73 (2017) 347–361.

[17] N. Birbilis, R. Zhang, M.L.C. Lim, R.K. Gupta, C.H.J. Davies, S.P. Lynch, R.G. Kelly, J.R. Scully, Quantification of Sensitization in AA5083-H131 via Imaging Ga-Embrittled Fracture Surfaces, Corrosion. 69 (2013) 396–402. doi:10.5006/0804.

[18] M.E. McMahon, R.L. Haines, J.M. Schulte, P.J. Steiner, J.T. Burns, Beta Phase Distribution in Al-Mg Alloys of Varying Composition and Temper, Corros. Draft. (n.d.).

[19] M.L.C. Lim, J.R. Scully, R.G. Kelly, Intergranular Corrosion Penetration in an Al-Mg Alloy as

a Function of Electrochemical and Metallurgical Conditions, Corrosion. 69 (2013) 35–47. doi:10.5006/0722.

[20] M.L.C. Lim, J.R. Scully, R.G. Kelly, Critical Electrochemical Conditions for Intergranular Corrosion in Sensitized AA5083-H131, in: Dep. Def. Virtual Corros. Conf., 2013.

[21] S. Jain, M.L.C. Lim, J.L. Hudson, J.R. Scully, Spreading of intergranular corrosion on the surface of sensitized Al-4.4Mg alloys: A general finding, Corros. Sci. 59 (2012) 136–147. doi:10.1016/j.corsci.2012.02.018.

[22] M.A. Steiner, S.R. Agnew, Modeling sensitization of Al–Mg alloys via β-phase precipitation kinetics, Scr. Mater. 102 (2015) 55–58. doi:10.1016/j.scriptamat.2015.02.012.

[23] W.J. Golumbfskie, K.T. Tran, J.M. Noland, R. Park, D.J. Stiles, G. Grogan, C. Wong, Survey of detection, mitigation, and repair technologies to address problems caused by sensitization of Al-Mg alloys on navy ships, Corrosion. 72 (2016) 314–328. doi:10.5006/1916.

[24] C.B. Crane, R.. Kelly, R.P. Gangloff, Crack chemistry control of intergranular stress corrosion cracking in sensitized Al-Mg, Corrosion. 72 (2016) 242–263. doi:10.5006/1852.

[25] C.B. Crane, R.P. Gangloff, Stress corrosion cracking of Al-Mg alloy 5083 sensitized at low temperature, Corrosion. 72 (2016) 221–241. doi:10.5006/1766.

[26] M.E. McMahon, P.J. Steiner, A.B. Lass, J.T. Burns, The effect of loading orientation on intergranular stress corrosion cracking in Al-Mg alloys, Corrosion. 73 (2017) 713–723.

[27] M.E. McMahon, J.R. Scully, J.T. Burns, Mitigation of intergranular stress corrosion cracking in Al-Mg by electrochemical potential control, J. Miner. Met. Mater. 69 (2017) 1389–1397. doi:10.1007/s11837-017-2362-2.

[28] P. Steiner, J. Burns, Mechanistic Studies of Intergranular Stress Corrosion Cracking in Al-Mg Alloys under Atmospheric Exposure Conditions, Corrosion. 74 (2018) 1117–1131. doi:10.5006/2853.

[29] P.M. Natishan, W.E.O. Grady, E. Mccafferty, D.E. Ramaker, Chloride Uptake by Oxide Covered Aluminum as Determined by X-Ray Photoelectron and X-Ray Absorption Spectroscopy, J. Electrochem. Soc. 146 (1999) 1737–1740. doi:10.1149/1.1391835.

[30] E. McCafferty, Sequence of steps in the pitting of aluminum by chloride ions, Corros. Sci. 45 (2003) 1421–1438. doi:10.1016/S0010-938X(02)00231-7.

[31] J.-H. Ai, M.L.C. Lim, J.R. Scully, Effective Hydrogen Diffusion in Aluminum Alloy 5083-H131 as a Function of Orientation and Degree of Sensitization, Corrosion. 69 (2013) 1225–1239. doi:10.5006/0987.

[32] M.L.C. Lim, R. Matthews, M. Oja, R. Tryon, R.G. Kelly, J.R. Scully, Model to predict intergranular corrosion propagation in three dimensions in AA5083-H131, Mater. Des. 96 (2016) 131–142.

[33] M.E. McMahon, J.R. Scully, J.T. Burns, Mitigation of Intergranular Cracking in Al-Mg Alloys via Zn-Based Electrode Potential Control in Sodium Chloride Solution, Corrosion. (2019).

[34] M. Sakairi, K. Otani, R. Sasaki, Electrochemical noise evaluation of metal cation effects on galvanic corrosion of aluminum alloys in low concentration of chloride ion containing solutions, Procedia Eng. 86 (2014) 589–596. doi:10.1016/j.proeng.2014.11.084.

[35] M.G.A. Khedr, A.M.S. Lashien, The role of metal cations in the corrosion and corrosion inhibition of aluminum in aqueous solutions, Corros. Sci. 33 (1992) 137–151.

[36] M. Khedr, A. Lashien, Corrosion behavior of aluminum in the presence of accelerating metal cations and inhibition, J. Electrochem. Soc. 136 (1989) 968–972. doi:10.1149/1.2096895.

[37] S. Islam, Effects of Zn 2 + Concentration on the Corrosion of Mild Steel in NaCl Aqueous Solutions, J. Electrochem. Soc. 166 (2019) 83–90. doi:10.1149/2.1271902jes.

[38] E. Tada, S. Satoh, H. Kaneko, The spatial distribution of Zn2+during galvanic corrosion of a Zn/steel couple, Electrochim. Acta. 49 (2004) 2279–2285. doi:10.1016/j.electacta.2004.01.008.

[39] P. Volovitch, C. Allely, K. Ogle, Understanding corrosion via corrosion product characterization: I. Case study of the role of Mg alloying in Zn-Mg coating on steel, Corros. Sci. 51 (2009) 1251–1262. doi:10.1016/j.corsci.2009.03.005.

[40] P. Volovitch, T.N. Vu, C. Allély, A. Abdel Aal, K. Ogle, Understanding corrosion via corrosion product characterization: II. Role of alloying elements in improving the corrosion resistance of Zn-Al-Mg coatings on steel, Corros. Sci. 53 (2011) 2437–2445. doi:10.1016/j.corsci.2011.03.016.

[41] K. Ogle, V. Baudu, L. Garrigues, X. Philippe, Localized Electrochemical Methods Applied to Cut Edge Corrosion, J. Electrochem. Soc. 147 (2000) 3654. doi:10.1149/1.1393954.

[42] D.M. Drazic, L.Z. Vorkapic, Inhibitory effects of manganeous, cadmium, and zinc ions on hydrogen evolution reaction and corrosion of iron in sulphuric acid solutions, Corros. Sci. 18 (1978) 907–910.

[43] S. Zhang, T. Shibata, T. Haruna, Inhibition effect of metal cations to intergranular stress corrosion cracking of sensitized Type 304 stainless steel, Corros. Sci. 47 (2005) 1049–1061. doi:10.1016/j.corsci.2004.06.014.

[44] M.E. McMahon, P.J. Steiner, A.B. Lass, J.T. Burns, The effect of temper and composition on intergranular stress corrosion cracking in Al-Mg alloys, Corrosion. 73 (2017) 347–361. doi:10.5006/2317.

[45] R.P. Gangloff, D.C. Slavik, S. Piascik, R.H. Van Stone, Direct current electrical potential measurement of the growth of small cracks, in: J.M. Larsen, J.E. Allison (Eds.), Small-Crack Test Methods, American Society for Testing and Materials, Philadelphia, PA, 1992: pp. 116–168.

[46] A. Popernack, Loading Rate Effects on the Hydrogen Enhanced Cracking Behavior of Ni- and Co-based Superalloys for Marine Applications, University of Virginia, 2017.

[47] R. Gangloff, H. Ha, J. Burns, J. Scully, Measurement and Modeling of Hydrogen Environment-Assisted Cracking in Monel K-500, Metall. Mater. Trans. A. 45 (2014) 3814–3834.

[48] M.L.C. Lim, Intergranular Corrosion Propagation in Sensitized Al-Mg Alloys, The University of Virginia, 2016.

[49] M.E. McMahon, R.J. Santucci Jr., J.R. Scully, Advanced Chemical Stability Diagrams to Predict the Formation of Complex Zinc Compounds in Chloride Environment, Sci. Rep. (n.d.).

[50] E. Rodil, J.H. Vera, Individual activity coefficients of chloride ions in aqueous solutions of MgCl2, CaCl2 and BaCl2 at 298.2 K, Fluid Phase Equilib. 188 (2001) 15–27.

[51] B.F. Brown, Stress Corrosion Cracking in High Strength Alloys, in: J.C. Scully (Ed.), Theory SCC Alloy., NATO Scientific Affairs Division, Brussels, Belgium, 1971: p. 186.

[52] P. Buckley, B. Placzankis, J. Beatty, R. Brown, Characterization of the Hydrogen Embrittlement Behavior of High-Strength Steels for Army Applications, in: Corros. 94, NACE International, Houston, TX, 1994: p. Paper No. 57.

[53] Z.D. Harris, J.D. Dolph, G.L. Pioszak, B.C. Rincon Troconis, J.R. Scully, J.T. Burns, The Effect of Microstructural Variation on the Hydrogen Environment-Assisted Cracking of Monel K-500, Metall. Mater. Trans. A Phys. Metall. Mater. Sci. (2016) 1–23. doi:10.1007/s11661-016-3486-7.

[54] N. Totsuka, Z. Szklarska-Smialowska, Effect of Electrode Potential on the Hydrogen-Induced Igscc of Alloy 600 in an Aqueous Solution At 350 C., Corrosion. 43 (1987) 734–738. doi:10.5006/1.3583860.

[55] G. Burnell, D. Hardie, R.N. Parkins, Stress corrosion and hydrogen embrittlement of two precipitation hardening stainless steels, Br. Corros. J. 22 (1987) 229–237.

[56] K.B. Das, W.G. Smith, R.W. Finger, J.N. Masters, Hydrogen embrittlement of cathodically protected 15-5 PH stainless steel, in: Proc. 2nd Int. Congr. Hydrog. Met., Pergamon, Oxford, UK, 1977.

[57] P.S. Tyler, M. Levy, L. Raymond, Investigation of the conditions for crack propagation and arrest under cathodic polarization by rising step load bend testing, Corrosion. 47 (1991) 82–87. doi:10.5006/1.3585857.

[58] B.A. Kehler, J.R. Scully, Predicting the effect of applied potential on crack tip hydrogen concentration in low-alloy martensitic steels, Corrosion. 64 (2008) 465–477. doi:10.5006/1.3278484.

[59] W.H. Hartt, C.C. Kumria, R.J. Kessler, Influence of potential, chlorides, pH, and precharging time on embrittlement of cathodically polarized prestressing steel, Corrosion. 49 (1993) 377–385. doi:10.5006/1.3316064.

[60] R. Nishimura, The effect of potential on stress corrosion cracking of type 316 and type 310 austenitic stainless steels, Corros. Sci. 34 (1993) 1463–1473. doi:10.1016/0010-938X(93)90241-8.

[61] L.M. Young, G.A. Young, J.R. Scully, R.P. Gangloff, Aqueous environmental crack propagation in high-strength beta titanium alloys, Metall. Mater. Trans. A. 26 (1995) 1257–1271. doi:10.1007/BF02670620.

[62] D.G. Kolman, J.R. Scully, Understanding the potential and pH dependency of high-strength β-titanium alloy environmental crack initiation, Metall. Mater. Trans. A Phys. Metall. Mater. Sci. 28 (1997) 2645–2656. doi:10.1007/s11661-997-0021-x.